# ABSTRACT

Title of dissertation: MORPHING WAVERIDERS
FOR ATMOSPHERIC ENTRY

Jesse R Maxwell
Doctor of Philosophy, 2019

Dissertation directed by: Professor Elaine S. Oran
Department of Aerospace Engineering

The primary challenge for vehicles entering planetary atmospheres is surviving the intense heating and deceleration encountered during the entry process. Entry capsules use sacrificial ablative heat shields and sustain several g deceleration. The high lift produced by the Space Shuttle geometry resulted in lower rates of heating and deceleration. This enabled a fully reusable vehicle that was protected by heat shield tiles.

Hypersonic waveriders are vehicles that conform to the shape of the shock wave created by the vehicle. This produces high compression-lift and low drag, but only around a design Mach number. Atmospheric entry can reach speeds from zero to as high as Mach 40. A morphing waverider is a vehicle that deflects its flexible bottom surface as a function of Mach number in order to preserve a desired shock wave shape. It was demonstrated in this work that doing so retains high aerodynamic lift and lift-to-drag ratio across a wide range of Mach number.

Numerical simulations were conducted for case-study waveriders designed for

Mach 6 and 8 for flight at their design conditions as well as with variations in angle-of-attack and Mach number. A single-species air model was used between Mach 1 and 12 with the RANS $k-\omega$ SST and LES-WALE turbulence models. A seven-species air model was used for Mach 15 at 60km altitude and Mach 20 at 75km.

Analytical methods were used to construct a reduced-order model (ROM) for estimating waverider aerodynamic forces, moments, and heating. The ROM matched numerical simulation results within 5-10% for morphing waveriders with variations in angle-of-attack, but discrepancies exceeded 20% for large deviations of rigid vehicles from their design Mach numbers.

Atmospheric entry trajectory simulations were conducted using reduced-order models for morphing waverider aerodynamics, the Mars Science Laboratory (MSL) capsule, and the Space Shuttle. Three morphing waveriders were compared to the Space Shuttle, which resulted in reduced heating and peak deceleration. One morphing waverider was compared to the MSL capsule, which demonstrated a reduction in the peak stagnation heat flux, a reduction in the peak and average deceleration, and a reduction in the peak area-averaged heating.

# MORPHING WAVERIDERS FOR ATMOSPHERIC ENTRY

by

Jesse R Maxwell

Dissertation submitted to the Faculty of the Graduate School of the
University of Maryland, College Park in partial fulfillment
of the requirements for the degree of
Doctor of Philosophy
2019

Advisory Committee:
Professor Elaine S. Oran, Chair/Advisor
Associate Professor Johan Larsson, Dean's Representative
Professor Emeritus John D. Anderson, Jr.
Research Associate Professor Carolyn Kaplan-Solomond
Professor James Baeder
Professor Norman M. Wereley

# Dedication

For my wife, Zoë, who brings out the best in me and always challenges me to do better; for my parents, who taught me the value of education and curiosity from a young age; and for my in-laws, who have been very encouraging and helpful since the day we met.

# Acknowledgments

I would like to thank my adviser, Dr. Oran, for helping me shape this collection of work into a coherent, meaningful dissertation.

I have had many conversations with colleagues who contributed to the development of these concepts, methods, the direction of this work, and extension to other applications. Specifically, I'd like to thank Robert Baldauff, Triem Hoang, Tim Holman, Evan Hyde, Austin Phoenix, Gabe Goodwin, Evan Rogers, and Brandon Powell.

The graduate school professors who taught me the material I would directly use to develop this work are Balakumar Balachandran, David Akin, James Baeder, Johan Larsson and Stuart Laurence. I am deeply grateful to have learned from and been inspired by these excellent educators.

I would like to thank the leadership, administrative staff, and scientists and engineers at the U.S. Naval Research Laboratory for enabling an exhilarating, challenging, and meaningful career. I'd like to specifically acknowledge the Edison Graduate Training Program for supporting me in the pursuit of this degree, the NRL Base Program for supporting my related work in hypersonics, and supervisory support and oversight by Robert Baldauff.

Finally, I would like to thank the educator and author who inspired my interest in aerospace engineering upon independent study of his Introduction to Flight book and every one of his books since, Dr. John D. Anderson, Jr.

# Table of Contents

# List of Tables

# List of Figures

# List of Abbreviations

| | |
|---|---|
| AUSM | Advection Upstream Splitting Method |
| CFD | Computational Fluid Dynamics |
| CFL | Courant-Friedrichs-Lewey number |
| COM | Center of Mass |
| CPU | Central Processing Unit |
| DOF | Degree of Freedom |
| DSMC | Direct-Simulation Monte Carlo |
| EV | Entry Vehicle |
| FVM | Finite-Volume Method |
| GTO | Geostationary Transfer Orbit |
| LEO | Low-Earth Orbit |
| LER | Leading-Edge Radius |
| LES | Large-Eddy Simulation |
| MSL | Mars Science Laboratory |
| NASA | National Aeronautics and Space Administration |
| ODE | Ordinary Differential Equation |
| PO | Polar Orbit |
| PVO | Planform Vertical Offset |
| ROM | Reduced-Order Model |
| SEF | Sharp-Edge Fillet |
| SSO | Space Shuttle Orbiter |
| SST | Shear-Stress Transport |
| TPS | Thermal Protection System |
| UHTC | Ultra-High Temperature Ceramic |
| WALE | Wall-Adapted Local Eddy Viscosity |
| WRAITH | Waverider Reduced-order Analysis and Investigative Tool for Hypersonics |

# Chapter 1: Introduction

The NASA Space Shuttle Orbiter (SSO) marked the reusable vehicle in the history of space flight, a capability that promised to reduce the complexity and increase the frequency of space access. This achievement was enabled by improvements in materials and by modifying the aerodynamic design so that they could withstand the extreme conditions endured during atmospheric reentry.

Now we ask: *Can we do better than the Space Shuttle?* Can we use our knowledge of the fundamental principles of high-speed flow and modern computational tools to design an entry vehicle with even better high-speed aerodynamic properties? Is it possible that such improvements could result in atmospheric entry conditions and vehicles not much different than those in routine commercial air travel?

The objective of this work is to evaluate a concept for Earth and Mars entry vehicles, the "morphing waverider," that produces high aerodynamic performance across the wide range of conditions encountered in atmospheric entry. The introduction includes a discussion of atmospheric flow regimes and how entering vehicles interact with the background atmosphere. The discussion of entry physics and aerodynamics is presented as it relates to near-Earth space access and planetary exploration. Specific examples are considered for low-altitude orbit of Earth and

interplanetary missions from Earth to Mars. Hypersonic waveriders are then introduced. These are a class of vehicles that produce the highest known aerodynamic performance at entry speeds. Reduced-order models for aerodynamics and the importance of dynamic stability are then discussed. This is followed by a review of related work, the scope of the present work, and a thesis outline.

## 1.1 Flow Regimes for Vehicles Entering Earth's Atmosphere

Flight in Earth's atmosphere from zero to atmospheric entry speeds can be categorized into the regimes outlined in Fig. 1.1. Each flight regime has physical properties that must be accounted for in the context of atmospheric entry [1]. There are features of high-speed flight that are insignificant at lower speeds. For example, as the flight speed increases beyond Mach 1, flow features include shock waves, high temperatures and rates of heating, chemical reactions, ionization, and nonequilibrium chemistry and molecular kinetics. The entire entry process into the Earth's atmosphere from low-Earth orbits of 150-500km spans approximately Mach 25-30 down to zero [2]. Each of the flight regimes listed in Fig. 1.1 is discussed in the following paragraphs.

Early aircraft and modern general aviation aircraft typically fly at speeds less than 100 m/s, approximately 30% of the speed of sound [1]. As shown in Fig. 1.1, the flow in this regime is "incompressible," which greatly simplifies the analysis of the aerodynamics. For incompressible flow, the near-body density field changes by less than 5% and can be assumed constant. Temperatures do not noticeably change,

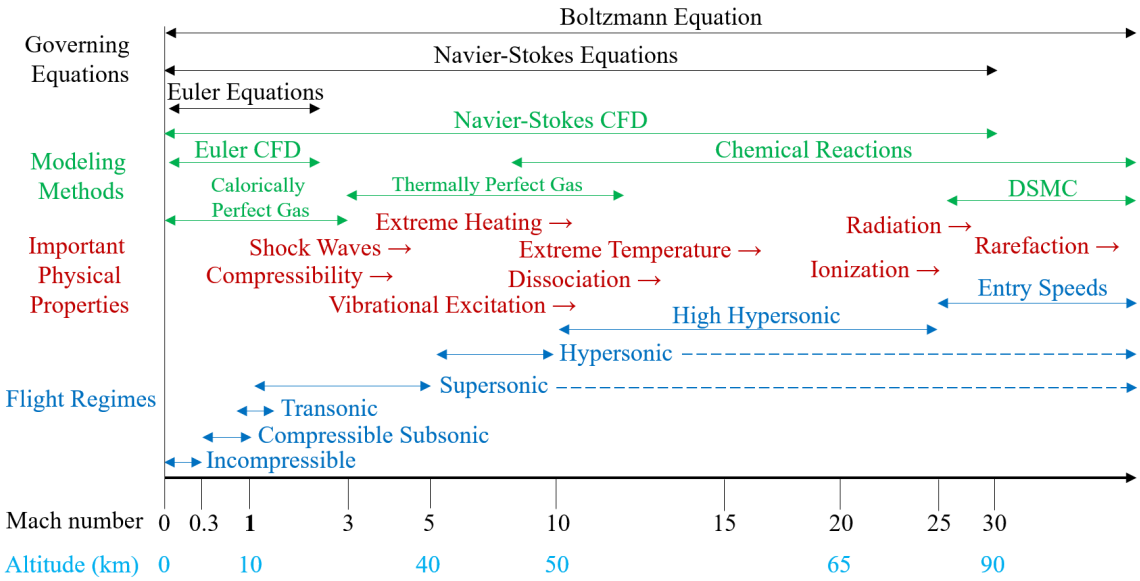


Figure 1.1: Flight regimes of low-Earth orbit entry vehicles as a function of Mach number and relevant altitude. The governing equations are also shown in their approximate realm of applicability in these flow regimes, modeling methods, important physical properties and effects, and the named flight regimes [2]. The subsonic and supersonic flight regimes have a precise border at Mach 1, whereas all other flight regimes, important physical properties, and modeling method ranges are approximate.

friction may be neglected, and only the pressure and velocity fields are allowed to vary.

As conditions increase beyond Mach 0.3 but less than Mach 1, free-stream air is compressed by a vehicle. This flight regime is appropriately described as "compressible." For most commercial and military aviation, the density variations in the flow are significant enough that they must be accounted for in estimating aerodynamic properties of a vehicle. Similar to incompressible flow, however, temperature variations are not significant and friction is a minor contributor to the net drag force [3].

The regime between approximately Mach 0.8 and 1.3 is referred to as "transonic." Local variations in flow speed around a vehicle can exceed the speed of sound in transonic flight [3]. Flow fields can include shock waves, supersonic regions, and subsonic regions simultaneously at different locations throughout the flow. Shock waves cause rapid pressure jumps and can greatly affect the lift, drag, control, and stability of vehicles in transonic flight.

In the supersonic flow regime, above Mach 1, shock waves are created by all vehicles [1]. Post-shock flow and the near-body flow field may have regions of subsonic flow or the entire near-body flow field may remain supersonic. Pressure, temperature, and density change discontinuously across a shock wave created by a vehicle. The relative magnitude of the change in these variables is related to how blunt the local vehicle geometry is and how fast it is flying. The angle of a shock wave on the vehicle becomes smaller as the Mach number increases. The rise in pressure and temperature across the shock increases with Mach number, which

pushes the hotter, denser flow closer to the vehicle's surface. As the flight speed of the vehicle increases further, friction and heating become increasingly important and must be accounted for at speeds above approximately Mach 2. Between Mach 2 and 3, the choice of vehicle material becomes severely limited by the high temperatures encountered. Materials considerations are described separately in Section 1.1.1. By approximately Mach 3, the bonds between the diatomic oxygen and nitrogen air molecules, $O_2$ and $N_2$, begin to vibrate. This "vibrational excitation" begins to change the physical properties of air with increasing flight speed, and these property changes begin to affect the aerodynamic properties of vehicles.

The hypersonic flight regime begins at approximately Mach 5, or 1,500m/s. Aerodynamic heating becomes the most significant feature of increasing flight speed [4]. Thick, turbulent, viscous boundary layers along a vehicle's surface cause additional heating and drag. Diatomic oxygen begins to dissociate near the leading edge by Mach 6. The dissociated, highly reactive free-molecular oxygen cascades along the surface of the vehicle downstream. By Mach 8 in the stratosphere, 10% of the oxygen has become dissociated and envelopes the vehicle in a highly reactive sheath of free-molecular oxygen.

At hypersonic speeds, friction becomes a significant contributor to the drag force and heating due to turbulent flow along the surface of a vehicle. A viscous component as high as 20-30% of the overall drag force may be expected for a streamlined vehicle.

Between Mach 10 and 25, referred to as the "high-hypersonic" flight regime, chemically reactive flow becomes a dominant feature. Ninety percent of the oxygen

is dissociated by Mach 15 and ionization occurs in trace quantities. The stagnation region temperatures can exceed 10,000K and radiative heat transfer becomes increasingly important above Mach 20 [2]. Ionization requires such large amounts of energy and high temperatures that only a few percent of the flow field is ionized by Mach 25 [4]. Ultra-high-temperature ceramics (UHTCs) and refractory metals can be used for short-duration flight in this speed range.

At the highest hypersonic flight condition, "entry speeds" begin on the order of 7.8km/s for low-Earth orbit (LEO) and reach 11km/s for lunar return [1]. In this flow regime, ionization is a dominant feature. At least 10% of the flow field is ionized at lunar return speeds. Radiation is the dominant mechanism of heat transfer as flow temperatures reach tens of thousands of Kelvin. To a rough approximation, radiative power depends on Mach number to the eighth power [4], and so becomes increasingly important at the highest Mach numbers. Because temperatures above Mach 30 can reach tens of thousands of degrees kelvin, sacrificial heat shields, known as ablative thermal protection systems [2], are used to protect entry vehicles. Ablation removes thermal energy from the hot flow by absorbing it into the phase change of the sacrificial ablative material rather than allowing the vehicle to be heated by the extreme temperature gradients. Solid material sublimates into vapor and the mix of hot air and ablation products convect downstream, leaving the near-body flow field and taking thermal energy away with it. These gaseous ablation products affect the near-body flow field and the aerodynamic properties of a vehicle.

The first regime encountered by entry vehicles at their highest speed and altitude is hypersonic rarefied flow. While air is composed of discrete molecules,

the numbers of molecules involved in the flow around a vehicle can be billions of billions or larger [5]. Numerical simulation of each molecule individually in the high densities encountered at low altitude is an intractable problem. At lower altitudes, air can be considered a continuous medium and fields of flow variables are tracked rather than individual molecules. At altitudes above approximately 95km, however, the average distance between molecular collisions becomes large enough that the continuum-flow approximation no longer applies [6]. This occurs when the Knudsen number, $Kn = \lambda/L$, becomes large relative to the mean free path between molecular collisions, $\lambda$, and the wingspan or diameter of a vehicle, $L$. The wingspan or diameter of an entry vehicle typically ranges from 4m for a capsule to 24m for the Space Shuttle [1].

Though these thresholds are debated, locally rarefied flow must be considered for $Kn > 10^{-2}$, such as in the vehicle wake or around a control surface, and globally rarefied flow must be treated for $Kn > 10^{-1}$, which affects the entire near-body flow field and vehicle aerodynamic properties. Boundary layer effects due to rarefaction and complications that affect the viscous drag at a vehicle's wall must be treated for $Kn > 10^{-3}$ [7]. The variability of Knudsen number with altitude is depicted for Earth and Mars in Fig. 1.2 for a 10m vehicle. A depiction of rarefied flow about a 1m Mach 10 flat plate is presented with varied altitude in Fig. 1.3, from [8] using the discrete particle analysis method DSMC [11] solved in the analysis code MONACO [12]. This figure illustrates the highly rarefied nature of flow above 120km and the coherent shock structure that develops as a vehicle descends, coalescing from a "cloud" of particles at higher altitudes into the recognizable shock surfaces

of continuum flow fields.

At hypersonic speeds in the rarefied regime, chemical reactions between air constituents occur over finite time. These reactions must be explicitly accounted for over distance and time, described as "non-equilibrium" chemistry. Many thermodynamic properties and our estimates of their effects on the flow field are based on a known probability distribution of the molecular speeds. This is known as "kinetic" equilibrium. In rarefied flow, the probability distribution of molecular speeds may not conform to the equilibrium distribution [5]. This kinetic non-equilibrium cannot be analyzed with continuum methods, which are formulated based on the assumption of kinetic equilibrium. Particle analysis methods such as Molecular Dynamics for highly rarefied flows and Direct Simulation Monte Carlo for transitional and rarefied flows must be used to account for the effects of kinetic non-equilibrium [6]. For a 10m entry vehicle, the effects of kinetic non-equilibrium and rarefied flow become increasingly important above 95km and critical by 110km. As is discussed in section 2.1, the effects of rarefaction and kinetic non-equilibrium may be neglected for heavy, low-lift vehicles, while consideration of these effects become increasingly important for accurately estimating the aerodynamic properties and flight paths for lighter, high-lift entry vehicles.

These diverse flight regimes and the conditions experienced by vehicles passing through them illustrate the important considerations required for optimizing the aerodynamic properties of a vehicle through a dynamically changing atmosphere. For example, the SSO descended from the top of the atmosphere at nearly 8km/s and 120km to subsonic speeds 10km above ground in approximately 2,000 seconds.

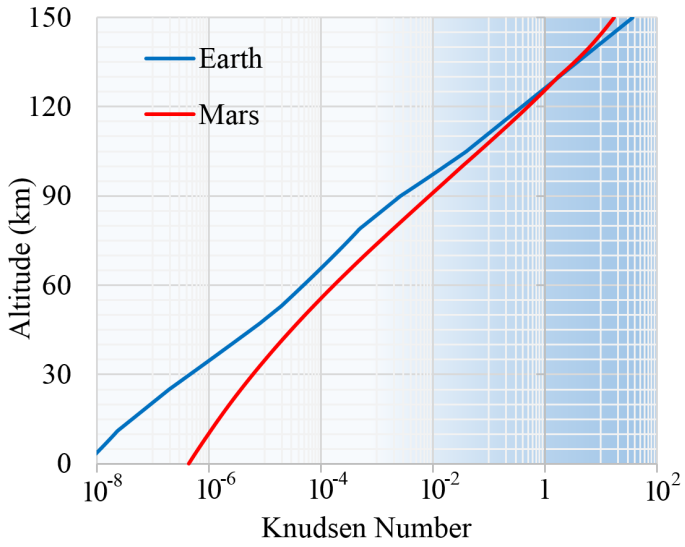


Figure 1.2: Knudsen number for Earth and Mars with altitude for 10m vehicle using atmosphere properties from [13–15].

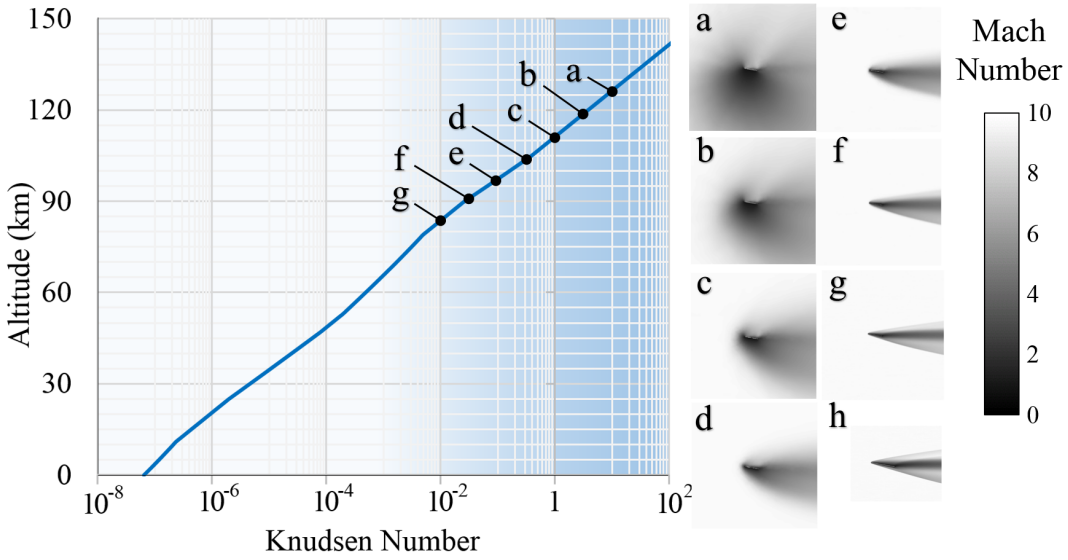


Figure 1.3: Mach number contours of a 1m Mach 10 flat plate at 10° angle-of-attack for various Knudsen number and corresponding altitude in Earth atmosphere. The Knudsen range is shaded to depict transition from continuum to rarefied regime. Adapted from [8–10].

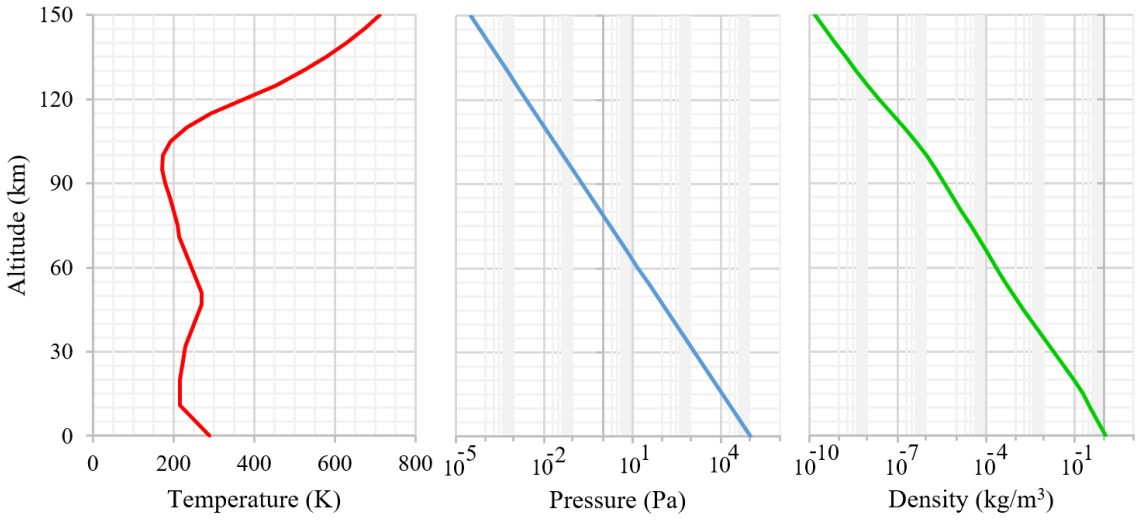


Figure 1.4: Temperature, pressure, and density with altitude based on the 1976 US Standard Atmosphere [13].

This variability is shown in the flight paths of several Earth entry vehicles in Fig. 1.5. The nominal flight paths of the Space Shuttle Orbiter and the Apollo capsule returning from LEO and the Apollo capsule returning from the moon are overlaid along with single-point flight conditions for various supersonic and hypersonic vehicles for comparison. The 10% and 90% thresholds for the fraction of molecules experiencing vibrational excitation and dissociation with speed and altitude in the flow field near the leading edge of a vehicle are also illustrated. The variability in these effects with speed and altitude are due to the variations in air density and temperature with altitude, depicted in Fig. 1.4 according to the 1976 US Standard Atmosphere [13, 16–18].

At more than twice the speed of a conventional airliner, the Concorde Supersonic Transport cruised at 18km altitude and 0.6km/s, Mach 2 in the stratosphere [19]. At this speed and altitude, the fraction of molecules that are vibra-

tionally excited in the near-body flow field is less than 10%. The SR-71 supersonic reconnaissance plane cruised at 24km and 1.0km/s, or Mach 3.3 [20]. At this speed, nearly 20% of the molecules are vibrationally excited and the associated changes in the physical properties of the air begin to affect the vehicle's aerodynamic properties. The X-51A WaveRider scramjet demonstrator cruised at 21km altitude and 1.5km/s [21], reaching the hypersonic flight regime where extreme heating and aerodynamic forces limited its flight duration to hundreds of seconds because of the high speed and air density. The X-15 piloted hypersonic research aircraft reached a maximum speed of 2.0km/s at 31km and a maximum altitude of 108km at 1.7km/s [22]. At the maximum speed condition, the vehicle flew like an aircraft in dense, turbulent flow, with the variability in the properties of air resulting in complications for aerodynamic performance and control. At the maximum altitude condition, the vehicle flew as a suborbital nearly-ballistic projectile through rarefied flow with minimal control authority. At this altitude and speed, a few percent of the diatomic oxygen became dissociated and accelerated oxidation of the aircraft's Inconel outer skin. The X-43A hydrogen-fuel scramjet demonstrator reached 3.3km/s, approximately Mach 9.6, at 34km and was self-propelled for 11 seconds [23, 24]. Despite record flight speeds and altitudes of these supersonic and hypersonic vehicles, none reached half of the speed of an entry vehicle and only the X-43A flew in a regime where air chemistry affected its aerodynamics.

The SSO and Apollo Capsule descend from a 200km LEO through an entry interface of 120km and approximately 7.9km/s. There is minimal control authority or flight path variation in the rarefied regime, and each vehicle follows the same

flight path despite substantially different aerodynamic and inertial properties until approximately 95km. Below this altitude, the vehicle aerodynamic and inertial properties result in a deviation of their flight paths by as much as 20km during deceleration from nearly 8km/s down to approximately 3km/s. The mechanism by which the SSO retains altitude and the implications for heating and deceleration are the subject of Section 1.2. Figure 1.5 shows that rarefied flow has minimal effects on the flight path for vehicles such as the SSO and Apollo Capsule. These vehicles spend much of their flight paths in reactive flow at altitudes between approximately 45km and 80km.

For the first half of the SSO descent from 120km, the nitrogen dissociation and reactions with dissociated oxygen are important. The flow along the SSO is primarily laminar. The majority of orbital energy is dissipated between 70 and 50km for the SSO and just 50 and 45km for the Apollo Capsule. These flow regimes include both the peak deceleration and the peak heating for these entry vehicles, spanning chemical reactions with nitrogen and oxygen as well as laminar through majority-turbulent flow. For the final third of the descent and deceleration, the flow field is very turbulent, chemical reactions are minimal, and the vibrational excitation of air molecules becomes negligible below approximately 25km.

In contrast to return from LEO, the Apollo Capsule returned from the moon at nearly 11km/s through highly reactive and ionized nitrogen and oxygen. The lunar return capsule reached a lower altitude for the majority of its deceleration, dissipating approximately three quarters of its initial energy between 45 and 40km. As is discussed in Chapter 2, this combination of higher speed and higher density

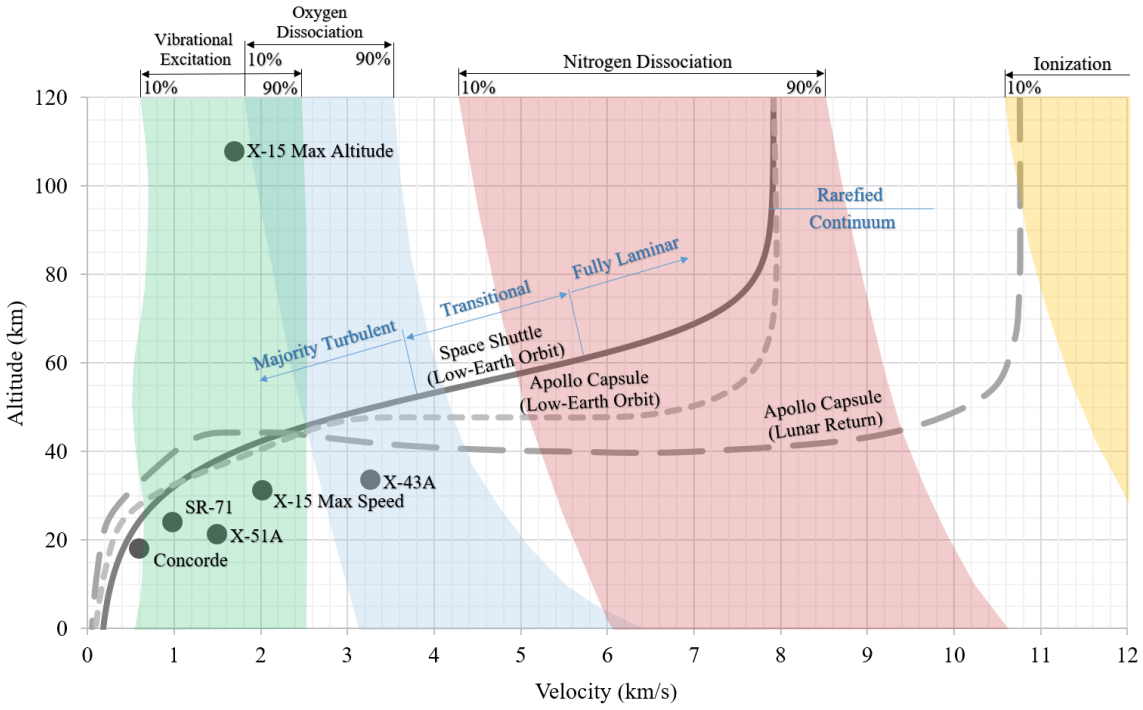


Figure 1.5: Air chemistry near the leading edge with speed and altitude for Earth entry vehicles. Velocity-altitude map adapted from [4] with vehicle data from [19–24] and flight paths adapted from [2].

and lower altitude results in substantially higher heating than a high-lift vehicle such as the SSO returning from LEO.

### 1.1.1 Materials Considerations

The temperature and rates of heating that a vehicle encounters during flight restrict the material options available. Peak temperatures and rates of heating near the leading edge may require different materials at the leading edge than are allowable on the windward or leeward planform of a vehicle. Conversely, materials limitations or capabilities may define requirements on vehicle aerodynamics or flight path. It is discussed in Section 2.1 that reducing the payload mass of a given vehicle correspondingly reduces the heating and peak deceleration of the vehicle during the entry process.

For incompressible through subsonic compressible flow, aluminum alloys are preferred for structural and external surface components due to their high strength-to-weight ratios and the temperatures encountered at these speeds. In transonic flow, temperatures may rise tens of degrees near the leading edge compared to the free stream, but maximum temperatures are of minimal concern for common aerospace materials such as aluminum alloys. As the flight speed of a vehicle increases, friction and heating become increasingly important and must be accounted for at speeds above approximately Mach 2. Aluminum alloys begin to rapidly weaken beyond 200°C and lose over 90% of their strength by 300°C [27]. At Mach 2, temperatures at the nose tips and leading edges of wings and fins are high enough that

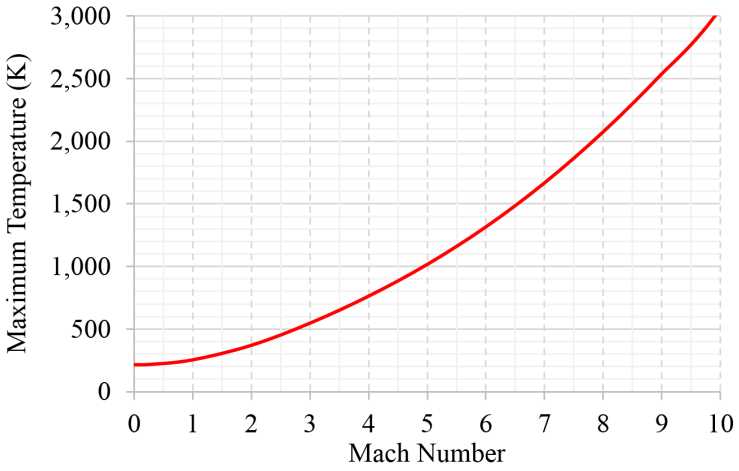


Figure 1.6: Maximum air temperature with Mach number in the stratosphere.

aluminum can no longer safely be used for extended durations. Higher service-temperature materials such as titanium and steels must be used in these regions, while aluminum may still be used for the majority of the planform and internal structure. The increase in temperature along with Mach number is depicted in Fig. 1.6 for equilibrium chemically reacting air in the stratosphere where the ambient air temperature is 217K. By Mach 3, approximately 1,000m/s, temperatures become hot enough that the entire exterior of a vehicle must be titanium or other heat-resistant material. For example, the Mach 3.3 SR-71 reconnaissance aircraft was primarily titanium [20]. Conventional turbojet engines may reach beyond Mach 2, but encounter rotational speeds and temperatures too high to operate at Mach 3 and above [25].

Entering the hypersonic regime, at Mach 5, temperatures at the leading edge exceed the service temperature of any titanium alloy. These high temperatures require the use of heavier high-temperature metals, high-temperature composites,

or cooling systems for sustained flight [26]. Oxidation-resistant materials must be used on all surfaces due to increased exposure to free-molecular oxygen and higher temperature-dependent reaction rates. Options are carbon-based composite materials and the refractory metals: primarily niobium, molybdenum, tantalum, tungsten, rhenium, and their alloys [27]. For extended flight durations above Mach 6, the entire exterior of an aircraft must be made of oxidation-resistant materials with higher service temperatures than titanium alloys. For example, the X-15 Hypersonic Research Aircraft used Inconel for speeds up to Mach 6.7 [22].

By Mach 8, 10% of the oxygen is dissociated and envelopes the vehicle in a highly reactive sheath of free-molecular oxygen. While specialized materials exist for sustained flight at speeds up to Mach 10, their use is accompanied by the penalties of increased cost and fabrication complexity. Even the least expensive refractory metal is more than an order-of-magnitude more costly than aerospace-grade aluminum alloys [28–31]. Refractory metal strength-to-weight ratios are much worse than aluminum alloys, which results in a heavier vehicle with mass-related performance penalties. Additionally, fabrication using these metals or high-temperature composites pose many challenges in comparison with conventional machining, casting, forming, and fastening. At speeds in the high-hypersonic regime, Mach 10-25, flight durations must be limited based on transient heating and a vehicle's thermal mass and thermal management. Vehicles entering from LEO, such as the SSO, may accomplish their descent with survivable, reusable materials by ensuring that transient temperatures along the trajectory never exceed critical thresholds [2].

For the highest heat fluxes such as during lunar return at 11km/s, ablative heat

shields are thought to be the only viable option [2,32]. There are four disadvantages to ablation. First, there is a minimum temperature required for pyrolysis of the sacrificial material. Second, the erosion of the surface increases roughness and adds to drag and heating. Third, the erosion changes the shape of a vehicle and is typically non-uniform, which introduces control and stability complications. Finally, ablation is inherently a consumable process that limits the possible duration of flight.

## 1.2 Early Entry Vehicles

Low Earth Orbit (LEO) begins at approximately 200km above mean sea level (MSL). Entry from LEO occurs typically at 7.8km/s with noticeable aerodynamic deceleration for an entry vehicle beginning at approximately 120km, where the atmosphere becomes sufficiently dense [33]. Enduring excessive deceleration is a challenge in Earth's atmosphere due to the relatively high density. By contrast, decelerating to sufficiently low speeds to touchdown safely is the challenge in the thinner Martian atmosphere [34]. In either case, it is shown in this section that minimizing the mass, maximizing the lift coefficient, and maximizing the lift-to-drag ratio of an entry vehicle yields less severe heating and deceleration during the entry process [2].

The development of entry vehicles includes suborbital ballistic capsules, lifting capsules that were used for entry from LEO and lunar return, and high-lift vehicles such as the Space Shuttle Orbiter (SSO) used for LEO return. Lifting capsules have also been used for interplanetary missions. This section describes the progression from ballistic capsules to the high-lift SSO and how the mechanism of lift enabled

flight paths that resulted in lesser heating and peak deceleration.

During the first U.S. human suborbital space flight experiment in 1961, Redstone 3, part of Project Mercury, astronaut Alan Shepard endured 11.6g peak deceleration during his ballistic descent back into the atmosphere. This and subsequent flight experiments flew along a trajectory intended to match the return from LEO [33]. The ballistic *Freedom 7* entry capsule used in this experiment produced no nominal lift force. These earliest entry vehicles fell into the atmosphere and relied purely on aerodynamic braking to slow the capsule during descent. This ballistic descent resulted in reaching the lower, denser atmosphere at high speeds. Purely ballistic entry forced an astronaut to endure a peak deceleration of 10-12g from low Earth orbit (LEO) [35], but it was discovered during Project Mercury that even small amounts of lift can reduce this to 8-9g [36]. Modern lifting capsules can limit this peak to approximately 5-6g [37], and high-lift vehicles such as the Space Shuttle Orbiter (SSO) reduce this to less than 3g [38] depending on vehicle loading and entry conditions. A ballistic capsule free body diagram is depicted in the left half of Fig. 1.7 and a lifting capsule is depicted in the right half of Fig. 1.7. A ballistic capsule can be made into a lifting capsule by offsetting the center of mass (COM) as depicted in Fig. 1.7. This COM offset enables a capsule to fly with a nonzero angle of attack, $\alpha$, generating a lift vector. This lift vector results in shallower flight path angles, $\alpha_p$, which allows a vehicle to dissipate its initial energy at higher altitudes where heating and drag are lesser than at lower altitudes. The shallow flight path angle and longer duration of deceleration and reduces peak deceleration and heating during entry; effects that are attributed to the lift vector and improved lift-to-drag

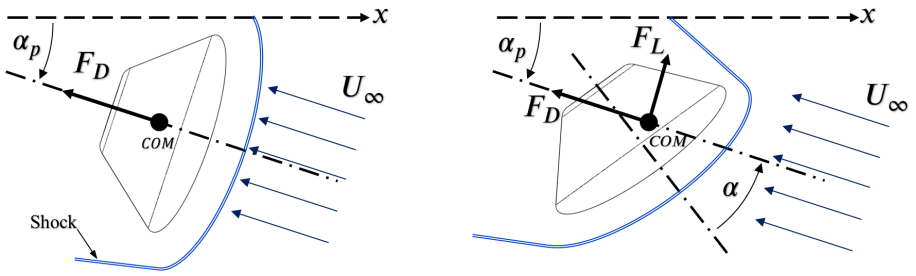


Figure 1.7: Ballistic entry-capsule free-body diagram (left) and lifting capsule (right). These diagrams illustrate that the offset center of mass (COM) creates an imbalance in pressure-based aerodynamic forces that result in an angle-of-attack and a net lift force.

ratio.

The Gemini capsules and the Apollo Command Module produced a lift-to-drag ratio of 0.3-0.4 in the hypersonic regime [39]. The TPS of the Apollo capsule eroded 50mm during entry, supported by a 250mm-thick support and interface structure to the capsule airframe. The combined mass of an ablative TPS and structure can account for more than 30% of the entry mass of a lifting capsule. The Space Shuttle Orbiter (SSO) improved upon the lift-to-drag ratio up to approximately 1 in the hypersonic regime [40]. This increase was enough to reduce the peak deceleration down to 1-3g depending on the initial flight path angle and landing weight [38, 40]. This also simplified the sacrificial ablative heat shield of the Apollo capsule to reusable 25mm-thick ceramic tiles across the windward planform and UHTCs at the leading edge of the SSO [38].

To illustrate the penalty of a more robust airframe or TPS, the empty SSO outweighed its payload by a factor of at least three. The thermal protection system

(TPS) accounted for 12.5% of the SSO empty mass, which reduced the possible payload mass by 25% had a TPS not been necessary at all for the SSO [41].

Heating rates and temperatures are extremely high for Earth and Mars entry, intimately coupling the design of an entry vehicle, its TPS, its payload, and its flight path. Higher peak deceleration requires more robust airframes and structures, resulting in added structural mass and decreased payload. Higher heating requires a more substantial TPS, adding mass. This added mass compounds the heating and deceleration endured by an entry vehicle, which requires further added inert mass for airframe robustness and thermal protection. This compounding mass penalty led to lifting capsule TPS mass fractions as high as 33%, and SSO payload mass fractions as low as 19% to the International Space Station [42].

A comparison of the flight paths for a ballistic capsule, a lifting capsule, and a high-lift body are presented in Fig. 1.8 based on a planar lifting entry model detailed in [43]. For generating the comparison plots in Fig. 1.8, the lifting capsule is based on the Apollo capsule aerodynamic properties [44], the ballistic capsule is the Apollo capsule with zero lift coefficient, and the high-lift vehicle uses the aerodynamic properties of the SSO [44]. All vehicles are assigned the same reference area, mass, and leading edge radius. Only their aerodynamic coefficients and flight path angle vary. The lift-to-drag ratios for these vehicles are 0, 0.3-0.4 depending on Mach number, and 1, in order of increasing lift.

For the same initial conditions, a higher lift coefficient results in reduced peak-deceleration and heating. This is due to flying higher in less dense air and dissipating initial energy over a longer entry duration. The mass-specific energy of a vehicle

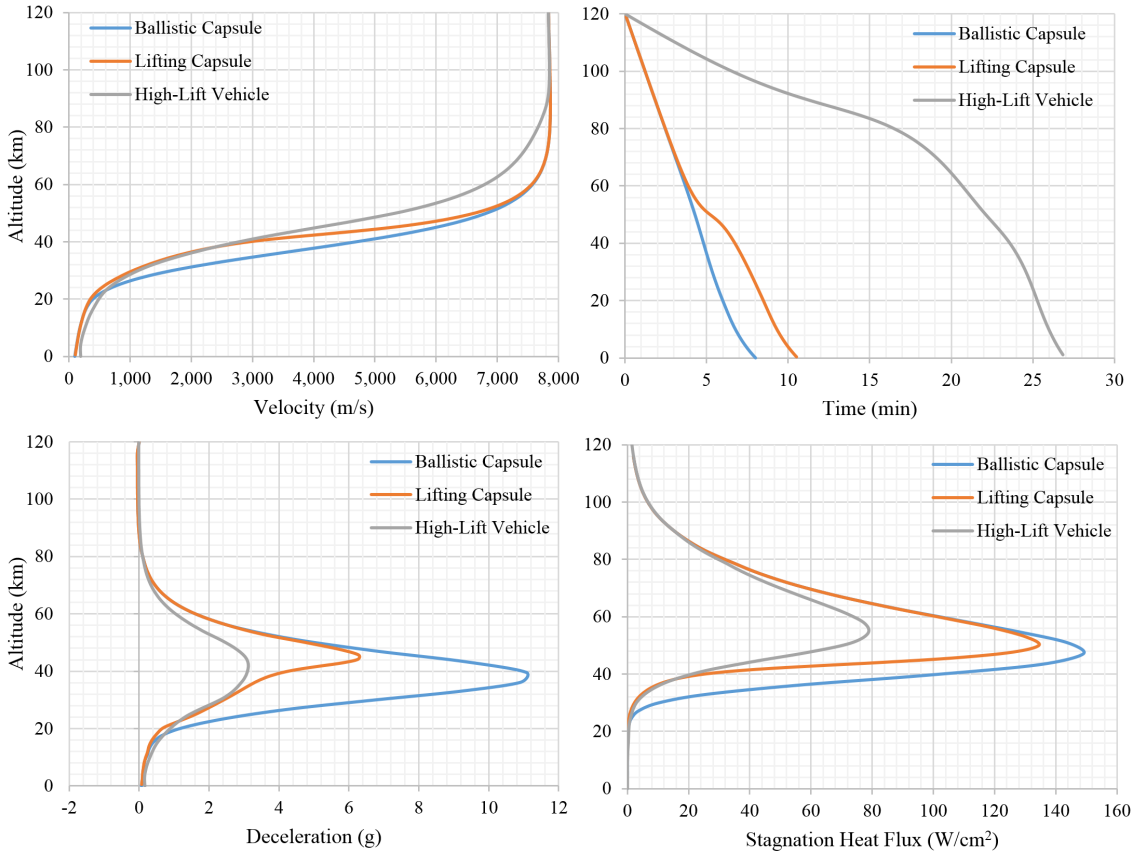


Figure 1.8: Ballistic capsule, lifting capsule, and high-lift vehicle entry conditions.

entering Earth's atmosphere at 120km is 31.8MJ/kg, all of which must be dissipated by touchdown. The entry duration is just 8 minutes for a ballistic capsule, 10-11 minutes for a lifting capsule, and nearly half an hour for the high-lift vehicle as depicted in Fig. 1.8. While this is a greatly simplified comparison, the high-lift vehicle flight path and entry duration agrees with flight data for the SSO [45]. The stagnation heat flux depicted in Fig. 1.8 is the instantaneous heating rate per unit area at the stagnation point for a wall fixed at the free-stream temperature and has a reference leading edge radius of 1m. The heating rate describes the instantaneous heat flux endured by the vehicle, whereas the total heat load is the heating rate integrated in time. A longer entry duration of a high-lift vehicle corresponds to a reduction in the heating rate despite a similar total heat load because it is spread out over a much longer period.

The transient temperature during the entry heating process is determined by the energy balance between the heating due to air compression and viscous friction, the heat rejection through convection and radiation, and the heat transport and absorption by the vehicle's thermal conductivity and thermal mass. The longer the entry duration, the lower the heating rate and the longer convection and radiation can reduce the buildup of thermal energy, which minimizes the peak temperature. Conversely, short entry duration results in higher heating rates and higher peak temperatures. While materials selection and structural design optimization can contribute to minimizing peak transient temperatures, the present work focuses on the flight trajectory dynamics of entry vehicles and their aerodynamics along the flight path. Extending the entry duration can be accomplished by an improvement

in a vehicle's lift coefficient, ballistic coefficient, or glide ratio. The lift coefficient, $C_L$, drag coefficient, $C_D$, ballistic coefficient, $\beta$, and glide ratio, $L/D$ are defined in Eqns. 1.1 - 1.5 as functions of the dynamic pressure $q = \frac{1}{2}\rho v^2$, the reference area $S$, the vehicle mass $m$, and the aerodynamic lift and drag forces. A quantity named the *entry parameter* has been found important in the context of lifting entry and is given in Eqn. 1.6.

$$C_L = \frac{F_L}{\frac{1}{2}\rho v^2 S} \tag{1.1}$$

$$C_D = \frac{F_D}{\frac{1}{2}\rho v^2 S} \tag{1.2}$$

$$L/D = F_L/F_D = C_L/C_D \tag{1.3}$$

$$C_{M_i} = \frac{M_i}{\frac{1}{2}\rho v^2 S c} \tag{1.4}$$

$$\beta = \frac{m}{C_D S} \tag{1.5}$$

$$\xi = \frac{m}{C_L S} \tag{1.6}$$

The lift and drag coefficients are dimensionless functions of the vehicle geometry, angle of attack, $\alpha$ Reynolds number, $Re = \rho v d/\mu$ [46], and Mach number, $M = v/a$, where $a$ is the local speed of sound given by $a = \sqrt{\gamma P/\rho} = \sqrt{\gamma RT/M_m} = \sqrt{\gamma k_B T/m_m}$. Here, $\gamma$ is the heat capacity ratio $c_p/c_v$, $R$ is the universal gas constant, $M_m$ is the molar mass of the gas, $k_B$ is Boltzmann's constant, $T$ is the static temperature, and $m_m$ is the average mass of a single molecule. The moment coefficient for the $ith$ axis is defined in Eqn. 1.4 using the chord of the vehicle, $c$. The ballistic coefficient is a dimensional quantity that represents a ratio of the vehicle's inertial

resistance to the fluid drag. A a large ratio indicates minimal effect of the fluid and a small ratio suggests substantial effect of the fluid; i.e., the vehicle will decelerate quickly. In the limit of an infinite ballistic coefficient, a vehicle's trajectory would match a vacuum trajectory. Typical ballistic coefficients are on the order of $10^2$ to $10^3$ kg/m$^2$ for spacecraft, and an order of magnitude larger for aircraft [47]. The entry parameter is a dimensional quantity that correlates to a vehicle's sink rate. A small entry parameter corresponds to a vehicle that remains aloft much longer and can bleed off speed at high altitude before descending into dense atmosphere below. A large entry parameter corresponds to a vehicle that would descend more quickly. A large entry parameter and quicker descent results in higher heating and deceleration magnitudes, as depicted in Fig. 1.8. Therefore, the desire is to produce entry vehicles with minimal entry parameter as a first-order approximation to minimize entry heating and peak deceleration.

The lift, drag, and moment coefficients are functions of Mach number, Reynolds number, orientation of the vehicle, and control surface deflections. The general schematic for a vehicle aligned with its free-stream flow in the $z$ direction is depicted in Fig. 1.9. The same vehicle is depicted in Fig. 1.10 in the planetary reference frame, $(x_p, y_p, z_p)$, with free-stream velocity $v$ at reference angle-of-attack $\alpha$ and flight path angle $\alpha_p$ relative to the planet's horizontal tangent coordinate in the flight direction, $z_p$. As illustrated in Fig. 1.10, the drag force is defined as parallel to and in the opposite direction of the vehicle velocity relative to the free-stream. The lift force is defined as perpendicular to the free stream.

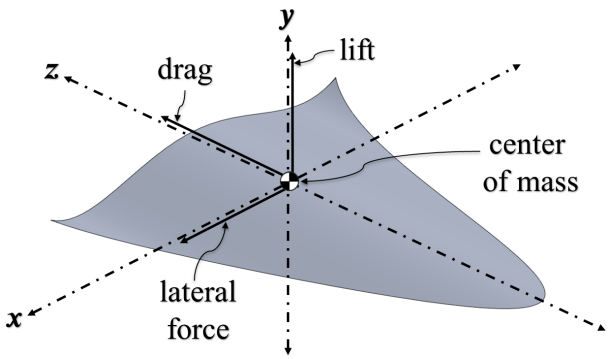


Figure 1.9: Aerodynamic forces on a vehicle aligned with the free-stream flow.

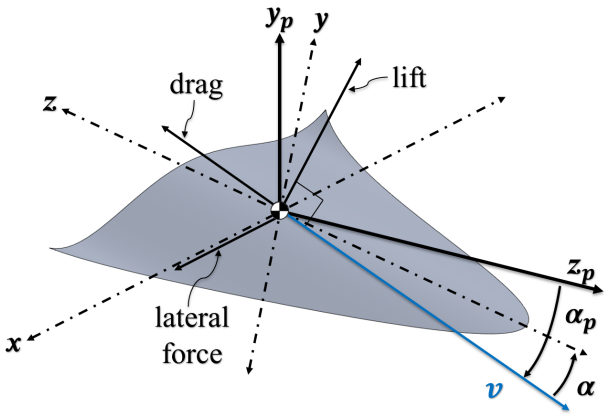


Figure 1.10: Aerodynamic forces on a vehicle with velocity $v$ at angle-of-attack $\alpha$ and flight path angle $\alpha_p$.

## 1.3 Hypersonic Waveriders

A hypersonic waverider is a vehicle with a shock attached all along its leading edge, from wingtip to wingtip [48]. The shock or flow field attached to the vehicle is known as the "design" shock or flow field. The originally proposed vehicle is referred to as the "caret" or "lambda" waverider, because its base profile resembles the caret character or Greek letter lambda, $\Lambda$. This vehicle is depicted in Fig. 1.11. As the figure demonstrates, a planar shock is attached along the leading edge underneath the vehicle. The lower surface of the vehicle corresponds to the stream surface location of the post-shock deflected flow for the "design" Mach number and "design" shock shape. Flow cannot penetrate the shock laterally or upstream, and flow cannot penetrate the vehicle. Because the shock is attached all along the leading edge, the high-pressure post-shock flow is captured between the shock and the vehicle as a temporally-stationary flow field. This high-pressure pocket creates significant compression lift. Following the stream surfaces with the upper and lower surfaces results in low drag. This combination of high lift and low drag yields very high lift-to-drag ratios for waveriders compared to any other vehicles flying in the hypersonic regime [2, 4].

There are many ways to construct a waverider and many shapes of design shocks that may be used, which is discussed in Chapter 2. A conical shock waverider, for example, is depicted in Fig. 1.12 for a 12° conical shock and Mach 6. A much more complex design shock is depicted in Fig. 1.13 for a Mach 5 waverider constructed using an approximate method known as "osculating flow fields." This

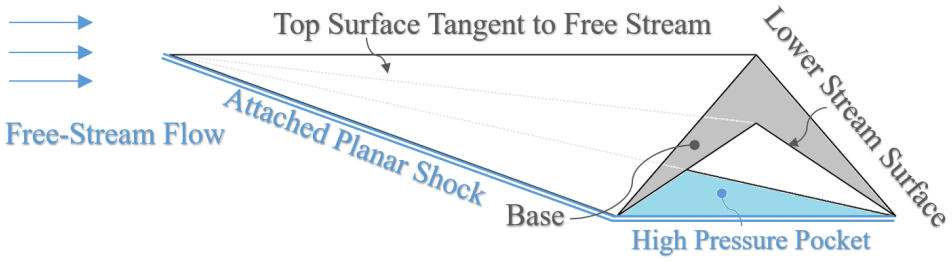


Figure 1.11: Planar shock hypersonic waverider schematic.

method is described in Chapter 2. A comparison of these three example vehicles in Figs. 1.11, 1.12, and 1.13 illustrates the range of design freedom available to waveriders considering that the only requirement for this class of vehicles is an attached shock all along the leading edge.

A morphing waverider is a vehicle with an attached shock all along its leading edge that maintains a constant design-shock shape as the Mach number changes by deflecting its lower surface to conform to the stream surface of the design flow field. As the Mach number increases for a given shock, the stream surface deforms closer to the design shock. A detailed description in the context of a conical-shock derived waverider is provided in Section 2.5.

### 1.3.1 Waverider Caveats

While waverider construction theory generates ideal geometries that can achieve a very high lift-to-drag ratio, there are important considerations that complicate their implementation and have implications for their realizable performance. These effects are discussed individually in the series of following paragraphs, each having a significant potential effect on the design and performance of a realistic vehicle.

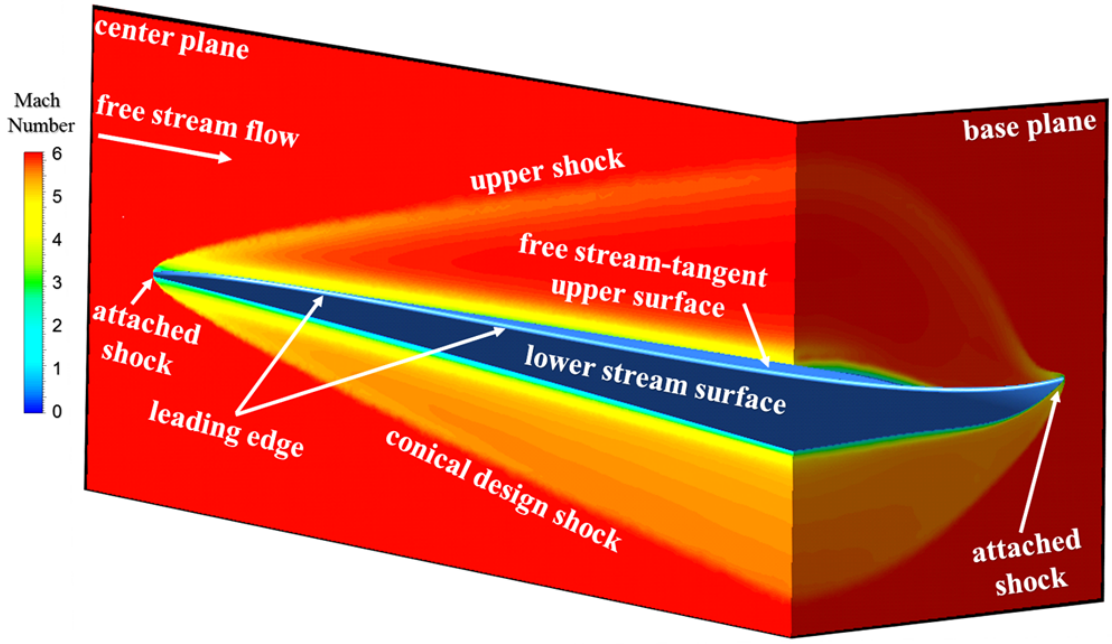


Figure 1.12: Conical shock hypersonic waverider flow field schematic.

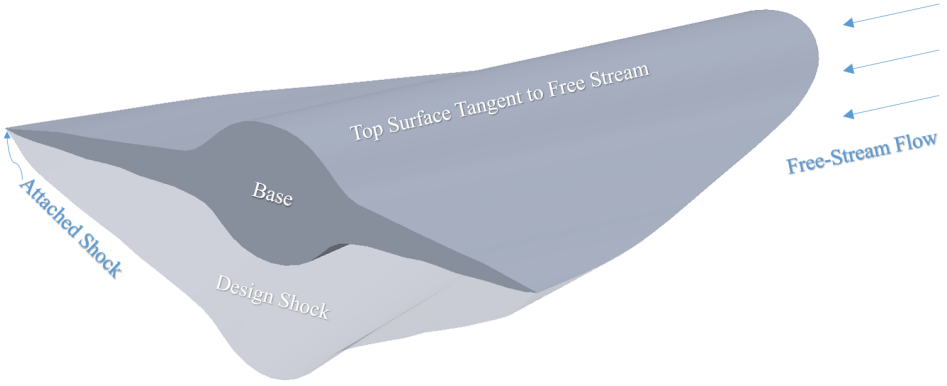


Figure 1.13: Mach 5 osculating flow field waverider riding its theoretical design shock constructed by interpolating between 25 adjacent wedge flow fields.

1. The "design point" is a restrictive flight condition. Waveriders are designed for a specific orientation, Mach number, and a specific shock shape. Deviating from this design point renders the design flow field invalid and will have implications for the vehicle performance. In many cases these effects are marginal, but pitching upward or slowing down eventually will cause shock detachment from the leading edge. Addressing this consideration and characterizing the effect of varying the speed and orientation has been the subject of past studies, e.g. [43, 50]. Practical vehicles have control surface and trim requirements that preclude operation at a fixed orientation. A transport vehicle or entry vehicle will also have to vary speeds as well. In the case of a transport, speed must be varied between zero and cruise. In the case of an entry vehicle, speed must vary between orbital speed and zero.

2. A sharp leading edge in not physical. Waveriders are constructed geometrically assuming a perfectly sharp leading edge. In reality, the leading edge of a vehicle must be fabricated with a finite thickness, technically making the idea of an "attached" shock impossible. Every waverider will have a finite thickness at its leading edge and realistically have a small region where a bow shock stands off from it. Bow shocks produce large amounts of localized pressure drag, localized heating, and local high temperatures. The effect of a finite-thickness leading edge on drag can be minimized for a small leading-edge thickness relative to the vehicle size.

3. Small leading-edge radii lead to excess heating. The rate of heating at the leading edge increases for smaller leading-edge radii, as is discussed in Chapter 2. Above approximately Mach 10 for extended periods of flight, the leading edge *must* be blunted in order to reduce heating of the vehicle and enable survivable

peak temperatures. Otherwise, with leading edge geometry that is too sharp, the stagnation temperature of the flow will heat the leading edge beyond the service temperature of any material. Active heat removal, blunting the leading edge, or a combination of methods is required for a vehicle to survive heating for an extended period.

4. Vehicle aerodynamic properties such as lift and drag are inherently surface-temperature dependent. For a colder wall, such as a cool vehicle newly inserted into a hot hypersonic flight condition, heat will flow from the near-body air into the vehicle surface due to the strong temperature gradient. This heat flux removes energy from the flow, increasing the viscous friction at the surface and increasing the net drag. viscosity increases nonlinearly with increasing temperature. This suggests that a cold vehicle newly inserted into a given flight condition will have lower drag and a higher L/D than a vehicle whose surface has heated up, allowing the near-body flow to stay hotter and yield more viscous drag at its surface. The viscous component of drag on a vehicle will increase as heating causes the surface temperature to increase.

5. Waverider construction methods neglect viscous effects on design-shock and post-shock flow-field properties. Waveriders are constructed using inviscid supersonic flow theory with attached shocks. Viscous effects, non-ideal sharpness, and transient flow structures may yield deviations in actual flow fields compared to the idealized design flow field. At a minimum, viscous effects due to the boundary layer must be accounted for.

6. Waverider flow fields assume equilibrium chemistry. At high Mach number,

non-equilibrium chemical reactions in the near-body flow field will affect vehicle performance. As we will see, there is a method that enables the use of equilibrium chemistry for flow fields at high speeds, but high-hypersonic speeds require the consideration of non-equilibrium chemistry in the near-body flow field.

7. Waveriders are constructed using approximate flow field solutions. The use of non-exact design flow field solutions will yield deviations in actual vehicle performance compared to predicted performance, particularly with the osculating flow field method and the computed flow field method. As will be elaborated in Chapter 2, there are conditions that lessen the error for these approximate-flow-field methods. Of related concern is the use of continuum flow fields at high altitudes where transitional and rarefied flow effects become important. A rarefied boundary layer allows a non-zero slip velocity at the wall, which will reduce the viscous drag compared to continuum theory. Rarefaction will also prevent the formation of a thin, coherent shock surface and allow flow to escape around the leading edge, reducing the geometry's effectiveness at capturing a high-pressure pocket as is the basis of its high performance from continuum theory.

With the exception of rarefied flow, each of these effects is addressed in the present work by either introducing a physical model or modifying the vehicle geometry. The mechanism for investigating the effects of these phenomena is numerical simulation of the waverider near-body flow fields. An example numerical simulation of the Navier-Stokes equations for a conical-shock-derived waverider was presented in Fig. 1.12. The detailed description of the fluid dynamics models used for numerical simulation is provided in Chapter 3.

### 1.3.2 Reduced-Order Models

Numerical simulations of the Navier-Stokes equations are valuable for understanding the detailed features and structures of a near-body flow field. However, the solution for a given three-dimensional waverider and flow-field configuration can be very expensive. These solutions are possible for a single flight condition, but are unreasonably expensive for the time scales of a full entry trajectory. For example, the time scales for the flight path of an entry vehicle can be thousands of seconds and the speed and orientation of the vehicle can vary throughout. Therefore, having an alternative and less expensive way to study the flight path is important.

A reduced-order model is an approximation of more detailed physics. In this context, a flight path does not depend explicitly on a precise value of a flow variable at a precise location. Instead, it is dependent upon the composite coefficients of forces and moments. Entry trajectory simulations are computed using two- to six-degree-of-freedom (6DOF) flight dynamics models. A 2DOF simulation uses lift and drag forces along a vertical flight plane. A 6DOF simulation allows variation in three spatial dimensions and three orientation dimensions. Force and moment coefficients of the vehicle in each flight condition are required for each degree of freedom. With estimates of the aerodynamic coefficients and their variability with Mach number, Reynolds number, and vehicle orientation, it is possible to construct an approximate flight path using a 2DOF to 6DOF flight dynamics model with immensely less computing resources than computing a a full near-body flow-field at each time step along the flight path. This has been the standard method of trajectory estimation

for ballistics and aerospace vehicles for the last century [51–54]. The accuracy of the constructed flight path is dependent upon the accuracy of the ROMs used.

To understand the utility of ROMs, consider the following comparison. The full numerical simulation of an entry vehicle such as the SSO would require integration of its flight path over approximately 2,500 seconds. Numerical solutions are solved in time by advancing the flow field from its current state by a small increment of time called the time step. If millimeter-sized elements are needed at its surface in order to yield accurate aerodynamics with CFD, a sub-microsecond time step would be required for much of the flight path. This would require several billion total flow-field time-step integrations and lead to a total computing time on the order of $10^8$ CPU-hrs. A 6DOF entry trajectory using a reduced-order model for aerodynamic coefficients, by contrast, would require sub-second time steps and produce a trajectory solution in $10^{-3}$ CPU-hrs. This simplification inherently incurs a penalty in accuracy but results in much faster computation.

A reduced-order model for aerodynamic coefficients may be constructed from simplified physics models compared to the numerical simulation of an entire flow field. Such methods may be Modified Newtonian Theory for hypersonic flow [4], discussed in Chapter 2, or similar approximations of flow fields from which lift and drag forces may be extracted. An example of the latter method is a wedge-derived or cone-derived hypersonic waverider using the analytical inviscid flow-field solutions for wedges and cones. Alternately, a ROM may be produced by the interpolation of a discrete data set produced with numerical simulations or experimental results. Consider an entry vehicle, for example, with an expected entry parameter

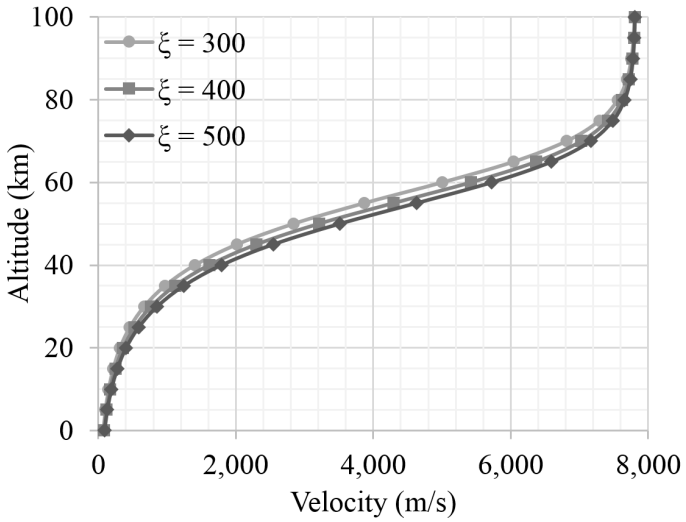


Figure 1.14: Bracketed flight path with discrete points for steady-state numerical solutions to be used for interpolation

of 400kg/m$^2$. Using the Equilibrium Glide Approximation to be provided in Section 2.1, one could produce a bracketed flight path using entry parameters of 300, 400, and 500kg/m$^2$. As depicted in Fig. 1.14, aerodynamic coefficients may be obtained at discrete points using numerical simulations of steady flow at intervals of Mach number and altitude. A flight path may then be simulated using a 6DOF trajectory model and interpolation of the discretely mapped aerodynamic coefficients. The total computational cost of numerical simulations using this approach is potentially many orders of magnitude less than a full numerical simulation of the actual vehicle's entry flight path.

Alternately, a wide parametric mapping of vehicle properties across Mach number and density altitude for a given vehicle, orientation, and control condition can provide interpolation functions to be used more generally, as depicted in Fig. 1.15. The bracketed flight path provided in Fig. 1.14 provides a more efficient use of

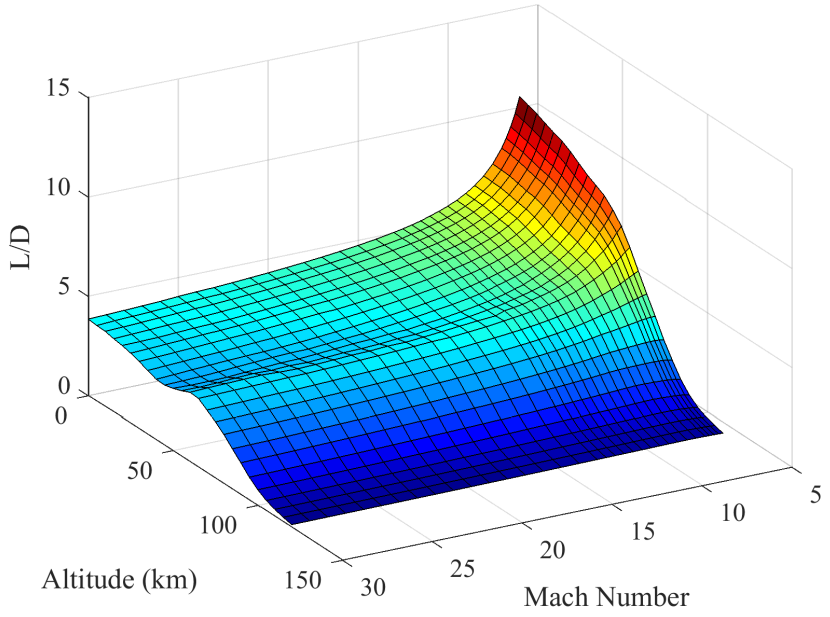


Figure 1.15: An example discrete surface function of L/D with Mach number and altitude to be used for interpolation

computing resources.

### 1.3.3 Dynamic Stability

An important and often under-examined subject of high-speed and entry vehicle aerodynamics is that of dynamic stability [2, 56]. Flight trajectory models are highly concerned with the entry parameter and the glide ratio under various flight conditions, while stability of vehicle orientation is often one of the last considerations. This is critical to consider earlier in the design and evaluation process for two reasons. First, a high-performing vehicle configuration may be analyzed at an unstable equilibrium, prone to destabilization. In order to investigate the stability of a vehicle, it must be perturbed from its trimmed flight condition, where orien-

tation moments are balanced. The resulting change in moments about the center of mass will either restore a vehicle to equilibrium, in which case it is stable, or the vehicle will further diverge from its unstable equilibrium. In the latter case, additional stabilizing features or control surfaces must be added in order to produce a practical, flyable vehicle. Stabilizing features and control surfaces inherently add drag and will penalize the lift-to-drag ratio of an uncontrolled initial design.

A well-known stable vehicle is the Cessna 172 Skyhawk, depicted in Fig. 1.16. While the main wing provides lift, the fixed horizontal stabilizer ensures that a stable pitch-angle can be maintained in the event of a perturbation from this equilibrium. Were the horizontal stabilizer constructed with a larger angle-of-attack than the main wing (in the same direction), a *destabilizing* moment would be produced.

In the context of a Cessna 172 Skyhawk, the vertical- and horizontal-stabilizers were designed specifically to produce restoring moments for an aircraft perturbed from equilibrium. Inherently, however, the addition of these features to the core fuselage and main wings add weight and drag to the vehicle. Similarly, the addition of stabilizing features and control surfaces to hypersonic vehicles will add weight and drag compared to the base geometry. This added drag can have significant effects on the performance of a hypersonic vehicle such as a waverider. The key to minimizing the effect of these added features is to design the core vehicle with inherent stability or minimal instability where possible so that the additional stabilizing forces and moments required are minimized. The stability of a vehicle is evaluated by first evaluating the baseline moments in the intended equilibrium configuration and then evaluating the change in these moments following a perturbation in the vehicle's

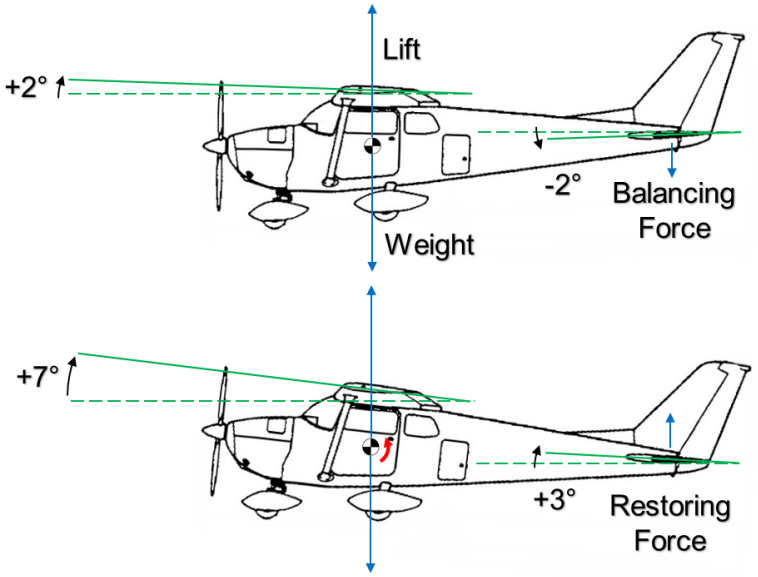


Figure 1.16: A Cessna 172 Skyhawk is in straight and level, unaccelerated flight (top). The main wings provide lift, while the horizontal stabilizer produces a balancing downward force so that the net pitch moment is zero. A deviation from this stable equilibrium, such as a 5° pitch-up (bottom), results in a *restoring force* induced by the horizontal stabilizer and an accompanying restoring moment (red) that pushes the aircraft back to its stable equilibrium condition. Aircraft outline adapted from [57].

orientation. During a glide ratio optimization, for example, configurations that yield high performance may be operating unrealistically at an unstable equilibrium and therefore may not be preferable to a stable, lower-performance configuration.

## 1.4 Review of Related Work

Waverider development dates back to the late 1950s. There are three categories of work that are discussed in this section. The first is the progress of design and construction methods for waveriders that have evolved for more than half a century. The design methods have been accompanied by reduced-order methods for estimating aerodynamic coefficients. These include waverider aerodynamics and thermodynamics, modifications for realistic leading edges, viscous effects, and off-design performance. These reduced-order models enable efficient flight trajectory simulations and wide searches for optimal configurations compared to higher-cost CFD flow-field simulations. This is followed by the numerical simulation of the waverider flow-field in order to analyze performance, both on- and off-design as well as with inviscid and viscous flow. The final category is the attempt to enable efficient operation across a wide range of speeds. This includes prior studies of the potential use of hypersonic waveriders at high-hypersonic speeds and at variable speeds as is important for entry vehicles.

### 1.4.1 Waverider Design and Analysis

In 1959, Terence Nonweiler proposed a supersonic vehicle shape for which a planar shock remains attached all along its leading edge [48]. The top surface of the vehicle would be tangent to the free-stream flow in order to not disturb it, and the lower surface would be defined by the stream surface that emanates from the leading edge, deflected downward by the planar shock. The vehicle would therefore not disturb the post-shock flow from inviscid theory, and a stationary high pressure region would be bounded between the vehicle lower surface and the shock wave. Such a vehicle can be described as "riding" the high pressure region between the body and the attached shock, providing significant advantages for compression lift in the hypersonic regime. Following the stream surface beneath the vehicle additionally results in low drag while producing high compression lift. If the lower surface of the vehicle deviates above the ideal fluid stream surface, the vehicle would produce lower drag but also lower lift due to the added expansion volume for the post-shock flow. If the lower surface of the vehicle deviates below the stream surface, the vehicle would produce higher lift but also higher drag due to adding more obstruction to the flow. Therefore, deviations in either direction from the post-shock stream surfaces either result in increased drag or reduced lift. Early designs from Nonweiler include the "caret" waverider, which is derived from a planar shock and resembles a sharp wedge as was depicted in Fig. 1.11.

Following this work, Nonweiler developed a more detailed description of the design and theory in "Delta Waves of Shape Amenable to Exact Shock Wave The-

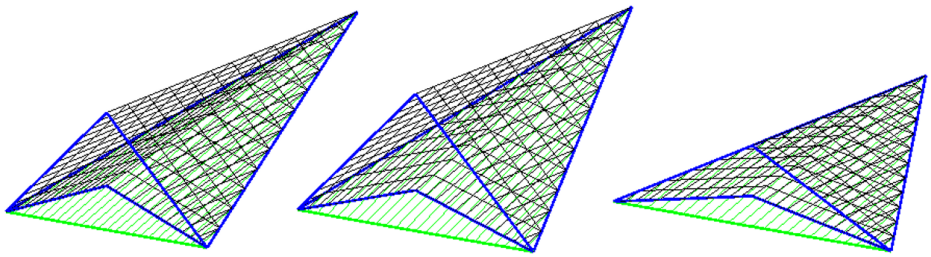

Figure 1.17: Caret-type waveriders designed from a planar shock at Mach 8 and (left to right) 15°, 20°, and 15° with half of the vertical aspect ratio. The models are depicted in wireframe in order to show underlying detail with external edges outlined in blue and the planar design shock highlighted in green.

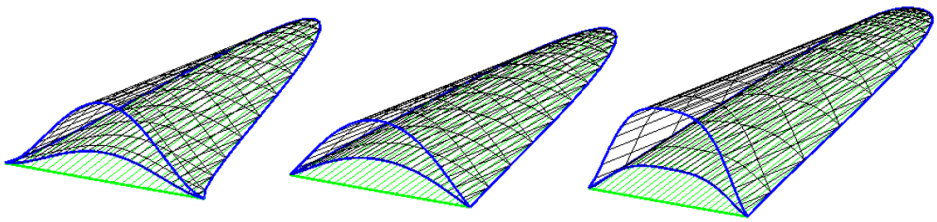

Figure 1.18: Various waveriders designed from a 12° planar shock at Mach 10.

ory," which included performance estimates from hypersonic inviscid oblique shock theory [58]. These waveriders were of the caret type, which Nonweiler calls "Delta Waves," and included variations in the design variables of Mach number, planar shock angle, and caret angle or, equivalently, aspect ratio. A key feature is that Nonweiler used a *known* inviscid flow field to both design and analyze his vehicles. It should be noted that more complex vehicle geometries are also possible with a planar shock, such as those depicted in Fig. 1.18.

In 1963, J.G. Jones used the Taylor-Maccoll solution for the supersonic flow

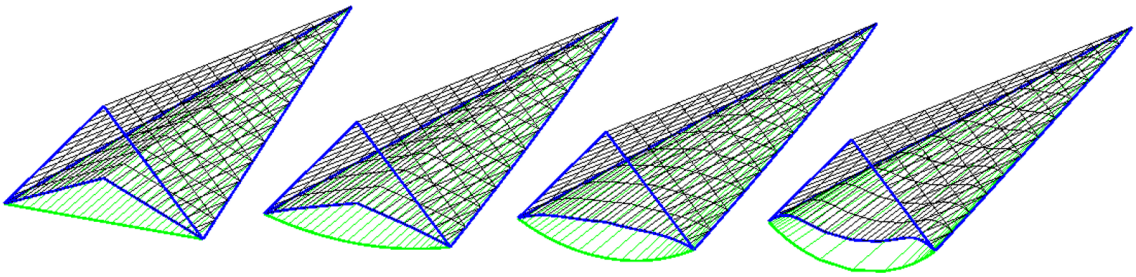

Figure 1.19: Caret-type waveriders designed from a 15° conical shock at Mach 8 and (left to right) ratio of wingspan to the radius from the conical axis to the wingtip of $\infty$, 2, 1, and 0.625.

produced by a cone [59, 60] as an extension of the simple wedge flow-field design [61]. Provided that a wedge flow field is simply a special case of a conical flow field for an infinitely large radius, Jones' method for conical-shock-derived vehicles afforded many more degrees of freedom while retaining the advantage that the design flow field was still known. Development of these attached-shock supersonic vehicles gained popularity around the United Kingdom in the 1960s, with conical flow fields extending to power-law bodies that are known to produce lower drag than cones [62, 63], integration of these idealized shapes into practical aircraft geometries [64], and experimental validation of conical-shock waveriders at Mach 4 [65]. Upper-surface lift was added by Moore [66]. A generic construction method is depicted in Fig. 2.9 for an example conical design shock.

Until the 1980s, waverider geometries were constructed and optimized from flow fields with known solutions [67]. In the early 1980s, interest in hypersonic waverider design and performance estimation returned, including inclined and elliptical cones and cones with longitudinal curvature by Rasmussen [68, 69]. Mundy [49] and

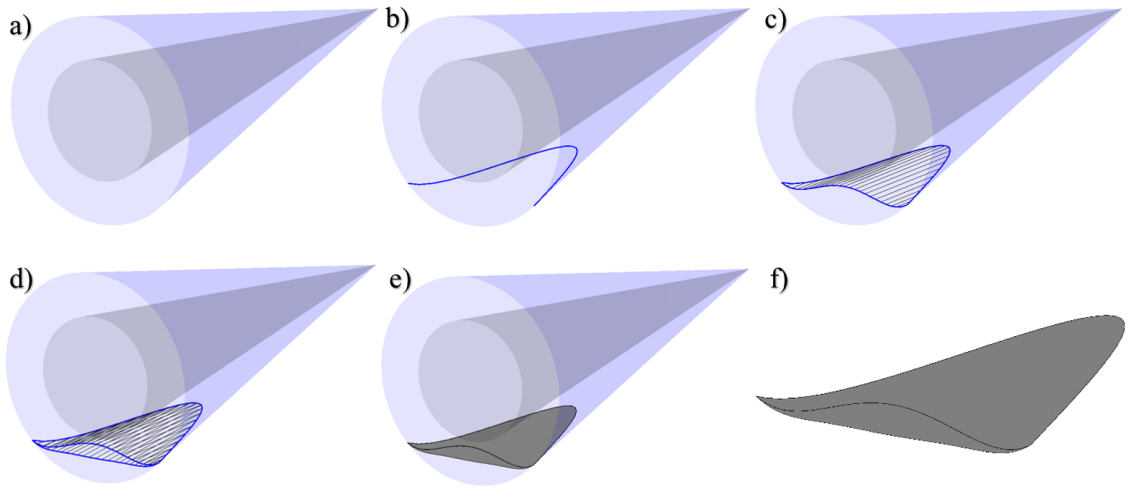


Figure 1.20: General Waverider Construction Method: Beginning with a selected design shock shape (a), one traces a leading edge along the shock (b). Shock and leading edge symmetry about a vertical plane ensures symmetrical aerodynamic forces, while constructing the vehicle below a horizontal symmetry plane such as the example conical shock ensures a lifting body will result. Stream surfaces are traced back from the shock in order to form each surface, as depicted in (c) for the upper surface and (d) for the lower surface. The point at which the stream surfaces are truncated downstream of the shock is termed the "base plane" and is a free design variable. The upper and lower stream surfaces and base plane enclose a volume that represents the internal vehicle volume, illustrated in the context of the conical shock flow field in (e) and the resulting vehicle alone in (f).

Rasmussen [50] included viscous effects with classical known flow fields such as cones and power-law bodies in the mid 1990s. Development continued with perturbation-based and linearized approximate flow fields such as thin shock-layer theory [70]. The late 1980s and early 1990s saw the emergence of computed flow fields. With the advent and proliferation of practical computing hardware, these models could be used for both design and computational estimation of complex geometries that still conform to known and computed flow fields, a practice that would have been intractable before high-speed computers. Examples include the viscous optimization of conical-shock-derived hypersonic waveriders by Bowcutt and Anderson [71, 72], power-law bodies [68], generalized shock geometries [73, 74], and the parametric optimization enabled by efficient evaluation of these flow fields [71, 75, 76]. Viscous effects in the case of Bowcutt and Anderson [71] and continued by Corda [75] are approximated using empirical relations for the friction coefficient on a supersonic flat plate, whereas the pressure-based forces are interpolated from the inviscid design flow field.

The design flow-fields were not entirely external [77–79]. Kothari [77] proposed waverider construction from inward-turning flow fields in 1996, reporting lower heating and a higher lift-to-drag ratio than was attainable by external flow fields. Yu reported similar findings in 2000 [79] using optimized convergent flow fields, and Billig determined that inward-turning flow fields for waverider-based engine inlets outperformed those constructed using external flow fields in the context of inlet pressure recovery and propulsion-related performance metrics [80]. The generalized computed flow fields yield more degrees of freedom for optimization, however it is

noted by Starkey that simple symmetric or similarity-solution flow fields are much more practical for large surveys of parametric optimization [81,82]. A high-degree-of-freedom and low-cost compromise between these two extremes began with the Osculating Cones method developed by Sobieczky [83] and experimentally validated by Mill [84].

The Osculating Cones method is based on the approximation that cross-flow components between adjacent planar cross sections of a high-speed flow field can be neglected. Therefore, the field may be constructed with a selectable number of osculating planar sections of a conical flow field at selectable distances between planes. Each osculating plane may have its own design conical flow field, and the space between osculating planes is simply interpolated between the bounding plane values. In principle, a singular conical flow field can be recovered with the appropriate planar flow field and inclination assigned to each of the osculating planes. The caveats with the osculating cones method are 1) positioning of each subsequent plane and leading edge point laterally does not guarantee continued shock attachment, and 2) cross-flow components may not be negligible for large geometric gradients. As long as the geometry does not change too abruptly and planar flow fields are selected that have minimal cross-flow components, the osculating cones method enables arbitrarily high degrees of freedom at a low computational cost.

The Osculating Cones method has been extended by Rodi to osculating power-law body flow fields [85,86] and generalized osculating flow fields [87] where a reference solution field is interpolated from a lookup table or curve-fit computational results. Perhaps the most prolific waverider technology developer in the public record

is P.E. Rodi. Rodi has demonstrated the utility of these approximate flow field methods for parametric optimization, including investigating osculating flow fields in the context of minimizing wave drag [88], maximizing boundary layer stability [89], increasing lift with the upper surface [90], reducing leading edge heating [91, 92], and minimizing acoustic signature [93]. In the context of optimization of aerodynamic coefficients and comparison to other non-waverider vehicles, it should be noted that Rodi reports inviscid lift-to-drag results.

Efficient and accurate evaluation of aerodynamics and heating is the goal of reduced-order modeling, which enables tractable flight trajectory computations and optimization with a large number of model evaluations. Aside from suggesting new design methods, e.g. [94–96], many contributions to reduced-order modeling are motivated by modification of waverider geometries for realism. These modifications include leading edge blunting and off-design operation with respect to orientation and speed. While early ROMs assumed nominally sharp leading edges, leading edge blunting was investigated for waveriders using Modified Newtonian Flow theory [4] by Santos beginning in 2009 [97, 98]. Supported by experimental evaluations of waveriders (e.g. [99, 100]), both investigations of leading edge blunting concluded that realistic radii will have a significant effect on the drag coefficient and the lift-to-drag ratio. For a typical slender vehicle, a leading edge radius just 0.1% of the vehicle's width can result in approximately a 10% reduction in lift-to-drag ratio.

Leading edge heating modeling was addressed by Vanmol for a circular cross section leading edge in 1991 [101, 102], and heating of the full bodies of power-law waveriders was addressed by Santos in 2005 for prescribed isothermal wall temper-

atures [103]. Both cases included classical round leading edge and flat plate heating models as described in [4]. Variable-geometry leading edge designs intended to minimize local heating and drag have been recently approached by Hinman and Rodi in 2017 [104] in the context of a two-dimensional nose tip with inviscid flow. Under this premise, various optimization outputs resulted in nearly 20% reduction in peak heating and nearly 10% reduction in pressure drag compared to the baseline circular cross section.

### 1.4.2 Numerical Simulation of Waverider Flow Fields

The practical use of hypersonic waveriders includes operation across a wide range of conditions that span speed, orientation, and altitude. As flow fields or geometry become too complex for reduced-order modeling, they must be analyzed with high-fidelity computations. The numerical simulation of waverider flow fields started with off-design angle-of-attack and speed investigations by Long in 1990 [105] and Jones in 1992 [106] for waveriders with sharp leading edges using the Euler Equations [3]. Long found advantages in increased lift with increasing pitch angle and maximum lift-to-drag occurring at small, positive angle of attack. Early attempts at viscous simulation include those of Takashima beginning in 1992 [107, 108], in which the compressible Navier Stokes equations are used. The computational resources available at that time, however, limited grid generation to 96k cells in Takashima's study and prohibited evaluation of turbulent flows or demonstration of grid convergence. While un-converged simulations can be deeply insightful for general features

and trends in variables, these results are subject to an unknown degree of uncertainty. Similar results were reported by Liao [109].

Perhaps the most insightful numerical investigation of waverider aerodynamics was conducted by He and Rasmussen in 1994 [110]. Due to computational resource limitations of the time, they used the inviscid Euler Equations to conduct the off-design investigations and the Navier-Stokes equations to investigate the effect of Reynolds number. He and Rasmussen were able to construct a 185k-element grid for the viscous simulations. The inviscid simulations spanned the effect of angle of attack, Mach number, and slightly blunted leading edges. They discovered that the optimal lift-to-drag ratio usually occurred at a non-zero angle of attack, sometimes negative, but that the magnitude of this maximum was within 10% of the zero angle-of-attack value. They also found a monotonically decreasing inviscid lift-to-drag ratio for each of the eight waverider configurations considered. However, the reduction in lift-to-drag between Mach 2 and Mach 8 was typically only about 10%. Note that this trend does not include the effects of viscosity or turbulence. The leading-edge blunting investigation included the baseline sharp leading-edge geometry and uniform filleting slight enough to retain 98% and 96% of the original vehicle's wingspan. The conclusion drawn from these configurations is that very slight blunting of the leading edge results in a slight decrease in the lift-to-drag ratio, but this reduction diminishes with increasing angle of attack. Finally, He and Rasmussen found that viscous effects for Reynolds numbers of $10^8$ to $10^6$ can reduce the inviscid lift-to-drag estimate by 10-30%, respectively. The computational resources of the time precluded the grid resolution required to capture turbulence

or demonstrate grid convergence. The inviscid results should be accepted with the caveat that viscous and turbulent effects are not accounted for. A viscous study by Jackson found low sensitivity in aerodynamic coefficients at Mach 14 on-design and Mach 8 off-design [111].

Y. Shi, *et al.* [112,113], investigated a conical-shock-derived caret waverider in 1996 and 1997 in a study similar in scope to part of He and Rasmussen's work. Because they had more capable computational power, they could include the turbulent and viscous effects for both on- and off-design conditions [112] as well as the additional effect of side-slip or yaw angle [113]. Shi's team was the first to investigate waveriders at high-Reynolds-number with turbulent flow models, which enable the approximate capture of fine-scale turbulence effects without requiring intractably fine computational grids. Their qualitative conclusions were similar to those of He and Rasmussen, however Shi's team also saw shock detachment, shock-boundary-layer interactions, and flow separation on the leeward surface with as little as $+5^\circ$ angle of attack. The effect of a small yaw angle did not have a large impact on the lift or lift-to-drag ratio, but did decrease both.

Silvester, *et al.*, investigated the viscous aerodynamics of a caret waverider in 2004 [114], particularly interested in the effects of blunting. Contrary to prior numerical investigations but corroborated by experimental results, Silvester's team found that small amounts of leading edge blunting can reduce the lift-to-drag ratio by as much as 30% [115,116]. They also found that the viscous component of drag can exceed the pressure component of drag for realistic flight dynamic-pressure. A more precise treatment of leading edge blunting was provided by Chen in 2011 [117]

and Li in 2017 [118], finding that small bluntness ratios can reduce the lift-to-drag ratio by as much as 30-50%.

At high altitudes, the air reaches sufficiently low density that the continuum assumption breaks down and boundary layers behave differently. For waverider entry vehicles, the effect of rarefaction must be considered. Osculating-cone waveriders at high altitude and zero angle of attack were numerically evaluated by Graves in 1999 and 2001 [7, 119]. Graves found a lift-to-drag ratio much lower than unity but higher than the estimate using continuum flow.

### 1.4.3 Hypersonic Waveriders Across a Range of Flight Conditions

Criticisms of the single "design point" operation of waveriders dates back to Nonweiler, who noted that the geometries amenable to exact shock wave shapes were only valid for the specific Mach number and orientation at which they were designed [58]. Preceding the discussion of the following attempts to enable efficient operation of waveriders on-design across a range of speeds, one must recall that prior studies had found only modest reductions in lift-to-drag ratio for increasing Mach number and that the optimal lift-to-drag ratio typically occurs at a nonzero angle of attack.

Past attempts to enable the high-performance operation across a wide range of speeds began with the numerical investigations of rigid waveriders at off-design speeds conducted in the 1990s [**?**, 105–113]. In 2009, Corda [120] suggested a four-part caret waverider called a "star body" waverider, where each of the waveriders

may be designed at a different Mach number. For example, the bottom waverider may be designed for Mach 4, the top waverider may be designed for Mach 8, and the lateral waveriders may be designed for Mach 6. These waveriders don't produce positive lift for zero angle of attack except when the highest design speed is on the bottom. When the two lateral waveriders that comprise the star body are not identical, a nonzero yaw moment and lateral force is produced. When inverted, a star-body waverider produces negative lift at zero angle of attack. The high-pressure pocket of the higher Mach number side outweighs the high-pressure pocket created by the lower Mach number side. For these reasons, the practical implementation of a star-body waverider requires operation at nonzero angles of attack and requires symmetry about the vertical plane.

The Boeing Company produced a patent in 2002 [121] on the concept of using actuated leading-edge slats to reach out and touch a variable-geometry shock as the speed of the vehicle is changed. One issue with this approach is that the aerodynamic forces depend strongly on the stream surface position. The positioning of the leading-edge slats correspond to the position of the design shock, but the vehicle's bottom surface does not correspond to the design flow field's stream surface. The deviation of the vehicle surface from the stream surface results in additional compression or expansion in the post-shock pocket of air beneath the vehicle.

Li proposed a two-part tandem waverider in 2013 [122], each with a distinct design Mach numbers. Liu proposed the dual-cone waverider in 2014 [123], a blended-body configuration that can operate half of its geometry on-design at each of two design Mach numbers. The composite vehicle does not operate on-design at either

speed or aside from these speeds. An overview of the attempts to operate on-design or efficiently at multiple speeds was provided by Ding [124], which highlighted the concept that waveriders are most efficient at their design speed, and performance compromises must be accepted for operation at other speeds.

A key feature of the present work, "morphing waveriders," is to fix the design-shock shape for various speeds and the associated leading edge and top surface [125,126]. As the speed changes, only the stream surface must change. This requires small in-plane strain of the stream surface and retains on-design performance with respect to angle-of-attack and Mach number. The concept was evaluated in the context of entry vehicles for Earth [127] and Mars [128] with a reduced-order model for entry dynamics and compared to conventional entry capsules and the Space Shuttle Orbiter.

Without fully entering an atmosphere and touching down on the planetary surface, waveriders for use in planetary atmospheres have been investigated by groups led by Anderson [129], Sims [130], Johnson [132, 133], Lavagna [134], Knittel [135], Rodi [136], and Edelman [137, 138]. Key results from the Anderson study include the high performance estimated for various planetary atmospheres. Venusian waveriders at lower altitudes reached a lift-to-drag ratio near 15. The generally more viscous atmosphere of Mars resulted in lower glide ratios, reduced by approximately two thirds. Johnson, Lavagna, and Knittel each separately investigated waveriders for aero-assist maneuvers, either for trajectory modification along an interplanetary route or for orbital-path modification such as transition from hyperbolic to elliptical orbits or to effect a change in orbital inclination angle. In each case, it was found

that the high lift and low drag of waveriders even at high altitudes was beneficial in creating the desired trajectory modification without the less efficient expenditure of thruster fuel or excessive loss of energy through aerodynamic drag-based aero-assist maneuvers.

## 1.5 Scope of the Present Work

The key questions addressed here are 1) Is there an advantage to morphing a waverider across the wide range of entry speeds? 2) Can a morphing waverider out-perform a lifting capsule on Mars or the Space Shuttle on Earth? 3) Is overcoming the technical challenges associated with morphing *worth* any advantage demonstrated? The present study seeks to answer the first two questions in an effort to advance an understanding of the potential of morphing waveriders. These answers determine whether the concept merits further investigation. The third question is deferred for future work.

The high lift and low drag enabled by waveriders makes them ideal candidates for entry vehicles, provided that the heating conditions are survivable. Prior analytical models for waverider aerodynamics and trajectory simulations were incomplete. Aerodynamics models have not been compared to numerical simulations in order to understand their accuracy. Errors in performance estimates are not known to originate from pressure or viscous components, or on which surface. Prior numerical investigations into waverider aerodynamics couldn't include the fidelity of turbulent flow structures and chemical reactions. The present effort includes the ad-

vantage that modern computing resources enable higher-cost investigations that can address these gaps in understanding of waverider aerodynamics and the accuracy of reduced-order models.

Formulating the strategy to address questions #1 and #2 leads to the following four goals. The first goal is to select appropriate models for numerical simulation and conduct simulations on a candidate vehicle with varied Mach number, angle of attack, and in reactive, hypersonic flow. While large leading edges such as capsules and the Space Shuttle allow much of the post-shock flow chemistry to develop, it remains unknown how a smaller-radius "cold wall" (relative to the adiabatic temperature) affects the post-shock flow chemistry. The second goal is to select appropriate analytical models in order to build a reduced-order model for pressure and viscous forces and moments. The third goal is to use numerical simulations to evaluate the accuracy of the reduced-order model for waverider aerodynamics across Mach number and angle of attack. The comparison of ROM accuracy will determine what level of confidence can be applied to flight path modeling. The fourth goal is to compare the entry trajectories of morphing waveriders computed using the developed ROM to classical lifting entry vehicles for Earth and Mars. This study will culminate in entry trajectory comparisons between a morphing waverider and two classical entry vehicles: the Space Shuttle for Earth's atmosphere and the Mars Science Laboratory (MSL) capsule for Mars' atmosphere.

The following topics are specifically outside the scope of the present work and are not addressed. Each of them is an important consideration that is recommended for future work, but does not fit within the present scope of effort and resources. The

first topic is rarefied flow at high altitude. Extremely-low entry-parameter vehicles will need proper treatment of the effects of rarefied flow. For the entry conditions and vehicle comparisons chosen for the present work, aerodynamics and flight path differences in the rarefied regime for Earth and Mars are minimal. Significant deceleration, heating, and flight path angle change only occur in the continuum regime. The second topic is surface interactions, including gas-wall chemical reactions, erosion, and ablation. It is expected that comparison vehicles will be designed with stagnation heating rates lesser than the Space Shuttle, enabling a fully reusable vehicle and rendering the consideration of these effects unnecessary. The third topic is optimization. Neither the vehicle geometry nor the angle of attack throughout the entry trajectory will be formally optimized. The final comparison vehicles will be the result of design iterations that represent reasonable vehicle configurations.

### 1.5.1 Thesis Outline

In the next chapter, entry dynamics models are presented, which illustrate the benefits of high lift and high lift-to-drag ratio. A method for constructing a hypersonic waverider and estimating its near-body flow field is presented. The conical-shock method is selected for case study vehicles. Two methods of blunting the leading edge are presented, followed by models for hypersonic aerodynamics, friction and heating, and transition to turbulence.

In the third chapter, numerical methods for simulating high-speed, turbulent, reactive flows are presented, with case studies that illustrate the convergence and

order of accuracy of the proposed methods. For high-speed flow, a variable heat capacity ratio model and a seven-species reactive flow model are used. Verification and validation of the proposed methods is provided in the context of a flat plate in turbulent hypersonic flow and a cylinder in reactive hypersonic flow.

In the fourth chapter, the results of the case study vehicles are presented for on-design operation and off-design orientation and Mach number. The effect of leading edge blunting is summarized, and the implication of off-design orientation on stability is discussed. A seven-species reactive flow model is used to present the waverider near-body flow field at Mach 15 at 60km and Mach 20 at 75km with a discussion of the species concentrations in the near-body flow field.

The fifth chapter is a comparison of the aerodynamic forces and moments compiled from numerical simulation results to the reduced-order aerodynamics model proposed. Considerations include viscosity and turbulence, angle of attack, and Mach number, with a focus on the comparable agreement between the ROM and CFD results and implied degree of accuracy. The effect of altitude and wall temperature are also summarized. The fifth chapter closes with a comparison between rigid and morphing waveriders and important considerations such as L/D across Mach number and the associated surface deflection and strain.

The sixth chapter is a comparison between morphing waveriders and classical entry vehicles. The Space Shuttle is chosen for comparison in Earth's atmosphere and the Mars Science Laboratory capsule is chosen for Mars' atmosphere. The results are presented to emphasize the heating and deceleration during the entry process.

The conclusion chapter summarizes the efforts of the present work and the resulting insights gained. Unique contributions are highlighted, primarily demonstrating that the morphing-waverider entry-vehicle concept merits further investigation and summarizing the advantages discovered in the present work. Caveats and limitations of the models used and case studies presented are discussed, and recommendations are made for future work.

# Chapter 2: Analytical Approach

This chapter describes a collection of models that together allow the efficient estimation of waverider aerodynamics, heating, and entry flight paths. The collection of the models used in their specified regions of application is called the author's Waverider Reduced-order Analytical and Investigative Tool for Hypersonics, or "WRAITH." Any future reference in this work to the waverider reduced-order model (ROM) or WRAITH are synonymous. First, the simple Equilibrium Glide model is presented and discussed. This model provides insights into how entry heating and deceleration generally scale with vehicle properties and constant aerodynamic coefficients. Next, the Planar Lifting Entry equations are used as the basis of entry trajectory comparisons. Entry heating models are then presented, which use hypersonic flow theory and empirical calibration. Hypersonic aerodynamics models are then selected for the reduced-order model formulation. The second half of this chapter includes simplified models for hypersonic aerodynamics and high-speed, high-temperature air.

## 2.1 Equilibrium Glide Entry Model

Consider the atmospheric entry of a lifting vehicle from a low, circular orbit with a constant entry parameter (Eqn. 1.6) along the entire entry trajectory. This vehicle executes no pitch or banking maneuvers and descends along an equilibrium glide path as it decelerates. If we approximate the variation of density with altitude as an exponential, $\rho(h) = \rho_p e^{-h/h_s}$ [139], we arrive at an algebraic approximation for the entry conditions with altitude as a function of the entry parameter, the planetary radius and surface density, and the atmosphere's scale height [139, 140]:

$$\frac{v}{v_e} = \left[1 + \left(\frac{\rho_p r_p}{2}\frac{C_L S}{m}\right) e^{-\frac{h}{h_s}}\right]^{\frac{1}{2}} \tag{2.1}$$

Here, we used the approximation that the circular orbit velocity is equal to the entry velocity. For context of this velocity approximation, the SSO's entry speed was 98.8% of its circular orbit velocity [47]. We have also taken advantage of the stationarity of dynamics in equilibrium glide so that the velocity at any altitude is a specifically defined fraction of its initial circular-orbit velocity. Using this approximation for velocity as a function of altitude, the average dissipated power per unit area, deceleration, and entry duration can be approximated as [4, 141–143].

$$\frac{Q}{S}(h) = \frac{1}{2}\rho(h)v^3(h)C_D \tag{2.2}$$

$$a(h) = \frac{q(h)C_D S}{m} \tag{2.3}$$

$$t(h) = \frac{1}{2}\sqrt{r_0/g_0}\frac{L}{D}\ln\left(\frac{1+(v/v_e)^2}{1-(v/v_e)^2}\right) \tag{2.4}$$

One stagnation heat flux model commonly used for planetary atmospheres is the Chapman Method [47], presented in Eqn. 2.5. The instantaneous stagnation heat

flux depends on the vehicle speed, $v$, and leading edge radius, $R_{LE}$, the local flow density, $\rho$, specific heat capacity at constant pressure, $c_{p,\infty}$, free-stream temperature, $T_\infty$, the enthalpy at the wall, $h_w$, and some calibration constants unique to a particular vehicle and atmosphere. Defining the heat flux at the stagnation point at the wall as

$$q_{w,0} = \frac{c}{\sqrt{R_{LE}}} \rho^m v^n \left(1 - \frac{h_w}{h_{aw}}\right) \tag{2.5}$$

the model uses the assumption that the specific heat capacity is constant. This is called a "calorically perfect" gas. High-temperature effects are corrected for using the recommended closure coefficients of $m = 0.5$ and $n = 3.04$ for Mars and $n = 3.00$ for Earth [47, 139]. The proportionality constant, $c$, is dependent upon vehicle geometry. For a capsule in Earth or Martian atmosphere, a value on the order of $c = 2 \times 10^{-8}$ matches experimental and flight test results.

The adiabatic wall enthalpy and wall enthalpy at temperature $T_w$ are defined as [4]

$$h_{aw} = \int_0^{T_\infty} c_p(T) dT + \frac{rv^2}{2} \tag{2.6}$$

$$h_w = \int_0^{T_w} c_p(T) dT \tag{2.7}$$

where $r$ is the "recovery factor," approximated as $Pr^{1/2}$ for laminar flow near the stagnation point. The latter quantity is defined using the specific heat capacity and temperature at the wall, $c_{p,w}$ and $T_w$. For a constant heat capacity, these integrals simplify to $h_{aw} = c_{p,\infty} T_\infty + \frac{1}{2} r v^2$ and $h_w = c_{p,\infty} T_w$.

A key feature of the Chapman Method is that $q_{w,0} \propto R_{LE}^{-1/2}$, so doubling the leading-edge radius results in approximately 30% lower stagnation heat flux. There

is also a strong dependence of the heat flux on the flight velocity and moderate dependence on density, indicating that stagnation heating will be minimized for vehicles that can slow their speed while retaining higher altitude. For identical initial velocity and altitude, and the same end condition of zero speed at zero altitude, lower heating is achieved by decelerating before descending into denser atmosphere.

Results from the Equilibrium Glide entry approximation are presented in Fig. 2.1 for entry parameters of 1,000, 500, 250, and 100kg/m$^2$. A lifting capsule typically has an entry parameter on the order of $10^3$kg/m$^2$, while high-lift vehicles such as the Space Shuttle, Boeing's X-37, and Sierra Nevada Corporation's Dream Chaser pictured in Fig. 2.2 lie in the range of 250-500kg/m$^2$ depending on their loading configuration [44]. These high-lift vehicles are depicted in Fig. 2.2 along with the Apollo lifting capsule.

For depicting the equilibrium glide entry approximation in Fig. 2.1, the glide ratio was set to 1/4, 1/2, 3/4, and 1 to produce the listed entry parameters. The results are depicted for entry from a 200km LEO into Earth's atmosphere in 2.1. In each case, a reference nosetip radius of 1m was used for illustrating how the stagnation point heat flux varies with entry parameter. The dissipated power flux is the instantaneous power dissipated by the vehicle per unit area through drag and heating. This value corresponds fairly well to the average surface heat flux and stagnation heat flux by a small scalar. The dissipated power flux is much larger than even the stagnation heat flux. Fortunately for entry vehicles and their thermal protection systems, nearly all of the dissipated power for an entry vehicle is carried away by the convective atmosphere and radiation. Only a small fraction is absorbed

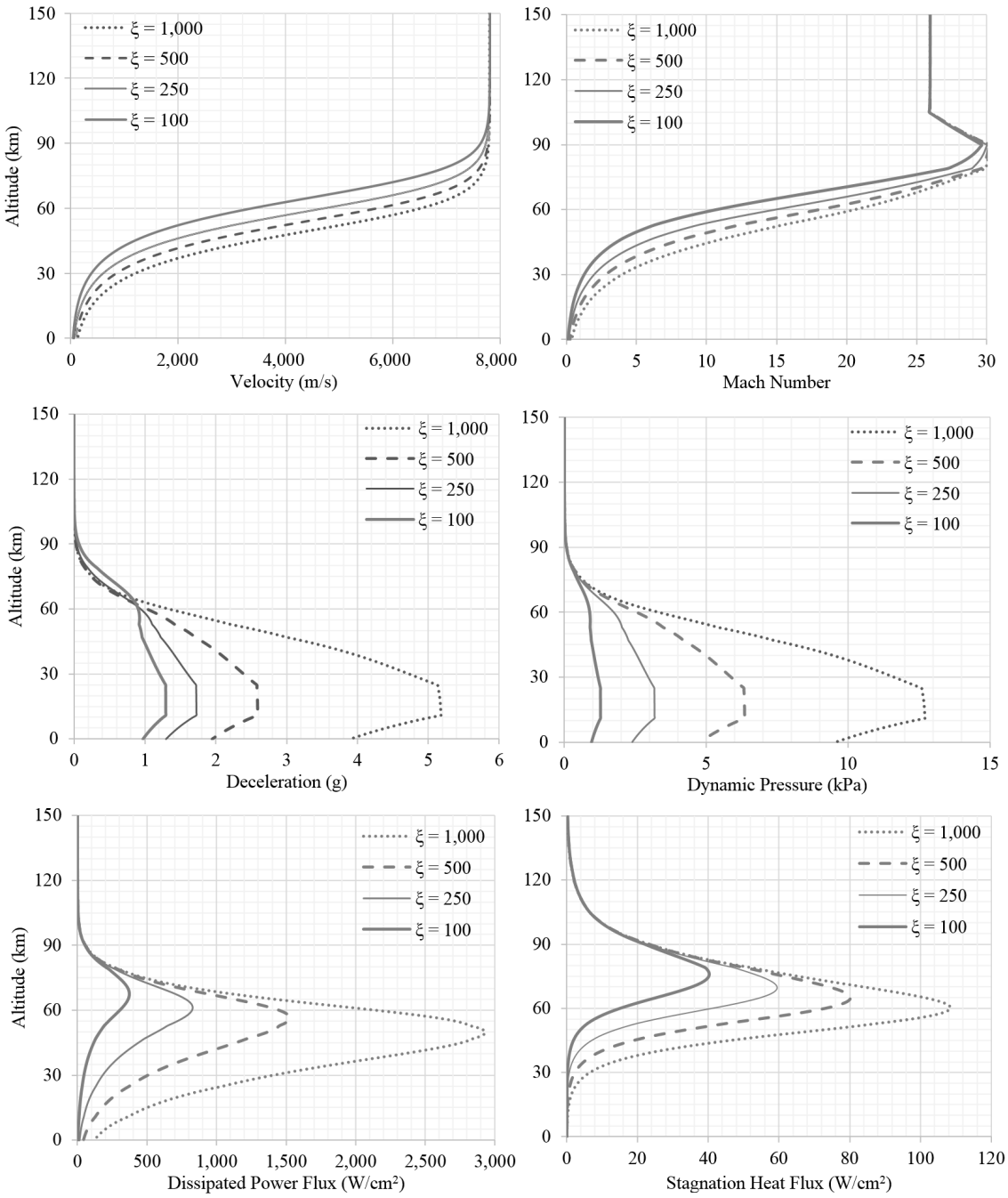


Figure 2.1: Equilibrium glide entry approximation of entry conditions for Earth's atmosphere


Figure 2.2: Apollo lifting capsule [144], NASA Space Shuttle Orbiter [145], Boeing X-37 [146], Sierra Nevada Corporation Dream Chaser [147]

by the vehicle as thermal loading [2].

Figure 2.1 shows the consistent flight path envelope of velocity and altitude across vehicles with large differences in their entry parameter. As shown in the velocity plot and the accompanying heating and deceleration plots, vehicles that descend more steeply incur higher stagnation heat fluxes, higher dissipated power, and higher peak deceleration than those that dissipate their energy higher in the atmosphere before descending.

The scaling factor between the stagnation heat flux and the dissipated power flux is illustrated in Fig. 2.1, for example, by the $\xi = 1000\text{kg/m}^2$ vehicle. The vehicle must dissipate $1600\text{W/cm}^2$ on average across its reference surface at 60km in order to decelerate, but its stagnation heat flux is only $76\text{W/cm}^2$. The typical magnitude of average heat flux is on the order of 1% of the dissipated power flux [2].

The Equilibrium Glide entry approximation estimates velocity, Mach number, and dissipated power profiles with altitude accurately. The approximation produces a moderately accurate estimate of stagnation heat flux and integrated heat load, while qualitative trends are preserved very well. This is largely due to the assumption of uniform aerodynamic coefficients across Mach number, Reynolds number, and Knudsen number, constant angle of attack, and a flight path angle always near zero. The total entry duration is well matched, but its prediction of time along with altitude is not. Because of this temporal accuracy issue, the deceleration is erroneously biased toward the lower altitudes of the flight path. The peak-deceleration magnitude matches more complex entry trajectory models fairly well.

A final note on the accuracy of the approximation is that the peak deceleration

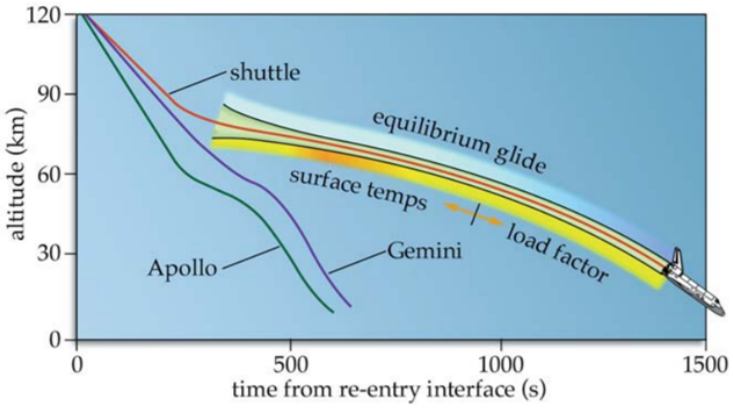


Figure 2.3: Entry altitude and time for SSO and Apollo and Gemini capsules [148]

tends to lie on the conservatively benign limit of the practical range of a flight vehicle because the entry angle and glide angle are always assumed to be close to zero. A steeper initial entry angle will result in higher peak deceleration, while a shallower initial entry angle will result in lower peak deceleration. Since the Equilibrium Glide entry approximation does not provide accurate temporal information, a summary of descent over time is presented in 2.3 of the entry profile for the Space Shuttle and capsules used for Gemini and Apollo [148]. This graph shows the difference between reentry profiles for Apollo, Gemini, and the Space Shuttle [148]. The Gemini and Apollo reentered much more steeply than the Space Shuttle. The Shuttle's reentry profile must stay within a tight corridor between the equilibrium glide limits. This ensures that it will slow enough to avoid skipping out of the atmosphere and not over-shoot the runway if it is too high. If it is too low, it will encounter excessive surface temperatures and load factor.

## 2.2 Planar Lifting Entry Model

The equations that govern the entry into planetary atmospheres of lifting vehicles can be separated into the constants unique to a given planet and the dynamics equations that are updated at each increment of time. For a planar lifting entry, the dynamics equations are summarized in Eqns. 2.8-2.12 [56]:

$$g = g_0 \left( \frac{r_p}{r} \right)^2 \tag{2.8}$$

$$\frac{d\alpha_f}{dt} = \frac{1}{v} g_0 \left( \frac{F_L}{m} - \left( 1 - \frac{v^2}{v_c^2} \right) g \cos(\alpha_f) \right) \tag{2.9}$$

$$\frac{dv}{dt} = -\frac{F_D}{m} - g \sin(\alpha_f) \tag{2.10}$$

$$\frac{dr}{dt} = v \sin(\alpha_f) \tag{2.11}$$

$$\frac{d\theta}{dt} = \frac{v}{r} \cos(\alpha_f) \tag{2.12}$$

where $g$ is the local value of the planetary gravity for the orbital distance $r$, $\alpha_f$ is the local flight path angle, $v$ is the vehicle velocity, and $\theta$ is the orbital angle. The quantities $F_L$ and $F_D$ are functions of angle of attack, $\alpha$, as well as Mach number, Reynolds number, and control surface deflections. These variables are depicted in the orbital schematic for Earth in Fig. 2.4. Equations 2.13-2.15 are pre-computed constants used to integrate the dynamics equations:

$$g_0 = GM_p / r_p^2 \tag{2.13}$$

$$\mu_p = G(M_p + m) \tag{2.14}$$

$$v_c = \sqrt{\frac{\mu_p M}{r}} \tag{2.15}$$

In this context, $g_0$ is the surface gravity of the planet, $G$ is the universal gravitational constant ($6.674 \times 10^{-11} m^3 kg^{-1} s^{-2}$), $r_p$ is the planet's mean radius, $M_p$ is the planet's mass, $\mu_p$ is the planet's reduced mass, $m$ is the vehicle mass, and $v_c$ is the circular orbit velocity for the radial distance from the center of the planet, $r$, where $r > r_p$, and orbital altitude is described as the height above the planetary surface, $h = r - r_p$.

## 2.3 Entry Heating Models

Heating must be evaluated at locations along the vehicle and at the stagnation point for various Mach and Reynolds numbers. While the Chapman model is a relatively simple method for estimating the stagnation heat flux for an entry capsule, a newer model was developed by Van Driest [149]. In the newer method, the stagnation point heating for a vehicle's blunted leading edge can be approximated as that for a cylinder, given by

$$q_{0,cyl} = 0.57 Pr^{-0.6} (\rho_0 \mu_0)^{1/2} (h_{aw} - h_w) \sqrt{\frac{du}{ds}\Big|_0} \tag{2.16}$$

or a sphere, given by

$$q_{0,sph} = 0.763 Pr^{-0.6} (\rho_0 \mu_0)^{1/2} (h_{aw} - h_w) \sqrt{\frac{du}{ds}\Big|_0} \tag{2.17}$$

where $Pr = c_p \mu / k$ is the Prandtl number, $k$ is the thermal conductivity, $\rho_0$ and $\mu_0$ are the stagnation density and viscosity, and $\frac{du}{ds}|_0$ is the rate at which the velocity at the outer edge of the boundary layer increases along the surface curvature coordinate

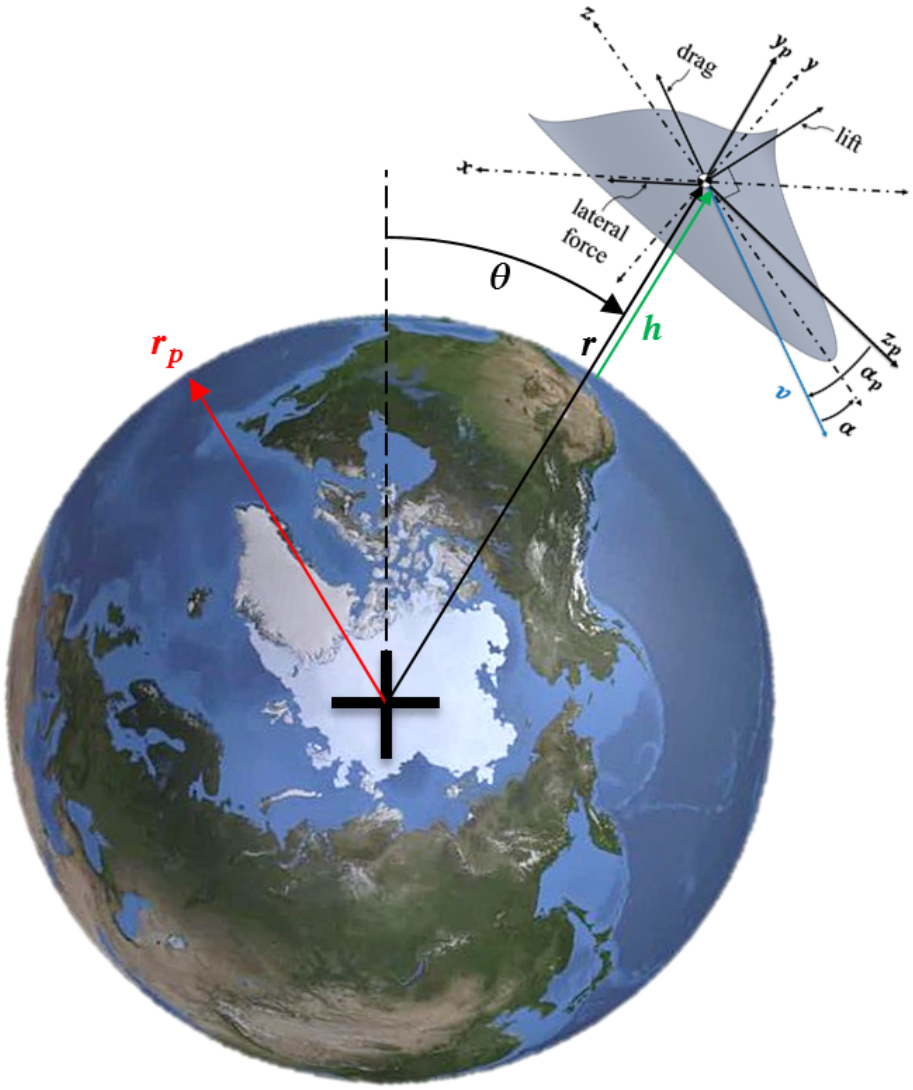


Figure 2.4: Schematic for entry variables for a vehicle at position $(r, \theta)$, velocity $v$ at angle-of-attack $\alpha$, and flight path angle $\alpha_p$. The Earth image is taken from NASA GSFC [150].

from the stagnation point, $s$. This value is approximated as

$$\frac{du}{ds}\Big|_0 = \frac{1}{R_{LE}}\sqrt{\frac{2(p_{0,2} - p_\infty)}{\rho_0}} \tag{2.18}$$

Beginning with the free-stream temperature and pressure, the stagnation density is computed using the stagnation temperature and stagnation pressure behind a normal shock, given by [151]

$$T_0 = T_\infty\left(1 + \frac{\gamma - 1}{2}M^2\right) \tag{2.19}$$

$$p_{0,2} = p_\infty\left[\frac{(\gamma+1)M^2}{2 + (\gamma-1)M^2}\right]^{\frac{\gamma}{\gamma-1}}\left[\frac{\gamma+1}{2\gamma M^2 - (\gamma-1)}\right]^{\frac{1}{\gamma-1}} \tag{2.20}$$

Using the ideal gas equation of state [3],

$$p = \rho RT \tag{2.21}$$

the stagnation point density is computed using $p_{2,0}$, $T_0$, and the gas constant for air, $R = 287 J/kg/K$. Viscosity is computed using the stagnation temperature and Sutherland's Law [152]:

$$\mu(T) = \mu_{ref}\frac{T_{ref} + C}{T + C}\left(\frac{T}{T_{ref}}\right)^{3/2} \tag{2.22}$$

where $\mu_{ref} = 1.789 \times 10^{-5} Pas$ is the reference viscosity at reference temperature $T_{ref} = 288K$, and $C = 110K$ [4].

Now consider the stagnation heat-flux components as evaluated from Eqns. 2.6 - 2.22. A spherical leading edge inherently has higher stagnation heating than a cylindrical leading edge. This is due to the greater opportunity for compressed and heated flow to escape the stagnation region for the axisymmetric flow compared

to the planar symmetric flow. This "relieving" effect causes the sphere to have a thinner boundary layer, which increases the thermal gradients normal to the wall and results in a higher heat flux [4]. Although free-stream velocity and Mach number don't explicitly appear in Eqns. 2.16 and 2.17, they are implicitly included in the stagnation temperature and pressure behind the normal shock, Eqns. 2.19 and 2.20, and the adiabatic wall enthalpy, Eqn. 2.6. At high speeds, the dependence works out to $q_0 \propto M^3$, which agrees with Chapman's Method of Eqn. 2.5.

Along the leading edge away from the stagnation point, Lee developed a heat flux estimate using laminar boundary layer theory and the local inclination angle, $\theta$, [153]:

$$q_{w,LE}(\theta) = \frac{2q_0\theta\sin(\theta)\left[\left(1-\frac{1}{\gamma M^2}\right)\cos^2(\theta)+\frac{1}{\gamma M^2}\right]}{\sqrt{(1-\frac{1}{\gamma M^2})\left[\theta^2-\frac{\theta}{2}\sin(4\theta)+\frac{1-\cos(4\theta)}{8}\right]+\frac{4}{\gamma M^2}\left[\theta^2-\theta\sin(2\theta)+\frac{1-\cos(2\theta)}{2}\right]}} \tag{2.23}$$

where the stagnation heating value, $q_0$, is obtained from either 2.16 or 2.17, depending on the vehicle geometry. An example of the heating predicted around the leading edge using the Lees method is provided for various Mach numbers and leading edge radii in Fig. 2.5.

Heating away from the leading edge requires another estimation method. The Stanton number is a dimensionless heat transfer metric defined using the heat flux at the wall, $q_w$, density and velocity of the free-stream, $\rho_\infty$ and $v$, and the current and adiabatic wall enthalpy [4]:

$$C_H = \frac{q_w}{\rho_\infty v(h_{aw}-h_w)} \tag{2.24}$$

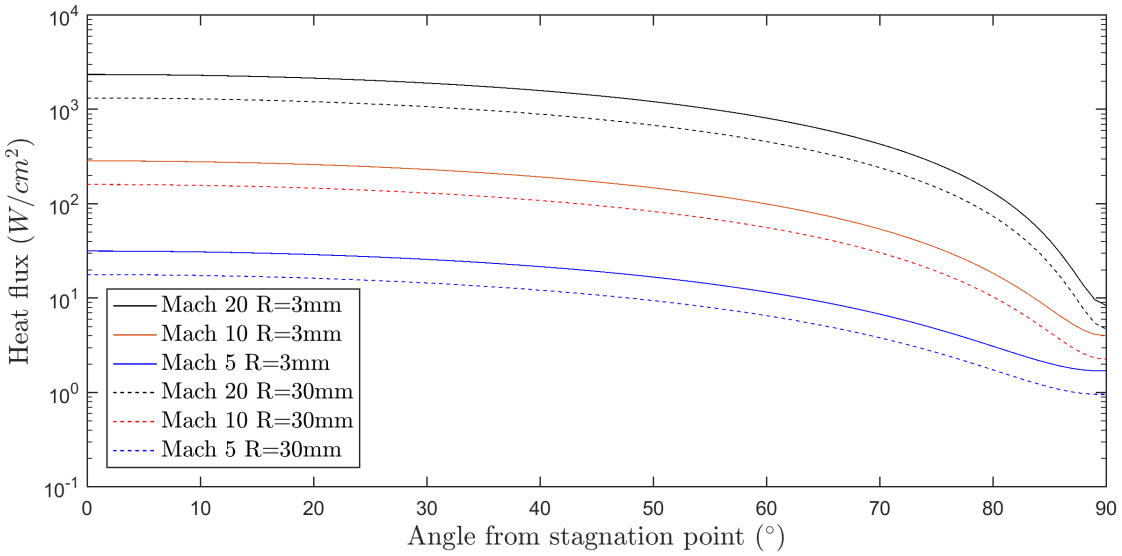


Figure 2.5: Heat flux about the leading edge from Eqn. 2.23 for 30km altitude and Mach 20, 10, and 5 with leading edge radii of 3mm and 30mm.

The current wall enthalpy and adiabatic wall enthalpy were previously defined in Eqns. 2.6-2.7. The Stanton number may be estimated in relation to the friction coefficient using the Reynolds analogy as [149]:

$$C_H = \frac{1}{2} c_f Pr^{-2/3} \tag{2.25}$$

The friction coefficient calculation method will be described in section 2.6.5.

### 2.3.1 Radiative Heating

In the present work, radiation between surfaces on the waverider will be neglected. Instead, what will be considered is the radiation between each surface panel and either cold space or the surface of the Earth. The surface of the Earth is assumed to be a standard day, for which $T = 288.15K$. The altitude of the vehicle is assumed to be sufficiently high that the effective temperature of the sky above is

that of space, at $2.7K$. The heat transfer due to radiation for panel $i$ with emissivity $\epsilon_i$, area $A_i$, and temperature $T_i$, is given by [154]:

$$q_{rad,i} = \epsilon_i A_i \sigma (T_i^4 - T_{2,i}^4) \tag{2.26}$$

where $\sigma = 5.67 \times 10^{-8} W/m^2/K^4$ is the Stefan-Boltzmann constant and $T_{2,i}$ is the temperature of the surface that the panel is radiating to. Bottom-surface panels are assumed to be radiating to Earth's surface, therefore $T_{2,i} = 288.15K$; whereas top-surface panels are assumed to be radiating to cold space, therefore $T_{2,i} = 2.7K$.

## 2.4 Waverider Construction

As discussed in 1.3, waveriders can be constructed from known, computed, or approximate flow fields. This section uses the known flow field about an axisymmetric cone at zero angle of attack as the design flow field. The steps of construction form the subsections of the present section, as outlined in the following procedure:

1. Select and solve a design flow field
2. Define the leading edge on the design shock
3. Trace the stream surfaces from the leading edge to the base plane

Following the construction procedure, the aerodynamic forces and moments can be computed for a waverider's stream surface at the design Mach number and zero angle of attack using the flow field solution. The forces on the other surfaces and the effects due to off-design Mach number or orientation are addressed in subsequent sections.

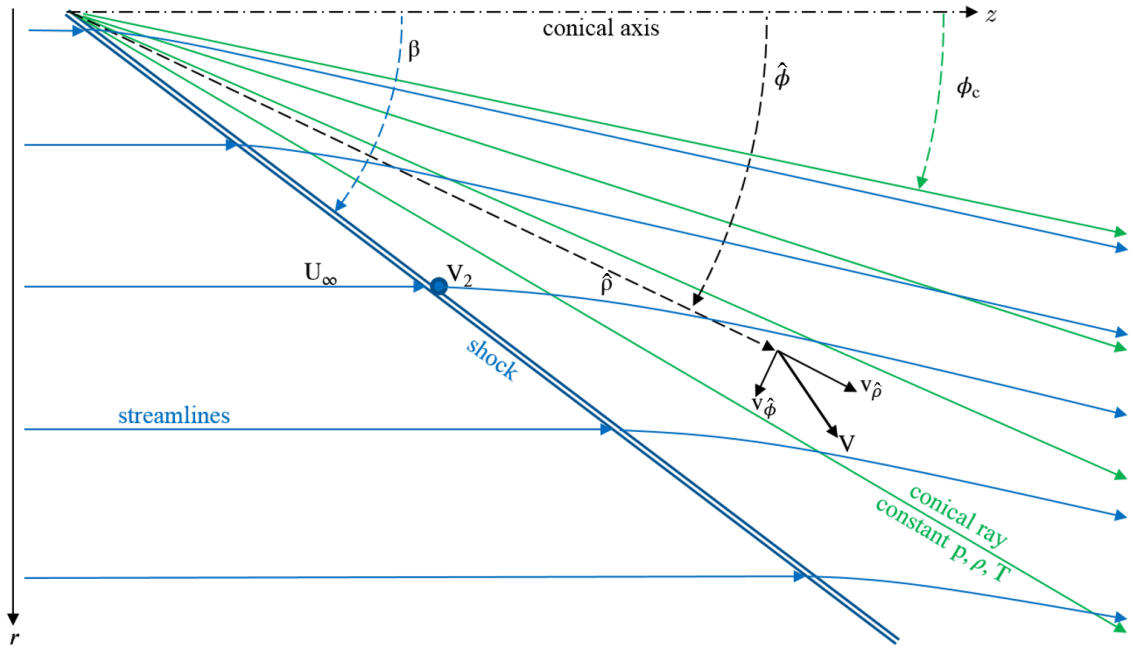


Figure 2.6: Taylor-Maccoll flow field schematic and coordinates.

### 2.4.1 Solution for the Conical-Shock Flow Field

The design flow field is a cone at zero angle of attack, described by a similarity solution derived by Taylor and Maccoll in 1933 [60]. This is given by the set of governing ordinary differential equations shown in Eqns. 2.27-2.28.

$$\frac{\gamma-1}{2}\left(1-v_{\hat{\rho}}^2-\left(\frac{dv_{\hat{\rho}}}{d\hat{\phi}}\right)^2\right)\left(2v_{\hat{\rho}}+\cot\hat{\phi}\frac{dv_{\hat{\rho}}}{d\hat{\phi}}+\frac{d^2v_{\hat{\rho}}}{d\hat{\phi}^2}\right)-\frac{dv_{\hat{\rho}}}{d\hat{\phi}}\left(v_{\hat{\rho}}\frac{dv_{\hat{\rho}}}{d\hat{\phi}}+\frac{dv_{\hat{\rho}}}{d\hat{\phi}}\frac{d^2v_{\hat{\rho}}}{d\hat{\phi}^2}\right)=0 \tag{2.27}$$

$$v_{\hat{\phi}}=\frac{dv_{\hat{\rho}}}{d\hat{\phi}} \tag{2.28}$$

The solution to the Taylor-Maccoll equations is a flow field of a single similarity variable, $\hat{\phi}$, with solutions in the form of $v_{\hat{\rho}}(\hat{\phi})$ and $v_{\hat{\phi}}(\hat{\phi})$. Flow variables along a ray of constant $\hat{\phi}$ emanating from the cone vertex are constant. Flow field variables only vary across rays, illustrated along with the coordinate system in Fig. 2.6.

First, a flight Mach number and shock angle, $\beta$, are chosen. The shock angle has a minimum value for a given Mach number according to the Mach angle $\beta_{min} = \arcsin(\frac{1}{M})$. The solution to Eqns. 2.27-2.28 is found by integrating the equation from the shock angle to the cone surface where $v_{\hat{\phi}} = \frac{dv_{\hat{\rho}}}{d\hat{\phi}} = 0$. The classical Runge-Kutta 4th-Order method (RK4) is implemented for the integration [155]. An angular increment of $0.01^\circ$ is used in the present work, empirically found to be sufficient to determine the flow variables to at least three significant figures. The zero-crossing is cubically interpolated from the integration points. The RK4 algorithm is listed in Eqns. 2.29-2.34 for a generic function $y(x)$ with initial value $y(x_0) = y_0$ and increment $\Delta x$, where the value at $x_{n+1} = x_n + \Delta x$.

$$\frac{dy}{dx} = f(x, y) \tag{2.29}$$

$$y_{n+1} = y_n + \frac{1}{6}(k_1 + 2k_2 + 2k_3 + k_4) \tag{2.30}$$

$$k_1 = \Delta x f(x_n, y_n) \tag{2.31}$$

$$k_2 = \Delta x f(x_n + \frac{1}{2}\Delta x, y_n + \frac{1}{2}k_1) \tag{2.32}$$

$$k_3 = \Delta x f(x_n + \frac{1}{2}\Delta x, y_n + \frac{1}{2}k_2) \tag{2.33}$$

$$k_4 = \Delta x f(x_n + \Delta x, y_n + k_3) \tag{2.34}$$

Conversion from the Taylor-Maccoll spherical coordinate system to Cartesian coordinates is accomplished using Eqns. 2.35-2.39

$$v_x = v_{\hat{\rho}} \sin\hat{\phi} \cos\hat{\theta} \tag{2.35}$$

$$v_y = v_{\hat{\rho}} \sin\hat{\phi} \sin\hat{\theta} \tag{2.36}$$

$$v_z = v_{\hat{\rho}} \cos \hat{\phi} \tag{2.37}$$

$$v = (v_{\hat{\rho}}^2 + v_{\hat{\phi}}^2)^{1/2} \tag{2.38}$$

$$M(\hat{\phi}) = \frac{v}{\sqrt{\gamma RT/M_w}} \tag{2.39}$$

Note that the azimuthal velocity, $v_{\hat{\theta}}$, is zero for the selected conical flow field. The post-shock Mach number, $M_2$, pressure, $p_2$, temperature, $T_2$, density, $\rho_2$, and deflection angle, $\delta$, can be computed once the Taylor-Maccoll solution is obtained using the Oblique Shock Relations for conditions immediately behind the shock, listed in Eqn. 2.40 - 2.44 [156].

$$\cot \delta = \tan \beta \left( \frac{(\gamma+1)M^2}{2(M^2 \sin^2 \beta - 1)} - 1 \right) \tag{2.40}$$

$$M_2^2 \sin(\beta - \delta) = \frac{(\gamma-1)M^2 \sin^2(\beta) + 2}{2\gamma M^2 \sin^2 \beta - (\gamma-1)} \tag{2.41}$$

$$\frac{T_2}{T_1} = \frac{((\gamma-1)M^2 \sin^2(\beta) + 2)(2\gamma M^2 \sin^2 \beta - (\gamma-1))}{(\gamma+1)^2 M^2 \sin^2 \beta} \tag{2.42}$$

$$\frac{p_2}{p_1} = \frac{2\gamma M^2 \sin^2 \beta - (\gamma-1)}{\gamma+1} \tag{2.43}$$

$$\frac{\rho_2}{\rho_1} = \frac{(\gamma+1)M^2 \sin^2(\beta)}{(\gamma-1)M^2 \sin^2(\beta) + 2} \tag{2.44}$$

With the stagnation temperature, pressure, and density behind the shock,

$$\frac{T_0}{T_\infty} = 1 + \frac{\gamma-1}{2} M^2 \tag{2.45}$$

$$\frac{p_{0,2}}{p_\infty} = \left[ \frac{(\gamma+1)M^2}{4\gamma M^2 - 2(\gamma-1)} \right]^{\gamma/(\gamma-1)} \left[ \frac{1-\gamma+2\gamma M^2}{\gamma+1} \right] \tag{2.46}$$

$$\frac{\rho_{0,2}}{\rho_\infty} = \frac{p_{0,2}}{\frac{R}{M_w} T_0} \tag{2.47}$$

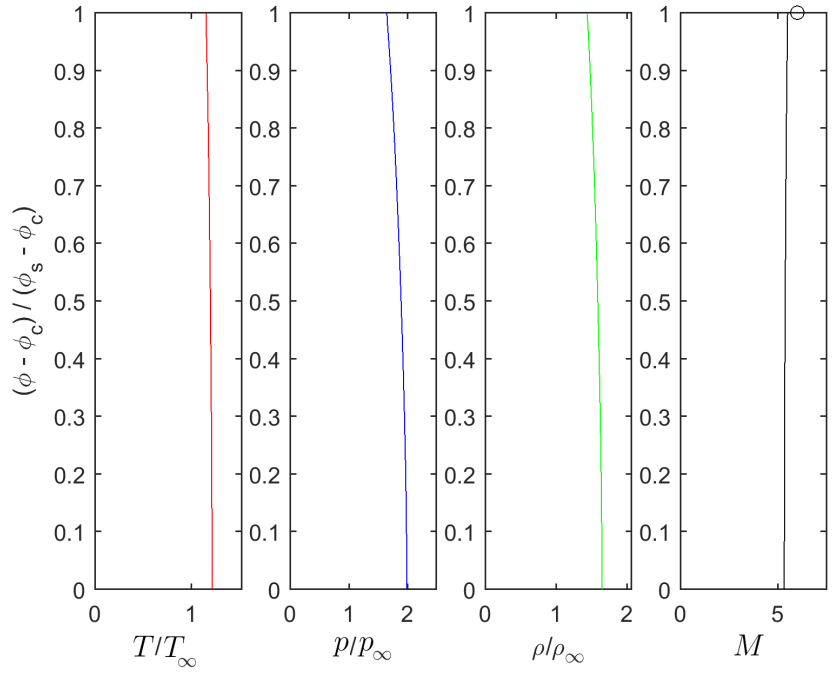


Figure 2.7: Example normalized Taylor-Maccoll solution field for a 7.09° cone, ($\phi_c$), producing a 12° shock angle, ($\phi_s$), at Mach 6 and 30km altitude.

the solution is constructed for each variable in the post-shock flow field using the Mach number solution, $M(\hat{\phi})$, and the Isentropic Flow Relations [3]:

$$T(\hat{\phi}) = \frac{T_0}{1 + \frac{\gamma-1}{2} M^2(\hat{\phi})} \tag{2.48}$$

$$p(\hat{\phi}) = \frac{p_{0,2}}{\left(1 + \frac{\gamma-1}{2} M^2(\hat{\phi})\right)^{\frac{\gamma}{\gamma-1}}} \tag{2.49}$$

$$\rho(\hat{\phi}) = \frac{\rho_{0,2}}{\left(1 + \frac{\gamma-1}{2} M^2(\hat{\phi})\right)^{\frac{1}{\gamma-1}}} \tag{2.50}$$

An example solution is provided for a 12° shock angle at Mach 6 and 30km altitude in Fig. 2.7.

### 2.4.2 Equilibrium Reacting Flow

In the preceding section, air was assumed to be a monolithic substance with properties based on the 1976 Standard Atmosphere, Sutherland Law viscosity, and molecular weight 28.966 g/mol. For air temperatures up to approximately 500K, air may be described as calorically perfect with a heat capacity ratio, $\gamma = c_p/c_v$, fixed at a constant value of $\gamma = 1.4$ [25]. For temperatures up to approximately 2,000K, the heat capacity ratio can be accurately modeled as a function of temperature only, described as thermally perfect.

The model used in the present work for thermally perfect air is based on kinetic theory and given in Eqn. 2.51 [157].

$$\gamma(T) = 1 + \frac{\gamma_0 - 1}{1 + (\gamma_0 - 1)\left[\left(\frac{T_{ref}}{T}\right)^2 \frac{e^{\frac{T_{ref}}{T}}}{\left(e^{\frac{T_{ref}}{T}} - 1\right)^2}\right]} \tag{2.51}$$

where $T_{ref} = 3055$K and $\gamma_0 = 1.4$. To determine the fixed-$\gamma(T)$ value with the present conical flow field, the Taylor-Maccoll equations are solved iteratively: an initial guess is made for $\gamma = 1.4$, and the post-shock temperature is used to assign a new fixed $\gamma(T)$ using Eqn. 2.51. This process is repeated until $\Delta\gamma(T) < 0.01$. This method allows for first-order effects of chemically reacting flow, but assumes the flow field reaches chemical equilibrium instantly after passing through the shock.

### 2.4.3 Leading-Edge Definition

The outer profile of the vehicle is called the "planform." Once the flow field has been found, the planform and leading edge may be designed in multiple ways. A

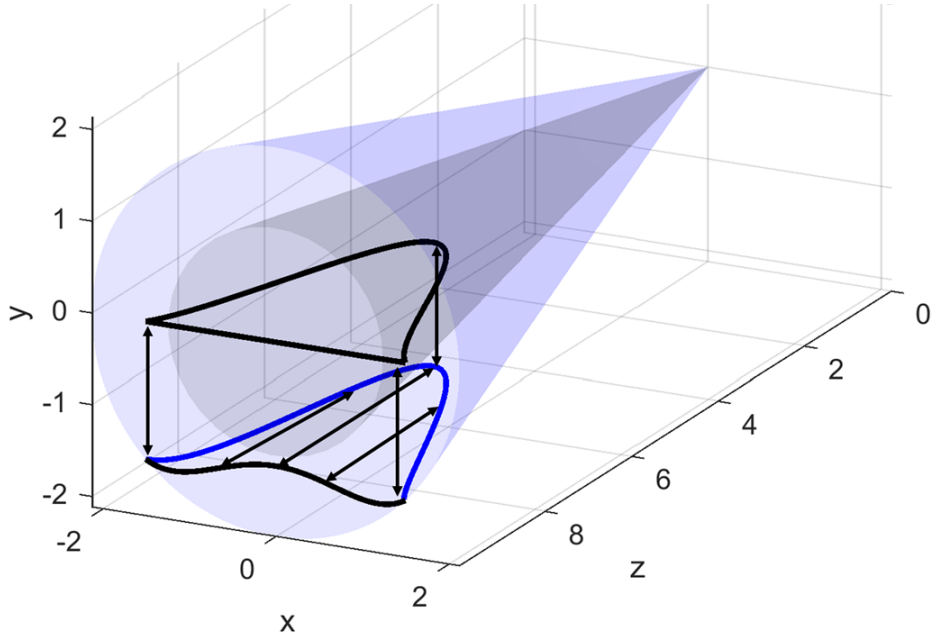


Figure 2.8: Waverider construction curves for a conical shock: leading edge, planform, and base-plane curves.

leading edge is traced along the shock, defined in three-dimensional space. The curve is projected in the horizontal plane to define the vehicle planform, and projected onto the base plane to define the vehicle's upper surface. Alternately, a planform may be defined initially with projections onto the design shock to define the leading edge and a subsequent projection of the leading edge onto the base plane to define the upper surface. Another alternative is that a "generating curve" may be defined on the base plane that is projected onto the design shock to define the leading edge, then onto the horizontal plane to define the planform. The relationship between these curves is depicted in Fig. 2.8.

There are a few requirements for a valid generating curve that must be adhered to. The wingtips must lie on the design shock. The base-plane generating curve

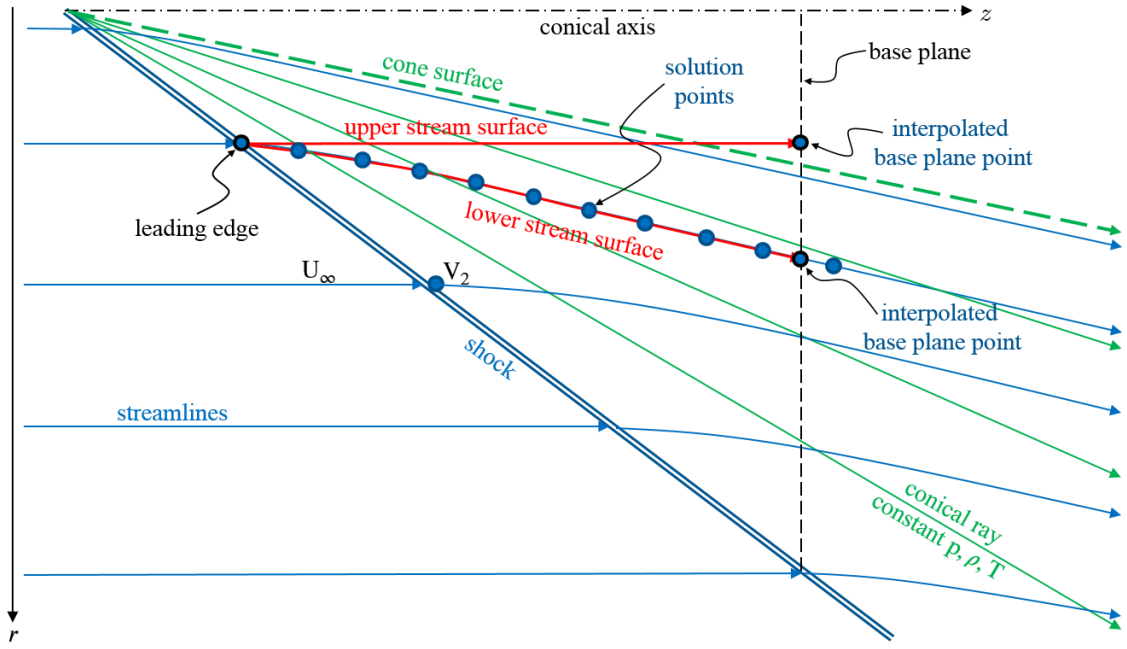


Figure 2.9: Waverider construction schematic along a vertical plane.

must lie entirely below the horizontal plane, but may lie partly within the imaginary cone. A generating curve with concave geometry on the upper surface must not be so sharp that it creates a self-intersecting vehicle when the stream surfaces are integrated.

### 2.4.4 Stream-Surface Tracing

With the flow field and the leading edge defined, discrete points are selected along the leading edge for integration of streamlines. The upper surface is defined as tangent to the free-stream flow. The lower surface is defined by numerically integrating the streamlines from the leading edge to the base plane, as depicted in Fig. 2.9. The tracing of streamlines for a 25-point leading edge is depicted in Fig. 2.10.

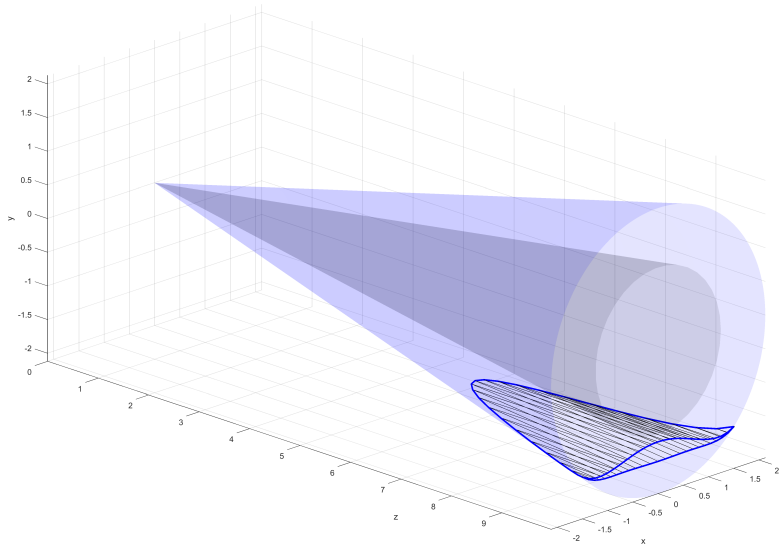

Figure 2.10: Waverider streamline tracing for a Mach 6 vehicle designed on a 12° conical shock with 25 leading edge points.

The streamlines are integrated via the sixth-order Runge Kutta method described in Section 2.4.1. The initial point for computing each $i^{th}$ streamline is each leading edge point, $\vec{x_i}|_0 = (x_{LE,i}, y_{LE,i}, z_{LE,i})$, and the velocity is taken from the flow field solution, $v_{\hat{\rho}}$ and $v_{\hat{\phi}}$. The integration time step is set to $\Delta t = 0.00025w/M/N_x$, where $N_x$ is the number of leading edge points and $w$ is the design wingspan. This time step was empirically found to yield solutions where the streamline solution was a minor contributor to the error in the aerodynamic coefficients.

The upper surface is discretized into triangular panels for a grid of $N_x \times N_x$ points. The lower-surface panels are created by cubically interpolating the streamline integration points. The resulting paneled vehicle is depicted in Fig. 2.11.

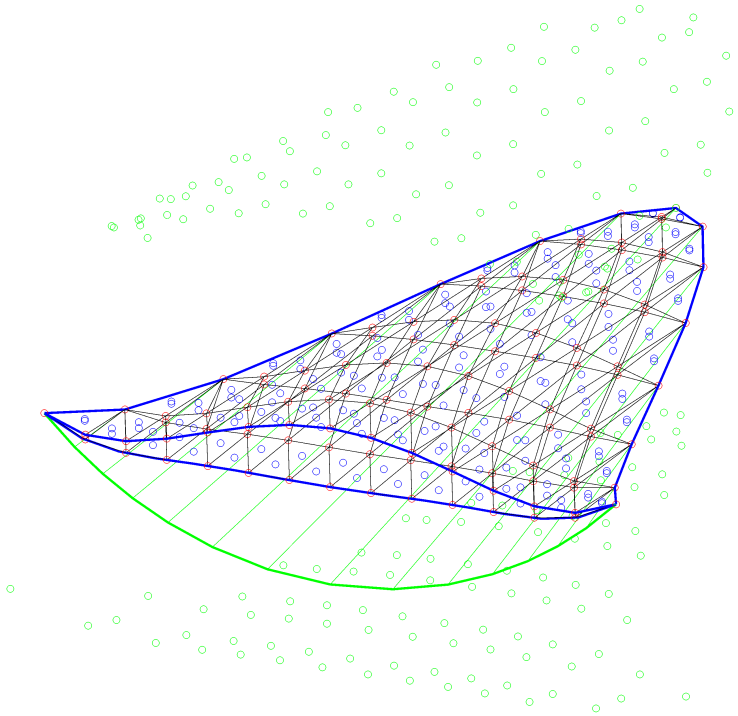

Figure 2.11: Waverider triangular surface panels (black), vertices (red), centroids (blue), and surface normal vectors (green), for a $15 \times 15$ grid and 196 surface panels. The design shock is shown in green.

## 2.5 Morphing Waveriders

The preceding sections have focused on waverider construction and analysis for both on-design and off-design flight regimes. As described in Section 1.3.1, waveriders are designed for a specific Mach number and orientation [4]. A practical vehicle, however, will likely need to operate at various speeds for ascent, descent, glide, or atmospheric entry. For entry vehicles in particular, the range of speeds spans at least Mach 25 at the entry interface (typically 120km) down to zero speed upon touchdown. A primary subject of this work is to evaluate how waveriders perform in their off-design configuration using the described reduced-order aerodynamics models and high-fidelity simulations.

Consider that a waverider designed for high Mach numbers would produce high pressure-drag at low-hypersonic speeds because of its larger flow-turning angle. A slender waverider designed for low-hypersonic flight would not produce much lift at high Mach numbers without pitching to a steeper angle of attack. At a positive angle of attack, the upper surface becomes a lower-pressure expansion surface that adds to drag. Additionally, a slender vehicle at a pitching angle gives up payload volume compared to an on-design waverider with a free-stream tangent upper surface. Conceptually, then, there should be inherent disadvantages for drag and the lift-to-drag ratio for operating a waverider off design compared to on design. Instead of a single design point at a single speed, suppose it is possible to retain an on-design flight condition across a wide speed range. How might this be accomplished? What advantages might this have?

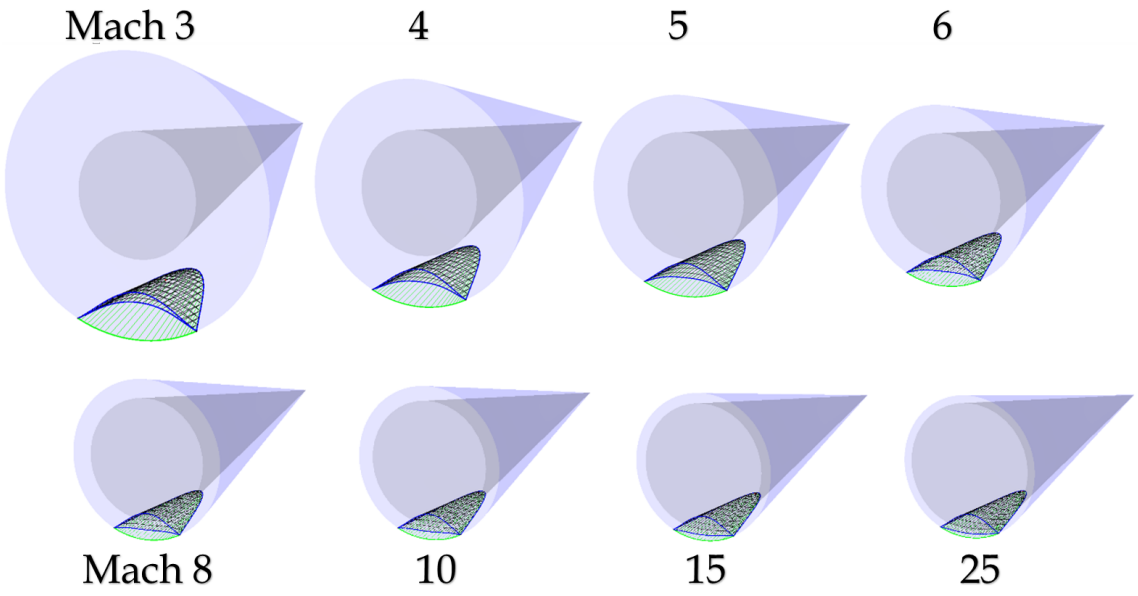


Figure 2.12: A waverider constructed from the flow field generated by a fixed cone across Mach number will have a variable leading edge, planform, upper and lower surfaces with changes in the flight Mach number. Vehicles are qualitatively different as Mach number is varied.

A cone in supersonic flow produces a conical shock wave and the wave angle is dependent upon the Mach number. A waverider constructed from this flow field would necessarily have different geometric features at each speed. Since the shock geometry changes, its leading edge changes, its upper surface changes, and its lower surface changes. Even its aspect ratio changes. This is illustrated in Fig. 2.12.

Instead, suppose the shock geometry is fixed and the imaginary cone varies as Mach number varies. With a fixed shock, the leading edge is fixed, the planform is fixed, and the top surface is fixed. Only the lower stream surface varies with Mach number, as illustrated in Fig. 2.13. As the Mach number increases, the generating body must move closer to the shock, pushing the stream surface toward the shock.

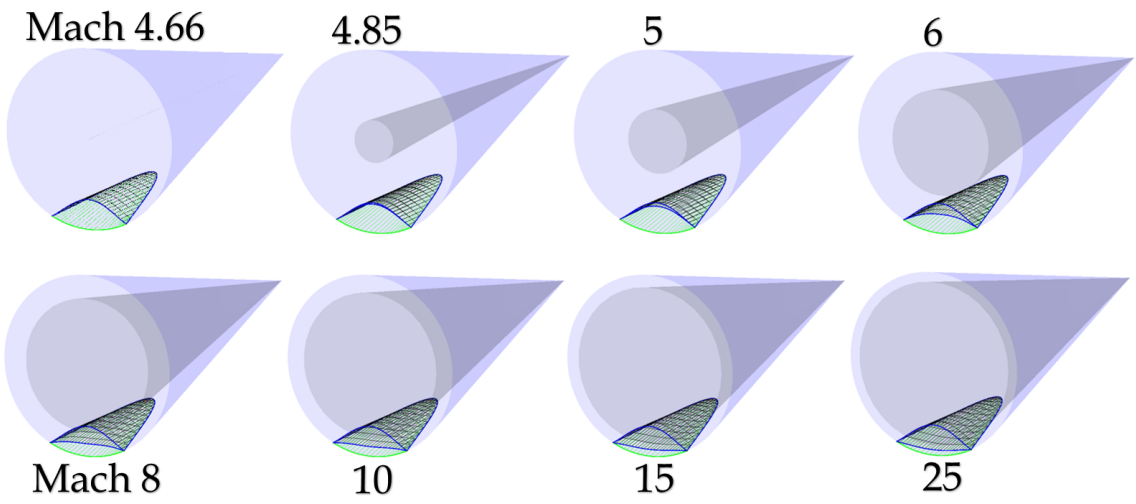


Figure 2.13: A waverider constructed from a fixed shock geometry across Mach number will have a fixed leading edge, planform, and upper surface. Only the lower surface must vary with Mach number. Variations appear as small deflections in the lower stream surface for hypersonic Mach numbers and demonstrate Mach number independence for high Mach number.

Since the leading edge is fixed, the stream surface can be thought of as a flexible plate with a pinned boundary defined by the leading edge. In principle, if a vehicle's lower surface could be "morphed" to conform to the stream surface as a function of Mach number, the vehicle would operate on design for a continuous range of Mach number. For the case chosen in Fig. 2.13, the generating cone collapses to infinitesimally thin at Mach 4.66. In this case, the post-shock streamlines are parallel to the free-stream flow and the upper and lower stream surfaces are identical. A lower Mach number will not be able to produce a shock at this small of an angle. Therefore, the shock angle choice results in a lower limit for on-design Mach number.

As the Mach number increases for a fixed shock shape, the vehicle volume becomes larger. Practicality dictates that the lower limit for on-design Mach number will require some minimum volume. The classical "volumetric efficiency" of a waverider design is a dimensionless comparison between reference area and internal volume:

$$\eta_V = V^{2/3}/S \tag{2.52}$$

where $V$ is the internal volume and $S$ is the planform area. While this morphing method would theoretically enable a waverider to operate on-design across a wide range of Mach number, there are a few key considerations that must be addressed:

1. What surface displacements are required to morph across a given range of Mach number?

2. What strain is produced in the lower surface during morphing?

3. How does an on-design morphing waverider compare to a rigid waverider off-design in terms of lift, drag, L/D, and payload volume?

4. What is the complexity of implementation required for morphing?

Questions 1-3 will be addressed in the results and discussions within the present work, while question 4 will be deferred for future work. Inherently, deflections in the stream-surface at low Mach number are significant whereas deflections in the stream-surface at high Mach number become insignificant. Morphing a waverider stream surface becomes increasingly feasible for large Mach numbers and small shock angles and increasingly difficult for small Mach numbers and large shock angles. The

strain induced in the stream surface, the effect of morphing on the aerodynamics of a waverider, and the comparison to a rigid waverider are discussed in Section .

### 2.5.1 Aerodynamic Forces and Moments

The pressure solution provided in Eqn. 2.49 is used to interpolate the pressure at each panel centroid. The on-design inviscid lift, drag, and pitch moment coefficients on the bottom surface are computed using the pitch inclination of each panel, $\alpha_i$, as:

$$C_{L,TM}(\alpha) = \sum_i C_{p,TM,i} \cos(\alpha_i) \tag{2.53}$$

$$C_{D,TM}(\alpha) = \sum_i C_{p,TM,i} \sin(\alpha_i) \tag{2.54}$$

$$C_{M,TM}(\alpha) = \sum_i C_{p,TM,i} r_{LE,i} \cos(\alpha_i) \tag{2.55}$$

where $r_{LE,i} = \sqrt{y_{LE,i}^2 + z_{LE,i}^2}$ is the moment arm to the $i^{th}$ panel centroid from the nose tip of the vehicle.

### 2.5.2 Modifications for Realistic Leading-Edge Bluntness

A waverider constructed with an ideally sharp leading edge is impractical to fabricate and will not survive the temperatures encountered at high Mach numbers. Waveriders must also be sufficiently stable and controllable to be useful along intended flight trajectories. Because of this, they must be modified from the geometry produced with the original construction method. Within the scope of the present work, we will incorporate the effects of a finite-thickness leading edge. Even a nominally sharp leading edge must be fabricated with some nonzero leading edge radius,

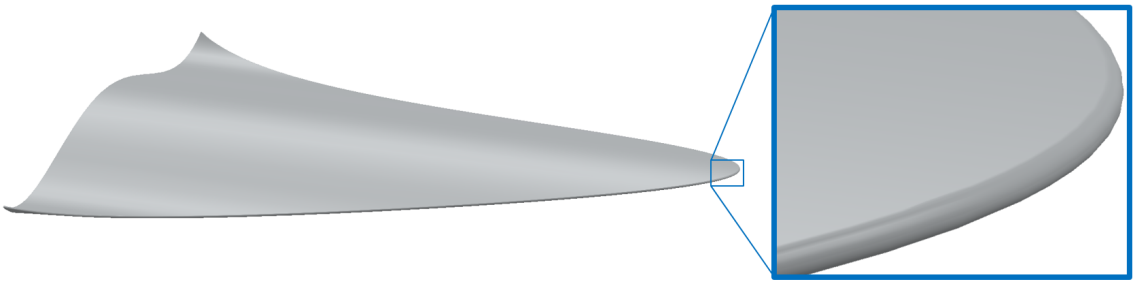

Figure 2.14: Waverider with 0.1% blunted leading edge.

as depicted in Fig. 2.14.

Classically, the leading edge is rounded uniformly. This operation, known as a "fillet," reduces the extent of the vehicle and creates a circular cross section that is tangent to the vehicle upper and lower surfaces [2]. This method is depicted in Fig. 2.15, and is referred to as "Sharp Edge Fillet (SEF)." As illustrated in 2.15, the disadvantage of the SEF method is that the planform is not preserved. As the degree of blunting is increased, the leading edge and lower stream-surface of the vehicle conform less and less to the original design flow field.

An alternative method is proposed in the present work that will be referred to as the Planform Vertical Offset (PVO) method. As depicted in Fig. 2.15, the leading edge is created by vertically extruding the planform with a uniform displacement. The resulting corners are filleted at the top and bottom of the extrusion so that the radius of the leading edge corresponds to half of the increased vehicle thickness.

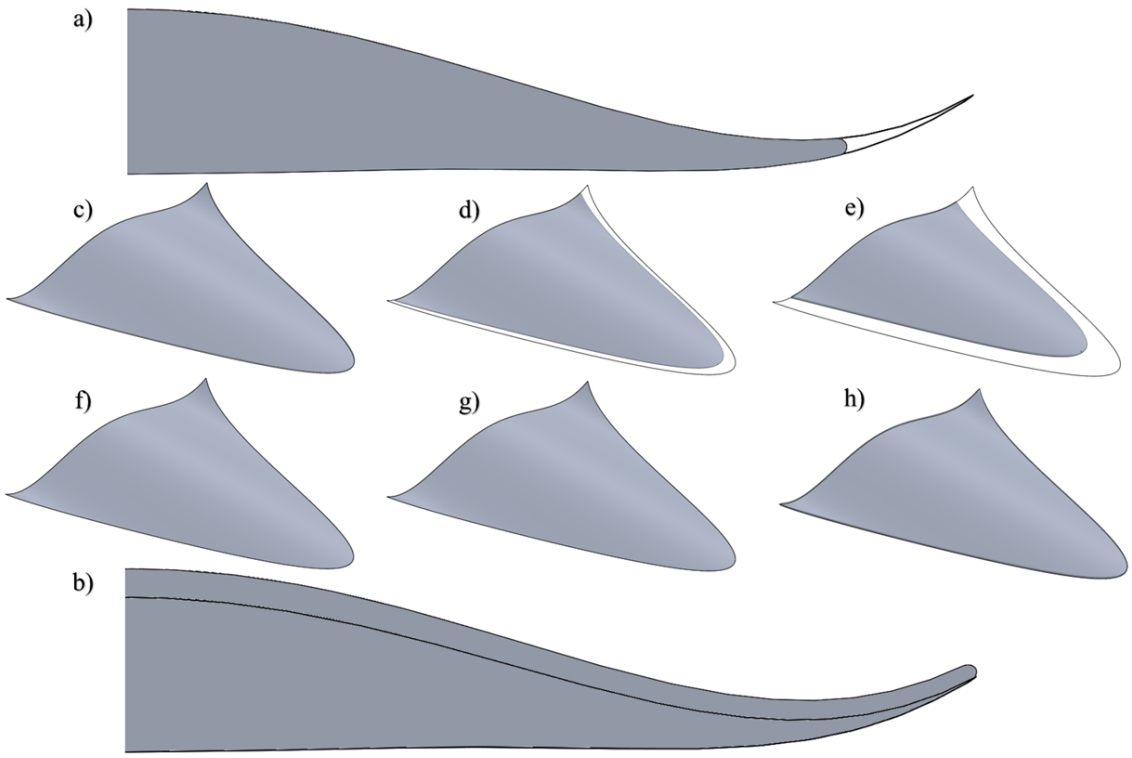


Figure 2.15: Method comparison of leading edge blunting with original sharp-edged vehicle silhouette. a) The sharp edge fillet (SEF) method, b) planform vertical offset (PVO) method, c) sharp-edged waverider, d) SEF 0.1% wingspan radius, e) SEF 0.5%, f) sharp-edged waverider, g) PVO 0.1% wingspan radius, h) PVO 0.5%.

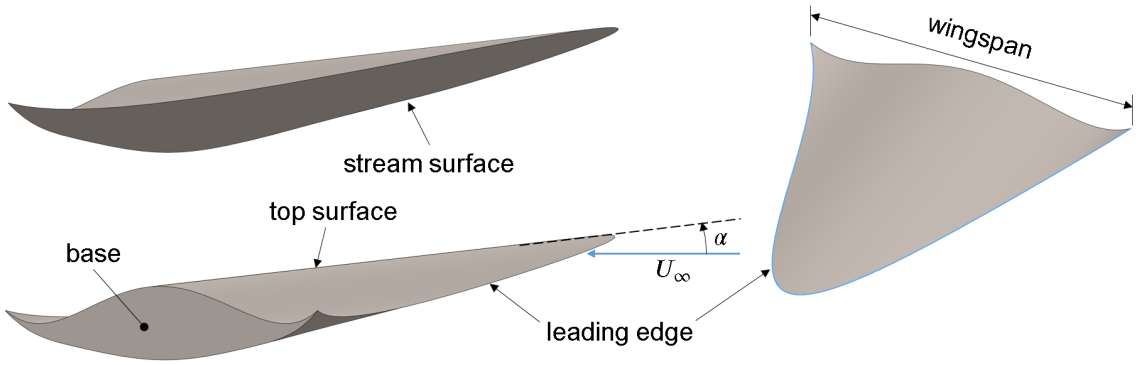


Figure 2.16: Annotated waverider multi-view at angle of attack $\alpha$ and speed $U_\infty$.

## 2.6 Models for Hypersonic Aerodynamics

The purpose of reduced-order modeling of aerodynamics is to develop an accurate model that can be used at minimum computational cost. The methods used for the reduced-order aerodynamics model are summarized in the following subsection and described in more detail in the subsequent subsections.

In order to compute the forces on the vehicle, the temperature and pressure must be estimated on all surfaces: the lower stream surface, the upper surface, the leading edge, and the base of the vehicle. The surface terminology is depicted in Fig. 2.16.

### 2.6.1 Summary for the Reduced-Order Model for Waverider Aerodynamics

The surface of the waverider is discretized in to panels, as described in Section 2.4. Each panel has a unique centroid and normal vector. The model begins

with Modified Newtonian Flow theory applied to the leading edge [4]. The leading edge is assumed to have a circular cross-section where each panel is accounted for individually for their inclination to the free-stream flow.

The vehicle surface parameters are interpolated from the known or computed design flow field in order to determine the forces on the lower surface for on-design orientation and Mach number. For varied angle-of-attack and Mach number, Modified Newtonian Flow theory calibrated for the design flow field is used. In the present work, we will focus on the case study of a conical shock as the design flow field, although the method is generalizable for substitution of any known or computed flow field.

A new model is proposed here for base pressure along with experimental justification. The pressure on the upper surface is approximated as the free-stream temperature, pressure, and Mach number when at zero angle of attack, or on-design. When the angle of attack is positive, Prandtl-Meyer expansion theory is used for the upper surface up to a maximum angle. Beyond this maximum angle, the base pressure model is applied to the upper surface. When the angle of attack is negative, two-dimensional Oblique Shock Theory is used for the upper surface.

Viscous effects are accounted for by using empirical relations for the friction coefficient for flow past a flat plate as a function of Mach number and Reynolds number. An empirical model is used to estimate the heat flux at the stagnation point, a local-inclination model is used to estimate heating elsewhere on the leading edge, and a relation between viscous friction and heating is used to estimate the heating on the upper and lower surfaces.

### 2.6.2 Modified Newtonian Flow

Isaac Newton showed using a momentum balance that the pressure exerted on an inclined flat plate in high-speed flow has the form [3]

$$C_{p,N} = 2\sin^2\alpha \tag{2.56}$$

which is referred to as the Newtonian pressure coefficient. It is inaccurate for low-speed flow, but it does yield useful results for high-speed flow. It was observed that the qualitative variation of the pressure coefficient with inclination angle was accurate when compared with analytical results and experiment, but its absolute value was not [4]. Additionally, the Newtonian flow pressure coefficient listed in Eqn. 2.56 does not include any variation with Mach number or fluid properties.

A more useful form for the pressure coefficient can be obtained using the Rayleigh pitot tube formula to calibrate the maximum pressure coefficient [52, 158]:

$$p_{0,2} = p_\infty \left[\frac{(\gamma+1)M^2}{4\gamma M^2 - 2(\gamma-1)}\right]^{\gamma/(\gamma-1)} \left[\frac{1-\gamma+2\gamma M^2}{\gamma+1}\right] \tag{2.57}$$

$$C_{p,max} = \frac{2}{\gamma M^2}\left(\frac{p_{0,2}}{p_\infty} - 1\right) \tag{2.58}$$

$$C_{p,MN} = C_{p,max}\sin^2\alpha \tag{2.59}$$

This Modified Newtonian Flow pressure coefficient is widely used and will be used as the method for estimating the pressure forces along the leading edge. For the lower stream-surface, however, this work proposes to calibrate the Newtonian pressure coefficient with the Taylor-Maccoll solution pressure at each individual panel and at zero angle of attack for the vehicle, $C_{p,TM,i}$. This calibration method is provided

in Eqn. 2.60 [55].

$$C_{p,i}(\alpha) = \frac{(P_{TM,i} - P_\infty)}{q_d \sin^2 \alpha_i} \frac{\sqrt{1+M_d^2}}{\sqrt{1+M_f^2}} \sin^2(\alpha + \alpha_i) \tag{2.60}$$

where $M_d$ and $q_d$ are the design Mach number and dynamic pressure, $M_f$ and $q_f$ the flight Mach number and dynamic pressure, and the effective offset angle is

$$\alpha_i = \arcsin \left[ \left( \frac{C_{p,TM,i}}{C_{p,max}} \right)^{1/2} \right] \tag{2.61}$$

where $C_{p,max}$ is computed using flight conditions at $M_f$ and $q_f$, while $C_{p,TM,i}$ is computed using the design condition $M_d$ and $q_d$ at panel $i$. The pressure lift and drag force coefficients for the lower surface are computed as

$$C_{L,TM}(\alpha) = \sum_i C_{p,i}(\alpha) \cos(\alpha) \tag{2.62}$$

$$C_{D,TM}(\alpha) = \sum_i C_{p,i}(\alpha) \sin(\alpha) \tag{2.63}$$

### 2.6.3 Tangent Wedge Method

In the Tangent Wedge Method, the temperature and pressure at each panel centroid are computed by treating each panel as an independent wedge, assuming an attached shock and using the Oblique Shock Relations, Eqns. 2.40-2.44 [3]. The $\theta - \beta - M$ equation, 2.64, is iteratively solved for $\beta$ with the panel inclination angle as $\theta$.

$$\tan(\theta) = 2 \cot(\beta) \frac{M^2 \sin^2(\beta) - 1}{M^2(\gamma + \cos(2\beta)) + 2} \tag{2.64}$$

The shock angle, $\beta$ is then used to compute the post-shock (i.e. panel surface) temperature and pressure using the Oblique Shock Relations. A schematic of a planar shock created by half-wedge is depicted in Fig. 2.17.

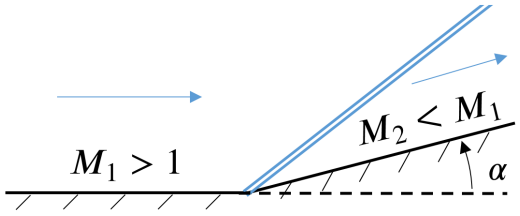


Figure 2.17: Oblique shock schematic: flow initially at $M_1$ turned by an angle $\alpha$ through a shock at angle $\beta$, which decelerates to $M_2$ [3]. The post-shock properties are related to the free-stream properties using Eqns. 2.40-2.44.

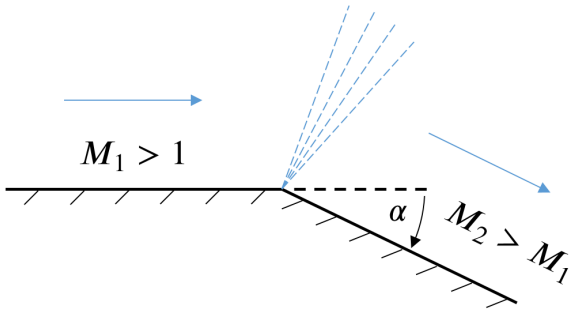


Figure 2.18: Prandtl-Meyer expansion schematic: flow initially at $M_1$ is isentropically turned by an angle $\alpha$, which accelerates to $M_2$ [3].

### 2.6.4 Prandtl-Meyer Expansion

Consider supersonic flow turned by an angle $\alpha$, as depicted in Fig. 2.18. This is a Prandtl-Meyer Expansion [3]. The flow variables are denoted $M_1$ prior to the flow turning and denoted $M_2$ after the flow turning. The relationship between the turning angle $\alpha$ and the flow variables is provided by

$$\alpha = \nu(M_2, \gamma) - \nu(M_1, \gamma) \tag{2.65}$$

where $\nu(M,\gamma)$ is the Prandtl-Meyer function, given in Eqn. 2.66 [3]:

$$\nu(M,\gamma) = \sqrt{\frac{\gamma+1}{\gamma-1}}\left[\arctan\sqrt{\frac{\gamma-1}{\gamma+1}(M^2-1)}\right] - \arctan(\sqrt{M^2-1}) \tag{2.66}$$

which is used to solve iteratively for $M_2$. Since the expansion is isentropic, the isentropic flow relations can be used to solve for post-turning flow variables once $M_2$ is known, summarized in Eqn. 2.68:

$$p_2 = p_1\left[\frac{1+\frac{\gamma-1}{2}M_1^2}{1+\frac{\gamma-1}{2}M_2^2}\right]^{\gamma/(\gamma-1)} \tag{2.67}$$

$$T_2 = T_1\left[\frac{1+\frac{\gamma-1}{2}M_1^2}{1+\frac{\gamma-1}{2}M_2^2}\right]^{\gamma/(\gamma-1)} \tag{2.68}$$

### 2.6.5 Friction Coefficient

Viscous effects on the waverider are modeled as the friction coefficient on a flat plate. The friction coefficient is computed for each surface panel as a function of the local Reynolds number using a reference temperature. The reference temperature method was first proposed by Rubesin and Johnson [159] and modified by Eckert [160] to include a reference enthalpy, which is the form used in the present work. The reference temperature is defined using the near-wall boundary layer edge temperature and Mach number as well as wall temperature in Eqn. 2.69.

$$T^* = T_e\left(1 + 0.032M_e^2 + 0.58\left(\frac{T_w}{T_e} - 1\right)\right) \tag{2.69}$$

The reference density $\rho^*$, viscosity $\mu^*$, constant-pressure heat capacity $c_p^*$, and thermal conductivity $k^*$, are all defined at the reference temperature. The reference Reynolds number is then found for panel centroid position from the local leading

edge $x_{LE}$ and near-wall velocity $u_e$:

$$Re_x^* = \frac{\rho^* u_e x_{LE}}{\mu^*} \tag{2.70}$$

For laminar flow, the local friction coefficient is given by

$$c_{f,lam} = \frac{0.664}{\sqrt{Re_x^*}} \tag{2.71}$$

$$c_{f,tur} = \frac{0.0592}{(Re_x^*)^{0.2}} \tag{2.72}$$

The transition to turbulence is depicted in Fig. 2.19, illustrating a laminar region, a finite-length transitional region, and a turbulent region [161]. The transition location is determined by a critical Reynolds number as referenced from the local upstream leading edge, $Re_{cr}$, as depicted in Fig. 2.20. The value of this critical Reynolds number for the reduced-order model is assumed to be an instantaneous transition from laminar to turbulent flow and is interpolated from experimental results for supersonic flow over a flat plate at zero angle-of-attack and varied free-stream Reynolds number [162]. This model was extended to a blunted flat plate with varied sweep angle [163], which estimates the critical Reynolds number for supersonic flow past a flat plate while accounting for variations in Mach number, free-stream Reynolds number, leading edge sweep angle, and bluntness. This will be referred to as the "Hopkins Method" for estimating the critical Reynolds number for transition to turbulence. For example, using the Hopkins Method [163] for a nominally sharp flat plate at $30km$ altitude and Mach 6, the unit Reynolds number is $1.2 \times 10^5 m^{-1}$ and the critical Reynolds number is $1.5 \times 10^6$. The critical Reynolds number increases to $4 \times 10^6$ for the same plate with a $3mm$ (1%) leading

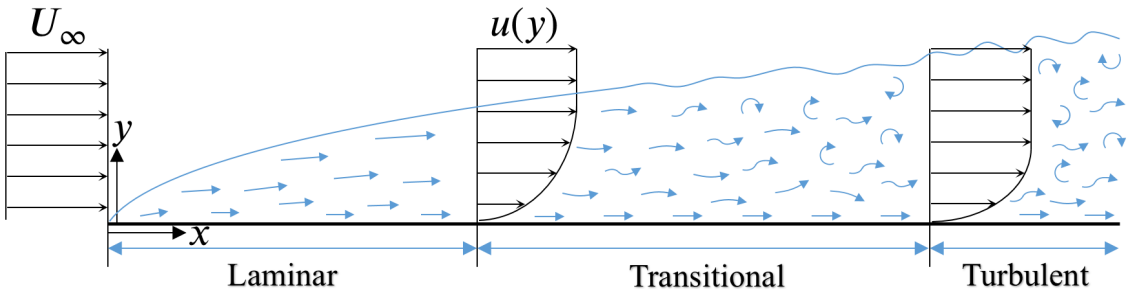


Figure 2.19: Schematic of flow past a flat plate depicting regions of laminar flow, transitional fluctuating flow, and fully turbulent flow.

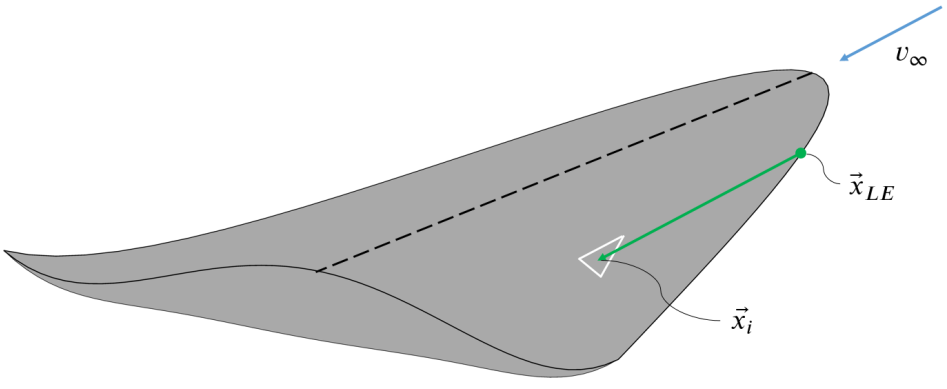


Figure 2.20: Local leading edge reference length coordinate for critical Reynolds number in the Hopkins Method for the $i^{th}$ panel [163].

edge radius. Adding a 60° leading-edge sweep, the critical Reynolds number reduces to approximately $1 \times 10^6$.

With this estimate for the local friction coefficient we may revisit the Stanton number, 2.73, and use the Reynolds Analogy 2.25 to compute the local heat flux as [149]:

$$q_w = \frac{1}{2} c_f Pr^{-2/3} \rho_\infty v (h_{aw} - h_w) \tag{2.73}$$

An alternative to using the friction coefficient and the Reynolds Analogy for is Churchill's Method for estimating the local heating of a flat plate in supersonic flow [164]. In this method, a reference temperature is computed according to Eqn. 2.74.

$$T^* = T_\infty + 0.5(T_{w,i} - T_\infty) + 0.22(T_{aw} - T_\infty) \tag{2.74}$$

The heat flux is then computed using fluid properties at the reference temperature as:

$$q_w = (T_{w,i} - T_{aw}) Pr^{-2/3} \rho^* c_p^* v x_i \tag{2.75}$$

where the length dimension, $x_i$, is dependent upon the Reynolds number of the panel referenced to the upstream leading edge and the reference temperature, $Re^*$, according to Eqn. 2.76:

$$\left\{ \begin{array}{ll} x_i = 0.332 (Re^*)^{-1/2} & Re^* \leq Re_{cr} \\ x_i = 0.0296 (Re^*)^{-1/5} & Re^* > Re_{cr} \leq 10^7 \\ x_i = 0.185 (\log Re^*)^{-2.584} & Re^* > 10^7 \end{array} \right\} \tag{2.76}$$

The Churchill Method is semi-empirical, based on a model fit to experimental data. The three regimes in Eqn. 2.76 correspond to laminar, transitional, and fully turbu-

lent heating regimes. While Churchill uses a fixed $Re_{cr} = 5 \times 10^5$ for unswept, sharp, flat plates at zero angle of attack, the present work will use the Hopkins Method of estimating $Re_{cr}$ that accounts for all of these effects.

### 2.6.6 Base Pressure and Temperature

There are two models frequently used for base pressure, $p_b$, in supersonic flow. The first is a zero pressure coefficient, $C_p = 0$ [4]. This corresponds to a pressure equal to the free-stream pressure, $p_b = p_\infty$. The second is zero pressure, $p_b = 0$, which corresponds to a pressure coefficient of $C_p = p_\infty/q \propto 1/M^2$ [3]. When compared with experimental data, however, neither approach appears to represent the trend with Mach number or an accurate base pressure for low and moderate Mach numbers [165–167]. This thesis uses a phenomenological model for base pressure based on experimental studies, provided in Eqn. 2.77. The comparison of the three models with experimental data is provided in Fig. 2.21.

$$p_b = \frac{p_\infty}{M} \tag{2.77}$$

The comparison with experimental data is provided in Fig. 2.21, illustrating qualitative agreement with the proposed base-pressure model. While the quantitative comparison between the proposed model and the experimental data depicts errors on the order of $20 - 30\%$, the proposed model is demonstrably more accurate than the two legacy models for supersonic and low-hypersonic Mach numbers. It is possible that future adaptations of the proposed model may include modification factors for scaling, offsetting, or skewing the general form of the proposed model based on

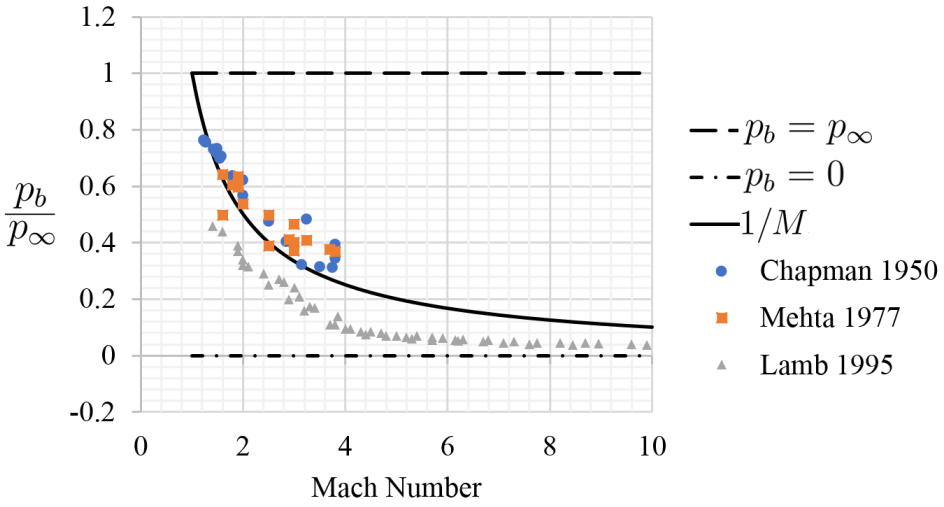


Figure 2.21: Base pressure model comparison plot with empirical data for 10° cone-cylinders with length-to-diameter ratio 5 and 6 [167], a rearward facing axisymmetric step [166], and 9° blunted-nose cones [165].

geometry and Reynolds number. The base temperature is estimated by taking the stagnation temperature and pressure behind the shock created by the vehicle and isentropically expanding the stagnation flow to the base pressure, summarized in Eqn. 2.78.

$$T_b = T_0 \left( \frac{p_\infty}{p_{0,2} M} \right)^{\frac{\gamma-1}{\gamma}} \tag{2.78}$$

### 2.6.7 Model Summary and Convergence

The composite model described in the preceding sections is called the "Waverider Reduced-order Analysis Investigative Tool for Hypersonics," or "WRAITH" for shorthand. A summary of the models used in each context is as follows for varied angle-of-attack and Mach number. The Taylor-Maccoll solution is used to interpolate the pressure-based forces on the lower surface for on-design Mach number and

orientation. The Van Driest-Lees heat flux models are used for the leading edge, Eckert's friction coefficient is used for the top and bottom surface, Hopkins' transition to turbulence for the critical Reynolds number, and the proposed base pressure model $p_b = p_\infty/M$. For off-design angle-of-attack, Taylor-Maccoll-calibrated Modified Newtonian Flow is used for the lower surface. When the angle-of-attack is positive, Prandtl-Meyer theory is used for the top surface up to the critical angle, beyond which the proposed base pressure model is used. When angle-of-attack is negative, Tangent Wedge theory is used for the top surface.

An important feature of any numerically solved model is that it is self-convergent, meaning that it reaches a stationary value with increasingly refined step sizes in time and space. The sample vehicle designed at Mach 6 and 30km from a 12° shock angle is used to demonstrate the convergence of the construction method and reduced-order aerodynamics models. The error in coefficients is given in Fig. 2.22 and a depiction of various levels of resolution of the vehicle surface is provided in Fig. 2.23. The reference solution for computing the error magnitude in Fig. 2.22 is that with 40,000 surface panels. As depicted in Fig. 2.22, the approximate convergence slope is different for each coefficient.

The lift and pitch moment are almost exclusively due to pressure-based forces, which are computed using ordinary differential equations (ODEs) and high-order solution methods such that they converge approximately first-order. The drag and the lift-to-drag ratio, however, include friction coefficient "sampling" at each surface panel rather than ODE solution with a high-order method. Sampling methods converge with a slope of 1/2 [168], which is observed in Fig. 2.22. Overall, the

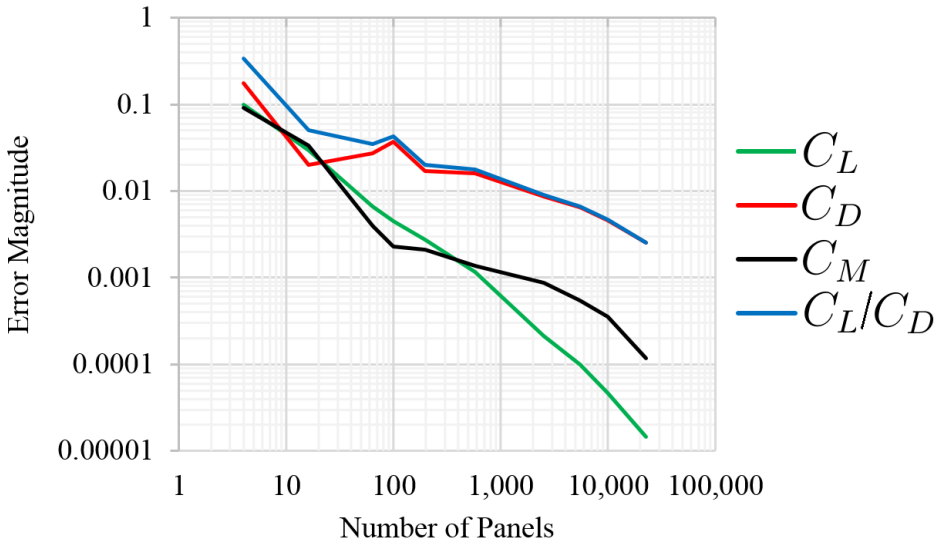


Figure 2.22: Convergence of reduced-order aerodynamic coefficients model with number of surface panels for Mach 6 waverider at 30km.

reduced-order model of waverider aerodynamics should be approximately half-order convergent. Examining Fig. 2.22, approximately 2,000 surface panels are required to achieve 1% convergence. Following the half-order convergence assumption, 200,000 surface panels should be expected to achieve 0.1% convergence.

### 2.6.8 Entry Trajectory Comparison

A trajectory is computed using the Mars COSPAR reference atmosphere [15] and the aerodynamic coefficients from [2] for the Mars Science Laboratory (MSL) capsule. The capsule parameters are listed in Table 2.1 and the simplified model trajectory is depicted in Fig. 2.24 along with flight path data from [169].

Note that there is no explicit control implemented in the capsule aerodynamics model except for halving the lift coefficient below 25km in order to prevent too steep

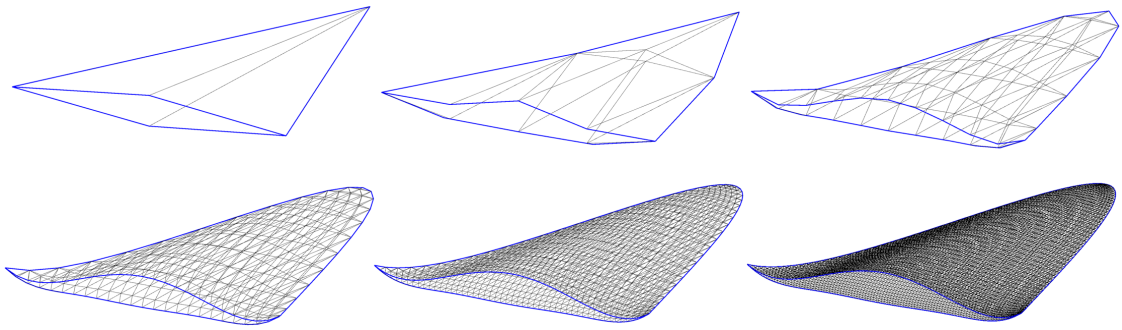

Figure 2.23: Waverider used for convergence study with 4, 16, 100, 576, 2,500, and 10,000 surface panels to illustrate surface geometry resolution.

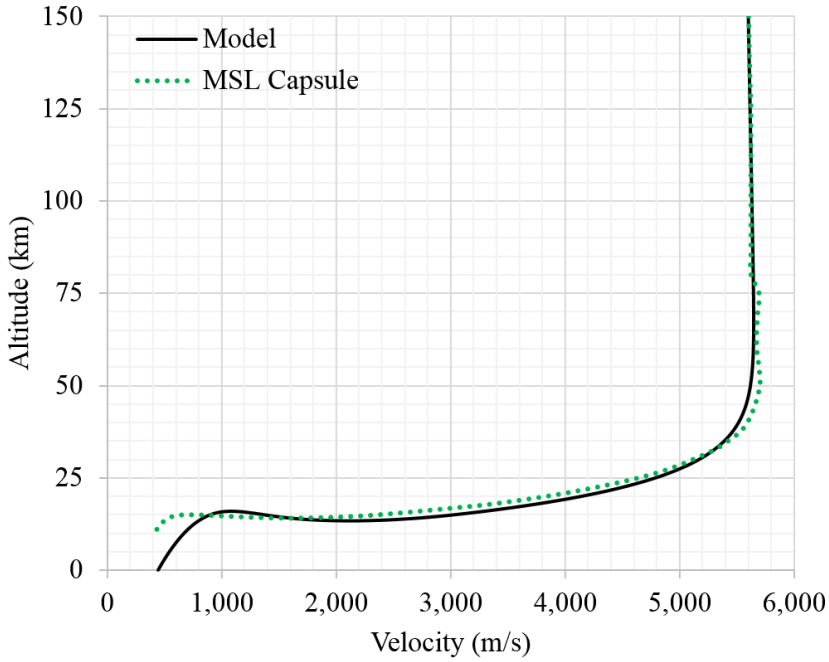


Figure 2.24: Velocity entry profile with altitude for the Mars Science Laboratory capsule: comparison between detailed flight trajectory data [2] (dotted) and the planar lifting entry dynamics model (solid).

| $m\ (kg)$ | $D\ (m)$ | $h\ (km)$ | $v\ (km/s)$ | $\gamma\ (^\circ)$ | $\beta\ (kg/m^2)$ | $L/D$ |
|---|---|---|---|---|---|---|
| 3380 | 4.5 | 150 | 5.6 | -15 | 148 | 0.24 |

Table 2.1: Parameters for the Mars Science Laboratory capsule at its entry interface [2].

of a climb. Below 1,000m/s, complex control and retro-thrust is implemented in the MSL capsule, whereas the simplified model used in the present study continues gliding to the surface because those detailed effects are outside the scope of the present work. Upon examination of the flight path comparison, the model agrees with the provided data qualitatively and quantitatively and will be satisfactory for entry vehicle comparisons. Note that the touch-down speed of approximately 450m/s of the model capsule is exemplary of the "supersonic decelerator problem," where even a high-lift vehicle entering a low-density atmosphere cannot sufficiently decelerate under aerodynamic forces alone [171]. For Mars entry, the touch-down speed of high-lift or high-drag concept vehicles is still typically supersonic, requiring additional mechanisms such as the Sky Crane [171], retro-thrust, and parachutes [170] in order to touch down safely.

# Chapter 3: Computational Approach

This chapter discusses the numerical methods and fluid dynamics models used to solve the flow field. This includes the numerical models for solving the compressible Navier-Stokes equations, models for equilibrium and non-equilibrium chemistry, the geometry discretization, adaptive mesh refinement, and the time advancement methods. Two turbulence models are used in the present work, each with distinct advantages and disadvantages. The chapter closes with two test cases to demonstrate the accuracy and convergence of the tools used for a flat-plate friction coefficient in hypersonic flow and a cylinder in viscous, reactive hypersonic flow.

## 3.1 Numerical Methods

The numerical simulation of a waverider flow field requires a model for the fluid, governing equations for fluid dynamics, models for turbulence, and solution methods. These are summarized here and discussed in more detail in the following subsections. Two types of fluids are considered in the present work. The first is a model for single-species air, the use of which significantly reduces the computational cost and allows for a wider array of simulations. The second is a seven-species reactive air model, which includes the effects of chemical non-equilibrium but is

much more computationally expensive. Two turbulence models are used in the present work. The more expensive turbulence model, LES-WALE, captures the effects of large-scale turbulent flow structures in space and time. The lower-cost turbulence model, $k-\omega$ SST, averages transient features of the flow in time and space but allows for a wider survey of configurations.

### 3.1.1 Fluid Model

The fluid model for air is based on the ideal gas equation of state, given in Eqn. 3.1, and two models for air chemistry: one for equilibrium chemistry and one for non-equilibrium chemistry.

$$p = \rho \mathscr{R} T / M_w \tag{3.1}$$

where $\mathscr{R} = 8.314 \frac{J}{mol-K}$ is the universal gas constant and $M_w$ is the molecular mass. The first treatment of high-temperature air includes a model of reacting flow with equilibrium chemistry. Air is assumed to be a monolithic substance with molecular weight 28.966g/mol. For air temperatures up to approximately 500K, air may be described as calorically perfect with a heat capacity ratio, $\gamma = c_p/c_v$, fixed at a constant value of $\gamma = 1.4$ [25].

For temperatures up to approximately 2,000K, the heat capacity ratio can be modeled as a function of temperature only, a regime described as thermally perfect. The model used for thermally perfect air is based on kinetic theory and is given in

Eqn. 2.51 [157].

$$\gamma(T(\vec{x})) = 1 + \frac{\gamma_0 - 1}{1 + (\gamma_0 - 1)\left[\left(\frac{T_{ref}}{T}\right)^2 \frac{e^{\frac{T_{ref}}{T}}}{\left(e^{\frac{T_{ref}}{T}} - 1\right)^2}\right]} \tag{3.2}$$

where $T_{ref} = 3055\text{K}$ and $\gamma_0 = 1.4$, and both temperature and $\gamma$ are scalar fields in space. In this model, air is assumed to be in chemical equilibrium, where variations in $\gamma$ with temperature account for effects of chemically reactive flow.

For a waverider, the stagnation region is small and confined near the leading edge. The planform of the vehicle, where the vast majority of forces occur, is much closer to the free-stream temperature than the stagnation temperature. This is illustrated in Fig. 3.1 for the stagnation region and conical shocks across Mach number. In these particular cases, the fluid model is approximately valid to Mach 8 in the stagnation region, but valid to Mach 20 behind a 20° conical shock, and valid beyond entry Mach numbers behind a shallower 10° conical shock for a sharp-edged vehicle. The more the leading edge is blunted and the faster the vehicle travels, the more the stagnation region has transient effects that propagate downstream.

The second treatment for reactive air includes finite-rate chemical reactions being explicitly accounted for using the Dunn-Kang reaction model and rates [172]. Air up to 9,000K is treated as a mixture of seven molecular species: $N_2$, $O_2$, $NO$, $N$, $O$, $NO^+$, and $e^-$. The reactions considered are summarized as:

$$O_2 + M \rightleftharpoons 2O + M \tag{3.3}$$

$$N_2 + M \rightleftharpoons 2N + M \tag{3.4}$$

$$NO + M \rightleftharpoons N + O + M \tag{3.5}$$

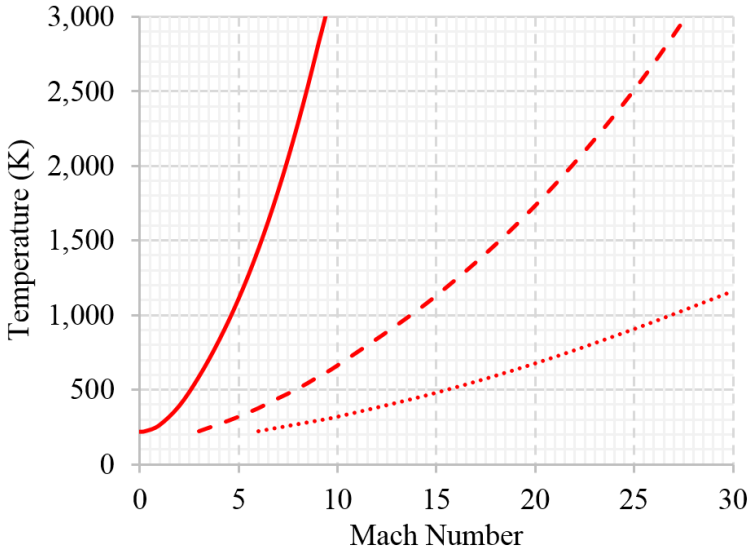


Figure 3.1: Temperature at the stagnation point (solid) and behind a 20° conical shock (dashed) and a 10° conical shock (dotted) with Mach number.

$$O_2 + N \rightleftharpoons NO + O \tag{3.6}$$

$$N_2 + O \rightleftharpoons NO + N \tag{3.7}$$

$$N_2 + O_2 \rightleftharpoons 2NO \tag{3.8}$$

$$N + O \rightleftharpoons NO^+ + e^- \tag{3.9}$$

where $M$ represents a collision partner and each reaction equation with each collision partner has both a forward and backward reaction rate [4]. Eqns. 3.3-3.5 are dissociation reactions, Eqns. 3.6-3.7 are known as bimolecular exchange reactions, and Eqn. 3.9 is the single ionization reaction considered below $9,000K$. Eqns. 3.3-3.9 represent 20 single-direction reactions when all collision partners are considered, each with temperature-dependent reaction rates according to:

$$k_f(T) = C_f T^{\eta_f} e^{-K_f/\mathcal{R}T} \tag{3.10}$$

where $C_f$, $\eta_f$, and $K_f$ are parameters unique to each reaction and $\mathcal{R} = 8.314 \frac{J}{mol-K}$ is the universal gas constant, and are summarized in Table 3.1 [172].

### 3.1.2 Governing Equations

In addition to the Ideal Gas Equation of State, Eqn. 3.1, the fluid dynamics is modeled using the compressible, viscous Navier-Stokes equations [4]. These include the conservation of mass, momentum, and energy, as well as species conservation for reacting flow. The continuity equation and momentum equations for each of the three Cartesian directions with directional velocity components $\mathbf{V} = (u, v, w)$ are:

$$\frac{\partial \rho}{\partial t} + \nabla \cdot (\rho \mathbf{V}) = 0 \tag{3.11}$$

$$\frac{Du}{Dt} = -\frac{\partial p}{\partial x} + \frac{\partial \tau_{xx}}{\partial x} + \frac{\partial \tau_{yx}}{\partial y} + \frac{\partial \tau_{zx}}{\partial z} \tag{3.12}$$

$$\frac{Dv}{Dt} = -\frac{\partial p}{\partial y} + \frac{\partial \tau_{xy}}{\partial x} + \frac{\partial \tau_{yy}}{\partial y} + \frac{\partial \tau_{zy}}{\partial z} \tag{3.13}$$

$$\frac{Dw}{Dt} = -\frac{\partial p}{\partial z} + \frac{\partial \tau_{xz}}{\partial z} + \frac{\partial \tau_{yz}}{\partial y} + \frac{\partial \tau_{zz}}{\partial z} \tag{3.14}$$

where

$$\tau_{xy} = \tau_{yx} = \mu \left( \frac{\partial v}{\partial x} - \frac{\partial u}{\partial y} \right) \tag{3.15}$$

$$\tau_{yz} = \tau_{zy} = \mu \left( \frac{\partial w}{\partial y} - \frac{\partial v}{\partial z} \right) \tag{3.16}$$

$$\tau_{zx} = \tau_{xz} = \mu \left( \frac{\partial u}{\partial z} - \frac{\partial w}{\partial x} \right) \tag{3.17}$$

$$\tau_{xx} = \lambda(\nabla \cdot \mathbf{V}) + 2\mu \frac{\partial u}{\partial x} \tag{3.18}$$

$$\tau_{yy} = \lambda(\nabla \cdot \mathbf{V}) + 2\mu \frac{\partial v}{\partial y} \tag{3.19}$$

$$\tau_{zz} = \lambda(\nabla \cdot \mathbf{V}) + 2\mu \frac{\partial w}{\partial z} \tag{3.20}$$

where $\mu$ is the viscosity based on Sutherland's Law [152] and $\lambda$ is the bulk viscosity, which is simplified using the Stokes' Hypothesis that $\lambda = -\frac{2}{3}\mu$. The material derivative operator on a variable $\chi$ is given by

$$\frac{D}{Dt}(\chi) = \frac{\partial}{\partial t}\chi + \mathbf{V} \cdot \nabla\chi \tag{3.21}$$

The energy equation is given by

$$\begin{aligned}\rho\frac{D(e+V^2/2)}{Dt} = &\frac{\partial}{\partial x}\left(k\frac{\partial T}{\partial x}\right) + \frac{\partial}{\partial y}\left(k\frac{\partial T}{\partial y}\right) + \frac{\partial}{\partial z}\left(k\frac{\partial T}{\partial z}\right) \\ &+ \frac{\partial(u\tau_{xx})}{\partial x} + \frac{\partial(u\tau_{yx})}{\partial y} + \frac{\partial(u\tau_{zx})}{\partial z} \\ &+ \frac{\partial(v\tau_{xy})}{\partial x} + \frac{\partial(v\tau_{yy})}{\partial y} + \frac{\partial(v\tau_{zy})}{\partial z} \\ &+ \frac{\partial(w\tau_{xz})}{\partial x} + \frac{\partial(w\tau_{yz})}{\partial y} + \frac{\partial(w\tau_{zz})}{\partial z} \\ &+ \rho\dot{q} - \nabla\cdot(p\mathbf{V})\end{aligned} \tag{3.22}$$

where $e$ is the specific internal energy and $k$ is the thermal conductivity based on kinetic theory [11].

The system is solved using ANSYS Fluent 16 computational fluid dynamics software [173]. The governing equations are discretized using a Finite Volume Method (FVM) formulation with second-order upwind gradients [173]. The flux between elements is computed using the Advection Upstream Splitting Method (AUSM) [174], which is selected because it is capable of excellent resolution of shock discontinuities and eliminates numerical oscillations near discontinuities. The discretized equations are advanced in time with a second-order implicit predictor-

corrector method. Steady-state results are achieved with advancement until important aerodynamic properties vary by less than 0.1% per characteristic flow time, defined as the length of the vehicle divided by free-stream velocity.

The method used is globally first-order convergent, meaning that uniform refinement of the grid spacing and time step by one order of magnitude results in one order of magnitude reduction in error of the aerodynamic properties simulated. The results can be improved by adaptively refining the grid rather than uniformly refining it. Once a steady state is reached, the mesh is adaptively refined in the regions of large first- and second-order gradients of flow variables. Since density jumps appreciably across a shock and a shock is ideally a discontinuity, 10% of the normalized magnitude of curvature of density is used as a refinement threshold. Since Mach number varies significantly across a shock, in the boundary layer, and in the wake region, 10% of the normalized magnitude of gradient of Mach number is used as a refinement threshold. Both variables are used with each refinement step, the flow field is allowed to march forward in time one characteristic flow duration in order to relax, and a total of three levels of grid refinement are conducted. This results in local resolution increase up to a factor of 8 finer than the initial grid.

For transient results, a steady result is first reached and used as an initial condition. Time is then advanced for ten characteristic flow times, and then fluctuations are sampled and averaged over three characteristic flow durations. An initial unstructured grid of approximately 20 million elements is depicted in Fig. 3.2 along with the adapted grid of 98.6 million elements in Fig. 3.3. The initial grid includes boundary layer refinement with a 15% layer-to-layer growth rate and a

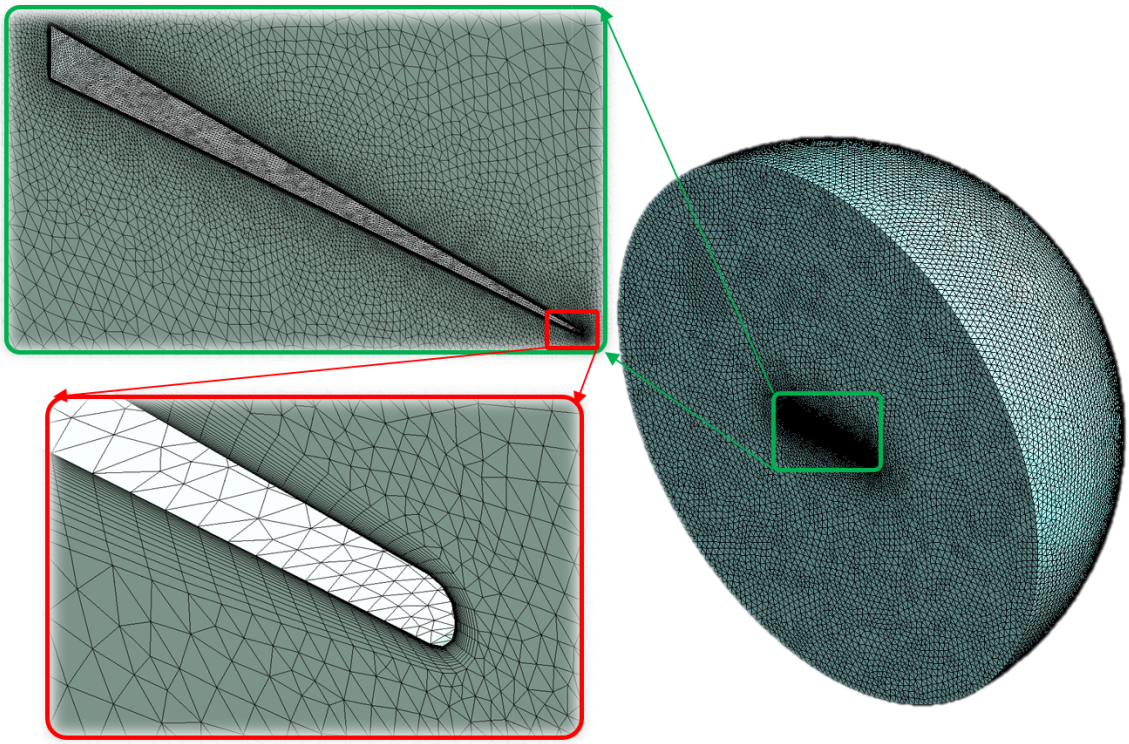

Figure 3.2: Hemispherical computational domain and initial mesh close-ups for the Mach 6 waverider with 20 million elements. Note the boundary layer refinement, the 0.1% leading edge radius, and the near-body resolution. The grid spacing required at the vehicle surface is approximately 30$\mu$m in the normal direction and 600$\mu$m laterally.

maximum aspect ratio of 20:1 per the ANSYS best practices guideline for LES [175] and recommended by Pope [177].

Solving the system of Eqns. 3.11 - 3.22 is referred to as Direct Numerical Simulation (DNS) when solved in this form without further modeling to reduce or eliminate physics in the model [178]. Because of the high computational cost of resolving turbulent flow structures at the high Reynolds numbers that are typically encountered in Earth's atmosphere, various simplified models are used to approx-

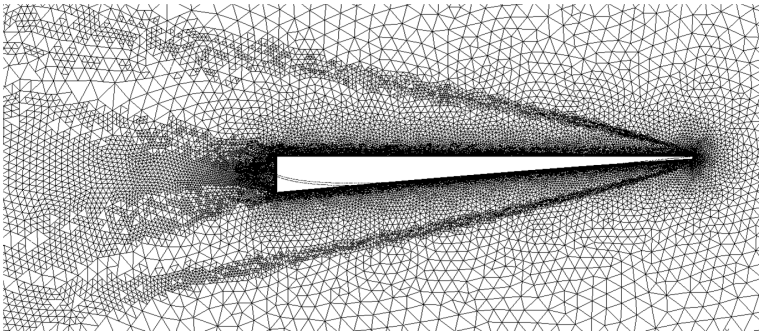

Figure 3.3: Adapted mesh close-up for the Mach 6 waverider with 98.6 million elements. Note the shock, wake, and boundary layer refinement.

imate the effects of small-scale turbulence [178]. The present work will use the Reynolds-Averaged Navier-Stokes $k-\omega$ Shear Stress Transport (SST) model as well as the Large-Eddy Simulation (LES) Wall-Adapted Local Eddy Viscosity (WALE) model for turbulent flows. Each of these is discussed in the following sections.

### 3.1.3 Reynolds-Averaged Navier-Stokes (RANS) k-$\omega$ Shear-Stress Transport (SST)

In Reynolds averaging, the flow field variables are decomposed into the mean and fluctuating components about the mean [**?**]. Mathematically, $u_i = \overline{u_i} + u_i'$. When substituted into the Navier-Stokes equations, this yields the Reynolds-averaged momentum equations, given in tensor notation for components $i, j, k$:

$$\frac{\partial}{\partial t}(\rho u_i) + \frac{\partial}{\partial x_j}(\rho u_i u_j) = +\frac{\partial}{\partial x_j}(-\rho\overline{u_i' u_j'}) - \frac{\partial p}{\partial x_i} + \frac{\partial}{\partial x_j}\left[\mu\left(\frac{\partial u_i}{\partial x_j} + \frac{\partial u_j}{\partial x_i} - \frac{2}{3}\delta_{ij}\frac{\partial u_k}{\partial x_k}\right)\right] \quad (3.23)$$

The Reynolds stress, $-\rho\overline{u_i' u_j'}$, must be modeled in order to close the system of equations. The method selected for the present work

The compressible formulation for the $k-\omega$ turbulence model includes the following equations transport equations for the turbulence kinetic energy, $k$, and the specific dissipation rate, $\omega$, was developed by Wilcox as [180]:

$$\frac{\partial}{\partial t}(\rho k) + \frac{\partial}{\partial x_i}(\rho u_i k) = \frac{\partial}{\partial x_j}\left(\Gamma_k \frac{\partial k}{\partial x_j}\right) + G_k - Y_k + S_k \tag{3.24}$$

$$\frac{\partial}{\partial t}(\rho \omega) + \frac{\partial}{\partial x_i}(\rho u_i \omega) = \frac{\partial}{\partial x_j}\left(\Gamma_\omega \frac{\partial \omega}{\partial x_j}\right) + G_\omega - Y_\omega + S_\omega \tag{3.25}$$

In each of the equations above, the left-hand sides represent the change in variables in time and direction $\hat{x_i}$. $G_k$ represents generation of turbulence kinetic energy, $k$, and $G_\omega$ represents increase of the specific dissipation rate, $\omega$. The $\Gamma_k$ and $\Gamma_\omega$ terms govern diffusivity of their respective variables, and $Y_k$ and $Y_\omega$ are dissipation of each due to turbulence. The production terms are modeled as:

$$G_k = -\rho\overline{u_i' u_j'}\frac{\partial u_j}{\partial x_i} \tag{3.26}$$

$$G_\omega = \frac{\alpha\omega}{k} G_k \tag{3.27}$$

where the Boussinesq Hypothesis, $G_k = \mu_t S^2$ is used, where $S$ is the modulus of the mean rate-of-strain tensor, defined as:

$$S = \sqrt{2 S_{ij} S_{ij}} \tag{3.28}$$

where

$$S_{ij} = \frac{1}{2}\left(\frac{\partial u_j}{\partial x_i} + \frac{\partial u_i}{\partial x_j}\right) \tag{3.29}$$

The effective diffusivities are given by

$$\Gamma_k = \mu + \frac{\mu_t}{\sigma_k}$$

$$\Gamma_\omega = \mu + \frac{\mu_t}{\sigma_\omega}$$

where $\sigma_k$ and $\sigma_\omega$ are the turbulent Prandtl numbers for $k$ and $\omega$. The turbulent viscosity is computed as

$$\mu_t = \alpha^* \frac{\rho k}{\omega}$$

where $\alpha^*$ provides a correction at low Reynolds number by dampening the turbulent viscosity and is defined as

$$\alpha^* = \alpha^*_\infty \left( \frac{\alpha^*_0 + Re_t/R_k}{1 + Re_t/R_k} \right)$$

The turbulent Reynolds number is $Re_t = \rho k/(\mu\omega)$, and the model parameters $R_k = 6$, $\alpha^*_0 = \beta_i/3$, and $\beta_i = 0.072$ have been found to work well for wall-bounded flow [173]. The production of $\omega$ is modeled as

$$G_\omega = \frac{\alpha\omega}{k} G_k \tag{3.30}$$

where the coefficient $\alpha$ is

$$\alpha = \frac{\alpha_\infty}{\alpha^*} \left( \frac{\alpha_0 + Re_t/R_\omega}{1 + Re_t/R_\omega} \right)$$

where $R_\omega = 2.95$. The dissipation of $k$ is modeled as

$$Y_k = \rho\beta^* f_{\beta^*} k\omega \tag{3.31}$$

where the constituent terms are defined as

$$f_{\beta^*} = \begin{cases} 1 & \chi_k \leq 0 \\ \frac{1+680\chi_k^2}{1+400\chi_k^2} & \chi > 0 \end{cases}$$

$$\chi_k = \frac{1}{\omega^3}\frac{\partial k}{\partial x_j}\frac{\partial \omega}{\partial x_j} \tag{3.32}$$

$$\beta^* = \beta_i^*[1 + \zeta^* F(M_t)] \tag{3.33}$$

$$\beta_i^* = \beta_\infty^*\left[\frac{4/15 + (Re_t/R_\beta)^4}{1 + (Re_t/R_\beta)^4}\right] \tag{3.34}$$

where $Re_t = \rho k/(\mu\omega)$, and $\zeta^* = 1.5$, $R_\beta = 8$, and $\beta_\infty^* = 0.09$ are recommended model parameters for high-speed flows where external friction is important across a wide range of Reynolds number [173]. The compressibility function is given by

$$F(M_t) = \begin{cases} 0 & M_t \leq M_{t0} \\ \\ M_t^2 - M_{t0}^2 & M_t > M_{t0} \end{cases}$$

where $M_t^2 = 2k/c^2$, $M_{t0} = 0.25$, and the speed of sound is $c = \sqrt{\gamma RT}$. The dissipation of $\omega$ is given by

$$Y_(\omega) = \rho\beta f_\beta \omega^2 \tag{3.35}$$

where

$$f_\beta = \frac{1 + 70\chi_k^2}{1 + 80\chi_k^2} \tag{3.36}$$

$$\chi_\omega = \left|\frac{\Omega_{ij}\Omega jk S_{ki}}{(\beta_\infty^*\omega)^3}\right| \tag{3.37}$$

$$\beta^* = \beta_i^*[1 + \zeta^* F(M_t)] \tag{3.38}$$

$$\Omega_{ij} = \frac{1}{2}\left(\frac{\partial u_i}{\partial x_j} + \frac{\partial u_j}{\partial x_i}\right) \tag{3.39}$$

$$\beta = \beta_i\left[1 - \frac{\beta_i^*}{\beta_i}\zeta^* F(M_t)\right] \tag{3.40}$$

The $k - \omega$ model was formulated for wall-bounded flows where boundary layers and shear stress are important. The shear stress predicted by the $k - \omega$ turbulence

model, however, is highly sensitive to the free-stream turbulence as a form of far-field boundary condition for the model behavior in the near-wall region. The Shear Stress Transport variation couples a free-stream formulation for $k-\epsilon$, where $\epsilon$ is the rate of dissipation of turbulence kinetic energy, $k$. The transport equations in the free stream are given by Launder and Spalding as [181]:

$$\frac{\partial}{\partial t}(\rho k) + \frac{\partial}{\partial x_i}(\rho u_i k) = \frac{\partial}{\partial x_j}\left(\alpha_k \mu_{eff} \frac{\partial k}{\partial x_j}\right) + G_k - \rho\epsilon - Y_M \tag{3.41}$$

$$\frac{\partial}{\partial t}(\rho \epsilon) + \frac{\partial}{\partial x_i}(\rho u_i \epsilon) = \frac{\partial}{\partial x_j}\left(\alpha_\epsilon \mu_{eff} \frac{\partial \epsilon}{\partial x_j}\right) + C_1 \frac{\epsilon}{k} G_k - C_2 \rho \frac{\epsilon}{k} - R_\epsilon \tag{3.42}$$

where $C_1 = 1.44$, $C_2 = 1.92$, and $C_\mu = .09$ are model constants, $\alpha_k$ and $\alpha_\epsilon$ are the inverse Prandtl numbers for $k$ and $\epsilon$, and $Y_M$ is the effect on the dissipation rate due to fluctuating compressibility effects, found as $Y_M = 2\rho\epsilon M_t^2$. The effective viscosity is given by

$$\mu_{eff} = \rho C_\mu \frac{k^2}{\epsilon} \tag{3.43}$$

The location of transition can be specified in reference to a leading edge or inlet when using the $k-\omega$ SST model within ANSYS Fluent by writing a User-Defined Function (UDF) and compiling or interpreting the function [175]. Laminar flow is solved with no turbulence model before this location, while elements beyond this location are allowed to develop turbulence. The method selected for the present work is a critical-length Reynolds number where the value is pre-assigned using the Hopkins Transition estimates [163] based on the free-stream unit Reynolds number, the leading edge bluntness, and the average leading-edge sweep angle.

### 3.1.4 Large-Eddy Simulation (LES) with Wall-Adapted Local-Eddy Viscosity (WALE)

The Large-Eddy Simulation (LES) turbulence model [173, 176, 182] has been demonstrated to preserve subgrid-scale turbulence in compressible flows with shock waves [183]. The fundamental basis for LES is the observation that mass, momentum, and energy are mostly transported by large eddies, which are largely geometry- and boundary-condition-dependent and should be explicitly solved for. Small eddies, by contrast, may be approximated as isotropic and homogeneous throughout a turbulent flow field, independent of geometry and boundary conditions. Therefore, small eddies may be modeled as a uniform turbulence based on the system Reynolds number with little loss of system information despite this simplification. For a Finite Volume formulation [173], a filtered variable is defined as

$$\overline{\phi(x,t)} = \int_{-\infty}^{\infty}\int_{-\infty}^{\infty} \phi(r,t)G(x-r,t-\tau)d\tau dr \tag{3.44}$$

The filter kernel $G$ has cutoff length scale $\Delta_c$ and time scale $\tau_c$, where smaller scales are dropped from explicit treatment. A field variable $\phi$ can be split into its filter-scale and sub-filter scale elements as

$$\phi = \overline{\phi} + \phi' \tag{3.45}$$

This filter is applied to Eqns. 3.11 - 3.22 to yield the filtered compressible Navier Stokes equations. A density-weighted filter is used for compressible flows, known as a Favre filter:

$$\tilde{\phi} = \frac{\overline{\rho\phi}}{\overline{\rho}} \tag{3.46}$$

The sub-filter scale stresses are not explicitly known and require modeling:

$$\tau_{ij} - \frac{1}{3}\tau_{kk}\delta_{ij} = -2\mu_t\overline{S_{ij}} \tag{3.47}$$

where $\overline{S_{ij}}$ is the rate-of-strain tensor at the filter scale, given by

$$\overline{S_{ij}} = \frac{1}{2}\left(\frac{\partial\overline{u_i}}{\partial x_j} + \frac{\partial\overline{u_j}}{\partial x_i}\right) \tag{3.48}$$

The subgrid stress tensor is given by

$$\tau_{ij} = \overline{\rho}u_i\tilde{u}_j - \overline{\rho}\tilde{u}_i\tilde{u}_j \tag{3.49}$$

which is split into its isotropic and deviatoric components

$$\tau_{ij} = \tau_{ij} - \frac{1}{3}\tau_{kk}\delta_{ij} + \frac{1}{3}\tau_{kk}\delta_{ij} \tag{3.50}$$

The deviatoric part is computed using Smagorinski's model:

$$\tau_{ij} - \frac{1}{3}\tau_{kk}\delta_{ij} = -2\mu_t\left(S_{ij} - \frac{1}{3}S_{kk}\delta_{ij}\right) \tag{3.51}$$

where $\tau_{kk} = \gamma M_{SGS}^2\overline{p}$, where $M_{SGS}$ is the subgrid Mach number. The subgrid-scale turbulent flux $q_j$ of a scalar field $\phi$ is modeled with an effective subgrid Prandtl number as

$$q_j = -\frac{\mu_t}{\sigma_t}\frac{\partial\phi}{\partial x} \tag{3.52}$$

The eddy viscosity used in the present work is the Wall-Adapted Local Eddy viscosity (WALE) model

$$\mu_t = \rho L_s \frac{\left(S_{ij}^d S_{ij}^d\right)^{3/2}}{\left(\overline{S_{ij}S_{ij}}\right)^{5/2}\left(S_{ij}^d S_{ij}^d\right)^{5/4}} \tag{3.53}$$

where $L_s$, the subgrid mixing length, and $S_{ij}^d$ are defined as

$$L_s = min\Big(\kappa d, C_w V^{2/3}\Big) \tag{3.54}$$

$$S_{ij}^d = \frac{1}{2}\Big(\overline{g_{ij}}^2 + \overline{g_{ji}}^2\Big) - \frac{1}{3}\delta_{ij}\overline{g_{kk}}^2 \tag{3.55}$$

where $\overline{g_{ij}} = \frac{\partial \overline{u_i}}{\partial x_j}$, $\kappa$ is the von Karman constant, 0.41, $d$ is the distance to the wall, and $V$ is the volume of the grid element. The model constant $C_w = 0.325$ is used to produce proper wall shear for compressible laminar and turbulent flow.

## 3.2 Numerical Model Test Cases

The methods described in the preceding sections are tested in the following two cases: 1) the friction coefficient for a flat plate at Mach 6 and zero angle of attack, and 2) the reactive flow past a cylinder at Mach 20.

### 3.2.1 Flat Plate in Supersonic Flow

Consider the simulation of a 1m-long adiabatic flat plate at zero angle of attack in Mach 6 flow with a unit Reynolds number of $10^7 \mathrm{m}^{-1}$, for which the computational mesh is illustrated in Fig. 3.4. The aspect ratio for plate surface elements is fixed at 20:1 according to the ANSYS best practices for resolving turbulent flow outlined in [175] and recommended by Pope [177]. The grid is adaptively refined uniformly with CFL fixed at 1 until the $y^+$ value reaches unity. According to the flat plate turbulent transition model of Reference [163], the critical Reynolds number is estimated at $Re_{cr} = 2 \times 10^6$, corresponding to a transition location of 20% down the length of the plate. The $k-\omega$ transition is assigned to this location. The friction coefficient

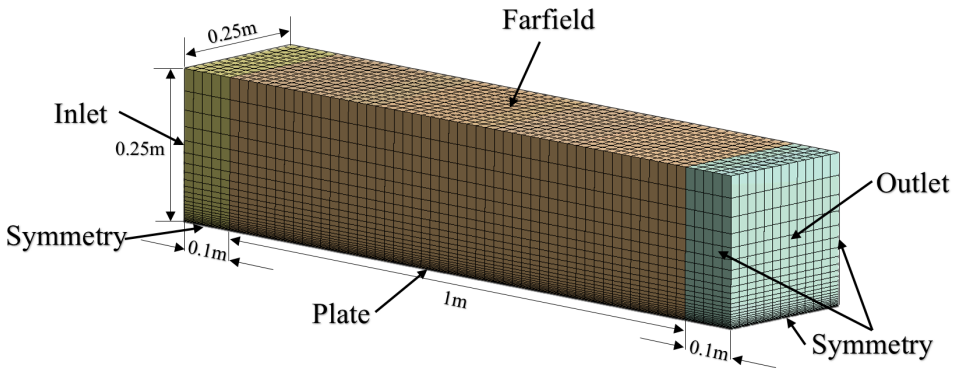


Figure 3.4: Computational domain and initial mesh of 19,500 elements for friction coefficient evaluation with various turbulence models.

from Eckert [160] with this critical Reynolds number is compared to the $k-\omega$ SST turbulence model with fully laminar, assigned transition, and fully turbulent flow in Fig. 3.5. The models are solved in a domain of 1.2m×0.25m×0.25m, where a 0.1m lead-in and lead-out surround an infinitesimally thin plate at zero angle of attack.

The convergence of the assigned-transition model with fixed-element aspect ratio and CFL as described, and at this specific unit Reynolds number, is depicted in Fig. 3.6. The convergence of the viscous drag force on the plate at the selected unit Reynolds number corresponds to the intended Mach 6 waverider at its flight condition of Mach 6 and 30km for a predicted required resolution of 3-5mm lateral dimension and 0.2-0.3mm first layer height for a viscous force convergence on the order of 1%.

### 3.2.2 Reactive Flow around a Cylinder at Mach 20

Consider the simulation of a 10cm-radius cylinder immersed in a Mach 20 air stream at 75km altitude, corresponding to a likely flight condition for a lifting entry

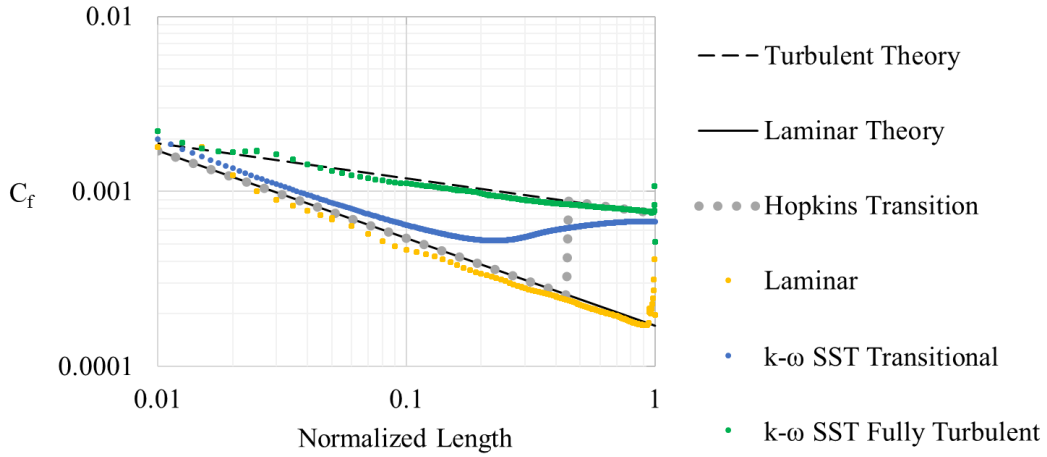


Figure 3.5: Comparison of the friction coefficient obtained for laminar flow, fully turbulent $k-\omega$ SST, Transitional $k-\omega$ SST, and LES-WALE turbulence models. The theoretical laminar and turbulent curves are illustrated along with the transition location predicted using the Hopkins method.

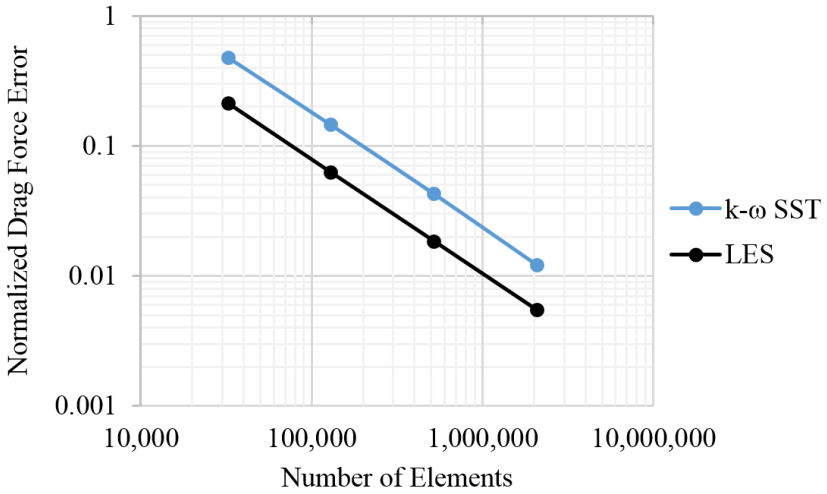


Figure 3.6: Viscous drag force convergence.

vehicle in Earth's atmosphere. The unit Reynolds number at this altitude is 1.5 $\times 10^4$ m$^{-1}$. Provided that transitional Reynolds numbers using the Hopkins Method [163] for high-speed flow begin typically above $10^6$ and increase with leading-edge bluntness, this suggests strongly laminar flow around this cylinder. The ambient temperature and pressure are 183.7K and 1.85Pa, respectively. For the 7-species model for air, the free-stream composition is 22% $O_2$ and 78% $N_2$ by mass. Under these conditions, the local speed of sound is 303m/s and Mach 20 corresponds to 6,063m/s. The initial computational grid is illustrated in Fig. 3.7, with 10,000 elements and boundaries assigned clock-wise from the bottom as symmetry, far-field, outlet, and the cylinder wall. The wall temperature is assigned isothermal at 2,500K.

The 7-species air model is solved as laminar flow with a time-step limited by the smaller of CFL = 0.5 or a change in any species mole fraction per cell by greater than 10% of its current value per time step. The grid is initially 10,000 elements and is adaptively refined in gradients and curvature of Mach number and species concentration until the maximum steady normalized mole fraction of $NO^+$ is less than 1% with further refinement. This convergence criteria is achieved for a final grid of 168,346 elements and a computing time of $1.1 \times 10^3$ CPU-hrs, resulting in a maximum mole fraction of $NO^+ = 1.50 \times 10^{-7}$ and maximum temperature of 10,546K. The adapted grid, temperature, pressure, density, and species mole fractions are depicted in Fig. 3.9. The species mole fraction computed along the stagnation line are illustrated in Fig. 3.10. Using the Normal Shock Relations [157] and the thermally perfect $\gamma = 1.286$ for high temperature, Eqn. 2.51, the predicted

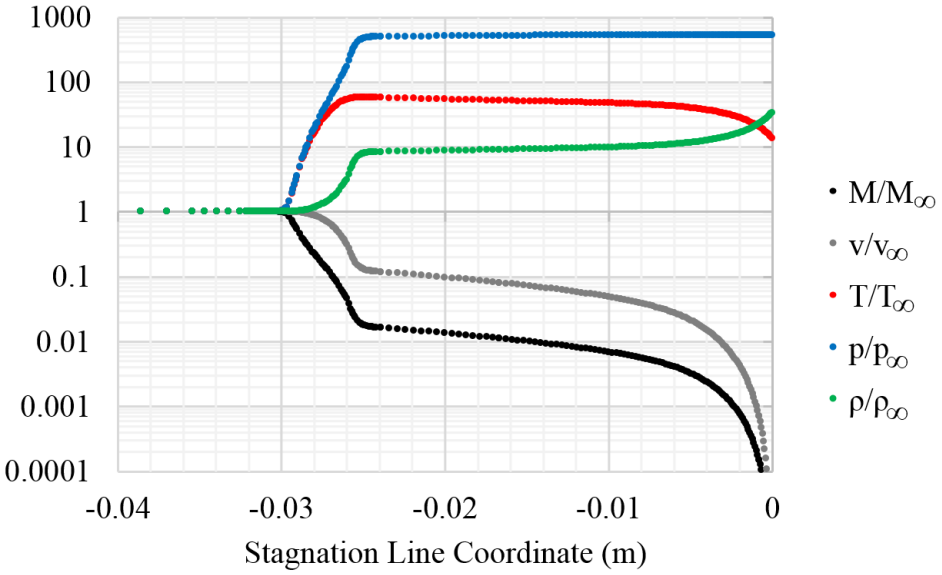


Figure 3.7: Flow variables along the stagnation line at each grid point for final adapted solution. The coordinate points away from the leading edge in the upstream direction.

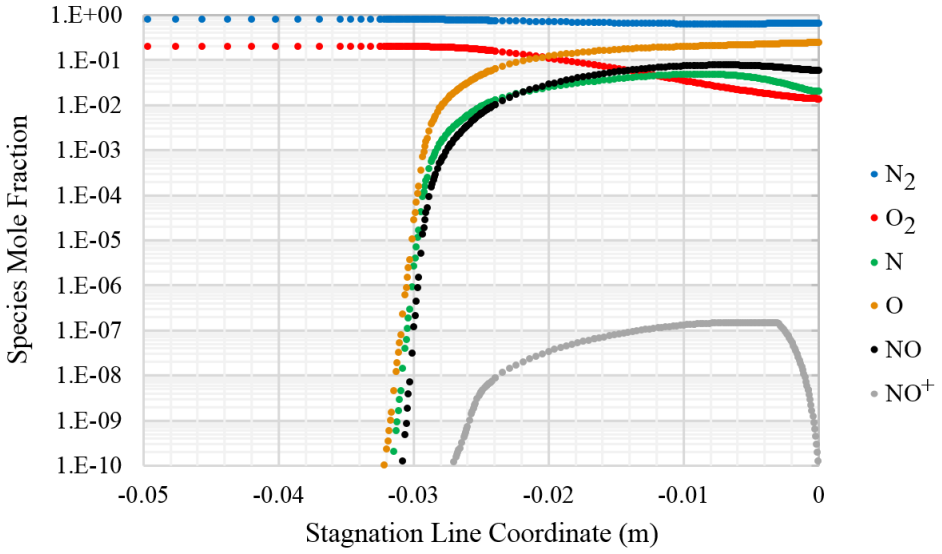


Figure 3.8: Species mole fraction along the stagnation line at each grid point for final adapted solution. The coordinate points away from the leading edge in the upstream direction.

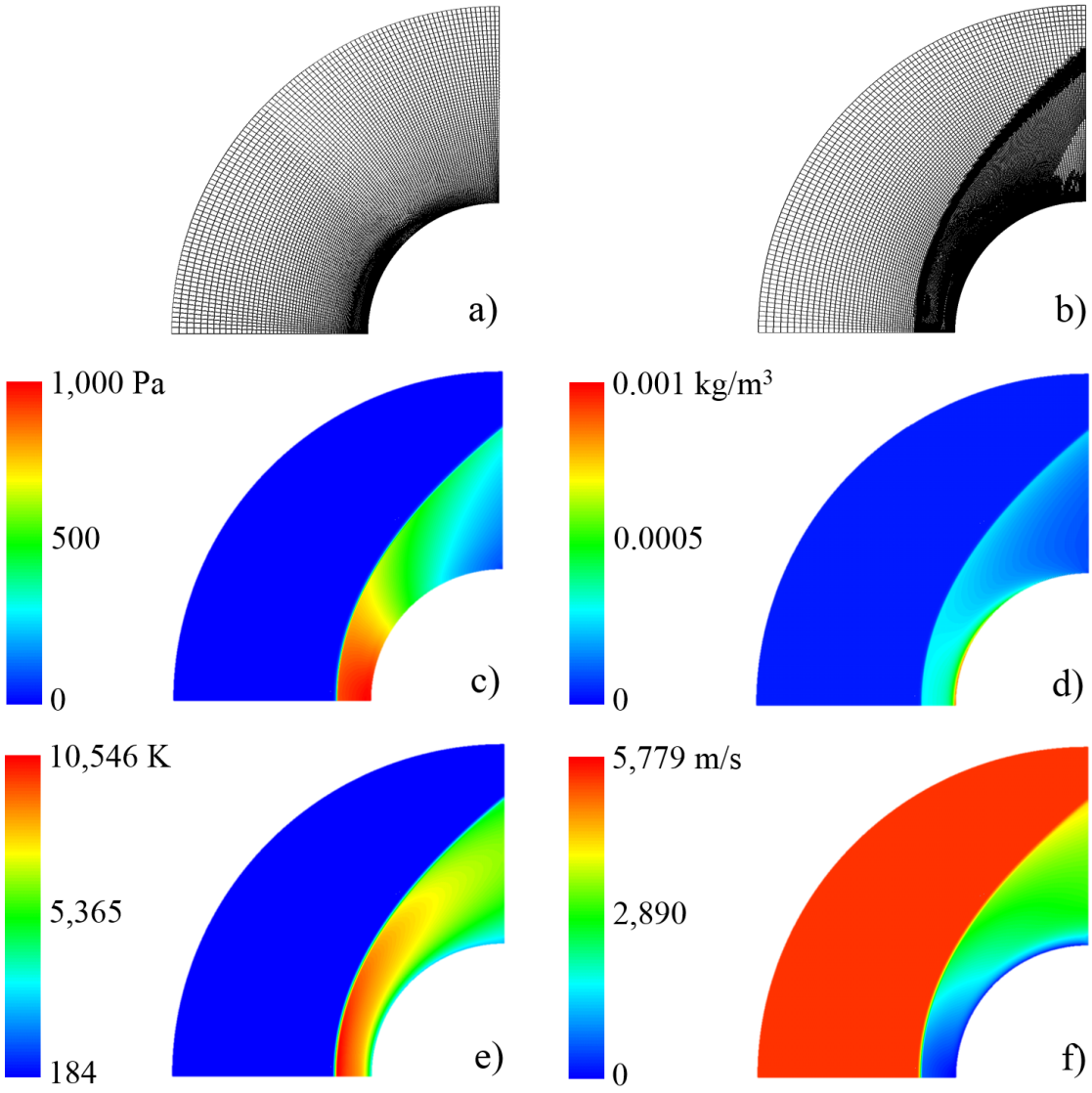


Figure 3.9: Numerical solution contours for 10cm-radius cylinder in Mach 20 flow at 75km depicting a) original mesh, b) adapted mesh, c) pressure, d) temperature, e) density, and f) velocity.

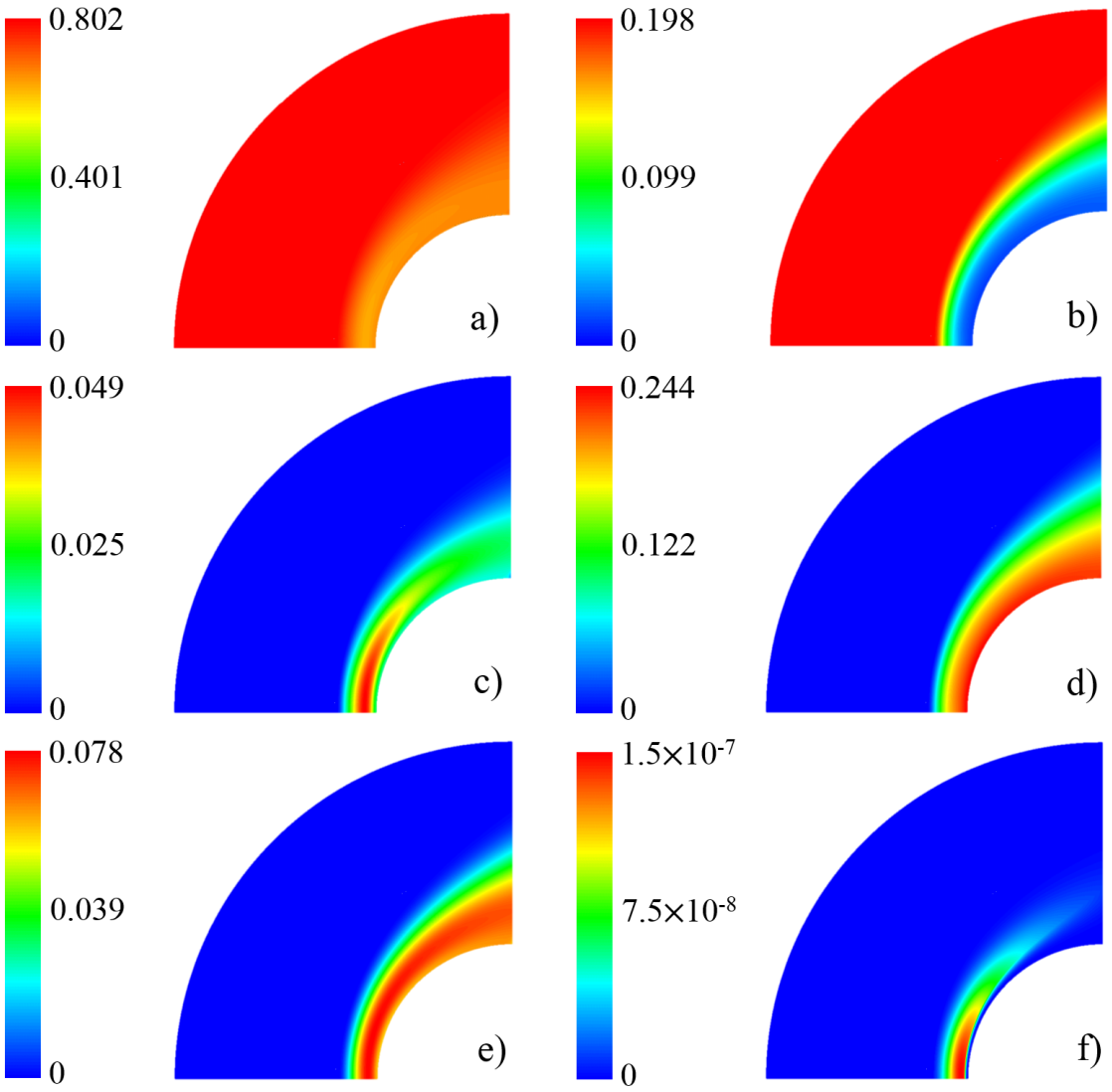


Figure 3.10: Numerical solution contours for 10cm-radius cylinder in Mach 20 flow at 75km depicting mole fractions for a) $N_2$, b) $O_2$, c) $N$, d) $O$, e) $NO$, and f) $NO^+$.

post-shock flow variable ratios to their free-stream values are listed in Table 3.2.

The shock occurs between approximately 25-30mm standoff from the geometrical stagnation point, with a finite thickness of approximately 5mm on the stagnation line. The flow variables reach a steady state post-shock value at approximately 25mm standoff, with relatively stationary values until the thermal boundary layer is approached ahead of the leading edge. This provides locally consistent conditions for chemical reactions to occur and begin to taper off to a steady equilibrium value, which is partly seen in Fig. 3.8 until the thermal boundary layer within approximately 10mm standoff is encountered, pulling down the local temperature to the prescribed wall condition and interrupting the march toward post-shock chemical equilibrium.

The reaction products of air persist downstream of the hot region that led to the reactions, despite lower local temperature. This is particularly important in consideration of relatively-sharp-edged hypersonic vehicles such as waveriders: the non-equilibrium chemistry in a small, hot region such as a leading edge is unlikely to have a significant impact on the aerodynamics of a vehicle when compared to thermally perfect air; however, the reaction products that propagate downstream into cooler regions have low molecular mass compared to standard air and will have a finite recombination time and distance. As these light molecules propagate along the vehicle planform, they may produce a non-negligible impact on the net vehicle forces and moments. There may be important implications for surface chemistry that are not apparent when using the thermally perfect gas model.

For $\gamma = 1.4$, the stagnation temperature is predicted to be 14,876K, whereas

the stagnation temperature predicted for thermally perfect air with $\gamma(T) = 1.286$ is 10,689K. In comparison to the 7-species non-equilibrium air numerical solution with $T_0$ =10,495K, the thermally perfect gas model provides a reasonably accurate estimate for the stagnation temperature, which is further used in estimating adiabatic wall temperatures and heat fluxes in reduced-order models.

| Reaction | $C_f$ | $\eta_f$ | $K_f$ |
|---|---|---|---|
| $O_2 + N \rightarrow 2O + N$ | 3.60E18 | -1.00 | 1.188E5 |
| $O_2 + NO \rightarrow 2O + NO$ | 3.60E18 | -1.00 | 1.188E5 |
| $N_2 + O \rightarrow 2N + O$ | 1.90E17 | -0.50 | 2.260E5 |
| $N_2 + NO \rightarrow 2N + NO$ | 1.90E17 | -0.50 | 2.260E5 |
| $N_2 + O_2 \rightarrow 2N + O_2$ | 1.90E17 | -0.50 | 2.260E5 |
| $NO + O_2 \rightarrow N + O + O_2$ | 3.90E20 | -1.50 | 1.510E5 |
| $NO + N_2 \rightarrow N + O + O_2$ | 3.90E20 | -1.50 | 1.510E5 |
| $O + NO \rightarrow N + O_2$ | 3.20E09 | 1.00 | 3.940E4 |
| $O + N_2 \rightarrow N + NO$ | 7.00E13 | 0.00 | 7.600E4 |
| $N + N_2 \rightarrow 2N + N$ | 4.09E22 | -1.50 | 2.260E5 |
| $O_2 + O \rightarrow 2O + O$ | 9.00E19 | -1.00 | 1.190E5 |
| $O_2 + O_2 \rightarrow 2O + O_2$ | 3.24E19 | -1.00 | 1.190E5 |
| $O_2 + N_2 \rightarrow 2O + N_2$ | 7.20E18 | -1.00 | 1.190E5 |
| $N_2 + N_2 \rightarrow 2N + N_2$ | 4.70E17 | -0.50 | 2.260E5 |
| $NO + O \rightarrow N + 2O$ | 7.80E20 | -1.50 | 1.510E5 |
| $NO + N \rightarrow O + 2N$ | 7.80E20 | -1.50 | 1.510E5 |
| $NO + NO \rightarrow N + O + NO$ | 7.80E20 | -1.50 | 1.510E5 |
| $O + N \rightarrow NO^+ + e^-$ | 1.40E06 | 1.50 | 6.380E4 |
| $O_2 + N_2 \rightarrow NO^+ + e^-$ | 1.38E20 | -1.84 | 2.820E5 |
| $NO + N_2 \rightarrow NO^+ + e^- + N_2$ | 2.20E15 | -0.35 | 2.160E5 |

Table 3.1: Reaction parameters for the Dunn-Kang model for 7-species reacting air.

| Method | $M_2$ | $T_2/T_\infty$ | $p_2/p_\infty$ | $\rho_2/\rho_\infty$ |
|---|---|---|---|---|
| Thermally Perfect Gas | .336 | 57.3 | 450 | 7.86 |
| Post-Shock Numerical Solution | .366 | 57.7 | 462 | 7.80 |

Table 3.2: Comparison between thermally perfect gas and numerical solution flow variable ratios behind the normal shock on the stagnation line.

# Chapter 4: Numerical Analysis of Waveriders

## 4.1 Case-Study Vehicles

The flow fields about two case study vehicles are used for numerical analysis in the present work: a waverider designed at Mach 6 and a waverider designed at Mach 8. These will be referred to as the "Mach 6 waverider" and the "Mach 8 waverider," respectively, referring to the Mach number at which they were designed. Each waverider is designed with an identical base-plane generating curve and conical shock. Each waverider is used on-design for comparison with analytical predictions using thermally perfect air. The Mach 6 and Mach 8 waveriders are used to compute the aerodynamic coefficients for a rigid waverider with varied Mach number. The Mach 6 waverider is used to evaluate variation in angle of attack, yaw angle, and both combined. The Mach 6 waverider is also used to survey the effect of Reynolds number variation. The Mach 8 waverider is used to evaluate the effect of leading edge radius and compare the SEF and PVO methods for blunting the leading edge.

Finally, the Mach 8 waverider is simulated in a fully reactive flow field with 7-species air at 75km and Mach 20 and at 60km and Mach 15. This environment corresponds to an expected mid-flight-path condition for a lifting entry vehicle as illustrated in Fig.1.5. Each of the case study vehicles is depicted in Figs. 4.1 -

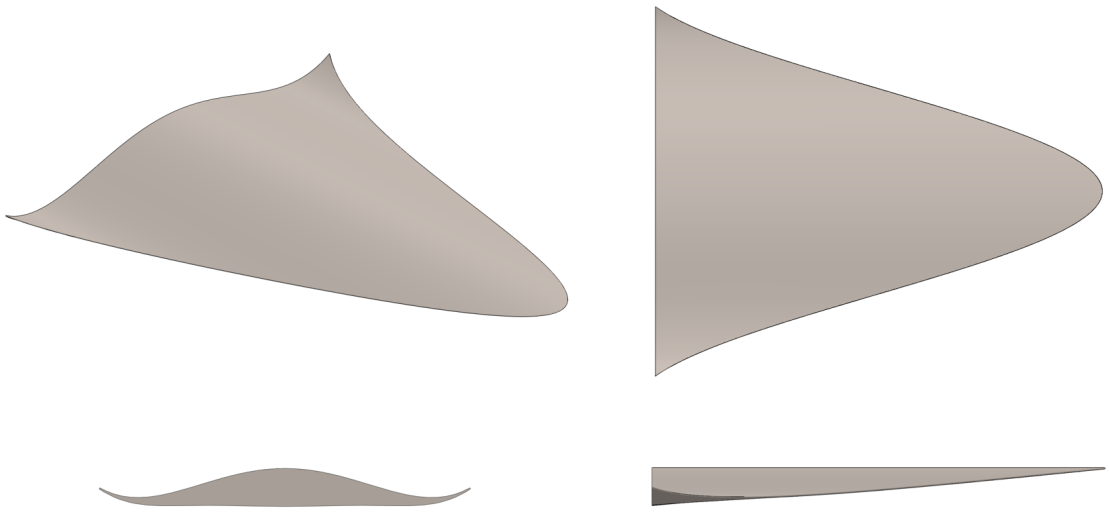

Figure 4.1: Mach 6 waverider with 3m wingspan and 3mm leading edge radius.

4.2. The Mach 6 and 8 waveriders use the same leading edge as the "optimum of the optimums" configuration produced by the optimization of viscous waveriders by Bowcutt and Anderson [72].

## 4.2 Results

Numerical simulations were used to investigate the near-body flow field for waveriders designed at Mach 6 and Mach 8 first on-design and then with varied angle of attack, varied Mach number, and varied orientation. The on-design conditions yielded the expected design flow fields beneath the waveriders. The Mach 6 waverider was computed on-design with both $k-\omega$-SST and LES-WALE turbulence models. The Mach 8 waverider leading edge was blunted with various radii to investigate the associated penalties in performance. The Mach number was varied for each waverider between Mach 1 and 12 and showed decreasing lift and drag co-

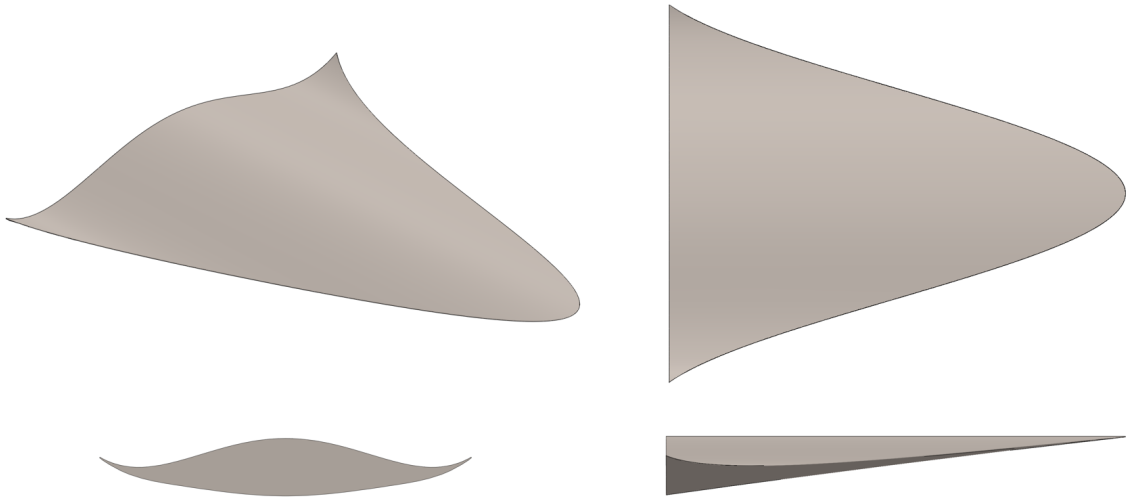

Figure 4.2: Mach 8 waverider with 3m wingspan and 3mm leading edge radius.

efficients for increasing Mach number. Each vehicle produced its highest lift-to-drag ratio at its design Mach number. The base pressure was found to be proportional to the proposed base pressure model from Section 2.6.6. The angle of attack was varied for the Mach 6 waverider, which matched the qualitative aerodynamic coefficients of a flat plate. The waverider reached a maximum lift-to-drag ratio at a small, positive angle of attack. The Mach 6 waverider was found to be pitch-stable with angle of attack, but unstable in the yaw and roll axes when a nonzero yaw angle was introduced.

A reactive flow field for the Mach 6 waverider was computed for a laminar, continuum flight condition of Mach 20 and 75km. The low Reynolds number resulted in thick boundary layers and a smooth, laminar flow field. The small leading-edge radius with a 2,500K prescribed wall temperature resulted in a small bow-shock standoff from the nosetip and nonequilibrium chemistry in the stagnation region. The post-shock flow produced low mole fractions of reactive species due to the

small spatial scale interrupting the progression toward chemical equilibrium and a prescribed wall temperature much lower than the adiabatic temperature.

### 4.2.1 On-Design Flight Condition

Numerical solutions are computed using using the $k-\omega$ SST and the LES-WALE turbulence models for the Mach 6 and Mach 8 waveriders at their design Mach number and zero angle of attack, referred to as their respective "design point" where a vehicle operates "on design." The flow fields for these vehicles are shown and discussed below.

First, consider the Mach 6 vehicle. The design shock and flow field beneath the vehicle are shown in Fig. 4.3. The shock location correlates well to the design conical-shock flow field despite the presence of a viscous boundary layer and a blunted leading edge. There is a small bow shock ahead of the leading edge, but aft of the leading edge the flow matches the design flow-field conditions beneath the vehicle. The flow passes through a shock near the leading edge on top of the vehicle, but expands back to near free-stream conditions above the vehicle. A close-up view of the leading-edge bow shock is provided in Fig. 4.5. There is a subsonic region near the stagnation point, and the boundary layer begins to grow around the nosetip and along the upper and lower surfaces. Figure 4.6 illustrates that the nosetip and boundary layer reach over 1600K while the temperature in the post-shock flow field rises to less than 300K from a free-stream temperature of 232K.

The location of transition to turbulence is important for the chosen flight

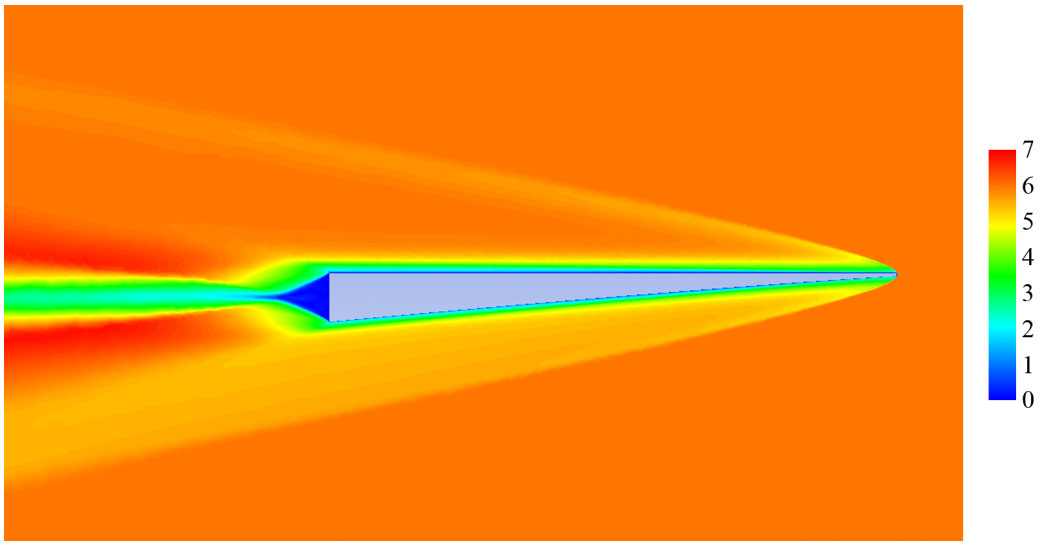


Figure 4.3: Mach number contour on symmetry plane for Mach 6 waverider on-design using $k-\omega$ SST turbulence and variable-$\gamma$ air model.

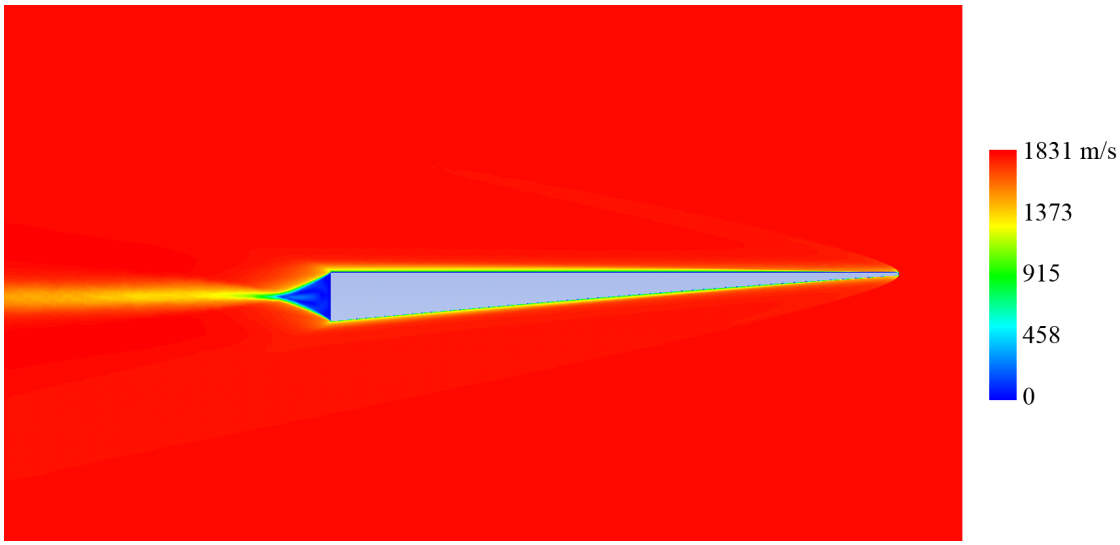


Figure 4.4: Velocity contour on symmetry plane for Mach 6 waverider on-design using $k-\omega$ SST turbulence and variable-$\gamma$ air model.

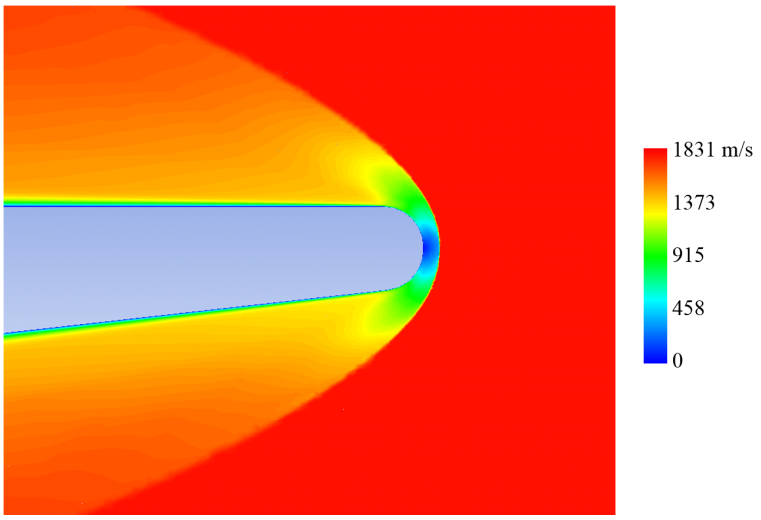


Figure 4.5: Velocity contour close-up of leading edge on symmetry plane.

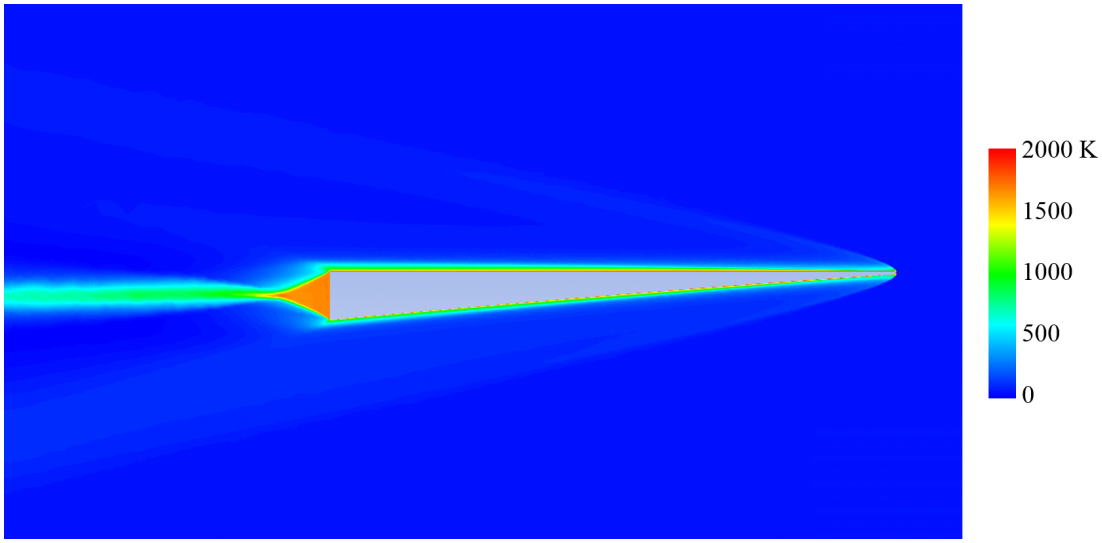


Figure 4.6: Temperature contour on symmetry plane for Mach 6 waverider on-design using $k-\omega$ SST turbulence and variable-$\gamma$ air model.

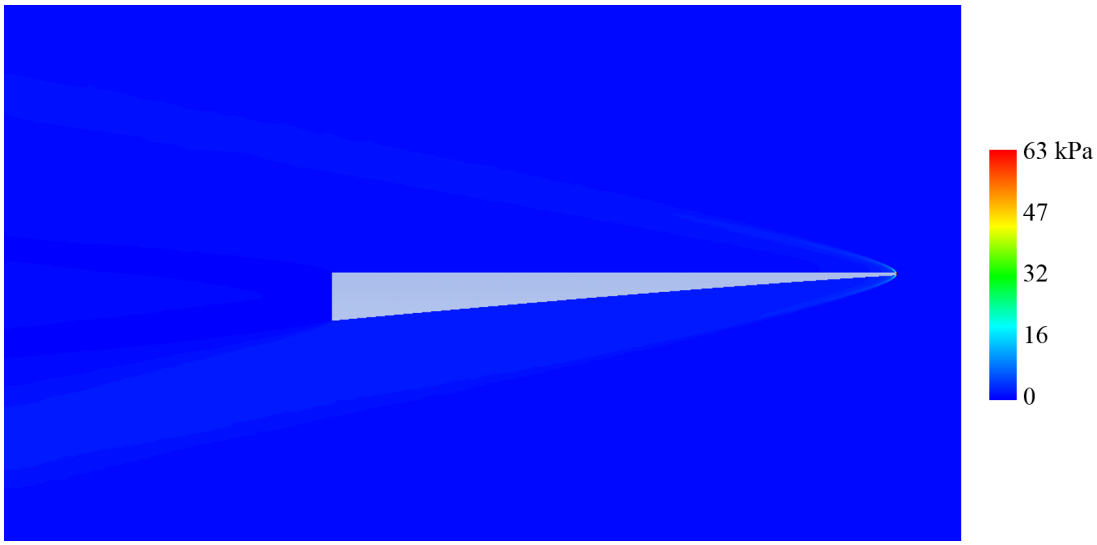


Figure 4.7: Pressure contour on symmetry plane for Mach 6 waverider on-design using $k-\omega$ SST turbulence and variable-$\gamma$ air model.

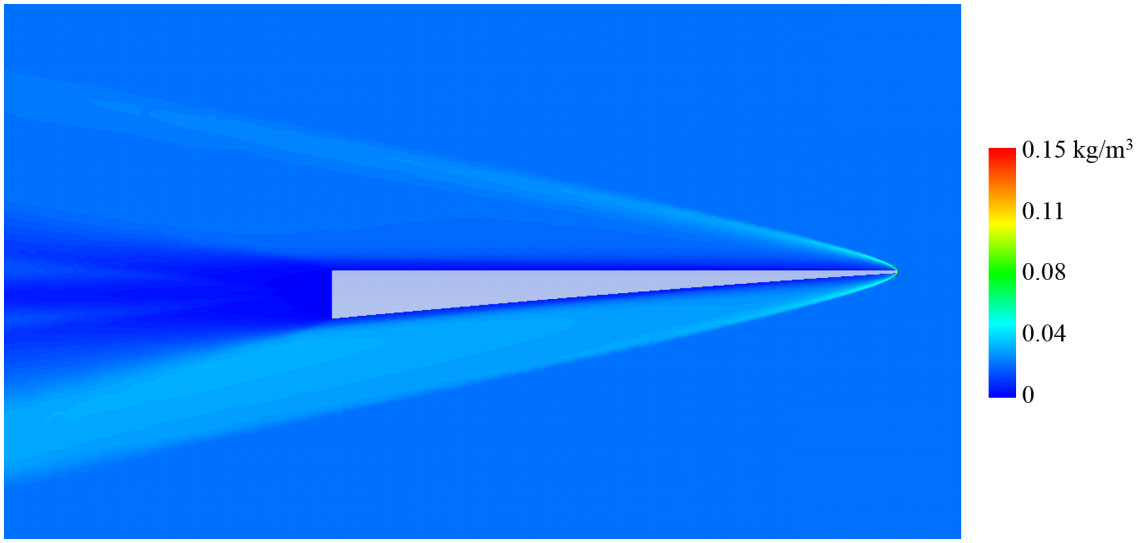


Figure 4.8: Density contour on symmetry plane for Mach 6 waverider on-design using $k-\omega$ SST turbulence and variable-$\gamma$ air model.

regime. Waveriders are streamlined vehicles with little pressure-induced drag and a large planform of wetted area subject to viscous drag. The friction coefficient depends upon the fraction of the flow along the surface of the vehicle that is laminar versus turbulent. As demonstrated in Section 3.2.1, the variability in the location of transition to turbulence can greatly affect the viscous drag on a flat plate in transitional flow. For example, a fully laminar flat plate has 80% less viscous drag than a fully turbulent flat plate. The friction coefficient also determines heating. The turbulent flow on the top surface computed using the LES-WALE turbulence model is shown in Fig. 4.9 by the striations in surface pressure, indicating instabilities that may precede the transition to turbulence. The friction coefficient is shown for the $k-\omega$ SST turbulence model in 4.10, where the transition to turbulence is indicated by the jump in friction coefficient aft of the leading edge. The location of transition to turbulence in Fig. 4.10 is assigned according to the Hopkins critical Reynolds number method described in Chapter 2.

The computed base pressure with varied Mach number is shown in Fig. 4.11 along with the proposed base-pressure model, $p_b = p_\infty/M$. For the two case study vehicles considered, the trend observed agrees with increasing Mach number but includes an approximately constant offset factor. For the Mach 6 vehicle, this factor is 0.76-0.78 across the range of Mach 1-12. For the Mach 8 vehicle, this factor is 0.62-0.64 across the range of Mach 1-12. While this factor is different for each vehicle, it appears relatively consistent across the range of speeds considered. It is expected that a streamlined vehicle would have less of a pressure drop in its wake than a blunt vehicle. The pressure drop computed is lesser for the more-streamlined

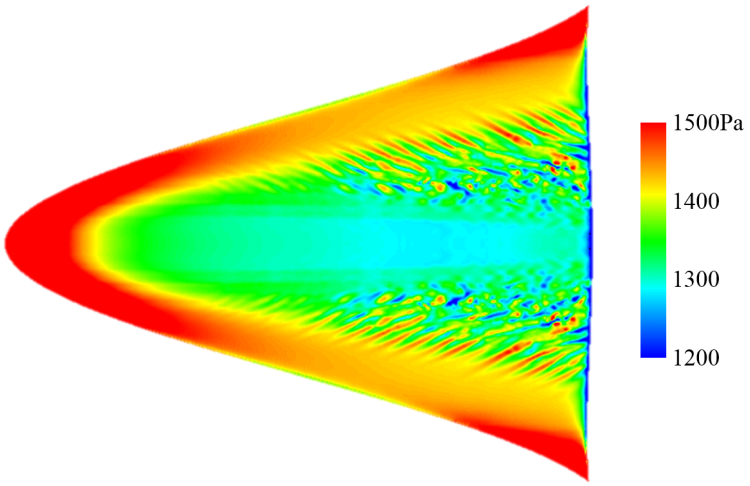


Figure 4.9: Pressure contour on the top surface of the on-design Mach 6 waverider computed using the LES-WALE turbulence model and the variable-$\gamma$ air model. The flow immediately aft of the leading edge is laminar. Instabilities in the flow appear further downstream as pressure striations along the surface of the vehicle.

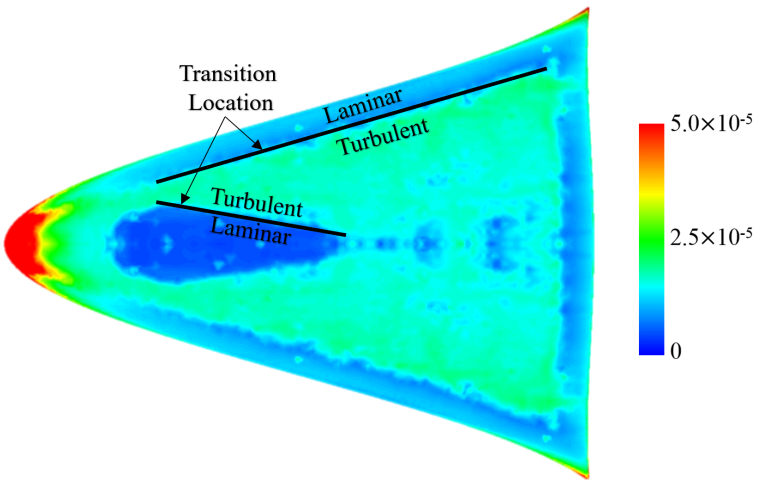


Figure 4.10: Friction coefficient contour on the top surface of the on-design Mach 6 waverider computed using the $k-\omega$ SST turbulence model and the variable-$\gamma$ air model. The location of transition to turbulence is indicated by the solid black line based on a prescribed critical Reynolds number. The friction coefficient decreases as flow moves downstream in the laminar region aft of the leading edge. The transition to turbulence on the planform of the waverider is indicated by the jump in friction coefficient, marked with a solid black line.

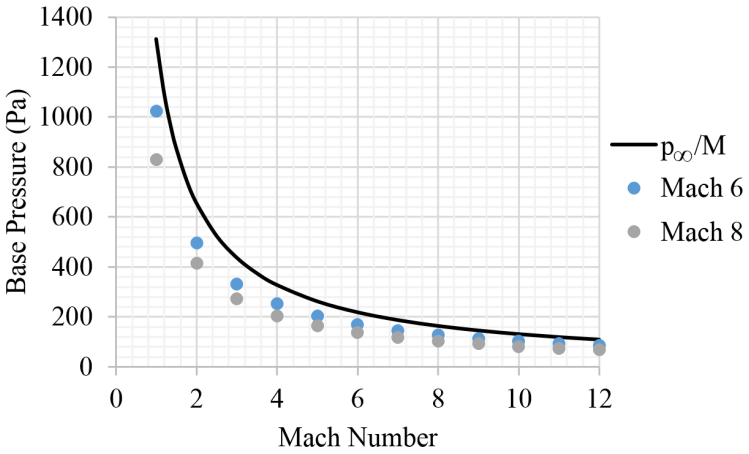


Figure 4.11: Base pressure results for Mach 6 and Mach 8 waveriders with varied Mach number and variable-$\gamma$ air model.

Mach 6 vehicle and larger for the Mach 8 vehicle, which has a larger cross-sectional area.

### 4.2.2 Off-Design Flight Condition

#### 4.2.2.1 Varied Leading-Edge Radius

Various leading-edge radii are depicted in Fig. 4.12 using the Sharp-Edge Fillet (SEF) and Planform Vertical Offset (PVO) methods described in Section 2.5.2. The leading-edge radii range from sharp 90mm. The sharp-edged vehicle is given a 3m wingspan. The volume of the blunted vehicles is fixed across all cases by scaling the geometry in order to match the reference volume for each leading-edge radius considered. The resulting aerodynamic forces computed using the $k-\omega$ SST turbulence model at a flight condition of Mach 8 and 30km altitude are shown in Fig. 4.13.

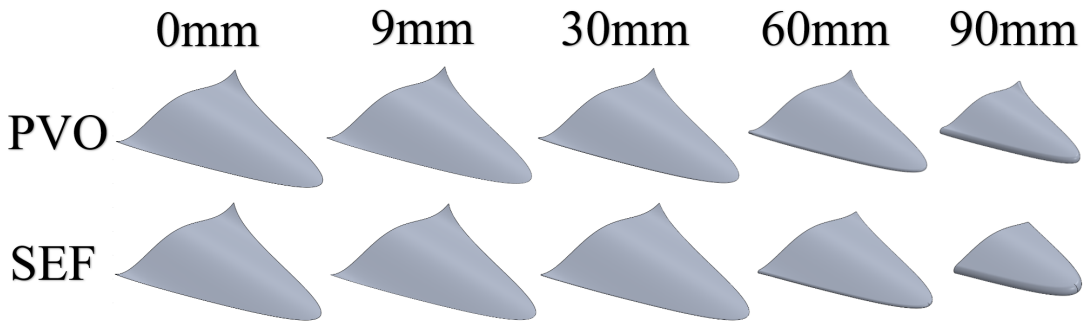


Figure 4.12: Mach 8 waverider with varied leading-edge radius (LER) using the Planform Vertical Offset (PVO) method and Sharp Edge Fillet method to blunt the leading edge. The vehicles are scaled in each case in order to maintain constant volume across all cases. The sharp-edged vehicle has a 3m wingspan.

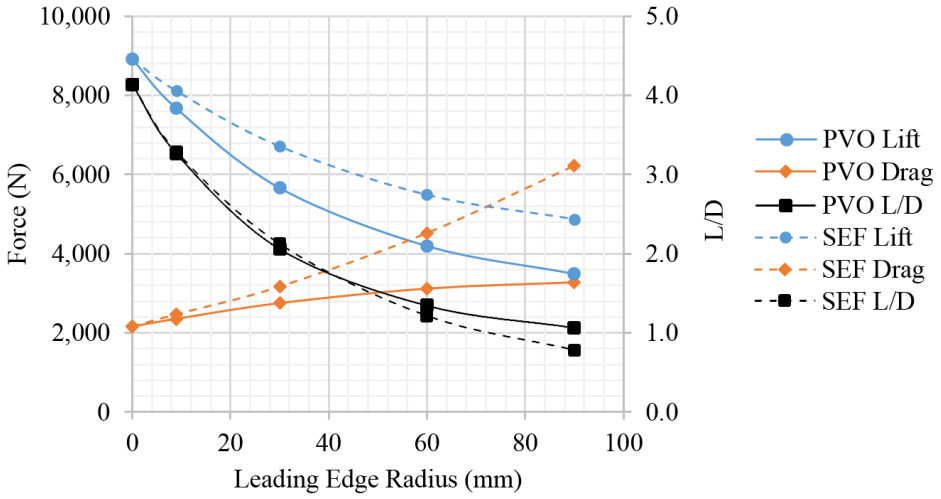


Figure 4.13: Comparison of forces with various leading-edge radii using the SEF and PVO methods. All cases use zero angle-of-attack and a flight condition of Mach 8 at 30km altitude.

The discussion begins with a comparison between methods and conclude with observations of the effect of increased blunting of the leading edge. For small leading-edge radii, the two methods produce similar geometry. For large leading-edge radii, the SEF lift and drag are larger than the PVO lift and drag. For the relatively large 90mm radius, the PVO method produces a 36% higher L/D ratio than the SEF method. The SEF method produces 39% higher lift, but at the expense of 90% higher drag. A higher lift coefficient can be achieved by increasing angle of attack. For small radii, however, the two methods are similar.

In comparison to this case study vehicle with a sharp leading edge, the glide ratio reduces by approximately 50% with just 30mm or 0.1% leading edge bluntness. The glide ratio reduces by approximately 75% with 90mm or 0.3% leading edge bluntness. The case study sharp-edged vehicle is fairly streamlined. Small increases in bluntness have a large effect on its glide ratio. By contrast, the reduction in glide ratio would not be as significant for a less-streamlined vehicle because the added leading-edge drag would be less significant.

#### 4.2.2.2 Effects of Varying the Mach Number

The variation of the aerodynamic coefficients with Mach number for the waverider designed at Mach 6 is depicted in Fig. 4.14. The cases were computed using the $k-\omega$ SST turbulence model and the variable-$\gamma$ air model at 30km altitude. The lift, drag, and moment coefficients decrease with Mach number and fall approximately as 1/M for hypersonic Mach numbers. The L/D ratio appears to reach

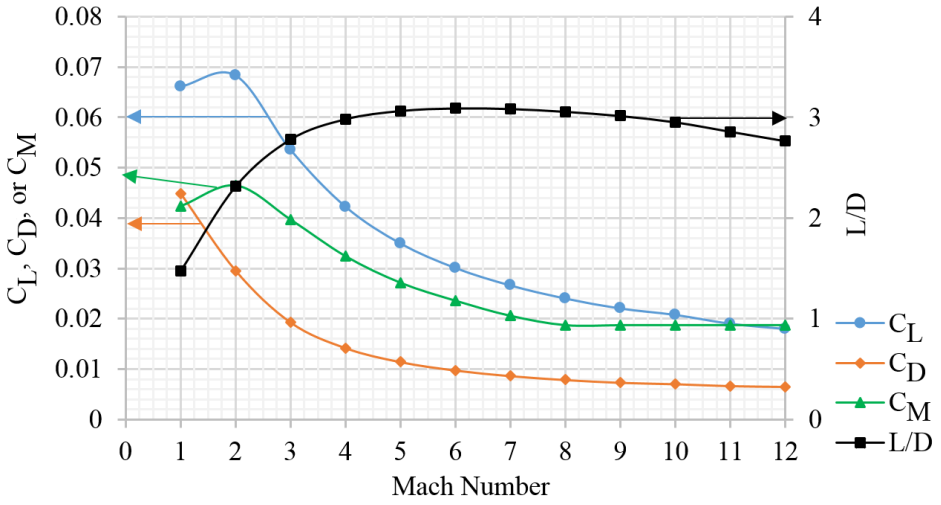


Figure 4.14: Variation of the aerodynamic coefficients with Mach number for the waverider designed at Mach 6. Aerodynamic coefficients are computed from the flow field that was solved using the $k-\omega$ SST turbulence model and the variable-$\gamma$ air model.

a maximum for the design Mach number of 6 and is reduced for large deviations from the design Mach number. For variations of two Mach numbers away from the design point, however, this particular waverider retains approximately 93% of the same L/D. The peak L/D for this case-study vehicle occurs at the design Mach number of 6.

The variation of the aerodynamic coefficients with Mach number for the waverider designed at Mach 8 is presented in Fig. 4.15. The cases were computed using the $k-\omega$ SST turbulence model and the variable-$\gamma$ air model at 30km altitude. The trends in aerodynamic coefficients with Mach number are similar to the results for the waverider designed at Mach 6. The lift, drag, and moment coefficients decrease with increasing Mach number. The L/D ratio reaches a maximum for the design

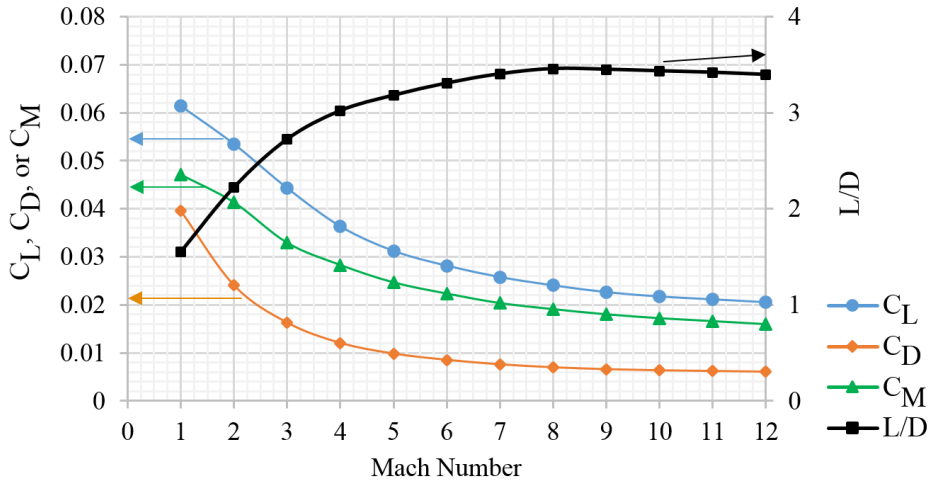


Figure 4.15: Variation of the aerodynamic coefficients with Mach number for the waverider designed at Mach 8. Aerodynamic coefficients are computed from the flow field that was solved using the $k-\omega$ SST turbulence model and the variable-$\gamma$ air model.

Mach number of 8 and is reduced for large deviations from the design Mach number. The aerodynamic coefficients begin to asymptote for large Mach number, consistent with hypersonic flow theory described in Section 2.6.

#### 4.2.2.3 Effects of Varying the Vehicle Orientation

The effect of varying the orientation of the on-design vehicle was evaluated by computing the flow field about a vehicle with varied pitch angle and yaw angle. A fixed flight condition of Mach 6 and 30km was used in all cases. The computational results for off-design orientation of the Mach 6 waverider suggest a pitch-stable vehicle. The vehicle experiences minor adverse pitch created with yaw, and destabilizing yaw- and roll-moments produced during yaw. Practical flight of a vehicle such as

this would require active stabilizing control for both the yaw and pitch axes.

The computed Mach number contours are illustrated in Fig. 4.16 for five selected angles-of-attack. The variation in aerodynamic coefficients is presented in Fig. 4.17. The force coefficients with varied yaw angle are presented in Fig. 4.18, and the yaw-induced moment coefficients are presented in Fig. 4.19.

The lift and drag coefficients increase similarly to those of a flat plate with angle of attack [4]. The maximum lift-to-drag ratio occurs for approximately $+3.5°$. The lift and drag coefficients can be modulated across a wide range by controlling angle of attack. The lift coefficient at $+50°$ reaches nearly 30 times the on-design value at zero angle of attack. The waverider produces zero lift at approximately $-2°$. Examining Fig. 4.18, the drag coefficient is minimally impacted for this low-cross-section vehicle with changes in yaw angle. The lift coefficient is only reduced for yaw deviations greater than approximately $\pm 5°$ and remains insensitive for small deviations about zero. The lateral force linearly increases as yaw angle is increased across the $\pm 10°$ range in yaw angle considered.

The moment coefficient may be trimmed by placing the center of mass at a location with zero net moment. In order to balance the lift and weight forces at zero angle of attack, the center of mass would be placed 2.62m rear of the leading edge for a 3.63m-long vehicle. At its peak lift-to-drag ratio condition of $+3.5°$, however, the center of mass would have to lie at 4.32m behind the nosetip, or 0.69m behind the vehicle's base. The implication is that this particular vehicle and flight condition is not pitch-stable at its peak lift-to-drag ratio without auxiliary control to counteract the excess aerodynamic pitch-over moment.

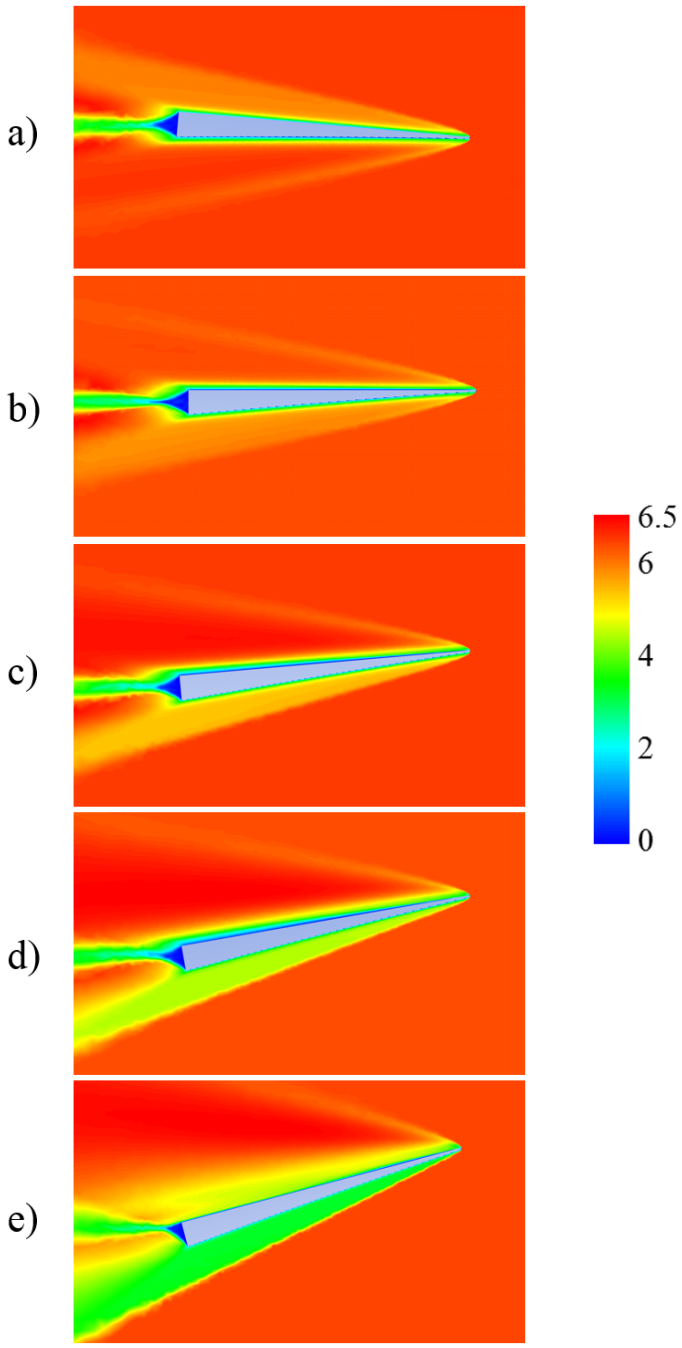


Figure 4.16: Mach number contours are shown for varied angle-of-attack computed using the $k-\omega$ SST turbulence model and the variable-$\gamma$ air model. The waverider is designed for Mach 6 with a 3m wingspan and a 3mm leading-edge radius. The flight condition is fixed at Mach 6 and 30km altitude. The pitch angles shown are a) $-5°$, b) $0°$, c) $5°$, d) $10°$, and e) $20°$.

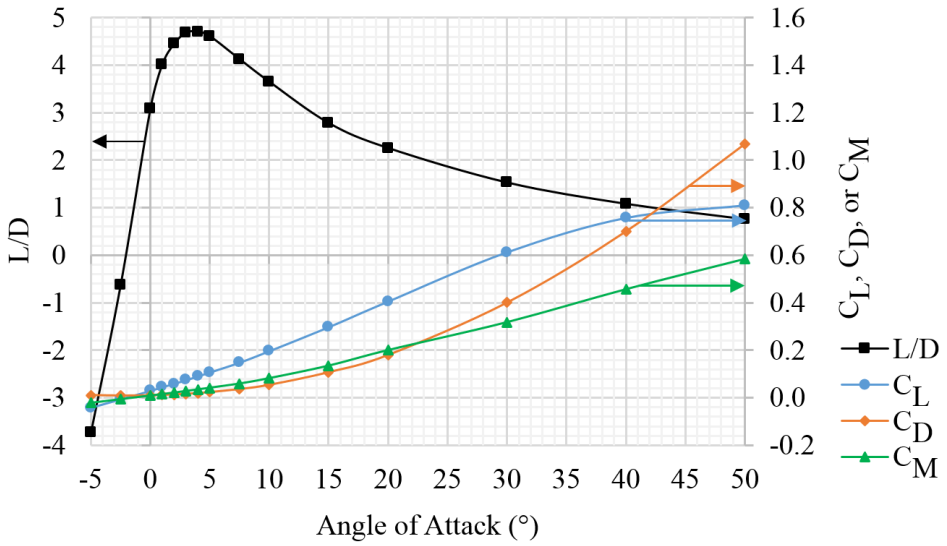


Figure 4.17: Aerodynamic coefficients are shown with varied angle-of-attack computed using the $k-\omega$ SST turbulence model and the variable-$\gamma$ air model. The waverider is designed for Mach 6 with a 3m wingspan and a 3mm leading-edge radius. The flight condition is fixed at Mach 6 and 30km altitude.

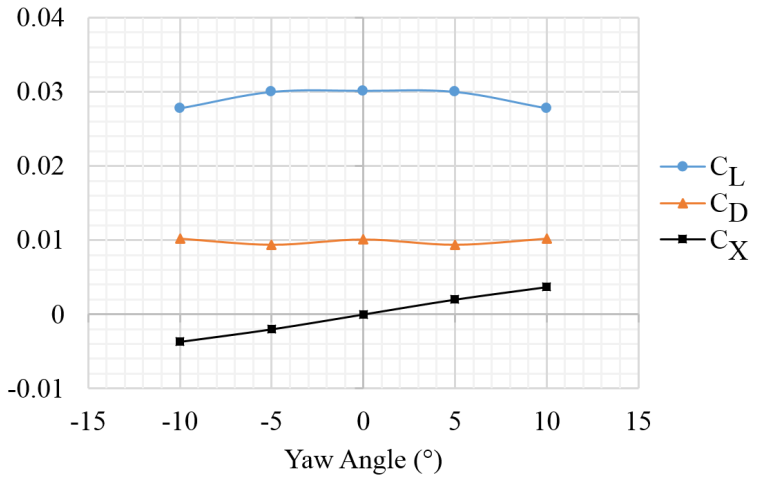


Figure 4.18: Aerodynamic lift ($C_L$), drag ($C_D$), and lateral ($C_X$) force coefficients are shown with varied yaw angle. Forces are computed using the $k-\omega$ SST turbulence model and the variable-$\gamma$ air model. The waverider is designed for Mach 6 with a 3m wingspan and a 3mm leading-edge radius. The flight condition is fixed at Mach 6 and 30km altitude.

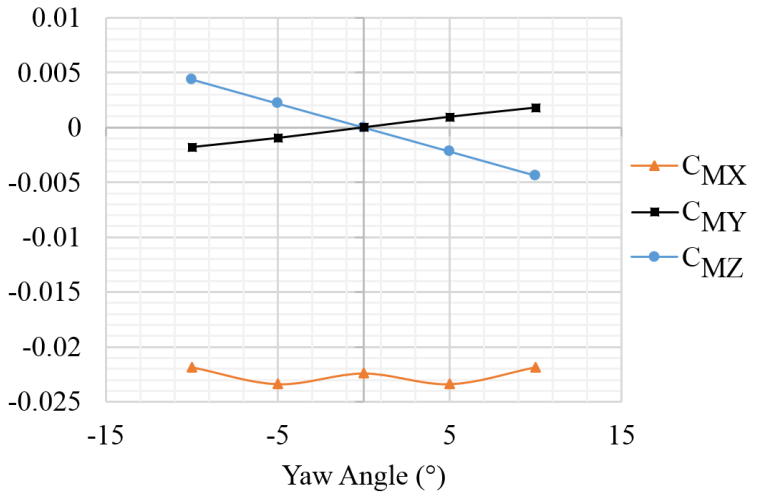


Figure 4.19: Aerodynamic pitch ($C_{MX}$), yaw ($C_{MY}$), and roll ($C_{MZ}$) moment coefficients with varied yaw angle. Moments are computed using the $k-\omega$ SST turbulence model and the variable-$\gamma$ air model. The waverider is designed for Mach 6 with a 3m wingspan and a 3mm leading-edge radius. The flight condition is fixed at Mach 6 and 30km altitude.

Increasing the angle-of-attack results in an increasing pitch-down moment, which is stabilizing along the pitch axis. At zero angle of attack, the lift coefficient degrades by 7%, and there is a relatively large yaw-angle deviation of $\pm 2^\circ$ from zero. The sensitivity in yaw moment is very low around zero yaw angle. The pitch moment is only slightly affected with increasing yaw angle. The roll moment is more largely affected with inverse sign: a positive yaw displacement causes a larger, negative roll moment. Positive yaw displacement induces a positive yaw moment, resulting in a destabilizing effect along the yaw axis. The lack of a stabilizing yaw and roll effects due to yaw displacements leads to a requirement for active control in order to maintain a yaw-stable and roll-stable vehicle. For a pitch-trimmed mass distribution at the design point, the adverse pitch created with increasing yaw creates a small pitch-up moment whose magnitude reverses beyond $\pm 5^\circ$ of yaw.

In summary, the preceding results have demonstrated that this case-study Mach 6 waverider is pitch-stable and experiences minor adverse pitch created with yaw. The vehicle is unstable due to adverse yaw- and roll-moments produced during yaw.

## 4.3 Waverider in Chemically Reacting Flow at High Altitude

### 4.3.1 Mach 20 and 75km

The Mach 6 waverider with a 10mm leading edge radius is immersed in Mach 20 reactive flow at 75km and zero angle of attack. At this altitude, the Reynolds number for the vehicle is $10^{4.7}$ and the Knudsen number is $5.6 \times 10^{-4}$ referenced to the

vehicle length, which represents laminar and continuum flow conditions. All vehicle walls are prescribed isothermal at 2,500K. The multi-species Navier-Stokes equations provided in Section 3.1.2 using the 7-species air model described in Section 3.1.1 were solved in ANSYS Fluent with no turbulence model. The domain was initialized with 22% $O_2$ and 78% $N_2$ by mass, with temperature and pressure 183.7K and 1.85Pa. The initial Mach number everywhere was set to the free-stream value of 20.

The solution was marched forward in time with the CFL limited by the smaller of 1 or any species concentration changing by more than 10% per time step in any cell. Once stabilized on the base mesh, the solution was adaptively refined in gradients of Mach number and temperature, second-order gradient of density, and the gradient of the mole fraction of $O$. Gradients in Mach number and temperature help to resolve the shock and boundary layer. Second-order gradients in density help to resolve the shock. Gradients in the mole fraction of $O$ help to resolve the stiff post-shock chemical reactions in space.

The following results represent an adapted mesh of approximately 130 million elements and slightly more than 200,000 CPU-hrs of computing time. The results are presented in Figs. 4.20 - 4.24 in terms of contours of Mach number, velocity, temperature, pressure, and density. A close-up of the temperature in the stagnation region is provided in Fig. 4.26. A close-up of the chemical species near the nosetip is provided in Fig. 4.27. The maximum temperature of the flow reached in the stagnation region is 9,388K. The heat flux on the top and bottom of the vehicle planform is presented in Fig. 4.25.

The free-stream unit Reynolds number at this speed and altitude is $10^{4.2}$ $m^{-1}$,

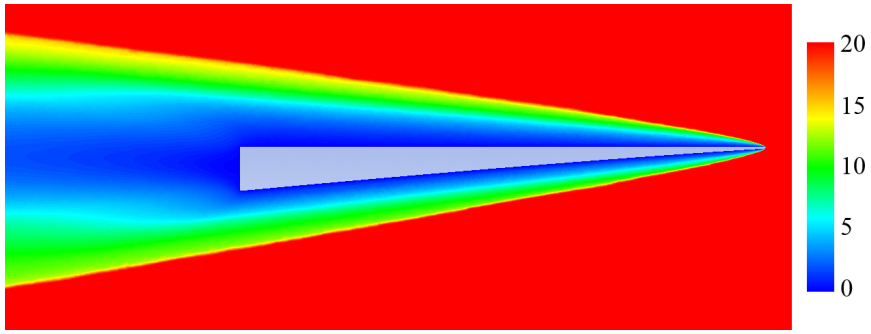


Figure 4.20: Mach number contours for the waverider designed at Mach 6 at a flight condition of Mach 20 and 75km.

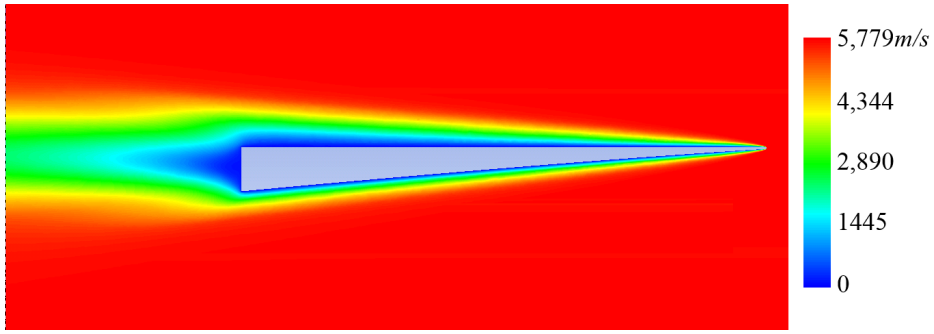


Figure 4.21: Velocity contours for the waverider designed at Mach 6 at a flight condition of Mach 20 and 75k.

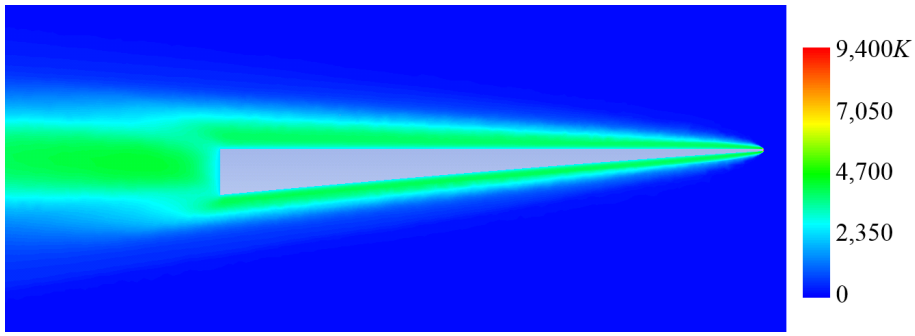


Figure 4.22: Temperature contours for the waverider designed at Mach 6 at a flight condition of Mach 20 and 75k.

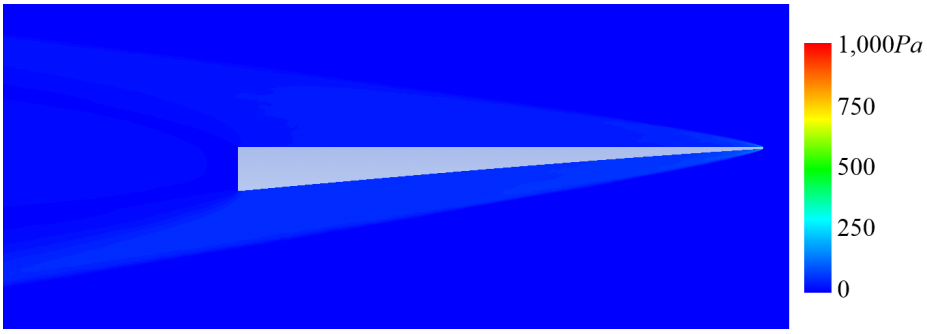


Figure 4.23: Pressure contours for the waverider designed at Mach 6 at a flight condition of Mach 20 and 75k.

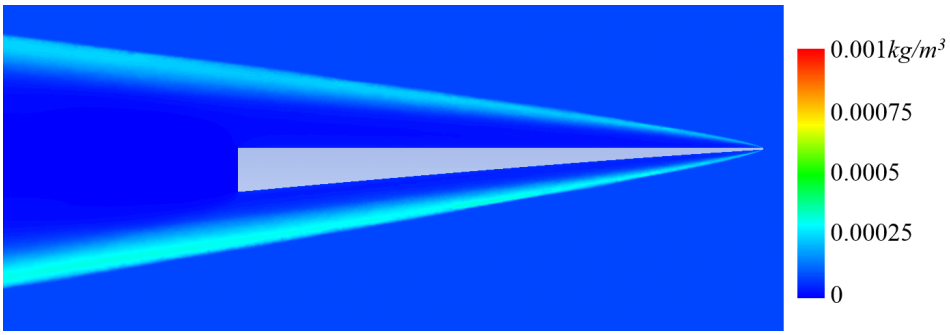


Figure 4.24: Density contours for the waverider designed at Mach 6 at a flight condition of Mach 20 and 75k.

which represents a laminar flow when compared to the critical Reynolds numbers predicted by the Hopkins transition method, which is usually of order $10^6$. A thick, laminar boundary layer is observed in the Mach and velocity contours in Figs. 4.20 and 4.21. Examining Fig. 4.22, the vehicle is enveloped in a post-shock region of hot gas on the order of 5,000K. There is a thin thermal boundary layer that reduces this post-shock temperature to 2,500K prescribed at the vehicle surface. The gradient in temperature in this thin thermal boundary layer drives the heat flux into the vehicle as depicted in Fig. 4.25. The average heat flux is approximately $1\text{W/cm}^2$.

The base pressure average is approximately 8Pa, well above the free-stream pressure of 1.85Pa and very different from the proposed base pressure model of $p_b = p_\infty/M$, which predicts 0.1Pa. At these high speeds, however, the contribution to total drag by the base pressure is negligible. Large errors in base pressure can be tolerated with minimal impact to composite force predictions.

The pressure imbalance visible above and below the vehicle in Fig. 4.23 is indicative of the lift that the vehicle creates. The bow shock at the leading edge emanates downstream in Fig. 4.24, which causes a large jump in density that then expands in the post-shock flow field. A close-up view of the temperature flow field near the 10mm nosetip is provided in Fig. 4.26. The peak temperature reached in the stagnation region reached 9,388K. The post-shock temperature rise and the thermal boundary layer at the vehicle surface is also visible, which reduces to the prescribed isothermal wall temperature of 2,500K. The species mole fractions are presented in Fig. 4.27, which illustrates the small degree to which reactions occur for this small leading-edge geometry. In comparison to the two-dimensional cylinder

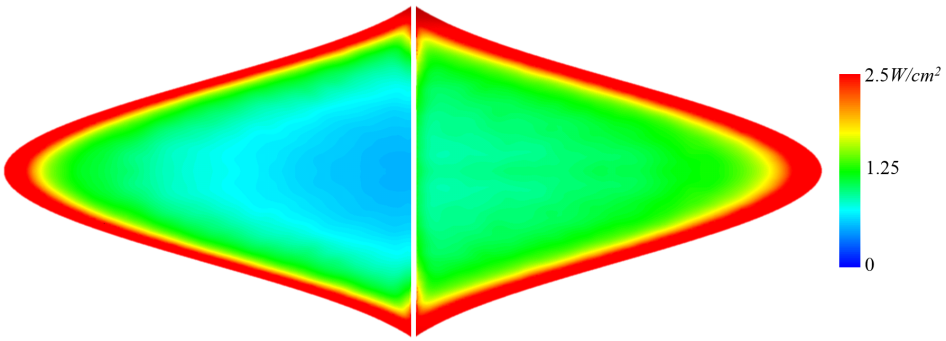


Figure 4.25: Top (left) and bottom (right) planform heat flux into the vehicle for the Mach 6 waverider at Mach 20 and 75km.

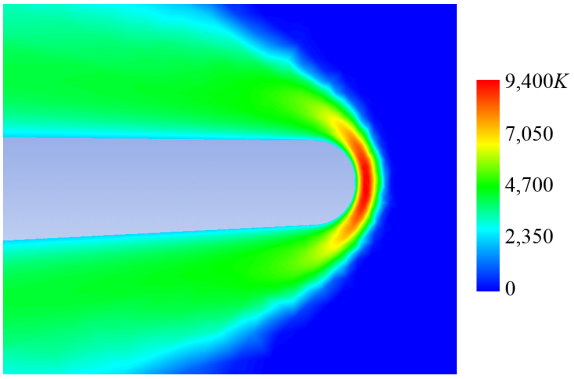


Figure 4.26: Temperature contours near the nosetip for the Mach 6 waverider at Mach 20 and 75km.

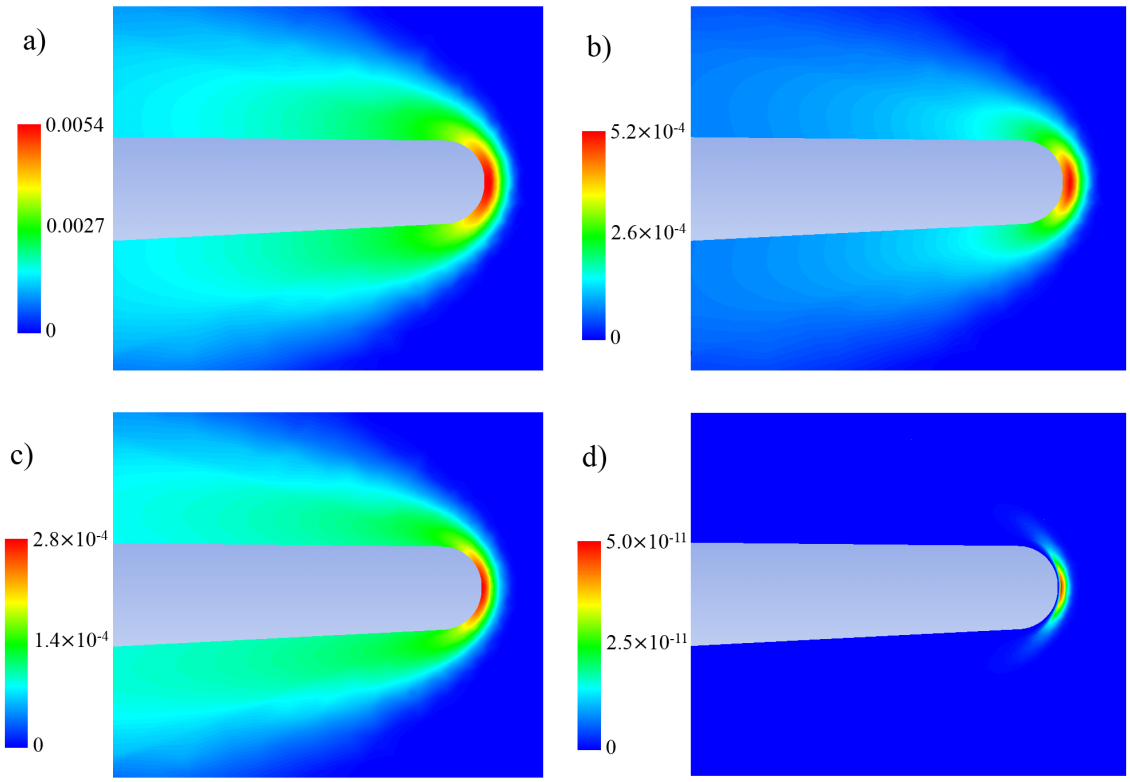


Figure 4.27: Reactive species mole fraction contours near the nosetip for the Mach 6 waverider at Mach 20 and 75km. Species provided are a) $O$, b) $N$, c) $NO$, and d) $NO^+$.

test case presented in Section 3.2.2 where near-equilibrium post-shock chemistry was achieved, this leading edge is ten times smaller in physical size. This leading edge is also not quite cylindrical as the 2-dimensional cylinder test case was, as illustrated by the planforms in Fig. 4.25, which results in an even smaller relative shock standoff distance [4]. The larger-diameter 2-dimensional cylinder test case yielded a maximum temperature of 10,546K. The additional flow "escape" avenue of this non-cylindrical nosetip geometry combined with the thin thermal boundary layer and prescribed 2,500K wall reduces this by 11% to 9,388K.

The non-equilibrium chemistry under these geometry and temperature conditions produces a maximum $O$ mole fraction of 0.0054 in contrast to the larger-cylinder maximum $O$ mole fraction of 0.244. Other species are similarly reduced to relatively trace amounts in the waverider flow field. The $NO^+$ mole fraction reaches a maximum of $5 \times 10^{-11}$, down from $1.5 \times 10^{-7}$ in the larger cylinder test case. Equilibrium chemistry predicts nearly complete dissociation of $O_2$ at these conditions and approximately 20% dissociation of the $N_2$ (see Fig. 1.5). The implication of these waverider leading-edge results compared to the near-equilibrium cylinder test case is that a small leading-edge radius can inhibit finite-rate chemistry in the near-body flow field under conditions relevant to Earth entry vehicles. For an adiabatic wall, inhibiting the flow chemistry would result in a hotter post-shock and stagnation region temperature because thermal energy is "sunk" into chemical reactions. For a wall colder than adiabatic, however, such as the present case, the maximum temperature reached due to the presence of a shock is also inhibited by the nearby cold wall. The proximity of the cold wall creates sharp thermal gradients

that pull down the peak temperature in the stagnation region.

### 4.3.2 Mach 15 and 60km

The Mach 6 waverider with a 10mm leading edge radius is immersed in Mach 15 reactive flow at 60km and zero angle of attack. At this altitude, the Reynolds number for the vehicle is $10^{5.4}$ and the Knudsen number is $9.1\times10^{-5}$ referenced to the vehicle length, which represents laminar and continuum flow conditions. All vehicle walls are prescribed isothermal at 2,500K. The multi-species Navier-Stokes equations provided in Section 3.1.2 using the 7-species air model described in Section 3.1.1 were solved in ANSYS Fluent with no turbulence model. The domain was initialized with 22% $O_2$ and 78% $N_2$ by mass, with temperature and pressure 251.2K and 16.5Pa. The initial Mach number everywhere was set to the free-stream value of 15.

The solution was obtained in the same manner as described in Section 4.3.1. A close-up of the chemical species near the nosetip is provided in Fig. 4.30. The maximum temperature of the flow reached in the stagnation region is 8,639K. The heat flux on the top and bottom of the vehicle planform is presented in Fig. 4.28. The average heat flux at this altitude and speed is approximately 1W/cm$^2$. The base pressure average is 1.1Pa, which matches the value predicted using the proposed base pressure model of $p_b = p_\infty/M$.

The stagnation temperature achievable without chemical reactions in 11,540K. The actual maximum temperature reached of 8,639K indicates a significant amount of energy absorbed by chemical reactions between the constituent molecules for this

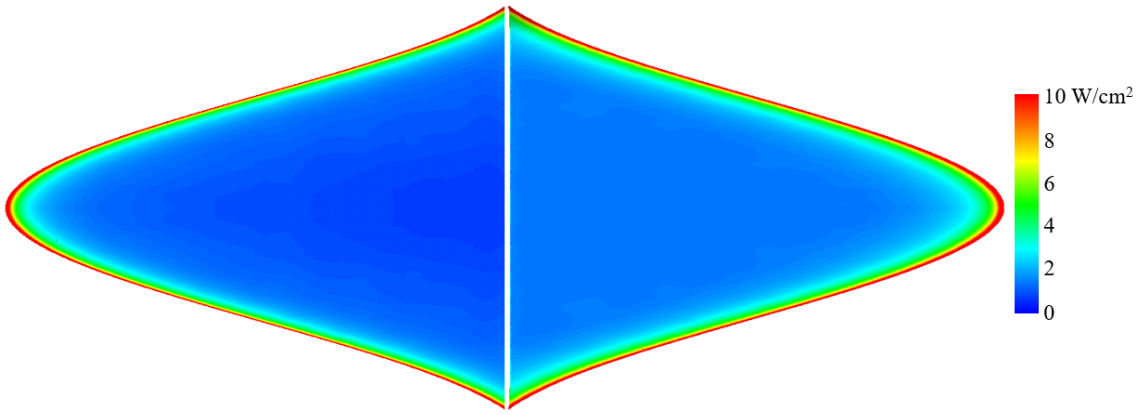


Figure 4.28: Top (left) and bottom (right) planform heat flux into the vehicle for the Mach 6 waverider at Mach 15 and 60km.

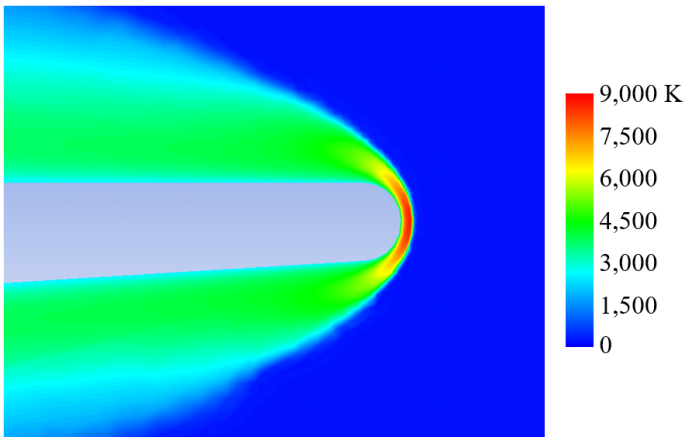


Figure 4.29: Temperature contours near the nosetip for the Mach 6 waverider at Mach 15 and 60km.

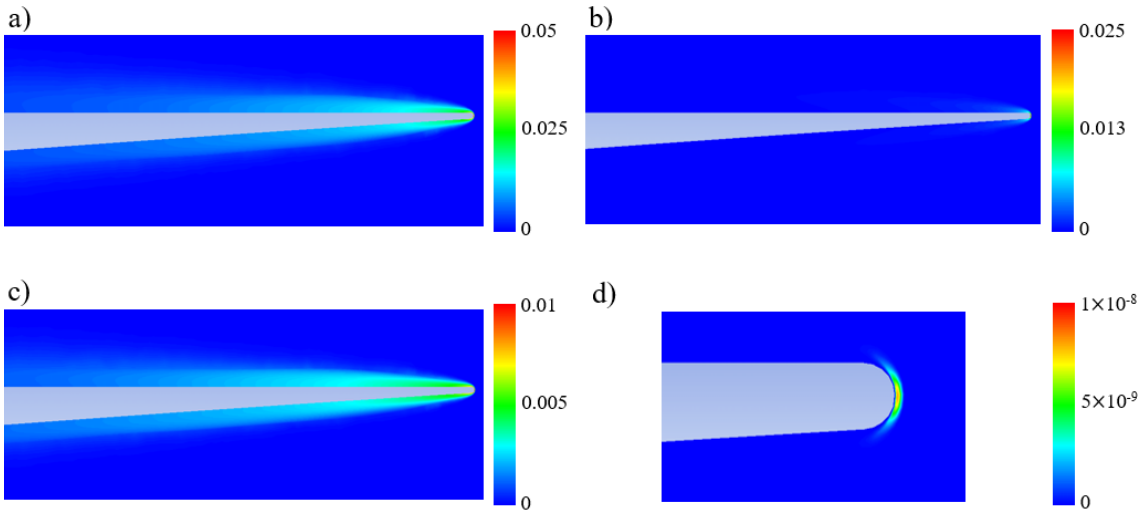


Figure 4.30: Reactive species mole fraction contours for front of Mach 6 waverider at Mach 15 and 60km. Species provided are a) $O$, b) $N$, c) $NO$, and d) $NO^+$.

flight condition of Mach 15 and 60km. A close-up view of the temperature flow field near the 10mm nosetip is provided in Fig. 4.29. The post-shock temperature rise and the thermal boundary layer at the vehicle surface is also visible, which reduces to the prescribed isothermal wall temperature of 2,500K. The species mole fractions are presented in Fig. 4.30, which illustrates the degree to which reactions occur for this small leading-edge geometry. In comparison to the two-dimensional cylinder test case presented in Section 3.2.2 where near-equilibrium post-shock chemistry was achieved, this leading edge is ten times smaller in physical size but is approximately ten times higher density. This increase in density allows the chemical reaction relaxation length to shrink by roughly an order of magnitude and the chemical reactions nearly reach their equilibrium values. The free-molecular oxygen mole fraction, for example, reached 4.6% at this flight condition and reached 4.9% in the

cylindrical flow case study from Section 3.2.2.

The dissociated molecules largely recombine by the end of the 3.63m vehicle simulated. The $NO^+$ mole fraction reaches a maximum of $8 \times 10^{-9}$ near the leading edge, but is reduced to below $10^{-17}$ by the end of the vehicle. Much of this may be due to the absorption of thermal energy into the vehicle by the isothermal wall. The temperatures reached in the boundary layer are inhibited by the nearby cold wall. The proximity of the cold wall creates sharp thermal gradients that pull down the temperature in the boundary layer and encourage the recombination of the molecules that were dissociated in the hot stagnation region.

## 4.4 Summary

Numerical simulations were used to investigate the near-body flow field for waveriders designed at Mach 6 and Mach 8 with blunted leading edges. The Mach 6 waverider was computed on-design with both $k-\omega$-SST and LES-WALE turbulence models. The $k-\omega$-SST model was modified by the author for an assigned location for transition to turbulence based on the Hopkins Method for critical Reynolds number. The drag force matched the LES prediction within 5%. The Mach 8 waverider leading edge was blunted with various radii while fixing vehicle mass, demonstrating severe penalties in performance for a 3%-wingspan leading edge radius compared to a sharp vehicle.

Both waveriders were simulated with varied Mach number, illustrating monotonically decreasing lift and drag coefficients for hypersonic Mach numbers. Both

vehicles produced the highest lift-to-drag ratio at their design Mach number. The base pressure was observed to follow a proportionality to $1/M$, where the constant of proportionality was different for each vehicle but consistent across Mach number. Angle of attack was varied for the Mach 6 waverider, which matched the qualitative variation in aerodynamic coefficients of a Newtonian flat plate. The Mach 6 waverider was found to be pitch-stable with angle of attack, then yawed off-design to illustrate yaw instability and roll instability due to yaw.

The Mach 6 waverider was then immersed in a Mach 20 flow at zero angle of attack at 75km. The low Reynolds number resulted in thick boundary layers and a smooth, laminar flow field. The small leading-edge radius with a 2,500K prescribed wall temperature resulted in a small bow-shock standoff from the nosetip and nonequilibrium chemistry in the stagnation region. The post-shock flow produced low mole fractions of reactive species, despite the high stagnation temperature, due to the small spatial scale.

The Mach 6 waverider was finally immersed in a Mach 15 flow at zero angle of attack at 60km. The laminar conditions resulted in a thick boundary layer and the high Mach number resulted in a small shock angle relative to the vehicle surface. The small leading-edge radius dissociated the oxygen to near equilibrium chemistry values. The ionization fraction reached two orders of magnitude higher than the Mach 20 flight condition due to the ability of reactions to occur in space. The high-temperature reaction products almost entirely recombined by the time they reached the end of the vehicle.

A note on computational cost scaling: a non-adapted solution requires in-

creased resolution in three spatial dimensions and one temporal dimension for increased accuracy. A globally first-order method halves the solution error for a doubling of the resolution. While gradients can be computed with higher order-order, certain features such as shock waves can only be resolved with first-order methods. Halving the grid size and time step results in a $2^4$ factor increase in computing time to reach the same instant in solution time. Similarly, a 1% error estimate requires 10,000 times the computing time as a 10% error solution for a uniformly refined grid. The utility of adaptive refinement is selectively resolving flow field details so that this factor of 10,000 can be reduced potentially by several orders of magnitude by using a good adaptive resolution strategy. A final note on the value of a variable-$\gamma$ air model (where it is appropriate to use) is the difference in computational cost between a 10-20,000 CPU-hr $k - \omega$ SST solution using thermally perfect air and the $> 200,000$ CPU-hr single case for reactive flow. This high cost for reactive flow is due to the extremely fine resolution needed in the post-shock region for stiff chemical reactions, the many species to simultaneously track, and the many solution iterations required to reach long-term fluid steady state conditions with propagating chemical reactions.

# Chapter 5: Reduced-Order Model Results

The reduced-order model for waverider aerodynamics is referred to as the "Waverider Reduced-order Analysis and Investigative Tool for Hypersonics" (WRAITH), and was formulated in Chapter 2. In this chapter, WRAITH is compared to the results of numerical simulations presented in Chapter 4. First, the pressure and viscous forces on each vehicle surface are compared for the Mach 6 waverider at its design flight condition and 30km altitude. Next, the net forces and glide ratio for both the Mach 6 and Mach 8 waveriders are compared to the CFD results at their design point. Agreement is found within 8% for net lift, drag, and moments of the waveriders on design. Comparisons are then made for off-design angle-of-attack for the Mach 6 waverider and off-design Mach number for both the Mach 6 and Mach 8 waveriders. WRAITH matches the CFD results for variation in angle-of-attack closely. WRAITH matches the lift and drag coefficients with variable Mach number closely; however, larger errors are observed in the lift-to-drag ratio away from the design Mach number. The Mach 6 waverider in a laminar, reactive flow field at Mach 15 and 60km and Mach 20 at 75km is compared to WRAITH predictions. WRAITH is found to predict forces and moments to within approximately 10%, but under-predicts the lift-to-drag ratio by 22%.

With an understanding of the degree of accuracy of the reduced-order model in comparison to CFD results, WRAITH is then used to illustrate the effect of altitude variation and wall temperature variation on the case-study waverider aerodynamic coefficients. The chapter closes with a comparison of the aerodynamic performance of a morphing waverider versus a rigid waverider and the surface deflection and strain required for morphing.

## 5.1 Comparison with CFD Results

### 5.1.1 Waverider Forces and Moments On the Design Condition

The lift and drag forces, lift-to-drag ratio, and moment produced by the Mach 6 waverider at its design point of Mach 6 and 30km altitude are presented in Table 5.1. The moment is listed in reference to the pitch axis centered at the nosetip. The WRAITH model is listed along with assigned fully laminar and fully turbulent friction factors for comparison. As shown in Table 5.1, a fully turbulent boundary layer produces 21% more net drag force than a fully laminar boundary layer. This difference in net drag illustrates the importance of accurately predicting the location of transition to turbulence. A comparison is then made in Table 5.1 between the WRAITH model and the numerical results for the $k-\omega$ SST and the LES-WALE turbulence models. Their differences are summarized in the final two rows of the table.

The lift forces on each of the major vehicle surfaces that were computed using the WRAITH model and two CFD turbulence models are presented in Table 5.2.

The drag forces on each of the major surfaces are presented in Table 5.3. The composite lift, drag, and moment for the Mach 8 waverider are presented in Table 5.4 along with a comparison to $k-\omega$ SST results.

| | $F_L$ $(N)$ | $F_D$ $(N)$ | $M_\alpha$ $(N-m)$ | $L/D$ |
|---|---|---|---|---|
| Fully Laminar | 6008.6 | 1840.4 | -14631.7 | 3.27 |
| Fully Turbulent | 5999.8 | 2220.9 | -14536.6 | 2.70 |
| WRAITH | 6004.3 | 1986.3 | -14584.3 | 3.02 |
| $k-\omega$ SST | 5978.0 | 1931.5 | -14041.9 | 3.09 |
| LES-WALE | 5862.6 | 1849.5 | -14106.0 | 3.17 |
| $\Delta$ WRAITH-$(k-\omega)$ | +0.4% | +2.9% | +3.9% | -2.3% |
| $\Delta$ WRAITH-LES | +2.4% | +7.4% | +3.4% | -4.7% |

Table 5.1: Comparison of total lift, drag, and pitch moment computed for the Mach 6 waverider at Mach 6, 30km, and zero angle of attack. The WRAITH predictions with assigned fully laminar boundary layer and fully turbulent boundary layer are provided to illustrate the bounds on the forces and the effect of the location of transition to turbulence. The WRAITH predictions agree within 4% with the $k-\omega$ SST net forces and moments, and within 8% with the LES-WALE computed forces and moments.

| | Leading Edge | Top | Bottom | Base |
|---|---|---|---|---|
| WRAITH | 0 | -8049.9 | 14062.3 | 0 |
| $k-\omega$ SST | 47.2 | -8344.2 | 14274.9 | 0.0 |
| LES-WALE | 51.4 | -8140.4 | 13957.5 | 0.0 |
| $\Delta$ WRAITH-$k-\omega$ | N/A | -3.5% | -1.5% | N/A |
| $\Delta$ WRAITH-LES | N/A | -1.1% | +0.8% | N/A |

Table 5.2: Comparison of lift forces on each major surface of the Mach 6 waverider. The WRAITH lift force predictions agree with both of the CFD models within 4% for the top, bottom, and base surfaces. The WRAITH model predicts zero net lift on the leading edge due to geometrical symmetry, whereas the CFD models each predict a consistent small, positive net lift due to the explicit resolution of asymmetry in the near-body flow field.

### 5.1.2 Waverider Forces and Moments Off of the Design Condition

The waveriders designed at Mach 6 and Mach 8 were simulated in flows off of their design points in order to evaluate the accuracy of WRAITH in this context. Off-design conditions considered for comparison between WRAITH and CFD models include the Mach 6 waverider flown at Mach 15 and 60km, Mach 20 and 75km, at various angles-of-attack at Mach 6, and at zero angle-of-attack across Mach number. The section closes with results of the Mach 8 waverider comparison between WRAITH and CFD across Mach number at zero angle of attack.

| | Leading Edge | Top | Bottom | Base |
|---|---|---|---|---|
| WRAITH | 660.6 | 134.6 | 1243.6 | -94.6 |
| $k-\omega$ SST | 690.4 | 118.0 | 1200.7 | -77.6 |
| LES-WALE | 704.4 | 94.6 | 1123.2 | -72.7 |
| $\Delta$ WRAITH-$k-\omega$ | -4.3% | +14.1% | +3.6% | +21.9% |
| $\Delta$ WRAITH-LES | -6.2% | +42.2% | +10.7% | +30.2% |

Table 5.3: Comparison of drag forces on each major surface of the Mach 6 waverider. The WRAITH model agrees with the CFD models within 6% for the leading edge drag. WRAITH over-predicts the drag on the top surface, exclusively due to viscous effects, by as much as 42% compared to the LES-WALE prediction. This indicates premature prediction of transition to turbulence by WRAITH and the $k-\omega$ models which use the Hopkins Method for assigning a critical Reynolds number [163]. WRAITH over-predicts drag on the bottom of the vehicle by as much as 11% compared to LES-WALE. This is less than the top surface because the dominant pressure-drag forces are modeled accurately by WRAITH, while the bottom-surface viscous drag is over-predicted by WRAITH. The WRAITH base pressure model over-predicts the base drag by as much as 30% compared to LES-WALE, while the two CFD models agree more closely.

| | $F_L$ $(N)$ | $F_D$ $(N)$ | $M_\alpha$ $(N-m)$ | $L/D$ |
|---|---|---|---|---|
| WRAITH | 17527.8 | 4855.6 | -42134.0 | 3.61 |
| $k-\omega$ SST | 16960.2 | 4903.8 | -40414.2 | 3.46 |
| $\Delta$ | +3.4% | -1.0% | -4.1% | +4.3% |

Table 5.4: Comparison of total lift, drag, and pitch moment computed for the Mach 8 waverider at Mach 8, 30km, and zero angle of attack. The WRAITH predictions agree within 5% with the $k-\omega$ SST net forces, moments, and the lift-to-drag ratio.

The net lift, drag, lift-to-drag ratio, and pitch moment produced by the Mach 6 waverider operated at Mach 15 and 60km are presented in Table 5.5. This table summarizes a comparison between the WRAITH model and the CFD solution using 7-species air.

The net lift, drag, lift-to-drag ratio, and pitch moment produced by the Mach 6 waverider operated at Mach 20 and 75km are presented in Table 5.6. This table summarizes a comparison between the WRAITH model and the CFD solution using 7-species air.

The primary difference between the Mach 15 and the Mach 20 flight conditions is the degree to which chemical reactions occur in the flow field. As was shown in Sections 4.3.2 and 4.3.1, the Mach 20 flow field produced minimal dissociation. The maximum mole fraction of $O$ was only 0.5%. The Mach 15 flow field, due to the higher ambient density, produced a maximum mole fraction of $O$ of 4.6%. WRAITH

| | $F_L$ $(N)$ | $F_D$ $(N)$ | $M_\alpha$ $(N-m)$ | $L/D$ |
|---|---|---|---|---|
| WRAITH | 194.3 | 223.9 | -443.2 | 0.87 |
| Laminar CFD | 230.8 | 237.5 | -549.5 | 0.97 |
| $\Delta$ | -15.8% | -5.7% | -19.3% | -10.3% |

Table 5.5: Comparison of total lift, drag, and pitch moment computed for the Mach 6 waverider at zero angle-of-attack flown at Mach 15 and 60km. WRAITH matches the drag force within 6% compared to the laminar, reactive CFD results. WRAITH under-predicts the lift, lift-to-drag ratio, and moment by 10-20%.

| | $F_L$ $(N)$ | $F_D$ $(N)$ | $M_\alpha$ $(N-m)$ | $L/D$ |
|---|---|---|---|---|
| WRAITH | 28.4 | 78.5 | -61.1 | 0.36 |
| Laminar CFD | 31.8 | 74.8 | -56.0 | 0.43 |
| $\Delta$ | -10.7% | +5.0% | +9.1% | -21.5% |

Table 5.6: Comparison of total lift, drag, and pitch moment computed for the Mach 6 waverider at zero angle-of-attack flown at Mach 20 and 75km. WRAITH matches the forces and moment within approximately 10% compared to the laminar, reactive CFD results. WRAITH under-predicts the lift-to-drag ratio by 22%.

matches drag within 6% in each case. WRAITH under-predicts lift by 11% in the near-frozen-flow case and by 16% in the near-equilibrium-flow case. WRAITH can account for reactive flow in the post-conical-shock flow field, but does not account for chemical reactions due to the bow shock that stands off from a small, blunt leading edge.

The Mach 6 waverider flow field was computed across $-5°$ to $+50°$ angle-of-attack using the $k-\omega$ SST turbulence model and the WRAITH model was computed at the same points. The aerodynamic coefficients are plotted in Fig. 5.1. The case study waveriders are used to compute aerodynamic coefficients as the Mach number varies between Mach 1 and 12 using the variable-$\gamma$ model, presented in Figs. 5.2 and 5.3.

As illustrated in Fig. 5.1, the WRAITH model captures both the absolute value as well as the qualitative trend of aerodynamic coefficients with varied angle-of-attack for on-design Mach number. The zero-lift angle, the on-design configuration, and the peak lift-to-drag ratio magnitude and angle are well-matched compared to the CFD result. The deviations between the models increase slightly with increasing angle of attack. Across the range of angle considered, agreement is maintained within approximately 6%.

As illustrated in Figs. 5.2 and 5.3, the on-design aerodynamic coefficients match between WRAITH and the CFD results. The lift and drag coefficients for hypersonic Mach numbers match within 5% for the waverider designed at Mach 6 and within 10% for the waverider designed at Mach 8. The agreement between WRAITH and the CFD decreases at low-supersonic Mach numbers or for large

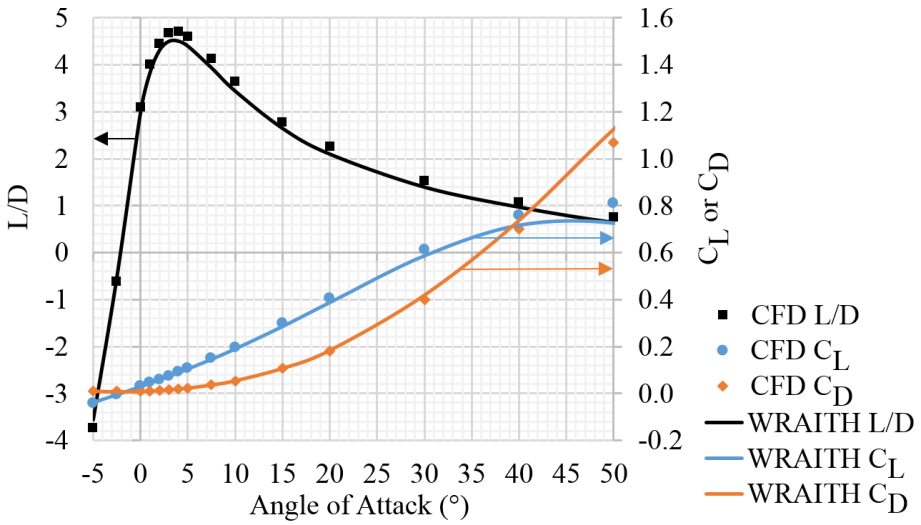


Figure 5.1: Aerodynamic coefficients with varied angle of attack for the waverider designed at Mach 6 flown at Mach 6 and 30km. WRAITH and CFD using the $k-\omega$ SST turbulence model and the variable-$\gamma$ air model were used to compute the lift and drag coefficients across angle of attack. WRAITH matches the CFD results with angle-of-attack qualitatively, and quantitatively within 6% across the range of angle considered.

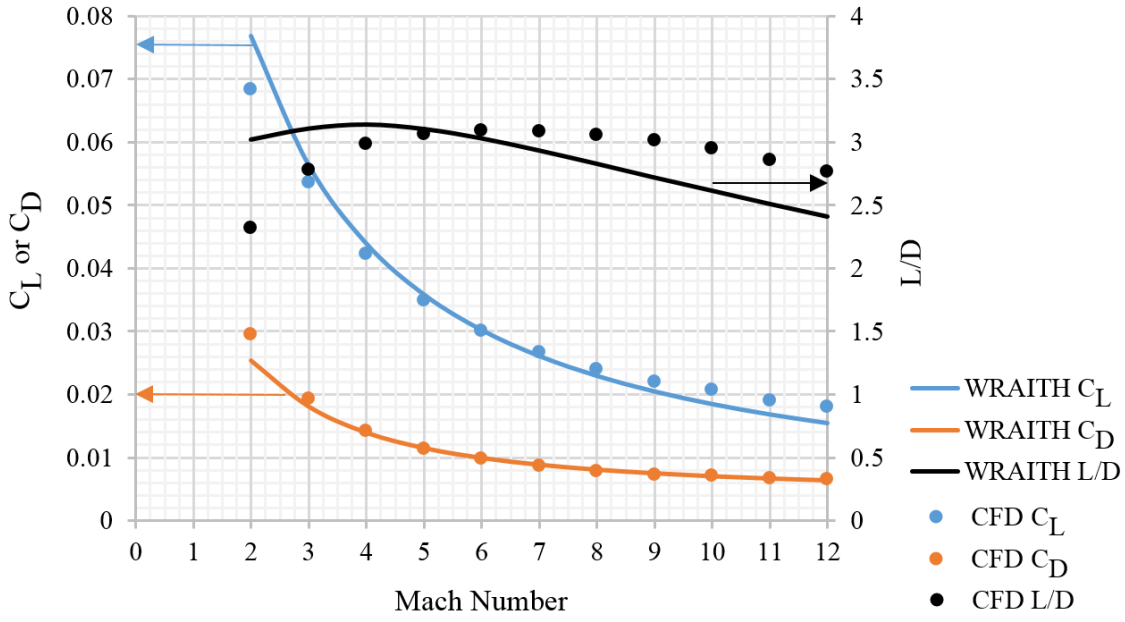


Figure 5.2: Aerodynamic coefficients with varied Mach number for the waverider designed at Mach 6 at zero angle-of-attack and 30km. WRAITH and CFD using the $k-\omega$ SST turbulence model and the variable-$\gamma$ air model were used to compute the lift and drag coefficients across Mach number. WRAITH matches the CFD results for lift and drag coefficients within 5% for Mach 3 and greater. The discrepancy between predictions for lift-to-drag ratio increase away from the design point.

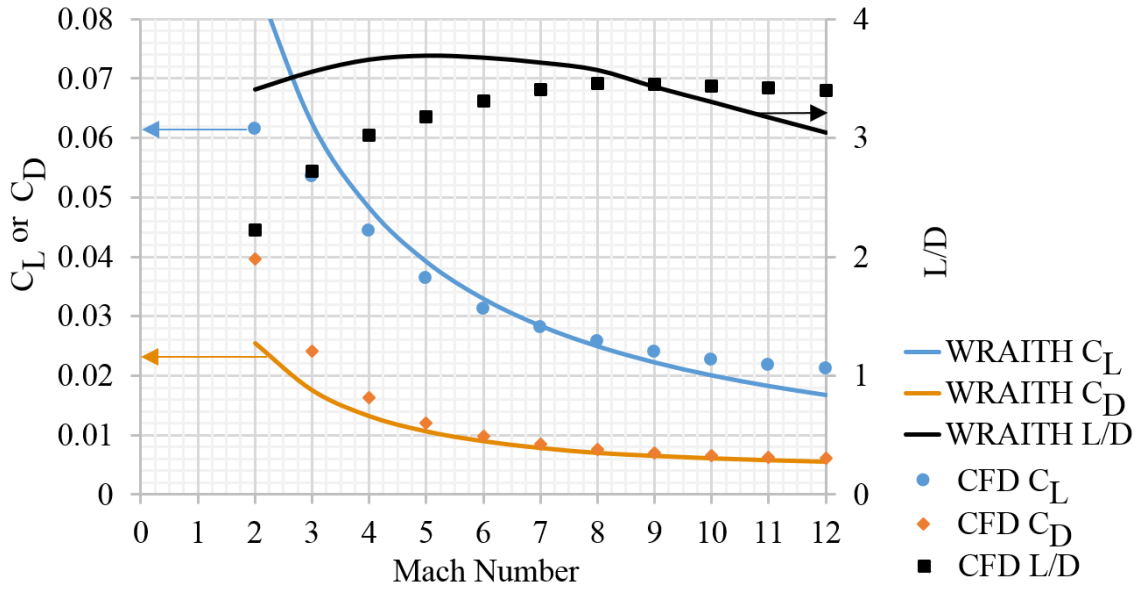


Figure 5.3: Aerodynamic coefficients with varied Mach number for the waverider designed at Mach 8 at zero angle-of-attack and 30km. WRAITH and CFD using the $k-\omega$ SST turbulence model and the variable-$\gamma$ air model were used to compute the lift and drag coefficients across Mach number. WRAITH matches the CFD results for lift and drag coefficients qualitatively across the range of Mach number considered, with decreasing accuracy away from the design point. Ten percent agreement is maintained between approximately Mach 4 and 10.

deviations from the design point.

The lift-to-drag ratio matches within approximately 15% for hypersonic Mach numbers and 30% for low-supersonic speeds. The concave-down shape of the L/D trend with Mach number from CFD is reproduced by WRAITH, but the prediction of the Mach number for peak lift-to-drag ratio is inaccurate by multiple Mach numbers. This discrepancy can be attributed to the shock detachment at low speeds and significant shock shape skewing at higher speeds. These deviations from the design-shock shape result in flow leakage around the leading edge and different reference pressure coefficients than the original design condition which is used in the WRAITH model.

## 5.2 Effect of Altitude

The WRAITH model is parametrically evaluated for four case-study configurations across changes in altitude from sea level to 120km, demonstrating the reduction in lift-to-drag ratio associated with increasing viscous effects with increasing altitude.

The Reynolds number decreases with increasing altitude, resulting in more significant viscous forces relative to pressure-based forces. As a waverider ascends into lower-density air, viscous forces reduce the lift-to-drag ratio attainable near sea level for a given vehicle. This is depicted in Fig. 5.4 using the 1976 Standard Atmosphere for a 3m-wingspan Mach 6 waverider on-design, a 30m Mach 6 waverider on-design, a 30m Mach 15 waverider on-design, and the same 30m Mach 15 waverider

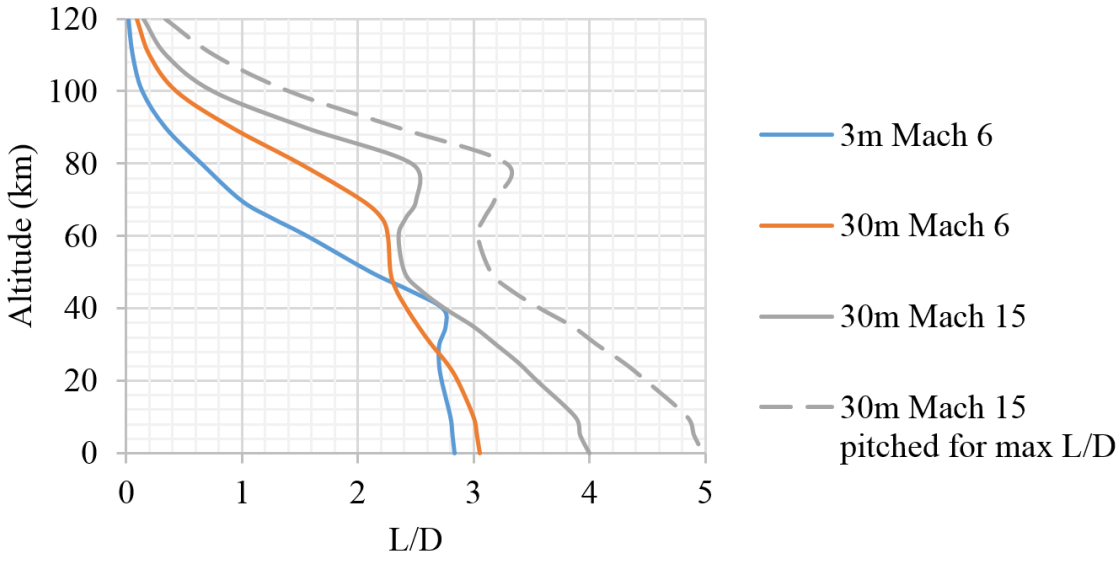


Figure 5.4: WRAITH computed lift-to-drag ratio for the Mach 6 waverider illustrated in Fig. 4.1 with a 3m wingspan and a 30m wingspan, both on design; a Mach 15 waverider on design, and the same waverider pitched for maximum lift-to-drag ratio. The maximum L/D is achieved at sea level, which is reduced with increasing altitude as viscous effects become more significant.

pitched for maximum lift-to-drag ratio at each altitude. As shown in Fig. 5.4, waveriders that achieve L/D of 3-5 near sea level are reduced below unity at high altitude. The ridges observed in the flight paths indicate the flight condition for which transition to turbulence sets in. Flight below the ridge altitude is more turbulent, whereas flight above the ridge altitude becomes laminar.

## 5.3 Effect of Wall Temperature

The WRAITH model is parametrically evaluated for three case-study vehicles across changes in prescribed isothermal wall temperature. Temperature affects the friction coefficient, demonstrating the reduction in lift-to-drag ratio associated with a cold wall.

According to boundary layer theory for a flat plate in high-speed flow, a hot wall yields a smaller friction coefficient than a cold wall [4]. This effect is built into WRAITH using the Eckert friction coefficient and reference temperature method. The variation in normalized lift-to-drag for one case study waverider is depicted in Fig. 5.5 at various altitudes and Mach number. The same Mach 6 vehicle used in the CFD investigation is used and operated at the altitudes and Mach numbers listed, with zero pitch and yaw angles. In each case, the wall is assigned an isothermal temperature between zero and 3,500K.

As shown in Fig. 5.5, a hot wall can yield a lift-to-drag ratio up to 50% higher than a cold wall for a vehicle whose friction drag represents a significant contribution to the total drag. Across the more practical wall temperature range of 300K to 2,500K this difference can still be on the order of 15-25%.

## 5.4 Morphing versus Rigid Waveriders

Rigid waveriders were found to be relatively insensitive to changes in speed for up to a 2-3 Mach numbers around their design point. They were also found

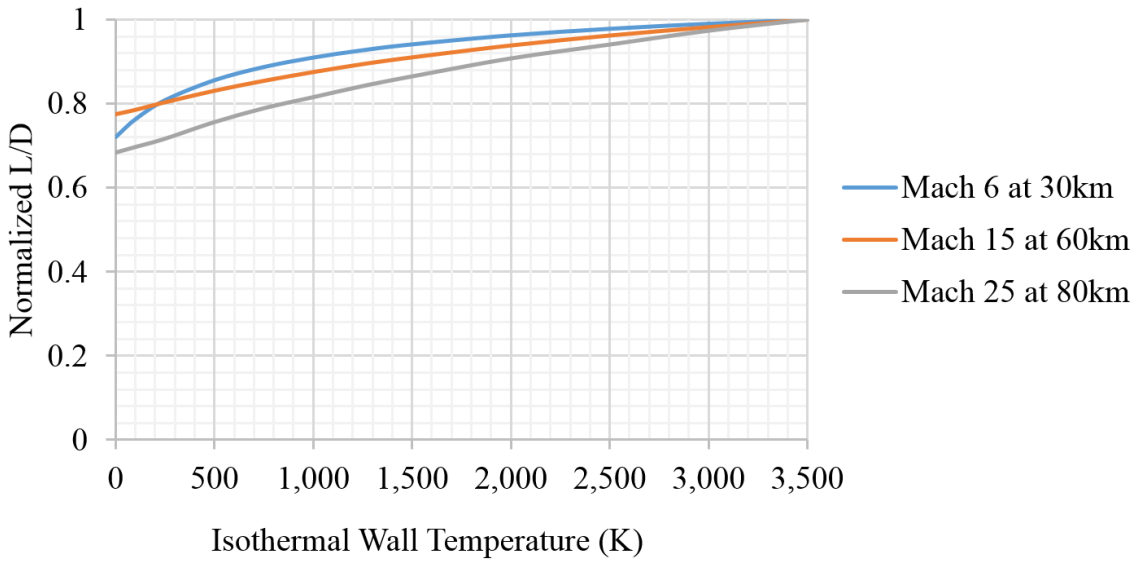


Figure 5.5: WRAITH computed lift-to-drag ratio for the Mach 6 waverider illustrated in Fig. 4.1 with varied wall temperature between 0 and 3,500K. Lift-to-drag ratio is normalized for each vehicle by its maximum value, each occurring for the maximum temperature. Lift-to-drag ratio decreases monotonically with decreasing wall temperature, although at different rates and by different magnitudes.

to have lift-to-drag ratios that can vary from zero to 50% higher than their design configuration by changing the angle of attack. The critical question is now: what advantage does a morphing waverider have? Can an optimally pitched, rigid vehicle designed for an intermediate Mach number achieve a high lift-to-drag ratio across the wide range of zero to entry speeds? Can a rigid waverider perform well enough to render the concept of morphing unnecessary due to its additional complexity?

A thorough investigation with optimization is deferred for future work, however a comparison of the case study vehicles from Chapter 4 is merited. The CFD results for the on-design waverider across Mach number are compared to the WRAITH model for a morphing waverider in Fig. 5.6.

The minimum drag condition for the case study vehicles was found to be at zero angle of attack. The maximum lift-to-drag ratio for the waverider designed at Mach 6 and flown at 30km occurs for approximately $+3.5^\circ$ angle of attack -a small, positive angle. It was observed with both WRAITH and the CFD results that the lift-to-drag curves tend to be concave-down across Mach number for rigid geometry. The CFD results indicate that the peak lift-to-drag occurs at the design point and diminishes for deviations away from the design point.

For small changes in Mach number about a design point, a rigid waverider is preferred due to the insensitivity of the lift-to-drag ratio and the ability to modulate aerodynamic coefficients with angle of attack. The lift-to-drag ratio was found to be consistent within 10% for deviations of $\pm 2 - 3$ Mach number away from the design point in Chapter 4. The lift-to-drag ratio for a rigid vehicle was found to increase by 50% for the optimal angle-of-attack.

As shown in Fig. 5.6, both the CFD and the WRAITH models predict significant reductions in the lift-to-drag ratio for large deviations away from the design Mach number for both case-study waveriders. The rigid vehicles produce a peak lift-to-drag ratio at their design Mach number, which decreases away from their respective design points. The morphing vehicle matches the rigid vehicles at their design Mach numbers of 6 and 8, to within the model error characterized earlier in this chapter. The Mach 6 waverider glide ratio falls quickly beyond its design point, resulting in a 32% higher L/D for the morphing waverider at Mach 12. The Mach 8 configuration drops less steeply beyond its design point. The Mach 8 waverider is less streamlined and its viscous forces comprise a lesser component of its total drag force than for the Mach 6 vehicle. Since the CFD models used for parametric variation are increasingly invalid for higher Mach number at this operating condition, we cannot directly compare the vehicle performances at entry speeds of Mach 30 with these CFD methods. WRAITH predictions are used to extrapolate an estimate for rigid vehicle behavior at high Mach number, illustrated by the orange and blue dashed curves in Fig. 5.6 between Mach 12 and 30.

The morphing advantage for lift-to-drag at high Mach number is a factor of 2-3 times as high for these case-study rigid vehicles. At low Mach number, the rigid vehicles outperform the morphing vehicle. The morphing vehicle can overcome this disadvantage by simply remaining rigid wherever it is advantageous to do so. In the context of these case-study vehicles, this occurs approximately below Mach 8. In summary, a morphing waverider will match the performance of a rigid waverider at its design point, may perform much higher at higher Mach numbers, and may

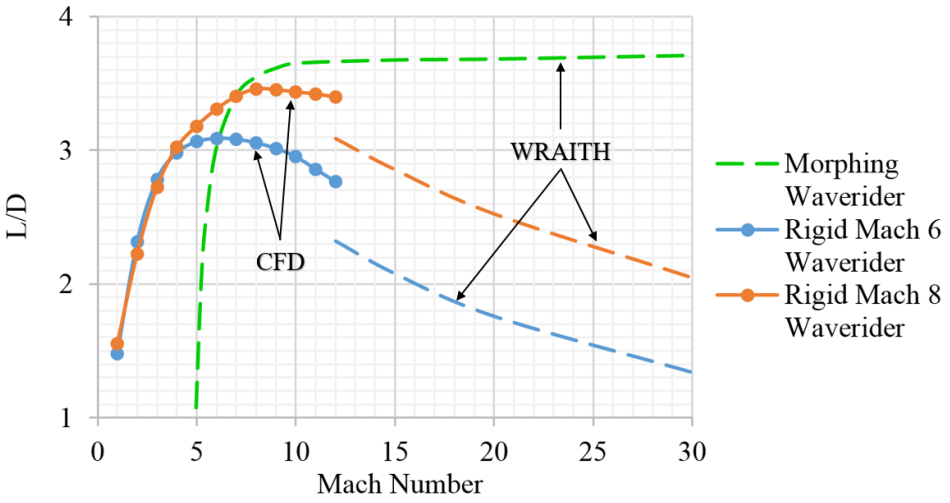


Figure 5.6: CFD-computed rigid case study vehicle lift-to-drag ratio and WRAITH-computed lift-to-drag ratio for Mach 0 to 30 fixed at 30km altitude. CFD-computed data points are indicated with dots whereas WRAITH-computed results are dashed lines with resolution of 0.5 Mach number. The rigid results are extrapolated beyond the CFD data set limit of Mach 12 using the WRAITH model between Mach 12 and 30. The morphing waverider matches each vehicle at their respective design points of Mach 6 and Mach 8, but achieves higher lift-to-drag ratio across all higher Mach numbers.

remain rigid whenever it is advantageous to do so.

As a first-order approximation to maximize entry vehicle performance, it is recommended that a rigid vehicle designed to operate across the wide range of entry speeds select an intermediate Mach number design point, such as Mach 15. Caution must be exercised, however, to avoid the steep drop in performance with lower Mach numbers than the design point, as depicted in Fig. 5.6. Pitching to higher angle-of-attack may help increase the glide ratio, particularly at low Mach number. How variable aerodynamic properties affect entry dynamics is not clear at this point because of competing nonlinear effects, but this is the subject of Chapter 6.

The final consideration for morphing waveriders is the degree of deflection and the strain induced in the lower surface. The maximum orthogonal deflection and the maximum in-plane strain occurs at the base of the vehicle. The deflection and strain closer to the leading edge is inherently less than at the base plane. The case study vehicle for Earth entry designed by the author is presented in Fig. 5.7.

At a 50km altitude, the normalized L/D across Mach number is depicted in Fig. 5.8. The maximum L/D is 2.5 for this vehicle at this intermediate altitude. The maximum deflection of the stream surface in reference to a Mach 40 position and normalized by the wingspan is presented in Fig. 5.9 across Mach number. The stream surface strain at the base plane across Mach number is presented in Fig. 5.10.

As Fig. 5.8 illustrates, the glide ratio is asymptotic with Mach number and varies by approximately 15% across Mach 5 to 40 for a fixed altitude. The maximum deflection in Fig. 5.9 illustrates the small morphing required for high Mach numbers

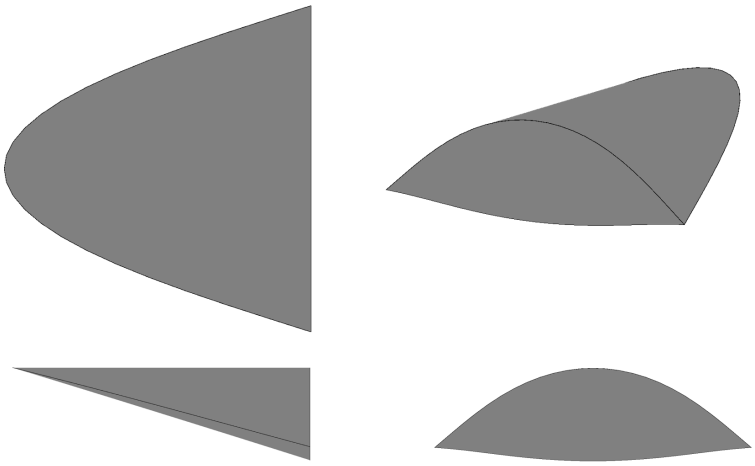

Figure 5.7: Baseline LEO-return waverider at Mach 20 configuration designed using WRAITH. The vehicle is scaled to the same reference area as the SSO and three leading-edge radii will be considered in Chapter 6.

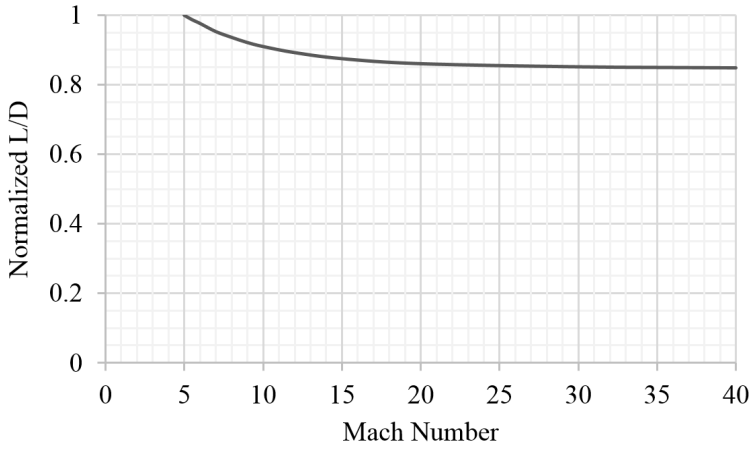


Figure 5.8: Normalized L/D for LEO-return waverider at 50km altitude when morphed on-design across Mach 5 to 40. The maximum L/D occurs at Mach 5 and asymptotically decreases to 85% of its maximum value at high-hypersonic Mach numbers.

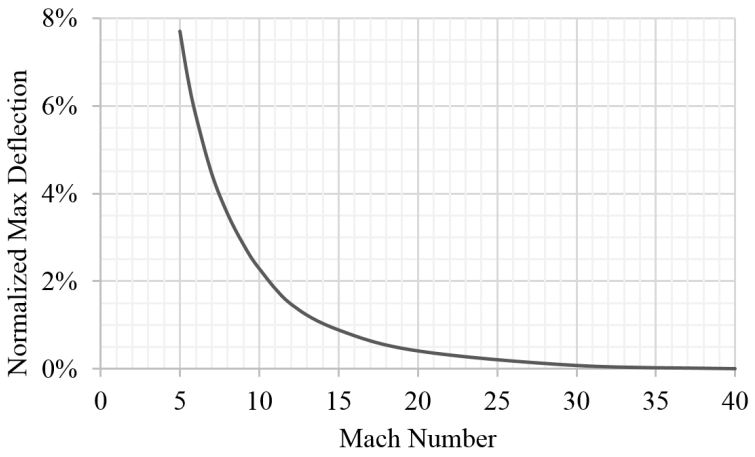


Figure 5.9: Maximum vertical deflection of the lower surface of the morphing waverider normalized by its wingspan. The waverider is morphed as a function of Mach number at zero angle of attack across Mach 5 to 40. Deflections are minimal far into the hypersonic regime and become large below the hypersonic regime.

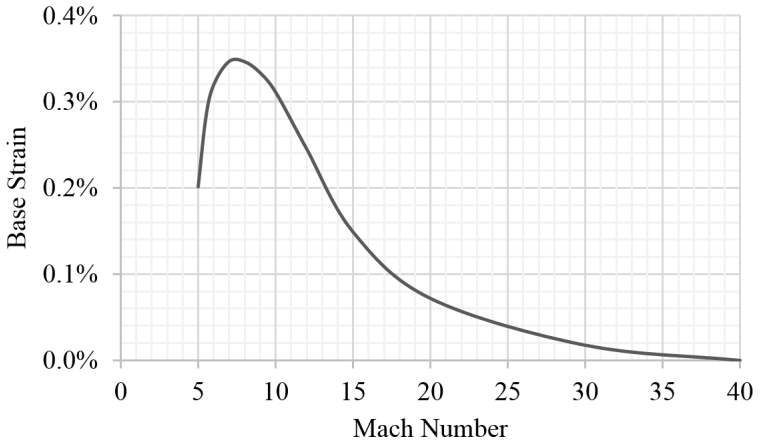


Figure 5.10: Stream surface lateral strain at the base plane for LEO return waverider when morphed on-design across Mach 5 to 40. The stream surface incurs minimal strain far into the hypersonic regime and reaches a maximum for low-hypersonic Mach number.

and the increasing flexibility needed at lower Mach numbers. The lower-surface stress in the base plane illustrated in Fig. 5.10 suggests that a reference design at Mach 14 would yield a strain requirement of $\pm 0.18\%$ across the range of Mach 5 to 40, which is well below the 2% linear-elastic-strain limit recommended for recoverable deformation [184].

The range of practical morphing is governed by the maximum allowable bending stresses, lateral strain, minimum usable volume, and the aerodynamic payoff for morphing at low speeds. Since peak stagnation heating, average heating, and deceleration conditions for lifting vehicles tend to occur above Mach 10, morphing for on-design operation below Mach 10 yields diminishing returns while increasing in complexity. Strain may be minimized by designing a vehicle to undergo a concave-to-convex transition in the mid-range of design Mach number.

In summary, there is potentially a significant advantage in lift-to-drag ratio across a wide range of Mach number for a morphing vehicle. The advantage is most pronounced across a wide range of Mach number and at high Mach number. The deflection and strain induced in a surface by morphing are within the realm of conventional engineering materials. The final step in evaluating the potential of morphing waveriders as entry vehicles is to simulate entry flight paths and compare metrics to reference vehicles. This is the subject of Chapter 6.

# Chapter 6: Morphing Waveriders for Atmospheric Entry

In this chapter, morphing waveriders are compared to the Space Shuttle Orbiter (SSO) entering Earth's atmosphere and the Mars Science Laboratory (MSL) capsule entering Mars' atmosphere. The Planar Lifting Entry model from Section 2.2 is used to compute the flight path and WRAITH is used to compute the waverider aerodynamics. Three low-drag waveriders are used in Earth's atmosphere that demonstrate improvements in performance metrics over the SSO for return from low-Earth orbit (LEO), primarily the average heating and peak deceleration. One of the Earth-entry waveriders is then compared to the MSL capsule for entry into the Martian atmosphere in the context of an interplanetary mission from Earth to Mars. The morphing waverider demonstrates approximately a 75% reduction in peak stagnation heat flux, a 90% reduction in peak deceleration, and a 95% reduction in peak area-averaged heating compared to the MSL entry capsule.

The metrics for performance comparison are acceleration, dynamic pressure, average dissipated power, and stagnation heat flux. The peak deceleration determines how robust and massive a vehicle airframe must be and how intense the entry is for passengers or payload. The dynamic pressure determines how controllable or maneuverable a vehicle is. It also indirectly determines heating and deceleration.

The average dissipated power of a vehicle correlates to the average heating into the vehicle. It also indirectly determines deceleration. The stagnation heat flux is a metric that describes peak local heating and correlates to average heating at each instant along the entry flight path.

The average dissipated power and the peak stagnation heat flux should be minimized. The peak deceleration should be minimized; however, there is diminishing value in reducing the aerodynamic deceleration much below the acceleration experienced at the planetary surface, which is 1g for Earth. The dynamic pressure should be minimized to as low as 1kPa. A vehicle loses aerodynamic controllability for dynamic pressure much below 1kPa.

The utility of a waverider is the ability to generate the same lift as a non-waverider vehicle for less induced drag [4]. Since heating and deceleration are directly related to drag, the application of waveriders for entry vehicles suggests that they may incur lesser heating and deceleration for a similar descent path. A waverider will result in a longer entry duration due to this reduced drag. The following subsections illustrate example flight paths for morphing waverider entry vehicles compared to a simplified model for the Space Shuttle Orbiter for Earth's atmosphere and the Mars Science Laboratory (MSL) in Mars' atmosphere. In all morphing waverider cases, the angle of attack is fixed at the value noted across the entire flight path and the vehicle is assumed to ideally morph at all points along the flight path as a function of instantaneous Mach number.

The model caveats for these entry simulations include 1) the effects of rarefaction at high altitude are neglected. Continuum theory is used to approximate the

aerodynamics in all regimes. 2) No control implementation effects on the aerodynamic coefficients are accounted for. The angle-of-attack is fixed in each case across the entire entry flight path. The ability of the vehicle to maintain the angle-of-attack along the flight path is assumed to induce no additional drag. 3) Waverider aerodynamic properties are frozen below Mach 4 at their Mach 4 value.

Caveat #1 is justified in this context because significant aerodynamic forces only emerge once the vehicles descend into the continuum regime, rendering rarefied effects minimal for these case studies. The relevant altitudes for vehicles of this scale where continuum theory breaks down is approximately 100km for Earth and 85km for Mars. Variations in vehicle dynamics for these case studies are minimal above this range. The peak heating and deceleration conditions occur at lower altitudes where continuum theory is valid.

Caveat #2 implies that aerodynamic performance may be degraded in future higher-fidelity investigations if it is determined that maintaining the prescribed angle of attack, for example, requires control surfaces that reduce lift or increase drag. The present study includes a single baseline waverider depicted in Fig. 5.7 with case-specific leading edge bluntness and angle of attack. The vehicles and cases were designed by the author through iterative comparison but do not represent the result of formal optimization. Optimization of the entry flight paths with higher degrees of freedom, such as varying the angle of attack during descent, is outside the scope of the present work.

Caveat #3 represents a conservative assumption for low-speed aerodynamic coefficients. It is expected that similar or higher aerodynamic coefficients are achiev-

able with a higher-order evaluation of vehicle aerodynamics at low-supersonic and subsonic speeds. Additionally, the high heating and deceleration conditions occur for hypersonic Mach numbers for which the selected aerodynamics models have been demonstrated to be accurate in Chapter 5.

## 6.1 Entry into Earth's Atmosphere

Four case-study vehicles are considered for comparison in the context of returning from LEO. The common entry interface for 200-400km LEO return is 7.8km/s at 120km altitude [2]. This is the prescribed initial condition for each case in the present study. The first vehicle is a simplified model for the Space Shuttle Orbiter (SSO), with S=250m$^2$, m=100,000kg, and aerodynamic coefficients prescribed along its flight path as reported in [2]. Three morphing waveriders are considered. Each waverider has an identical base design using a 20° conical shock as depicted in 5.7. All acceleration reported is the magnitude due to aerodynamic forces and all heat fluxes are in reference to a cold wall.

The first waverider is given a 250mm leading-edge radius and flown at a constant +25° angle of attack. This vehicle is designed to match the peak stagnation heat flux of the SSO while reducing the other three metrics. The second waverider is given a sharper 10mm leading-edge radius and flown at a constant +8° angle of attack. This vehicle is designed to reach a maximum stagnation-point heat flux equal to the radiation heat flux from a 2,500K wall radiating to 300K Earth. The wall is assigned an emissivity of 0.85, equivalent to that of the SSO windward tiles [2].

This approximation neglects thermal transients and assumes the wall will reach the hot condition of 2,500K. For reference, the maximum transient surface temperature of the SSO is estimated at 2,000K [2]. The third waverider is given a 10mm leading-edge radius and flown at a constant +30° angle of attack in order to minimize stagnation heating for a relatively sharp leading-edge radius. The planform area and mass of all vehicles are identical to the SSO so that any entry condition differences are due solely to the aerodynamic lift and drag coefficients. The waverider aerodynamic coefficients are solved using the WRAITH model from Chapter 2 and morphed as a function of Mach number. The aerodynamic coefficients for the 10mm leading-edge radius at +8° angle-of-attack, for example, are depicted in Fig. 6.1.

Using the results of the entry dynamics model, the SSO nominally produces a peak deceleration of 1g, a peak stagnation heat flux of 60W/cm$^2$ for a hemispherical leading edge of 600mm radius, a maximum average dissipated power of 4.7W/cm$^2$, and a peak dynamic pressure of 6kPa. These results agree with nominal results from more sophisticated models as described in [2]. While it is desirable to minimize peak deceleration, reducing this peak much below 1g has little value for human factors and airframe robustness. The total load factor felt by astronauts and for which the airframe must be designed is the vector sum of Earth gravity and this aerodynamic acceleration, which cannot fall below 1g in combined magnitude and will always include a design factor of safety. Peak dynamic pressure relative to average dynamic pressure is important to minimize in order to maintain consistent controllability without increasing required structural robustness because aerodynamic loading is directly dependent upon dynamic pressure. Dynamic pressures much below 1kPa,

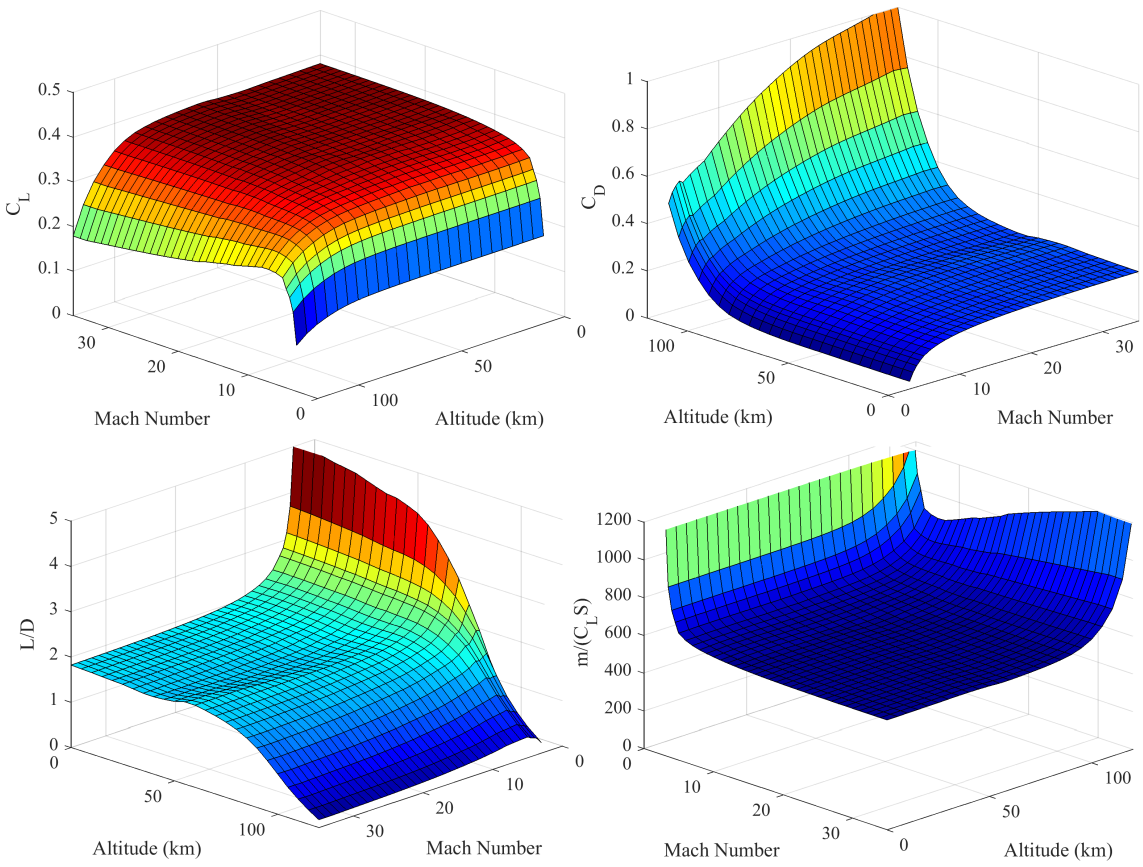


Figure 6.1: Aerodynamic coefficients with altitude and Mach number for the 10mm leading-edge radius morphing waverider fixed at +8° angle of attack. The lift coefficient is consistent below 90km for hypersonic Mach numbers. The drag coefficient decreases steeply with altitude in the laminar flow regime at high altitude. The small increase below 50km at hypersonic Mach numbers indicates the onset of turbulence, which represents a modest effect for this vehicle. The L/D diminishes at high altitude due to strong viscous effects and asymptotes at high speed below 50km, demonstrating Mach-number independence. The entry parameter maintains a consistent value throughout the continuum hypersonic regime. This vehicle's entry parameter is much higher in the low-supersonic or laminar regimes.

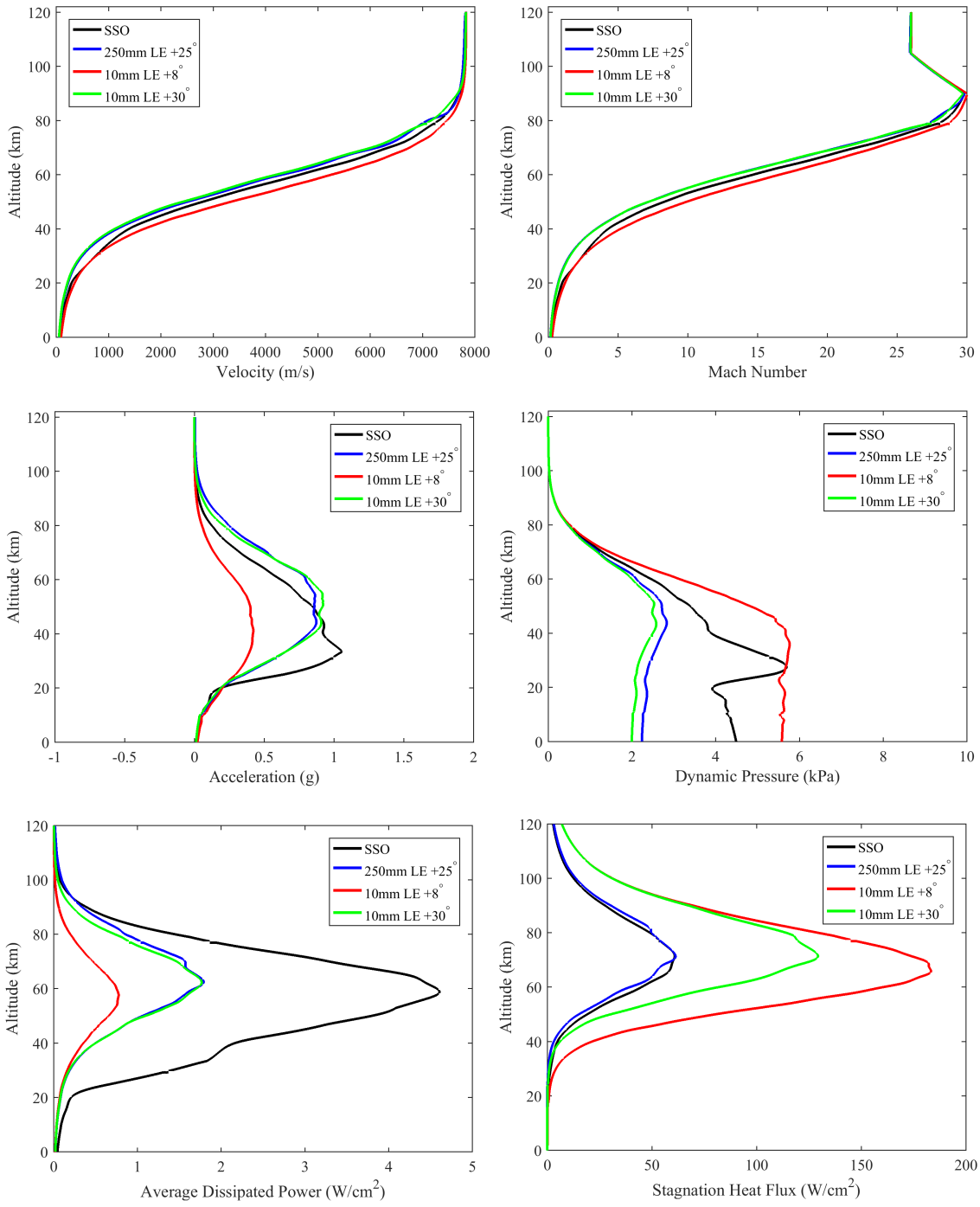


Figure 6.2: Space Shuttle comparison to various morphing waveriders for LEO return. The entry interface is 7.8km/s at 120km. All morphing waveriders have identical base design (Fig. 5.7) with unique leading edge radius and angle of attack.

however, diminish aerodynamic controllability. It is always desirable to fly at higher altitudes for a given speed in order to reduce stagnation heat flux and dissipated power.

The morphing waverider with a 250mm leading-edge radius pitched at a constant +25° was designed to match the maximum stagnation heat flux of the SSO despite having a smaller leading-edge radius. Because of its higher lift coefficient and lower drag coefficient, it glides along a flight path that is higher than the SSO, seen in the velocity-altitude plot of Fig. 6.2. Since heating is proportional to $\rho v^3$, flying at a lower speed for a given density (i.e. altitude) results in approximately the same velocity-based heating despite the sharper leading edge. The maximum average dissipated power is reduced by approximately 60% compared to the SSO for the same velocity-altitude reason. The peak deceleration is slightly reduced compared to the SSO, and the peak dynamic pressure is reduced by approximately 60%.

The morphing waverider with a 10mm leading-edge radius pitched at a constant +8° was designed to reach a maximum stagnation-point heat flux equal to the radiation heat flux from a 2,500K wall. For an assigned emissivity of 0.85, that of SiC at 2,500K [2], this peak value is 188W/cm$^2$. This waverider produces a much lower average drag coefficient than the SSO, but also produces much less lift. Because the SSO produces a higher lift coefficient, this waverider glides along a flight path that is lower than the SSO. Since heating is proportional to $\rho v^3$ and its radius is smaller than the SSO's, this waverider incurs its design peak heat flux of 188W/cm$^2$, higher than the SSO's. The average dissipated power due to this vehicle's lower drag coefficient, however, is approximately 80% less than the SSO.

Similarly, the peak deceleration is reduced by approximately 60% due to the lower drag coefficient. The peak dynamic pressure is found to slightly increase over the SSO, but maintains a consistent value below 60km.

The morphing waverider with a 10mm leading-edge radius pitched at a constant +30° was designed to minimize the peak stagnation heat flux for a relatively sharp leading edge. This waverider produces a lower average drag coefficient than the SSO and also produces more lift. This results in a higher-altitude glide path than the SSO, approximately double the stagnation heating due to its sharper leading edge, lesser maximum average dissipated power due to the lower drag coefficient, slightly lesser peak deceleration, and approximately 60% lesser peak dynamic pressure. The dynamic pressure is consistent below 60km.

While the peak heat flux for the SSO is approximately half that of the 10mm leading-edge morphing waverider with +30° angle of attack, it is important to note that the heat flux occurs over a much smaller area for the waverider, $\propto (10\text{mm}/600\text{mm})^2$, therefore the total integrated leading-edge heat load for the waverider is much less than for the SSO despite the higher peak value. The average dissipated power, which correlates to average and local heat flux, is approximately 1/5th that of the SSO because of the reduced drag coefficient of the waverider.

## 6.2 Entry into Mars' Atmosphere

The waverider used for Mars entry is identical to that used for Earth entry in the present study with a 10mm leading edge radius. The vehicle is compared to the

Mars Science Laboratory (MSL) capsule, using specifications previously provided in Table 2.1. The entry interface for Mars is 150km altitude and 5.6km/s. Unlike Earth entry from LEO, this Mars entry assumes an interplanetary approach path. The circular orbit velocity at 150km for Mars is 3.48km/s compared to the entry interface velocity of 5.6km/s for Earth-to-Mars transit. The aerodynamic braking on the first pass through the atmosphere must reduce the vehicle velocity by at least 2km/s in order to ensure that the vehicle descends to the surface and does not skip out of the atmosphere. Further along the entry trajectory, the lift coefficient is important to prevent the entry vehicle from descending too quickly into denser atmosphere before decelerating. Descending too quickly will result in excessive heating and deceleration.

The MSL capsule initial flight path angle is $-15°$, whereas the waverider initial entry flight path angle is $-9°$. Shallower initial angles can result in skipping out of the atmosphere and re-entering at a dangerously steep angle. Steeper entry angles result in higher peak deceleration and heat fluxes. The MSL capsule relies on a high drag coefficient for "aerocapture" in its initial entry phase. The small lift force produced following aerocapture helps the vehicle glide to the Martian surface with lesser peak deceleration and heating than a pure ballistic entry.

The morphing waverider entry vehicle is captured by aerodynamic forces at $+45°$ initial angle of attack for high drag in its initial aerocapture phase. At some point, the lift generated causes the descending vehicle to rise to a zero flight path angle, marked as point (1) in Fig. 6.4. The vehicle is then pitched downward for zero lift in order to maintain altitude while dissipating kinetic energy until the lift

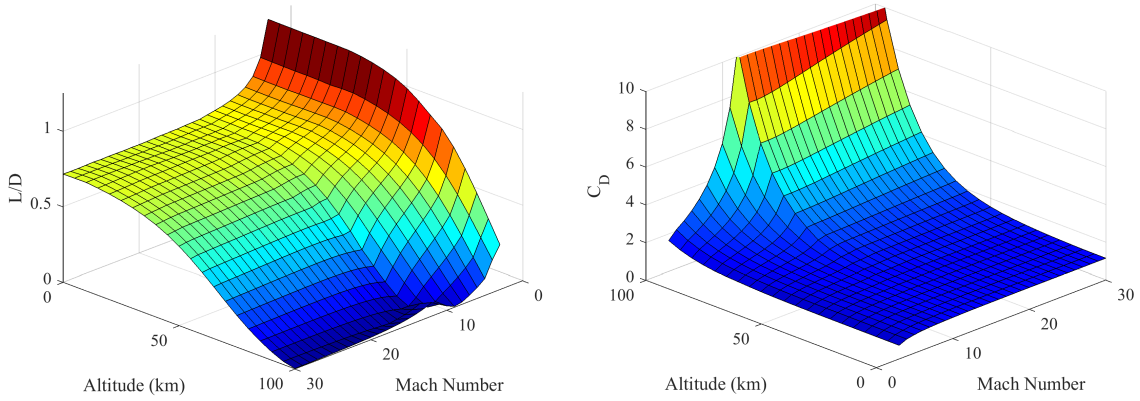


Figure 6.3: Lift-to-drag ratio and drag coefficient across Mach number and altitude for morphing waverider Mars entry vehicle as computed by WRAITH for +30° angle of attack. Mach-number independence can be seen for lift and drag at high Mach number in the continuum regime. Morphing produces a high lift coefficient and low drag coefficient, resulting in a consistent lift-to-drag ratio in the hypersonic continuum regime.

force can no longer support the vehicle's weight, marked as point (2) in Fig. 6.4. Once the vehicle has slowed to the point when its velocity can no longer support its altitude (when centripetal acceleration and lift match Mars' gravity), the angle of attack is adjusted to +30° for the remainder of the entry process, marked as point (3) in Fig. 6.4. The aerodynamic coefficients produced using WRAITH and the COSPAR Mars atmosphere for the morphing waverider at +30° angle of attack are presented in Fig. 6.3 across altitude and Mach number.

The trajectory results are compared in Figs. 6.4 and 6.5. Both vehicles follow the same initial velocity-altitude profile until approximately 80km. The waverider at this point has enough lift at +45° angle of attack to increase its flight path angle

to zero, corresponding to approximately "level flight" referenced to the Martian surface. Its altitude is maintained with centripetal acceleration and aerodynamic lift until decelerating to approximately 3.3km/s. This high-altitude deceleration allows for much of the initial kinetic energy to be dissipated at a very low average rate and while incurring very low stagnation heating due to the low ambient density. The deceleration process lasts approximately 70 minutes. When the vehicle can no longer sustain its own weight through aerodynamic lift alone, it descends with a $+30^{\circ}$ angle of attack, which is a compromise between glide ratio desirable for range or cross-range and the high drag coefficient necessary to decelerate in Mars' low-density atmosphere.

Because the morphing waverider decelerates slowly while retaining high altitude, it incurs approximately 90% lower peak deceleration than the MSL capsule and reaches a low, consistent, controllable dynamic pressure below 50km. The peak dynamic pressure is reduced by approximately 98% compared to the MSL capsule. Decelerating to a slower speed before descending into denser atmosphere and gliding for a longer duration to dissipate the vehicle's initial kinetic energy leads to much more benign heating at lower altitudes. The maximum average dissipated power is reduced by approximately 95% and the stagnation heat flux is reduced by more than 75% compared to the MSL capsule, despite the relatively sharp 10mm leading-edge radius on the waverider. The total "leading-edge heating" for the waverider is along its small leading-edge area, whereas the "leading-edge heating" for the MSL capsule is across its full-diameter heat shield. An important point related to heating is that this non-optimized vehicle with a non-optimized flight path has already

demonstrated the ability to incur a peak stagnation heat flux of 50W/cm$^2$, which is less than the SSO's 60W/cm$^2$ that was managed with reusable heat shield tiles. The SSO's low heat flux did not require an ablative heat shield like the MSL capsule. This implies that a morphing waverider entry vehicle for Mars should be possible without requiring an ablative TPS.

The range and time with altitude are depicted in Fig. 6.5, illustrating the significance of the high-altitude energy dissipation maneuver. Without lateral maneuvers, the morphing waverider travels approximately 20 times further than the MSL capsule. Since the vehicle has a lift vector and excess energy during its high-altitude dissipation maneuver, the vehicle may use some of this "energy budget" for cross-range maneuvering or course correction.

The case study interplanetary mission into Mars' atmosphere is distinctly challenging compared to LEO return because the process requires both a high-drag aerocapture maneuver as well as a high-lift descent through a very sparse atmosphere. Even with the significant advantages illustrated by the high-lift vehicle used in this comparison, the morphing waverider reaches the surface with a residual supersonic speed of 288m/s (Mach 1.2) at a flight path angle of $-25.1°$. While this is less than the 450m/s (Mach 1.9) of a purely-gliding MSL capsule, it illustrates the necessity of auxiliary deceleration and touch-down mechanisms in the Martian atmosphere.

The inability of high-lift and high-L/D vehicles to decelerate to safe touch-down speeds under aerodynamic forces alone is known in the Mars Entry, Descent, and Landing (EDL) community as the *supersonic decelerator problem* [171]. This case study vehicle simplifies the problem in comparison to the capsule, however, by

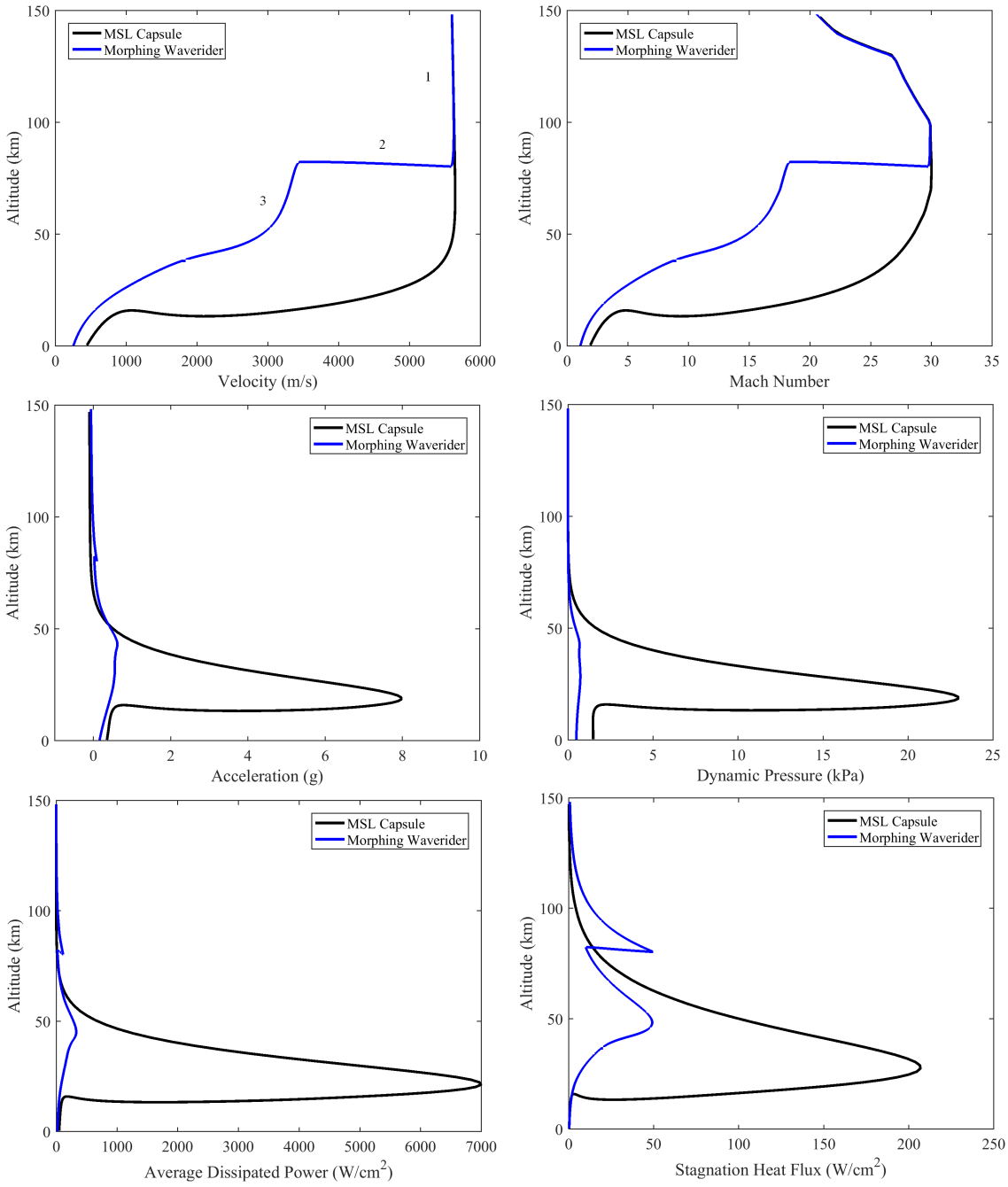


Figure 6.4: Entry profiles for the MSL capsule and a morphing waverider for an Earth-to-Mars mission. The entry interface is 5.6km/s at 150km. Both vehicles have identical reference area (15.9m$^2$) and mass (3380kg).

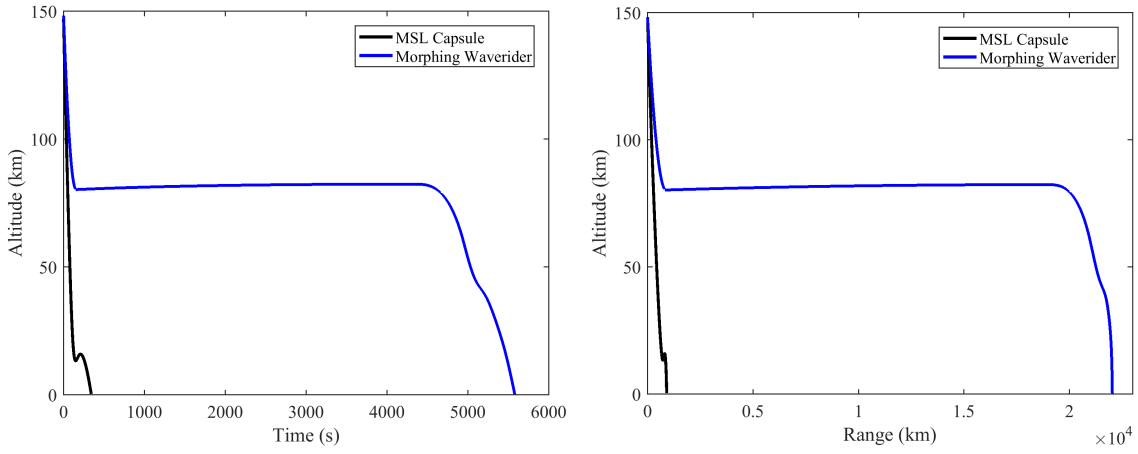


Figure 6.5: Entry profiles for range and time for the MSL capsule and a morphing waverider for an Earth-to-Mars mission. The high-altitude energy dissipation maneuver is what allows the morphing waverider to incur much less area-averaged heating, stagnation heating, and peak deceleration than the MSL capsule. This maneuver is enabled by the morphing waverider's high lift coefficient.

reaching the surface with 60% less kinetic energy to dissipate with non-aerodynamic mechanisms.

## 6.3 Summary

Three low-drag morphing waveriders were simulated entering Earth's atmosphere from LEO that demonstrated improvements in performance metrics over the SSO. These vehicles used a fixed angle-of-attack and a non-optimized flight path. It was demonstrated that a morphing waverider can achieve some combination of a 60% reduction in peak deceleration, a 60% reduction in peak dynamic pressure, or an 80% reduction in maximum area-averaged dissipated power. The vehicles considered did not produce less stagnation heat flux than the SSO due to their much smaller leading-edge radii.

One of the Earth-entry waveriders with a 10mm leading-edge radius was compared to the MSL capsule in the context of an interplanetary mission from Earth to Mars. The high lift and low drag of the morphing waverider produced approximately a 75% reduction in peak stagnation heat flux, a 90% reduction in peak deceleration, and a 95% reduction in peak area-averaged heating compared to the MSL entry capsule.

# Chapter 7: Conclusion

The conclusion chapter summarizes the efforts of this work and the resulting insights gained. The caveats and limitations of the models used and case studies presented are discussed in the following section. This dissertation's unique contributions are then highlighted, primarily demonstrating that the morphing waverider entry vehicle concept has potential and merits further investigation. The chapter closes with recommendations for future work.

## 7.1 Summary

The purpose of this work was to evaluate the potential of morphing waveriders as high-lift entry vehicles. In order to accomplish this evaluation, the author had to assemble, integrate, or develop specialized tools. These tools span analytical and numerical methods, planetary entry dynamics, hypersonic aerodynamics, aerothermodynamics, computational fluid dynamics, and reactive flow.

The key questions were 1) Is there an advantage to morphing a waverider across the wide range of entry speeds? It was demonstrated in Section 5.4 that a morphing waverider can produce a consistent lift-to-drag ratio across a wide range of speeds relevant for atmospheric entry while the performance of a rigid waverider

degrades away from its design point. For the case study vehicles evaluated, the morphing waverider could outperform the rigid waverider by up to 2-3 times at high Mach number.

The second key question was 2) Can a morphing waverider out-perform a lifting capsule on Mars or the Space Shuttle on Earth? It was demonstrated in Section 6.1 that a morphing waverider can enable a flight path with up to 60% less peak deceleration and dynamic pressure and up to 80% less peak area-averaged heating than the Space Shuttle returning from LEO. It was demonstrated in Section 6.2 that a high-lift morphing waverider can reduce the maximum area-averaged heating by 95% compared to the Mars Science Laboratory entry capsule. It can reduce the stagnation heating by more than 75%, the peak dynamic pressure by 98%, reduce the peak deceleration by 90%.

In order to arrive at these answers, the author used the following strategy. First, appropriate models and methods were selected and implemented for entry dynamics, hypersonic aerodynamics, construction of hypersonic waveriders, geometry modification, and the numerical simulation of turbulent flow and laminar, reactive flow. Second, the models were evaluated in comparison to one another in order to determine the accuracy of the reduced-order models. With sufficient confidence gained in the morphing-waverider aerodynamic property estimates, parametric evaluation of the model was used to characterize the effects of varied angle of attack, Mach number, leading-edge bluntness, wall temperature, and altitude. It was demonstrated that a morphing waverider enables a higher lift-to-drag ratio than a rigid waverider across a wide range of Mach number. The deflection and strain required to morph

a case study vehicle was reported, resulting in base-plane strain spanning ±0.15% across Mach 5 to 40. Finally, entry simulations were conducted for the morphing waveriders.

Reduced-order models for waverider aerodynamics have been previously developed, e.g. [72,85]. However, the accuracy of each specific analytical method used in each flow context had not previously been characterized. It was found that analytical methods for waverider aerodynamics at their design Mach number and varied angle-of-attack matched numerical simulations generally to within 5-10%. The accuracy of the WRAITH model was heavily dependent upon the analytical model chosen for each surface in each flight configuration. As the flight Mach number is varied away from the design Mach number, the discrepancy between analytical and CFD results grew to more than 20%. It is therefore recommended that these methods be used for on-design Mach number and variations in angle of attack, but not for rigid waveriders at Mach numbers far from their design points.

## 7.2 Unique Contributions

The unique contributions of this work to understanding hypersonic waverider aerodynamics in entry-relevant flows are discussed in the following section. The two primary contributions are 1) the author characterized the accuracy of analytical methods for hypersonic aerodynamics in comparison to numerical methods in the context of atmospheric entry. 2) The author demonstrated that morphing waveriders can lead to more benign entry conditions than classical lifting capsules or the SSO

and that the enabling mechanism is the low drag that waveriders incur.

The complete contributions of this work are itemized in the following list. The author specifically:

- Developed a reduced-order model for off-design viscous waverider aerodynamics, verified and validated against turbulent CFD, for varied angle-of-attack and Mach number
- Developed a leading-edge blunting method that preserves the planform and better preserves the approximation of an attached design shock
- Characterized the effect of off-design Mach number on the aerodynamic coefficients using CFD
- Characterized the effect of off-design orientation on the aerodynamic coefficients and dynamic stability using CFD
- Added heating correlations and the effect of a finite-thickness leading edge to waverider reduced-order aerodynamics model
- Demonstrated useful accuracy of a waverider reduced-order aerodynamics model when correlated to viscous CFD
- Proposed a method for estimating the base pressure, justified with CFD and existing empirical studies
- Proposed a method for estimating the base temperature using the proposed base-pressure model

- Proposed a waverider construction method that retains the attachment of a design shock and the design flow field across a wide range of Mach numbers when the lower surface is morphed to conform to the design flow field's stream surface emanating from the leading edge

- Proposed waverider construction guidelines that minimize morphing strain and demonstrated that this strain can be minimized below the linear elastic limit of 2% while retaining useful L/D across a wide range of Mach number

- Numerically demonstrated that a morphing waverider can achieve a higher lift-to-drag ratio than rigid waveriders across a wide range of Mach number

- Demonstrated the importance of entry-vehicle stability by demonstrating the inherent instability of a case-study waverider

- Numerically demonstrated that a morphing waverider can achieve more benign entry conditions for Earth and Mars than existing capsules and lifting vehicles by means of improved aerodynamics

## 7.3 Recommended Future Work

The recommended future work can be separated into two categories: near-term specific recommendations to continue the present study, and more general, long-term topics to investigate in order to aid the overall development of practical morphing waveriders. This includes evaluating rigid waveriders, optimization of morphing waveriders, materials and structural considerations, rarefied flow analysis,

and ascent vehicles. Each topic is briefly discussed below.

In the near-term, rigid waveriders should be evaluated as entry vehicles. They were omitted in the present work because the off-design Mach number estimates from WRAITH produced errors greater than 10% in the lift-to-drag ratio a few Mach numbers away from the design point (see Fig. 4.14) and 12-18% error in the lift and drag for the high-altitude reactive flow (see Table 5.6). The WRAITH model produced net lift and drag forces within a few percent of the CFD results for on-design aerodynamics and variation in angle of attack, but accuracy degrades for off-design Mach number.

The most straightforward extension of this work is to use the same tools for the optimization of morphing waverider entry vehicles and their flight paths. The case studies presented were the result of iterative design by the author, but may be far from optimal. The recommended cost function components are weighted aerodynamic performance, peak and average heating, peak deceleration, payload volume, range of deflection and strain, controllability, and sensitivity.

While the present study found advantages for morphing over conventional entry vehicles, the complexities associated with morphing have yet to be evaluated. This merits an investigation into the material, structure, and control requirements to morph a waverider in this context. The temperatures and heat fluxes described in Chapter 6 and the deflection and strain described in Section 5.4 provide initial guidelines.

The current study treated the morphing waveriders as monolithic, idealized aeroshells without internal detail. It is recommended that a more detailed design of

an entry vehicle be performed in order to characterize a practical inert mass fraction, payload fraction, and morphing system mass fraction. A reduced-order model may also be formulated for transient thermal simulations by using point-masses for components, prescribed conductances between components, and the heating already computed by WRAITH for each surface.

Another consideration is that of rarefied flow at high altitude. While the case was made to neglect rarefied flow in the present analysis, the accurate flight path prediction for a practical vehicle will necessitate a higher degree of accuracy. This will require analysis of rarefied flow. Additionally, as higher-performance vehicles are engineered for dynamics and maneuvers at higher altitudes, the rarefied flow regime may become just as critical as the continuum flow regime.

The final topic is related to ascent vehicles. The present study considered using waveriders as high-lift entry vehicles, but this is only half of the space-access challenge. Is there an efficiency advantage for high-lift ascent vehicles? What if they implement airbreathing propulsion, at least for part of their ascent? The hope of the author is that this work represents the first of a series of investigations into maximizing the use of the incredible features of hypersonic waveriders.

# Bibliography


[1] Anderson, J.D., *Introduction to Flight*, 6th ed, McGraw-Hill, NY, 2008.

[2] Hirschel, E.H., Weiland, C., *Selected Aerothermodynamics Design Problems of Hypersonic Flight Vehicles*, AIAA, 2009.

[3] Anderson, J.D., Jr., *Modern Compressible Flow*, 3rd Ed., NY: McGraw-Hill, 2002. ISBN: 978-0072424430

[4] Anderson, J.D., Jr., *Hypersonic and High Temperature Gas Dynamics*. NY: McGraw-Hill, 1989, pp. 60, 61-63, 203, 266.

[5] Bird, G.A., *Molecular Gas Dynamics and the Direct Simulation of Gas Flows*. New York: Oxford University Press, Inc., 2003.

[6] Bird, G.A., *Molecular Gas Dynamics and the Direct Simulation of Gas Flows*, Oxford University Press, New York, 1994.

[7] Graves, R.E. and Argrow, B.M., "Aerodynamic performance of an osculating-cones waverider at high altitudes," 35th AIAA Thermophysics Conference, Fluid Dynamics and Co-located Conferences, 2001. https://doi.org/10.2514/6.2001-2960

[8] Maxwell, J.R., "Supersonic Wind Tunnel with Rarefied Flow," *Proceedings of the 31st Rarefied Gas Dynamics Symposium*, Glasgow, UK, 2018.

[9] Galitzine, C. and Boyd, I.D., "An analysis of the convergence of the direct simulation Monte Carlo method," *Journal of Computational Physics*, Vol. 289, 2015; doi:10.1016/j.jcp.2015.02.039

[10] Dietrich, S., Boyd, I.D., "Scalar and Parallel Optimized Implementation of the Direct Simulation Monte Carlo Method," *Journal of Computational Physics*, Vol 126, No. 2, 1996. https://doi.org/10.1006/jcph.1996.0141.

[11] Bird, G. A., "Monte Carlo Simulation in an Engineering Context," Rarefied Gas Dynamics, edited by S. S. Fisher, Vol. 74 of *Progress in Astronautics and Aeronautics*, AIAA, New York, 1981, pp. 239–255.

[12] Boyd, I.D., "Scalar and Parallel Optimized Implementation of the Direct Simulation Monte Carlo Method," *Journal of Computational Physics*, Vol. 126 No. 2, pg. 328-342, 1996.

[13] *U.S. Standard Atmosphere, 1976*, U.S. Government Printing Office, Washington, D.C., 1976.

[14] Pitts, D.E., et al., *The Mars Atmosphere: Observations and model Profiles for Mars Missions*, NASA JSC-24455, 1990.

[15] Justus, C.G., James, B.F., Johnson, D.L., *Mars Global Reference Atmospheric Model*, NASA TM 108509, 1996.

[16] Picone, J.M.; Hedin, A.E.; Drob, D.P.; Aikin, A.C. (2002-12-01). "NRLMSISE-00 empirical model of the atmosphere: Statistical comparisons and scientific issues". *Journal of Geophysical Research: Space Physics*. 107 (A12): 1468. doi:10.1029/2002JA009430. ISSN 2156-2202.

[17] *Global Climatic Data for Developing Military Products (MIL-STD-210C)*, 9 January 1987, Department of Defense, Washington, D.C.

[18] Rycroft, M.J., Keating, G.M., Rees, D., (eds.), "Upper Atmosphere Models and Research," *Adv. Space Res. 10*, No. 6, 1990.

[19] Frawley, G., *The International Directory of Civil Aircraft*, Aerospace Publications, 2003. ISBN 978-1-875671-58-8.

[20] Suhler, P.A. *From RAINBOW to GUSTO: Stealth and the Design of the Lockheed Blackbird (Library of Flight Series)*, AIAA, 2009. ISBN 978-1-60086-712-5.

[21] The Boeing Company, "X-51A Waverider Background" Archived September 6, 2012, at the Wayback Machine.. Boeing, September 2012. Retrieved August 20, 2017. https://web.archive.org/web/20120906233323/http://www.boeing.com/defense-space/military/waverider/docs/X-51A_overview.pdf

[22] Jenkins, D., *X-15: Extending The Frontiers of Flight*, 2010. ISBN 978-1470025854.

[23] Voland, R.T., Huebner, L.D., and McClinton, C.R., "X-43A Hypersonic vehicle technology development," Acta Astronautica, Vol. 59, No. 1–5, p. 181–191, 2006.

[24] Thompson, E., Henry, K. and Williams, L. "Faster Than a Speeding Bullet: Guinness Recognizes NASA Scramjet." NASA Press Release, June 20, 2005. Retrieved: August 20, 2017. https://www.nasa.gov/home/hqnews/2005/jun/HQ_05_156_X43A_Guinness.html

[25] Heiser, W.H., Pratt, D.T., *Hypersonic Airbreathing Propulsion*, AIAA, Washington D.C., 1994.

[26] Kasen, S.D., *Thermal Management at Hypersonic Leading Edges*, Dissertation, University of Virginia, 2013.

[27] *Machinery's Handbook*, 28th ed., Industrial Press, NY, 2008.

[28] McMaster-Carr Company Website, https://www.mcmaster.com/aluminum, retrieved 6/18/2017

[29] McMaster-Carr Company Website, https://www.mcmaster.com/titanium, retrieved 6/18/2017

[30] McMaster-Carr Company Website, https://www.mcmaster.com/tungsten, retrieved 6/18/2017

[31] Rare World Metals Mint Company Website, https://www.rwmmint.com/collections/all, retrieved 6/18/2017

[32] Shepard, Jr., Alan B.; Slayton, Deke; Barbree, Jay; Benedict, Howard (1994). *Moon Shot: The Inside Story of America's Race to the Moon,* 1st Ed., Kansas City, MO: Turner. p. 356

[33] Hillje, E.R., *Entry Aerodynamics at Lunar Return Conditions Obtained from the Flight of Apollo 4 (AS-501)*, NASA TN D-5399, (1969). Pg. 356.

[34] Regan, F.J. and Anandakrishnan, S.M., *Dynamics of Atmospheric Re-entry*, Washington DC: AIAA, Inc., 1993.

[35] Whittington, K.T., *A Tool to Extrapolate Thermal Reentry Atmosphere Parameters Along a Body in Trajectory Space*. NCSU Libraries Technical Reports Repository. M.S. Thesis, North Carolina State University, 2011.

[36] Apollo, 1972 – *Apollo Program Flight Summary Report*, NASA, June 1972.

[37] NASA CP 2342-Part-1, *Space Shuttle Technical Conference* pg 258, 1983.

[38] "Ascent Timeline and Abort Boundaries - STS-135". *Spaceflight Now*. Retrieved February 2015.

[39] Hillje, Ernest R., *Entry Aerodynamics at Lunar Return Conditions Obtained from the Flight of Apollo 4 (AS-501),* NASA TN D-5399, (1969). Pg. 315

[40] *CSM06 Command Module Overview*, pp 39 - 52. National Aeronautics and Space Administration. Retrieved November 1, 2016.

[41] Wilhite, A.W., *Analysis of Separation of the Space Shuttle Orbiter from a Large Transport Airplane*, NASA TM X-3492, June 1977

[42] Woodcock, Gordon R. (1986). *Space stations and platforms*. Orbit Book Co. ISBN 9780894640018

[43] Maxwell, J.R., "Shapeable Hypersonic Waverider Entry Vehicles," 53rd AIAA/SAE/ASEE Joint Propulsion Conference, AIAA Propulsion and Energy Forum, (AIAA 2017-4880) https://doi.org/10.2514/6.2017-4880

[44] Hirschel, E.H., *Selected Aerothermodynamic Design Problems of Hypersonic Flight Vehicles*, Springer, Berlin, 2009

[45] Tauber, M.E., *Atmospheric Trajectories*. Chapter AA213 Atmospheric Entry. NASA/Ames Research Center, Stanford University, 1990.

[46] Reynolds, O., "On the Dynamical Theory of Incompressible Viscous Fluids and the Determination of the Criterion," *Philosophical Transactions of the Royal Society of London. A*, Vol. 186, pp. 123-164, 1895.

[47] Chapman, D.R., *An Approximate Analytical Method for Studying Entry into Planetary Atmospheres*, NACA TN-4276, May 1958

[48] Nonweiler, T.R.F., "Aerodynamic Problems of Manned Space Vehicles," *Journal of the Royal Aeronautical Society*, Vol. 63, pg. 521-528, 1959.

[49] Mundy, J.A., *The effects of viscosity on a conically-derived waverider*, Master's Thesis, Air Force Institute of Technology, 1992.

[50] Rasmussen, M.L., Brandes-Dunkam, B., "Hypersonic waveriders generated from power-law shocks," International Space Planes and Hypersonic Systems and Technologies Conferences, 1995. https://doi.org/10.2514/6.1995-6160

[51] McCoy, R.L., *Modern Exterior Ballistics: The Launch and Flight Dynamics of Symmetric Projectiles*, Schiffer Publishing, Ltd., Atglen, PA, 1999.

[52] Anderson, J.D., *Fundamentals of Aerodynamics*, 5th ed, McGraw-Hill, NY, 2010.

[53] Greenwood, D.T., *Principles of Dynamics*, Prentice-Hall, 1988.

[54] Regan, F.J., *Re-Entry Vehicle Dynamics*. AIAA Education Series, American Institute of Aeronautics and Astronautics, Washington, DC, 1984.

[55] Chernyi, G.G., translated and edited by Probstein, R.F., *Introduction to Hypersonic Flow*, Academic Press, NY, 1961.

[56] Bate, R.R., Mueller, D.D., White, J.E. *Fundamentals of Astrodynamics*, Dover, 1971.

[57] Cessna Aircraft Company, *Cessna Aircraft Company Information Manual: 1981 Model 172P*, Wichita, KS, 1980.

[58] Nonweiler, T.R.F., "Delta Waves of Shape Amenable to Exact Shock Wave Theory," *Journal of Royal Aeronautical Society*, Vol. 67, pg. 39, 1963.

[59] Maccoll, J.W., "The Conical Shock Wave Formed by a Cone Moving at a High Speed," *Proceedings of the Royal Society of London. Series A, Mathematical and Physical Sciences*, Vol. 159, No. 898, pp. 459-472, 1937.

[60] Taylor, G.I., Maccoll, J.W., "The air pressure on a cone moving at high speed," *Proceedings of the Royal Society of London A: Mathematical, Physical and Engineering Sciences* 139 (838) (1933) 278-311.

[61] Jones, J.G., "A Method for Designing Lifting Configurations for Highersonic dec Supersonic Speeds Using the Flow Fields of Non-Lifting Cones," Royal Aircraft Establishment, Report No. Aero. 2674, March 1963.

[62] Zien, T.F., *A Class of Three-Dimensional Optimum Wings in Hypersonic Flow*, Ph.D dissertation, May 1967, California Institute of Technology, Pasadena, CA.

[63] Cole, J.D., Zien, T.F., "A class of three-dimensional, optimum hypersonic wings," *AIAA Journal*, Vol. 7, No. 2 (1969), pp. 264-271.

[64] Pike, J., "A design method for aircraft basic shapes with fully attached shock waves using known axisymmetric flow fields," R.A.E. Technical Report No. 66069, 1966.

[65] Pike, J., "Experimental Results from Three Cone-Flow Waveriders," Agard Conference Proceedings 30, Hypersonic Boundary Layers and Flow Fields, Royal Aeronautical Society, London, Ref. 12, p. 20, 1-3 May 1968.

[66] Moore, K.C., "The application of known flow fields to the design of wings with lifting upper surfaces at high supersonic speeds," R.A.E. Technical Report No. 65034, 1965.

[67] Kim, B. S., Rasmussen, M. L., and Jischke, Mo C., "Optimization of Waverider Configuration Generated from Axisymmetric Conical Flows," *Journal of Spacecraft and Rockets*, Vol. 20, No. 5, pp. 461-469, 1983.

[68] Rasmussen, M. "Waverider Configurations Derived from Inclined Circular and Elliptic Cones," *Journal of Spacecraft and Rockets*, Vol. 17, No. 6 (1980), pp. 537-545

[69] Rasmussen, M.L., Clement, L.W., "Cone-derived waveriders with longitudinal curvature," *Journal of Spacecraft and Rockets*, Vol. 23, No. 5 (1986), pp. 461-469. https://doi.org/10.2514/3.25830

[70] Hemdan, H.T., "Waverider configurations according to thin shock-layer theory," *Acta Astronautica*, Volume 21, Issue 8, 1990, Pages 571-582, ISSN 0094-5765, https://doi.org/10.1016/0094-5765(90)90084-X.

[71] Bowcutt, K.G., Anderson, J.D., Jr., Capriotti, D. "Viscous Optimized Hypersonic Waveriders," AIAA Paper No. 87-0272, 1987.

[72] Bowcutt, K.G., *Viscous Optimized Hypersonic Waveriders*, Dissertation, University of Maryland, College Park, 1986.

[73] Jones, K., Dougherty, F., Seebass, A., and Sobieczky, H. "Waverider design for generalized shock geometries," 31st Aerospace Sciences Meeting, 1993.

[74] Jones, K.D., Sobieczky, H., Seebass, A.R., Dougherty, F.C., "Waverider design for generalized shock geometries," *Journal of Spacecraft and Rockets*, Vol. 32, No. 6 (1995), pp. 957-963. https://doi.org/10.2514/3.26715

[75] Corda, S., Anderson, J.D., Jr., "Viscous Optimized Waveriders Designed from Axisymmetric Flow Fields," AIAA Paper 88-0369, 1988.

[76] Golubkin, V.N., "Lifting wings of optimum shape in a viscous hypersonic stream," *Fluid Dynamics*, Vol. 30, p. 934, 1995. https://doi.org/10.1007/BF02078211

[77] Kothari, A., Tarpley, C., McLaughlin, T., Babu, B., Livingston, J., "Hypersonic vehicle design using inward turning flow fields," 32nd Joint Propulsion Conference and Exhibit, 1996. https://doi.org/10.2514/6.1996-2552

[78] Goonko, Y.P., Mazhul, I.I., Markelov, G.N., "Convergent-Flow-Derived Waveriders," *Journal of Aircraft*, Vol. 37, No. 4 (2000), pp. 647-654. https://doi.org/10.2514/2.2647

[79] Yu, P.G., Mazhul, I.I., and Markelov, G.N., "Convergent-Flow-Derived Waveriders," *Journal of Aircraft*, Vol. 37, No. 4 (2000), pp. 647-654. https://doi.org/10.2514/2.2647

[80] Billig, F.S., Kothari, A.P., "Streamline Tracing: Technique for Designing Hypersonic Vehicles," *Journal of Propulsion and Power*, Vol. 16, No. 3 (2000), pp. 465-471. https://doi.org/10.2514/2.5591

[81] Starkey, R.P., Lewis, M.J., "Simple Analytical Model for Parametric Studies of Hypersonic Waveriders," *Journal of Spacecraft and Rockets*, Vol. 36, No. 4, Jul-Aug 1999.

[82] Starkey, R.P., Lewis, M.J., "Analytical Off-Design Lift-to-Drag-Ratio Analysis for Hypersonic Waveriders," *Journal of Spacecraft and Rockets*, Vol. 37, No. 5, Sep-Oct 2000.

[83] Sobieczky, H., Dougherty, F.C., Jones, K. "Hypersonic Waverider Design from Given Shock Waves," Proc. 1st Int. Hypersonic Waverider Symposium, Univ. of Maryland, 1991.

[84] Mill, R.W., Argrow, B.M., Center, K.B., Brauckmann, G.J., and Rhode, M.N., "Experimental Verification of the Osculating Cones Method for Two Waverider Forebodies At Mach 4 and 6," AIAA Paper 98-0682, 36th Aerospace Sciences Meeting, Reno, NV, 1998.

[85] Rodi, P.E., "The Osculating Flowfield Method of Waverider Geometry Generation," Paper AIAA-2005-511, 2005.

[86] Rodi, P.E., Genovesi, D., "Engineering-Based Performance Comparisons Between Osculating Cone and Osculating Flowfield Waveriders," AIAA Paper No. 2007-4344, 2007. https://doi.org/10.2514/6.2007-4344

[87] Rodi, P.E., "Expanding the Osculating Flowfield Waverider Method Beyond Power Law Body Induced Flowfields," AIAA Paper No. 2018-3817, 2018. https://doi.org/10.2514/6.2018-3817

[88] Rodi, P.E., "Waverider Vehicle Optimization with Volumetric Constraints for Wave Drag Minimization," AIAA Paper No. 2018-1048, 2018. https://doi.org/10.2514/6.2018-1048

[89] Rodi, P.E. "Osculating Flowfield Waveriders Designed to Maximize Boundary Layer Stability: Preliminary 2D Concepts", AIAA Paper No. 2013-0828, 2013. https://doi.org/10.2514/6.2013-828

[90] Rodi, P.E., "On Using Upper Surface Shaping to Improve Waverider Performance," AIAA Paper No. 2018-0554, 2018. https://doi.org/10.2514/6.2018-0554

[91] Rodi, P.E., "Optimization of Bezier Curves for High Speed Leading Edge Geometries," AIAA Papaer No. 2013-1004, 2013. https://doi.org/10.2514/6.2013-1004

[92] Rodi, P.E., "Integration of Optimized Leading Edge Geometries Onto Waverider Configurations," AIAA Paper No. 2015-1700, 2015. https://doi.org/10.2514/6.2015-1700

[93] Rodi, P.E., "Waverider Vehicle Optimization with Volumetric Constraints for Sonic Boom," AIAA Paper No. 2018-0551, 2018. https://doi.org/10.2514/6.2018-0551

[94] Jones, K.D., and Center, K.B., "Waverider Design Methods for Non-Conical Shock Geometries," AIAA Paper 2002-3204, 3rd Theoretical Fluid Mechanics Meeting, St. Louis, MO, 2002.

[95] Ferguson, F. and Anderson Jr., J. D., "Expanding the Waverider Design Space Using General Supersonic and Hypersonic Generating Flows," 31st AIAA Aerospace Sciences Meeting and Exhibit, AIAA Paper No. 93-0505, Jan. 1993.

[96] Center, K.B., Sobieczky, H. and Dougherty, F.C., "Interactive Design of Hypersonic Waverider Geometries," AIAA Paper 91-1697, AIAA 22nd Fluid Dynamics, Plasma Dynamics and Lasers Conference, Honolulu, HI, June 1991.

[97] Santos, W.F.N., "Bluntness impact on lift-to-drag ratio of hypersonic wedge flow," *Journal of Spacecraft and Rockets* 2009; 46(2):329–39.

[98] Santos, W., "Bluntness Effects on Lift-to-Drag Ratio of Leading Edges for Hypersonic Waverider Configurations," 18th AIAA/3AF International Space Planes and Hypersonic Systems and Technologies Conference, 2011. https://doi.org/10.2514/6.2012-5802

[99] Norris, J.D., "Mach 8 high Reynolds number static stability capability extension using a hypersonic waverider at AEDC tunnel 9," AIAA Paper No. 2006-2815; 2006.

[100] Miller, R. W., Argrow, B. M., Center, K. B., Brauckmann, G. J., and Rhode, M. N., "Experimental Verification of the Osculating Cones Method for Two Waverider Forebodies at Mach 4 and 6," 36th AIAA Aerospace Sciences Meeting and Exhibit, AIAA Paper No. 98-0682, Jan. 1998.

[101] Vanmol, D.O. "Heat transfer characteristics of hypersonic waverider with emphasis on the leading edge effects," Master's Thesis, University of Maryland, College Park, 1991.

[102] Vanmol, D.O., Anderson, J.D., "Heat transfer characteristics of hypersonic waveriders with an emphasis on leading edge effects," AIAA Paper No. 92-2920; 1992.

[103] Santos, W.F.N., Lewis, M.J., "Aerothermodynamic Performance Analysis of Hypersonic Flow on Power Law Leading Edges", *Journal of Spacecraft and Rockets*, Vol. 42, No. 4 (2005), pp. 588-597. https://doi.org/10.2514/1.9550

[104] Hinman, W.S., Johansen, C.T., Rodi, P.E., "Optimization and analysis of hypersonic leading edge geometries," *Aerospace Science and Technology*, 70:549-558, 2017. https://doi.org/10.1016/j.ast.2017.08.034.

[105] Long, L.N. "Off-design performance of hypersonic waveriders," *Journal of Aircraft*, Vol. 27, No. 7 (1990), pp. 639-646. https://doi.org/10.2514/3.25334

[106] Jones, K.D., Dougherty, F.C., "Numerical simulations of high-speed flows about waveriders with sharp leading edges," *Journal of Spacecraft and Rockets*, Vol. 29, No. 5 (1992), pp. 661-667. https://doi.org/10.2514/3.11507

[107] Takashima, N., *Navier-Stokes computations of a viscous-optimized waverider*, Thesis, University of Maryland, College Park, 1992.

[108] Takashima, N., and Lewis, M.J., "Navier-Stokes computation of a viscous optimized waverider," *Journal of Spacecraft and Rockets*, Vol. 31, No. 3 (1994), pp. 383-391. https://doi.org/10.2514/3.26450

[109] Liao, J.R., Isaac, K.M., Miles, J.B., Tsai, B.J., "Navier-Stokes simulation for cone-derived waverider," *AIAA Journal*, Vol. 30, No. 6 (1992), pp. 1521-1528. https://doi.org/10.2514/3.11096

[110] He, X., Rasmussen, M.L., "Computational analysis of off-design waveriders," *Journal of Aircraft*, Vol. 31, No. 2 (1994), pp. 345-353. https://doi.org/10.2514/3.46493

[111] Jackson, K., Dwayne, J., "CFD analysis of a generic waverider," AIAA Paper No. 2006-2817; 2006.

[112] Shi, Y., Tsai, B.J., Miles, J.B., Isaac, K.M., "Cone-derived waverider flowfield simulation including turbulence and off-design conditions," *Journal of Spacecraft and Rockets*, Vol. 33, No. 2 (1996), pp. 185-190. https://doi.org/10.2514/3.26739

[113] Shi, Y., Miles, J.B., Isaac, K.M., "Computational Fluid Dynamics Simulation of Turbulent Waverider Flowfield with Sideslip," *Journal of Spacecraft and Rockets*, Vol. 34, No. 1 (1997), pp. 76-84.

[114] Todd, S., Richard, M., "Computational hypervelocity aerodynamics of a caret waverider," AIAA Paper No. 2004-3848; 2004.

[115] Jones, K.D., Bauer, S.X.S., Dougherty, F.C., "Hypersonic Waverider Analysis: A Comparison of Numerical and Experimental Results," AIAA Paper No. 91-1696, 1991.

[116] Jischke, M.C., Rasmussen, M.L., Daniel, D.C. "Experimental surface pressures on cone-derived waveriders for freestream M = 3-5", *Journal of Spacecraft and Rockets*, Vol. 20, No. 6 (1983), pp. 539-545. https://doi.org/10.2514/3.8584

[117] Chen, X.Q., Hou, Z.X., Liu, J.X., Gao, X.Z., "Bluntness impact on performance of waverider," *Computers & Fluids,*, 48:1, pg 30-43, 2011, https://doi.org/10.1016/j.compfluid.2011.03.011.

[118] Li, S., Wang, Z., Huang, W., Xu, S., Yan, L., "Aerodynamic performance investigation on waverider with variable blunt radius in

hypersonic flows," *Acta Astronautica*, Vol 137, pg. 362-372, 2017. https://doi.org/10.1016/j.actaastro.2017.05.001

[119] Graves, R. E., *Aerodynamic Performance of Osculating-Cones Waveriders at High Altitudes*, Dissertation, Department of Aerospace Engineering Sciences, University of Colorado, Aug. 1999.

[120] Corda, S., "Star-body waveriders with multiple design Mach numbers," *Journal of Spacecraft Rockets*, 46(6):1178–85, 2009. https://arc.aiaa.org/doi/pdf/10.2514/1.43933

[121] Bowcutt, K.G., The Boeing Company, Chicago, IL, U.S. Patent for "Hypersonic Waverider Variable Leading Edge Flaps," No. 6,634,594 B1, filed 3 May, 2002.

[122] S.B. Li, S.B. Luo, W. Huang, Z.G. Wang. "Influence of the connection section on the aerodynamic performance of the tandem waverider in a wide-speed range." *Aerospace Science and Technology*, 2013, 30: 50-65.

[123] Liu, J., Ding, F., Huang, W., Jin, L., "Novel approach for designing a hypersonic gliding-cruising dual waverider vehicle," *Acta Astronautica*, Volume 102, 2014, Pages 81-88, ISSN 0094-5765, https://doi.org/10.1016/j.actaastro.2014.04.024.

[124] Ding, F., Liu, J., Shen, C., Liu, Z., Chen, S., Fu, X., "An overview of research on waverider design methodology," *Acta Astronautica*, Volume 140, 2017, Pages 190-205, ISSN 0094-5765, https://doi.org/10.1016/j.actaastro.2017.08.027.

[125] Maxwell, J.R., "Hypersonic Waverider Stream Surface Actuation for Variable Design Point Operation," 52nd AIAA/SAE/ASEE Joint Propulsion Conference, AIAA Propulsion and Energy Forum, (AIAA 2016-4706) https://doi.org/10.2514/6.2016-4706

[126] Maxwell, J.R., "Efficient Design of Viscous Waveriders with CFD Verification and Off-Design Performance Analysis," 53rd AIAA/SAE/ASEE Joint Propulsion Conference, AIAA Propulsion and Energy Forum, (AIAA 2017-4879) https://doi.org/10.2514/6.2017-4879

[127] Maxwell, J.R., Phoenix, A.A. "Morphable Hypersonic Waverider and Trajectory Optimized for Atmospheric Entry," AIAA SPACE and Astronautics Forum and Exposition, AIAA SPACE Forum, (AIAA 2017-5357) https://doi.org/10.2514/6.2017-5357

[128] Maxwell, J.R., "Morphing Hypersonic Waverider for Mars Entry," AIAA Astrodynamics, AIAA Paper No. AAS18-487, 2018.

[129] Anderson, J.D., Lewis, M.J., Kothari, A.P., Corda, S. "Hypersonic waveriders for planetary atmospheres," *Journal of Spacecraft and Rockets*, Vol. 28, No. 4 (1991), pp. 401-410. https://doi.org/10.2514/3.26259

[130] Sims, J.A., Longuski, J.M., Patel, M.R., "Aerogravity-assist trajectories to the outer planets," *Acta Astronautica*, Vol. 35, No. 1, pg. 297-306, 1995. https://doi.org/10.1016/0094-5765(94)00195-R.

[131] Lewis, M.J., McRonald, A., "Design of Hypersonic Waveriders for Aeroassisted Interpanetary Trajectories," *Journal of Spacecraft and Rockets*, Vol. 29, 5:653-660, 1992. https://doi.org/10.2514/3.11506

[132] Johnson, W.R., Longuski, J.M., "Design of Aerogravity-Assist Trajectories," *Journal of Spacecraft and Rockets*, Vol. 39, No. 1, 2002.

[133] Johnson, W.R., Longuski, J.M., "Aerogravity assist maneuvers: coupled trajectory and vehicle shape optimization," *Journal of Spacecraft and Rockets*, Vol. 44, No. 5, 2007.

[134] Lavagna, M., Povoleri, A., Finzi, A.E., "Interplanetary mission design with aero-assisted manoeuvres multi-objective evolutive optimization," *Acta Astronautica*, Vol. 57, No. 28, 2005. https://doi.org/10.1016/j.actaastro.2005.03.052.

[135] Knittel, J., *Aero-Assisted Spacecraft Missions Using Hypersonic Waverider Aeroshells*, Dissertation, University of Maryland, College Park, 2015.

[136] Rodi, P.E., Bennett, G., "High Lift-to-Drag Ratio Waveriders for Missions in the Martian Atmosphere," AIAA Paper No. 2012-3221, 2012. https://doi.org/10.2514/6.2012-3221

[137] Edelman, P.J., *Interplanetary mission design with applications to guidance and optimal control of aero-assisted trajectories*, Dissertation, Purdue University, 2016.

[138] Henning, G.A., Edelman, P.J., Longuski, J.M., "Design and Optimization of Interplanetary Aerogravity-Assist Tours," *Journal of Spacecraft and Rockets*, Vol. 51, No. 6, p. 1849-1856, 2014. https://doi.org/10.2514/1.A32881

[139] Chapman, D.R., *An Approximate Analytical Method for Studying Entry Into Planetary Atmospheres*, NASA R-11, 1959.

[140] Li, P., Chen, W., Zhou, H., "Quasi-equilibrium Glide Trajectory Design of Wave rider-Based Hypersonic Vehicle," IEEE ICMET 2010.

[141] Allen, H.J. and Eggers, A.J., *A Study of the Motion and Aerodynamic Heating of Missiles Entering the Earth's Atmosphere at High Supersonic Speeds*, NACA RM-A53D28, Aug. 1953.

[142] Allen, H.J. and Eggers, A.J., *A Study of the Motion and Aerodynamic Heating of Ballistic Missiles Entering the Earth's Atmosphere at High Supersonic Speeds*, NACA-TR-1381, 1958.

[143] Putnam, Z.R., Braun, R.D., "Extension and Enhancement of the Allen-Eggers Analytic Solution for Ballistic Entry Trajectories," AIAA Paper No. 2014-2381.

[144] Apollo Capsule Image, retrieved 2-Dec-2017. <https://www.kennedyspacecenter.com/-/media/DNC/KSCVC/Attraction-Images/Apollo-Saturn-V-Zone/Apollo-Capsule>

[145] Space Shuttle Orbiter Image, retrieved 2-Dec-2017. <https://www.nasa.gov/sites/default/files/thumbnails/image/s31-s-131.jpg>

[146] X-37 Image, retrieved 2-Dec-2017. <https://www.nasa.gov/centers/ames/images/content/68703main_subpage_x37.jpg>

[147] Dream Chaser Image, retrieved 2-Dec-2017. <https://www.nasa.gov/sites/default/files/2013-3230_0.jpg>

[148] Federal Aviation Administration *Returning From Space: Reentry*, Sect. 4.1.7.4, United States Government Printing Office, 2010.

[149] Van Driest, E.R., "The Problem of Aerodynamic Heating," *Aeronautical Engineering Review*, Oct. 1956, pg. 26-41.

[150] NASA Goddard Space Flight Center (GSFC) *Pulse of Snow and Sea Ice*, May 14, 2012, retrieved 8/20/2018. https://svs.gsfc.nasa.gov/cgi-bin/details.cgi?aid=3944

[151] Hayes, W.D., Probstein, R.F., *Hypersonic Inviscid Flow*, Dover, 2004.

[152] Sutherland, W., "The viscosity of gases and molecular force," *Philosophical Magazine*, S. 5, 36, pp. 507-531 (1893).

[153] Lees, L., "Laminar heat transfer over blunt-nosed bodies at hypersonic flight speeds," *AIAA Journal Special Supplement*, vol. 41, no. 7, pg. 356–366, 2003.

[154] Holman, J.P., *Heat Transfer*, 10th Ed., McGraw-Hill, ISBN 978-0073529363, 2009.

[155] Chapra, S.C., *Applied Numerical Methods with MATLAB: for Engineers & Scientists*, 3rd Ed., 2011. ISBN 978-0073401102

[156] Cox, R.N., Crabtree, L.F., *Elements of Hypersonic Aerodynamics*, Academic Press, NY, 1965.

[157] Hirschfelder, J.O., Curtiss, C.F., Bird, R.B., *Molecular Theory of Gases and Liquids*, John Wiley & Sons, New York, 1954.

[158] DeJarnette, F.R., Ford, C.P., Young, D.E., "A New Method for Calculating Surface Pressures on Bodies at an Angle of Attack in Supersonic Flow," AIAA 1979-1552, July 1979.

[159] Rubesin, M.W., Johnson, H.A., "A Critical Review of Skin-Friction and Heat-Transfer Solutions of the Laminar Boundary Layer of a Flat Plate," *Transactions of the American Society of Mechanical Engineers*, Vol. 71, No. 4, pg. 383-388, May 1949.

[160] Eckert, E.R.G., "Survey of Boundary Layer Heat Transfer at High Velocities and High Temperatures," WADC Tech. Rep., pp. 59-624, April 1960.

[161] Inoue, M., *Large-Eddy Simulation of the Flat Plate Turbulent Boundary Layer at High Reynolds Numbers*, Dissertation, California Institute of Technology, 2012.

[162] Deem, R.E., Murphy, J.S., "Flat Plate Boundary Layer Transition at Hypersonic Speeds," AIAA Paper No. 65-128, 1965.

[163] Hopkins, J.E., Jillie, D.W., Sorensen, V.L., "Charts for Estimating the Boundary-Layer Transition on Flat Plates," NASA Technical Note D-5846, June 1970.

[164] Churchill, S.W., "A Comprehensive Correlating Equation for Forced Convection from Flat Plates," *AIChE Journal*, vol. 22, p. 264, 1976.

[165] Lamb, J.P., Oberkampf, W.L., "Review and Development of Base Pressure and Base Heating Correlations in Supersonic Flow," *Journal of Spacecraft and Rockets*, Vo. 31, No. 1, 1995.

[166] Mehta, G.K., Strahle, W.C., "A Theory of the Supersonic Turbulent Axisymmetric Near-Wake Behind Bluff-Base Bodies," *AIAA Journal*, Vol. 15, No. 8, 1977.

[167] Chapman, D.R., "An Analysis of Base Pressure at Supersonic Velocities and Comparison with Experiment," NACA TR-1051, 1950.

[168] Moin, P., *Fundamentals of Engineering Numerical Analysis*, Cambridge: Cambridge University Press, 2010. doi:10.1017/CBO9780511781438

[169] Edquist, K.T., Dyakonov, A.A., Wright, M.J., Tang, C.Y., "Aerothermodynamic Design of the Mars Science Laboratory Backshell and Parachute Cone," AIAA Paper 2009-4078.

[170] Jenkins, Dennis R. (2007). *Space Shuttle: The History of the National Space Transportation System*, Voyageur Press. p. 524 pages. ISBN 0-9633974-5-1.

[171] Edquist, K.T., Dyakonov, A.A., Wright, M.J., Tang, C.T., "Aerothermodynamic Environments Definition for the Mars Science Laboratory Entry Capsule," AIAA 2007-1206, 45th AIAA Aerospace Sciences Meeting and Exhibit, Reno, Nevada, 8 - 11 January 2007.

[172] Dunn, M.G., Kang, S.W., "Theoretical and Experimental Studies of Reentry Plasmas," NASA CR-2232, April 1973.

[173] *ANSYS FLUENT Theory Guide*, ANSYS, Inc., November, 2011.

[174] Chou, S.Y. and Baganoff, D., "Kinetic Flux-Vector Splitting for the Navier-Stokes Equations," *Journal of Computational Physics*, Vol. 130, 1997, pp. 217–230.

[175] Menter, F.R., *Best Practices: Scale Resolving Simulations in ANSYS CFD*, V2.00, ANSYS, Inc., 2015.

[176] Smagorinsky, J., "General Circulation Experiments with Primitive Equations," *Monthly Weather Review*, Vol. 91, No. 3, pp. 99-164. https://doi.org/10.1175/1520-0493(1963)091

[177] Pope, S.B., "Ten questions concerning the large-eddy simulation of turbulent flows," *New Journal of Physics*, Vol. 6, No. 35, 2004.

[178] Oran, E.S., Boris, J.P., *Numerical Simulation of Reactive Flow*, Cambridge University Press, 2001.

[179] Wilcox, D.C. "Formulation of the k-w Turbulence Model Revisited," *AIAA Journal*, Vol. 46, No. 11 (2008), pp. 2823-2838. https://doi.org/10.2514/1.36541

[180] Wilcox, D.C. (1988), "Re-assessment of the scale-determining equation for advanced turbulence models," *AIAA Journal*, Vol. 26, No. 11, pp. 1299-1310.

[181] Launder, B.E., Spalding, D.B., "The Numerical Computation of Turbulent Flows," *Computer Methods in Applied Mechanics and Engineering*, Vol 3, pg. 269-289, 1974.

[182] Deardorff, J., "A numerical study of Three-Dimensional Turbulent Channel Flow at Large Reynolds Numbers," *Journal of Fluid Mechanics*, Vol. 41, No. 2, pp. 453-480., 1970. https://doi.org/10.1017

[183] Hickel, S., Egerer, C.P., Larsson, J., "Subgrid-scale modeling for implicit large eddy simulation of compressible flows and shock-turbulence interaction," *Physics of Fluids*, Vol. 26, No. 10, 2014. http://dx.doi.org/10.1063/1.4898641

[184] Beer, F.P., Johnston, E.R., DeWolf, J.T., Mazurek, D.F., *Mechanics of Materials*, 5th Ed., McGraw-Hill, 2009. ISBN 9780073529387

# Glossary

**Ablation** The transition of solid material to its gas phase with the absorption of thermal energy.

**Airbreathing engine** An engine that uses the oxygen in ambient air as its oxidizer. Examples include a jet engine, a ramjet, and a scramjet.

**Analytical method** A method for modeling physical phenomena using mathematical theory and closed-form solutions. In this context, it is used to describe methods in contrast to the numerical simulation of discretized geometry and systems of differential equations.

**Ballistic entry** The entry into a planetary atmosphere by a vehicle that generates zero aerodynamic lift forces.

**Ballistic coefficient** A metric that describes the rate of deceleration of a vehicle $\beta = m/(C_D S)$.

**Base** The aft end of a waverider.

**Calorically perfect gas** A gas for which the ratio of specific heat capacity at constant pressure is invariant with temperature.

**Capsule** An axisymmetric spacecraft with a large-radius, blunt forebody that contains passengers or cargo intended to land on a planet. The forebody is covered with an ablative heat shield to protect the spacecraft from the intense thermal environment during atmospheric entry.

**CFL number** A measure of the time step taken for the discrete solution of convective differential equations related to the transfer of information between cells. The CFL of a simulation refers to the maximum value of $(U_i/_i)_j$ for all $i^{th}$ directions and $j^{th}$ cells in the computational domain.

**CPU-hr** A measure of computational resources used in units of the product of a number of computing processors operating for a number of hours.

**Computational Fluid Dynamics (CFD)** The collection of methods used to approximate solutions to the governing equations of fluid dynamics (the Navier Stokes equations) using computers and discretized geometry.

**Critical Reynolds number** The value of the Reynolds number as a function of the distance from a leading edge that initiates the transition from laminar flow to turbulent flow.

**Degree of Freedom (DOF)** Each of a number of independently variable factors affecting the range of states in which a system may exist. In particular, any of the directions in which independent displacement or orientation may occur.

**Design point** The specific Mach number and orientation at which a waverider is designed.

**Design shock or flow field** The user-selected flow field and shock wave from which a waverider is designed.

**Entry parameter** A metric that describes the rate of descent of a vehicle $\xi = m/(C_L S)$.

**Entry vehicle** A spacecraft orbiting a planet or transiting between planets that passes through a planet's atmosphere and lands personnel or cargo on the planet's surface.

**Equilibrium chemistry** Chemical reactions occur over a sufficiently rapid time scale that the conversion between reactants and products is approximated as instantaneous in time and space.

**Explicit method** The time integration of a discrete system of equations using information at the present time to solve for the new state of the system at a future time.

**Fillet** A geometry-modification method of rounding a sharp edge in two dimensions with a uniform radius and tangent end conditions.

**Finite-Volume Method (FVM)** A method representing discretized governing equations by applying a bounded surface around a system subdomain and accounting for internal system properties and fluxes through the bounded surface.

**Implicit method** The time integration of a discrete system of equations using information at the present time and at a future time to solve for the state of the system at the future time.

**In-plane strain** The ratio of the tangential deflection of a surface to its length in the same direction.

**Laminar flow** A flow field with constant, smooth streamlines.

**Leading edge** The portion of a vehicle that is exposed to undisturbed free-stream air during flight. For high-speed vehicles, the leading edge may extend from wingtip to wingtip along the front limit of the planform.

**Lifting entry** The entry into a planetary atmosphere by a vehicle that generates aerodynamic lift forces.

**Load factor** The ratio of net forces on an entry vehicle to its weight.

**Low-Earth Orbit (LEO)** A region of the Earth's exosphere approximately 200-500km above sea level where ambient molecular densities are low enough for a satellite to sustain its orbit for days to years before aerodynamic drag slows it sufficiently to de-orbit.

**Morphing waverider** A waverider with a shapeable bottom surface that conforms to the stream surface of a design flow field as a function of Mach number. The leading edge, top surface, and planform remain rigid.

**Non-equilibrium chemistry** Chemical reactions occur over a time scale that requires resolution in space and time for a particular system.

**Non-equilibrium kinetics** A state of sufficiently sparse gas molecules such that the velocity probability distribution function does not match the Maxwell-Boltzmann equilibrium distribution function.

**Numerical simulation** The discretization of a system of governing differential equations and geometry solved as a set of algebraic equations used to approximate the solution to the original system. Numerical simulations are used to resolve complex geometry and detailed interactions such as turbulent fluid flow and chemical reactions in space and time.

**Off-design** The operational state of a waverider that does not correspond to its original design Mach number or orientation.

**On-design** The operational state of a waverider at its original design Mach number and orientation.

**Osculating flow fields** A collection of discrete, adjacent, independent flow fields. Osculating flow fields are used to approximate a continuum flow field for waverider design with greater degrees of freedom.

**Planform** The area and shape bounded by a top-down projection of a vehicle or its wings.

**Pyrolysis** The irreversible thermal decomposition of materials at elevated temperature.

**Rarefied flow** When the average distance between molecular collisions becomes comparable to a characteristic length scale of a system or larger. For a 10m reference length, rarefied flow is encountered by entry vehicles above approximately 90-100km altitude for Earth and Mars.

**Reduced-order model (ROM)** A method or collection of methods that use simpler approximations or incur lesser computational expense than more detailed models or those with more complexity. A ROM is usually obtained by a simplification of the physics, geometry, or assumptions of a system.

**Reference area** Denoted by $S$, the reference area is the planform area of a winged vehicle or the two-dimensional projection of the frontal area of a capsule, $\pi r^2$.

**Refractory metal** A class of metals with high service-temperatures and resistance to oxidation and wear. Examples include $W$, $Ta$, $Mo$, $Nb$, and $Re$.

**Species** The distinct type of a fluid or molecule: oxygen and nitric-oxide are two separate molecular species.

**Stagnation point** A point in a flow field where the local velocity of the fluid is zero. Stagnation heating refers to the maximum heating at the nosetip or the leading edge.

**Stratosphere** The portion of the Earth's atmosphere spanning approximately 12-50km in altitude.

**Streamline** A curve that is tangent to the velocity vector field of a flow.

**Stream surface** A surface emanating from a continuous seed curve through which flow does not penetrate.

**Thermal Protection System (TPS)** The heat mitigation material, structure, or system. For capsules, the TPS is an ablative heat shield. For the Space Shuttle, the TPS is UHTCs and ceramic heat shield tiles.

**Thermally perfect gas** A gas for which the ratio of specific heats is purely a function of temperature.

**Troposphere** The portion of the Earth's atmosphere spanning sea level to approximately 12km in altitude.

**Turbulent flow** A flow field with streamlines that fluctuate chaotically in space and time.

**Ultra-high-temperature ceramics (UHTCs)** A class of refractory ceramics with service temperatures exceeding $2,000$°C. Examples are $TiC$, $TiN$, $TaC$, $SiC$, and $WC$.

**Waverider** A waverider is a vehicle that flies at supersonic speeds on top of the shock that the vehicle itself creates. A waverider has an attached shock all along its leading edge, from wingtip to wingtip. The shock is a known shape for the Mach number at which the waverider is designed.

**WRAITH** The Waverider Reduced-order Analysis and Investigative Tool for Hypersonics is a collection of analytical models that predict pressure and viscous forces in hypersonic flow on a panelized vehicle surface mesh.